Optimisation of Hydroxyapatite (HAp) for Orthopaedic Application via the Chemical Precipitation Technique

By

Sharon Kehoe, B.Eng.,

This thesis is submitted to Dublin City University as the fulfilment of the requirement for the award of the degree of

Doctor of Philosophy

Supervisor:
Dr. Joseph Stokes, BA, BAI, PhD

School of Mechanical and Manufacturing Engineering
Dublin City University

September 2008

DECLARATION

I hereby certify that this material, which I now submit for assessment on the programme of study leading to the award of **Doctor of Philosophy** is entirely my own work and has not been taken from the work of others save and to the extent that such work has been cited and acknowledged within the text of my own work.

Signed: _____ I.D. Number: 99094916

Date: September, 2008

TO

My parents, for all the encouragement and support

ACKNOWLEDGEMENTS

There were a great number of people who helped make this journey possible. Foremost, I would like to express my sincere gratitude to my supervisor, Dr. Joseph Stokes, of the School of Mechanical and Manufacturing Engineering, Dublin City University, for his relentless encouragement, constructive guidance and words of motivation throughout the duration of this research study and moreover for the inspiration he provided to ensure the completion of this work. His expertise, availability to discuss ideas and willingness to give of his knowledge were instrumental. For this, I will be eternally grateful.

I would also like to express my thanks to Dr. Malika Ardhaoiu, of the Surface Engineering Group of University College Dublin for her support and guidance and also with the biological testing techniques used during this research. A special word of thanks also goes to Professor Saleem Hashmi, Head of School of Mechanical and Manufacturing Engineering. My appreciation is due to Dr. Aran Rafferty, Ceramics Research Officer and Dr. Tim Prescott, Senior Research Officer, for their helpful advice and training provided on the powder characterisation equipment. I also acknowledge the help provided by Dr. Gomathi Natarajan, of the School of Electronic Engineering, Dublin City University for her provision of time in training on X-ray diffraction analysis. A heartfelt thanks also to Dr. Khaled Benyounis of the School of Mechanical and Manufacturing Engineering for his invaluable advice on the models developed using the Design Expert software.

My special thanks to both Mr. Liam Domican and Mr. Michael May for their helpful discussions and technical support and assistance. Also, to Mr. Jim Barry of the workshop for his advice in the design of the experimental set-up and Hall flowmeter device manufactured for the purpose of this research.

The author would also like to acknowledge the research support provided by the Irish Research Council for Science, Engineering and Technology, funded by the National Development Plan. My sincere gratitude also, for the invaluable expertise and use of equipment at the various visits to the HAp producing Irish Industrial plant.

Last but not least, I would like to express my thanks to my godmother, Sr. Cora McHale, for all her heartfelt prayers. And especially to my sisters, brothers, brother in law, friends and colleagues for all their good wishes of encouragement and support over the last few years, which will always be remembered with deep gratitude.

Optimisation of Hydroxyapatite (HAp) for Orthopaedic Application via the Chemical Precipitation Technique

By

Sharon Kehoe, B.Eng.

ABSTRACT

Hydroxyapatite, (HAp), $Ca_{10}(PO_4)_6(OH)_2$, is a naturally occurring mineral found in the inorganic component of human bone and enamel. The constituent elements of HAp are primarily calcium and phosphorous, with a stoichiometric calcium to phosphorous ratio of 1.667 capable of promoting intimate bone growth onto femoral implants. HAp is rendered a bioactive material since it has the ability to promote such growth with rapid fixation in what is also considered an osteoconductive process. The performance, lifespan and quality of the resultant biological coating in vivo is largely dependent on the coating morphology, phase composition, particle size and crystallinity of the powders pre-coating application.

The present study aims to synthesise phase pure HAp powders via the wet chemical precipitation technique, in order to evaluate the critical process parameters and their effect (main and interaction) on controlling the final HAp powder characteristics, such as, phase composition, purity, crystallinity, crystallite size, lattice parameters, particle size and particle size distribution. These powders were synthesised with a view to satisfying regulatory requirements. These effects were quantified using Design of Experiments (Design Expert) to develop mathematical models, in terms of the chemical precipitation process parameters.

HAp possessing optimum powder characteristics for orthopaedic application via the thermal plasma spray technique can therefore be prepared using the following chemical precipitation process parameters: reaction temperature 60ºC, ripening time 48h and stirring speed 1500rpm using high reagent concentrations. In the case of HAp synthesis at a lower reaction temperature, synthesis under a controlled environment (inert atmosphere) is desirable in order to achieve a high level of crystallinity: with an increase from 86.32% synthesised at 20ºC to 95.19% synthesised at 60ºC. The presence of an inert atmosphere appears less critical at synthesis under increased levels of reaction temperature. Ripening time and stirring speed significantly affect the final phase purity. An increase in both the ripening time (0.5 - 48h) and stirring speed (600 - 1500rpm) can result in an increase of purity by 77.74% (21.15 – 98.89%). Crystallite size, lattice parameters and mean particle size were also optimised within the research to find desired settings to achieve results suitable for FDA regulations.

TABLE OF CONTENTS

Figures

Tables

1 INTRODUCTION

HAp, $Ca_{10}(PO_4)_6(OH)_2$, is composed primarily of calcium and phosphorous with hydroxide ions that are eliminated at elevated temperatures. HAp and other related calcium phosphate minerals have been utilised extensively as implant materials for many years due to its excellent biocompatibility and bone bonding ability and also due to its structural and compositional similarity to that of the mineral phase of hard tissue in human bones. HAp coatings have good potential as they can exploit the biocompatible and bone bonding properties of the ceramic, while utilising the mechanical properties of substrates such as Ti6-Al4-V and other biocompatible alloys. While the metallic materials have the required mechanical properties, they benefit from the HAp which provides an osteoconductive surface for new bone growth, anchoring the implant and transferring load to the skeleton, helping to combat bone atrophy.

Their Ca/P ratio of 1.52±2.0 makes them an excellent choice for most dental and orthopaedic application in the form of bioceramic coatings. The quality of a coating is closely dependent on the overall attributes and characteristics of the synthesised powders. Such attributes include phase composition, purity, crytsallinity, particle size, particle-size distribution, specific surface area, density and particle morphology. These important factors determine the resulting success of the HAp coating deposited onto orthopaedic implants through plasma thermal spraying. The chemical nature of HAp, however, lends itself to substitution, meaning that it is not uncommon for non-stoichiometric HAp to exist. The most common substitutions involve carbonate, fluoride and chloride substitutions for hydroxyl groups, while defects can also exist resulting in deficient HAp.

1.1 AIMS OF THIS STUDY

The aim of this research is to synthesise phase pure HAp powders via the wet chemical precipitation technique in order to evaluate the critical process parameters and their effect (main and interaction) on controlling the final HAp powder characteristics, such as, phase composition, purity, crystallinity, crystallite size, lattice parameters, particle size and particle size distribution. These powders will be synthesised with a view to satisfying regulatory requirements.

It is the goal of this work to apply Design of Experiments (DoE) to develop mathematical models, in terms of the chemical precipitation process parameters. These models will assist researchers, engineers and industry to achieve desirable HAp powder characteristics. This approach assures the highest reliability, lowers process start-up costs and improves powder quality. Furthermore, DoE reduces the numbers of experiments without any significance loss in the accuracy of the models developed. In addition, the developed models are useful in predicting the effect of each response (that is, powder characteristic). It will also aid in the selection of the optimum process parameters to maximise or minimise the various response.

The aim in developing these mathematical models using Fractional Factorial and Box-Behnken designs, with the aid of Design-Expert (V7) statistical software, is to predict the following responses:

- Phase purity.
- Crystallinity
- Crystallite sizes in the 002 and 300 plane.
- Lattice parameter ratio
- Particle size.

The developed models will be presented in various plots (such as, 3D plots and contour graphs). These plots and graphs will explain the effect of the chemical precipitation parameters and their interactions on the above-mentioned responses.

Another aim is to demonstrate the individual effect of a certain parameter on a given response at such values of the remaining parameters and hence to determine the optimal combination of the process input variables, based on the developed models and numerical optimisation, to achieve the desired criterion.

1.2 THESIS OUTLINE

The thesis is divided into a number of sections. Chapter two discusses human bone composition and its mechanical properties. The various methods for synthesising HAp are considered. The end product of synthetic bone produced, that is, HAp, is then analysed on account of the physical and mechanical properties attainable and compared against those desired to simulate biological apatite. This chapter also discusses the great effect of the process parameters using the chemical precipitation technique for the synthesis of high HAp purity and crystallinity and examines the effect of varying these parameters on other HAp powder characteristics, such as, crystallite size, lattice parameters, particle size, morphology and its biocompatible and rheological properties. The chapter finishes with an outline of the standards pertaining to the requirements in fully satisfying the regulations (such as, FDA).

Chapter three describes the process adopted to synthesise the HAp in this study via the chemical precipitation technique. An overview of the apparatus designed to allow for optimum control over the numerous precipitation parameters (such as, synthesis temperature, stirring speed, acid addition rate) is also outlined. The experimental equipment involved in the production of the HAp powders is presented along with its associated procedures. A description of the experimental designs and optimisation approach used in the current research is outlined in this chapter. The materials characterisation equipment used in the current investigation in order to characterise the HAp powder characteristics under the various experimental conditions are described with respect to HAp powder phase purity, crystallinity, crystallite size, lattice parameters, particle size and powder morphology. The equipment and methods for observing the rheological properties of the HAp in a slurry and powder form are also presented. An investigation to evaluate the *in vitro* behaviour of the synthesised powders is presented with a description of the cell studies and procedures outlined.

In chapter four, the experimental results and discussions are presented for the various HAp powders analysed in the comparative analysis of commercial HAp and for powders prepared under the various conditions based on the experimental designs (fractional factorial and box-behnken). The results show the phase composition (purity) and crystallographic properties (such as, crystallinity, crystallite size and lattice parameters) for HAp, as obtained through x-ray diffraction data. The particle size and particle size distribution results are determined using laser diffraction and discussed in contrast to their respective specific surface areas using the BET (Brunnaeur Emmett Teller) method. A morphological evaluation is presented for each HAp produced. The rheological properties (in slurry and powder) of the HAp are also discussed. The results investigating the biological responses of the prepared powders is also presented in this chapter.

Finally, chapter five summarises conclusions from the results found within the present research, and presents recommendations for future research. The future research includes expanding the current study to investigate the effect of all the chemical precipitation process parameters on the final HAp powder characteristics using response surface methodology and also investigating the HAp precipitation mechanisms of which the transformation process could be investigated under different conditions, including the optimal ones.

2 LITERATURE REVIEW

2.1 INTRODUCTION

Ceramic materials for orthopaedic applications were introduced in the 1970s, where failures of the biomaterials in use then, such as steel, cobalt alloys and poly (methyl methacrylate), began to be detected. Hence, attention was directed to ceramic materials in an attempt to find good bone integration features.

Ceramic materials used in surgery can either be bioinert or bioactive. A bioinert material, is one which does not illicit a reaction with the surrounding physiological tissue upon implantation. A bioactive material, however, is one that allows a specific biological response at its interface, thus enabling the formation of links between the tissues and said material. [1]

Hydroxyapatite, (HAp), and other related calcium phosphate minerals are used extensively to improve the integration of femoral implants into the hip joint. HAp appears the most promising due to its outstanding biological properties such us atoxicity, lack of inflammatory response and absence of fibrous or immunological reactions [1]. HAp possesses identical chemical composition and high biocompatibility with natural bone [2].

The bioactive nature of HAp gives rise to a favorable reaction product, through a chemical transformation of its starting material to the desired final product. Subsequently, when HAp comes in contact with physiological fluids, a chemical reaction towards the production of newly formed bone takes place, in what is also

termed an osteoconductive process [1]. Bioactivity is related to a modification of the surface of the material with formation of naturally induced; biologically equivalent HAp as a result of dissolution, precipitation and ion exchange reactions with the physiological environment. This ability to bond to bone tissue without the formation of a fibrous tissue layer at the bone - implant interface is extremely important since it guarantees the fixation and stabilisation of implants and prostheses. The bone - implant interface mimics the type of interface that is formed when natural tissues repair themselves; it is dynamic in its nature, changes with time and requires a controlled degree of chemical reactivity of the ceramic [1]. Hence, the clinical advantage of HAp is due to its bioactive characteristics, which is dependent upon its synthetic structure such as chemical stoichiometry, crystallinity and surface morphology [1]. HAp has many crystallographic features that are similar to those of natural bone tissue; although they show insufficient mechanical reliability for medical applications where high loads are required [1].

Thermal spray processes have frequently been used to deposit functionally biomedical active coatings, such as HAp, onto prosthetic implants [3]. Kweh et al. [2] confirm from their investigation, that the quality of a HAp coating onto substrate is closely dependent on the overall attributes and characteristics of the synthesised powders. These attributes include particle size, particle-size distribution and particle morphology. These attributes help to determine the flow characteristics of the HAp particles in the powder-feeding systems and their subsequent melting behaviour in the plasma jet. Consequently, the use of powder particles with spherical geometry and narrow size distributions so as to induce excellent heat transfer and consistent melting capabilities, increase the deposition efficiency and decrease coating porosity [2]. Spherical powders in general have better rheological properties than irregular powders and, thus, produce better coatings for femoral implants [4].

Several attempts to determine the exact composition of HAp via chemical analysis were undertaken in the first half of the 18^{th} century. About a century later, the current concepts of synthesising materials comprising of the various calcium phosphate crystal phases was introduced [5]. Most calcium phosphates are classified as

resorbable biomaterials. This means that under physiological conditions they will dissolve. The benefit of calcium phosphate biomaterials is that the dissolution products can be readily assimilated by the human body.

The following section will discuss human bone composition and its mechanical properties. The various methods of synthesising HAp will also be considered, highlighting the advantages and disadvantages associated to each technique for industrial application. The end product of synthetic bone produced, that is, HAp, will then be analysed on account of the physical and mechanical properties attainable and compared against those desired of natural bone.

2.2 BIOLOGICAL APATITE

2.2.1 Natural Human Bone Mineral

Precise knowledge of the physical, chemical, and mechanical properties of natural human bone is critical for the development of bone-like materials. The study of biological apatite (that is, human bone mineral) has been widely investigated. As a result, their chemical composition and structure is well understood. Natural human bone has a varied arrangement of material structures at many length scales which work in harmony to perform diverse mechanical, biological and chemical functions; such as structural support, protection and storage of healing cells, and mineral ion homeostasis. Scale is of importance in discussing bone architecture as the structure is hierarchical and complex. In order to understand the mechanical properties of bone material, it is important to understand the structural relationship between them at the various levels of hierarchical structural organisation This section therefore, outlines the various levels associated with the hierarchical structure of human bone, the chemical composition for the biological apatite mineral (carbonated apatite), the physiology of bone, bone remodelling, and biological responses.

2.2.2 Hierarchical Structure Of Bone

Despite the variety of external forms, the internal structure of bone is relatively consistent. Bone structure is hierarchically organized, which means that bone displays different structural entities at different length scales [6, 7]. Four structural levels of hierarchy can be distinguished in adult human bone. These levels will be denoted as the continuum level (or level 0), tissue level (level 1), cellular level (level 2) and molecular level (level 3). The structural entities at each level will be denoted as the macrostructure, mesostructure, microstructure and nanostructure, respectively. The hierarchical structural organisation in human bone is summarised in Figure 2-1 below.

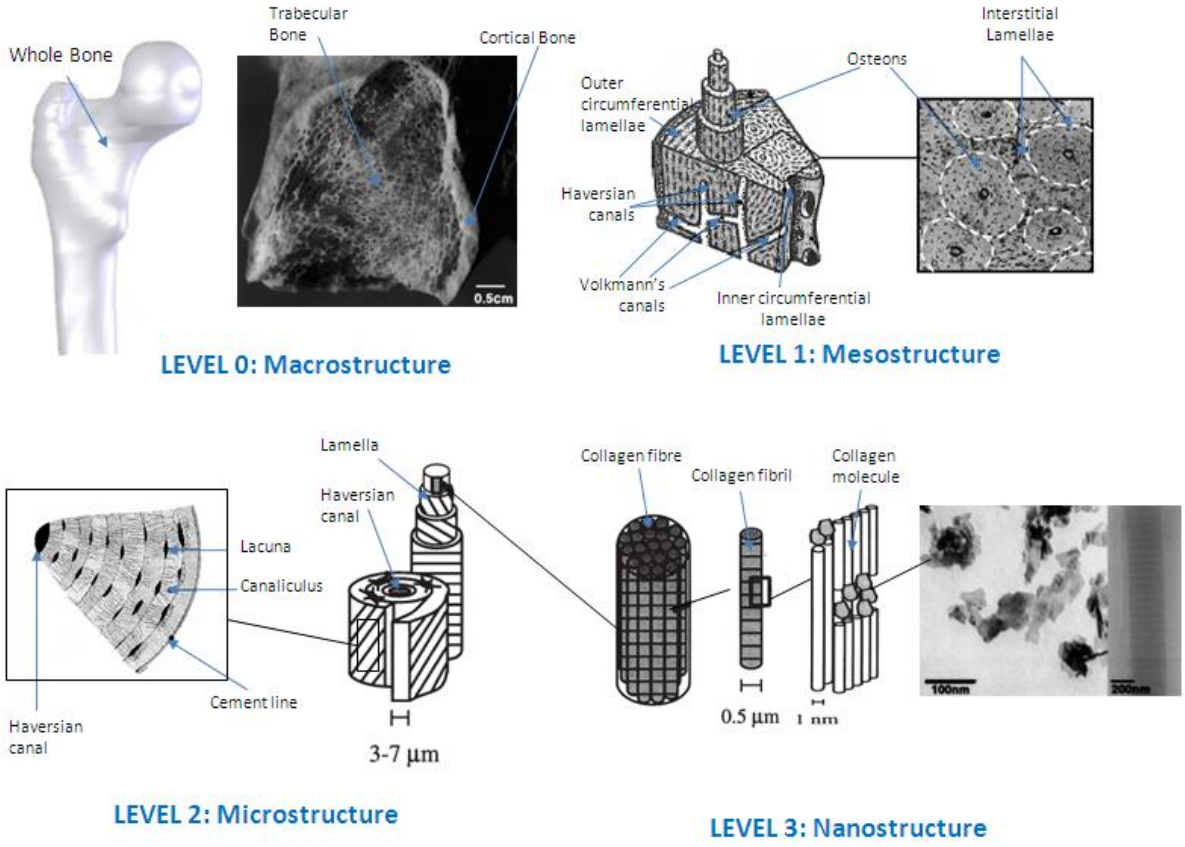

Figure 2-1: Hierarchical structural organisation of bone: Level 1: cortical and cancellous bone; Level 2: osteons with haversian systems and lamellae; Level 3: collagen fiber assemblies of collagen fibrils and Level 4: bone mineral crystals, collagen molecules, and non-collagenous proteins. Adapted from [6, 8, 9]

2.2.3 Macrostructure

At the continuum level, the scale of 5 mm and higher, the bone structure is classified according to its porosity. The two classifications are cortical (or compact) bone and trabecular (or cancellous) bone. Cortical bone has a porosity ranging between 5% and 10%, and it is usually found along the exterior shaft section of long bones. Cortical bone forms the outer shell around the trabecular bone in joints and in vertebrae [10]. Trabecular bone has a porosity ranging from 75% to 95%. It is usually found in cubicoidal bones (such as, vertebrae), flat bones (such as, the pelvis) and the end of long bones (such as, the femur). The non-mineralized spaces within trabecular bone contain bone marrow, which is a tissue composed of blood vessels, nerves and various types of cells. Cortical bone accounts for about 80% of the total skeletal mass while

trabecular bone constitutes some 70% of the skeletal volume. The anisotropic structure of bone leads to mechanical properties that exhibit directionality. This directionality results from the fact that bone has evolved to be both tough and stiff, two competing properties which are optimised in bone but with an inherent loss in isotropy. Nevertheless, bone exhibits extraordinary mechanical properties, displaying both viscoelastic and semi-brittle behaviour. The microstructure produced by the compaction of cancellous bone is composed of irregular, sinuous convolutions of lamellae. In contrast, the microstructure of cortical bone is composed of regular, cylindrically shaped lamellae. Therefore, reliable differentiation can only be achieved by microscopy methods.

2.2.4 Mesotructure

At the tissue level, the scale of 100 μm to 1 mm, major differences can be identified within the cortical and trabecular structures. Cortical bone is composed of osteons or Haversian systems. The osteons (150 to 300 μm in diameter and up to 3 to 5 mm in length) are embedded in a matrix of lamellar bone known as interstitial lamellae (see Section 2.2.) [8]. The central cavity inside an osteon is known as the Haversian canal. Haversian canals are typically 40 to 50 μm in diameter and run along the long axis of a bone. Normally a blood vessel (15 μm in diameter) as well as nerve terminations are found inside Haversian canals. Volkmann's canals are short transverse channels connecting the Haversian canals. These canals also contain blood vessels and probably nerves [10]. The mesostructure of trabecular bone is composed of plates and struts called trabeculae. Sometimes trabeculae appear organized into orthogonal arrays, but they are often more randomly arranged. Each trabecula is about 200 μm thick. Rarely, it is possible to find trabeculae thick enough to contain a blood vessel and some osteon-like structure. Within a trabecula, one can find trabecular packets, which are the product of new tissue formed after remodelling. A typical trabecular packet is about 50 μm thick and 1 mm long.

2.2.5 Microstructure

At the cellular level, the scale of 5 to 50 μm, two types of bone can be found: woven bone and lamellar bone. Woven bone is a poorly organised tissue and may usually be found in adults post fracture injury. With maturation, the woven bone is converted into lamellar bone. Lamellar bone, adversely, is a slowly formed, highly organised bone tissue consisting of lamellae. The lamellae are bands or layers, 3 to 7 μm thick, forming an anisotropic matrix of mineral crystals and collagen fibers. Woven bone may become more highly mineralized than lamellar bone, which may help to compensate for its lack of organisation [10]. Trabecular packets and osteons are formed of lamellae and attached to the bone matrix by cement lines. The cement lines are found where bone resorption ends and bone formation begins. They are about 1 to 5 μm in thickness. The "porosities" at this level are identified as lacunae (ellipsoidal holes) and canaliculi (micro-channels) (refer to Figure 2-1). Canaliculi are about 0.2 μm in diameter [11].

2.2.6 Nanostructure

At the molecular level, the scale of 100 nm and smaller, there exists three main materials of importance, such as biologic apatite crystals, collagens, and non-collagenous organic proteins. The mature crystals are not needle-shaped, but plate-shaped [6, 8]. Plate-like biological apatite crystals of bone occur within the discrete spaces within the collagen fibrils, thereby limiting the possible primary growth of the mineral crystals, and forcing the crystals to be discrete and discontinuous. The mineral crystals grow with a specific crystalline orientation—the *c* axes of the crystals are roughly parallel to the long axes of the collagen fibrils [6, 8]. The average lengths and widths of the plates are 50 x 25 nm. Crystal thickness is 2–3 nm [6, 8]. The nanocrystalline bone apatite has small but significant amounts of impurities such as HPO_4, Na, Mg, citrate, carbonate and K [8]. The carbonate apatite crystal, not only exhibit a hexagonal crystal structure but is shown to produce x-ray diffraction patterns, analogous to that of HAp [6]. An explanation for their plate-like structure is proposed by Weiner et al. [6] in that they grow via an octacalcium phosphate transition phase. Octacalcium phosphate crystals (explained in greater depth in

Section 2.5.4) are plate-shaped and have a structure very similar to apatite, except for the presence of a hydrated layer.

2.2.7 Chemical Composition Of Human Bone Mineral

Natural bone can be considered to comprise of both organic and inorganic material. Moreover, 90 – 95% of the organic component consists of collagen whilst the inorganic component consists primarily of calcium and phosphate [12, 13].

A typical wet cortical bone is composed of 25 wt. % organic phase (that is, the matrix), 62 wt. % inorganic phase (that is, carbonated apatite; HAp), 10 wt. % water and 3wt. % residual (See Figure 2-2). The organic phase consisting mainly of collagen laid down in the form of fibres aid in the provision of flexibility to bone. As discussed previously, the inorganic phase consists of submicroscopic crystals of an apatite of calcium and phosphate, whose crystal structure resembles that of carbonate HAp and other mineralised phases, such as, chlorapatite (ClAp), fluorapatite (FAp), sodium-containing apatite and magnesium-containing apatite. The mineral phase is made of a continuous cellular structure, which gives good mechanical strength. HAp is the main mineral constituent for bone, dentin and teeth. [12, 13]

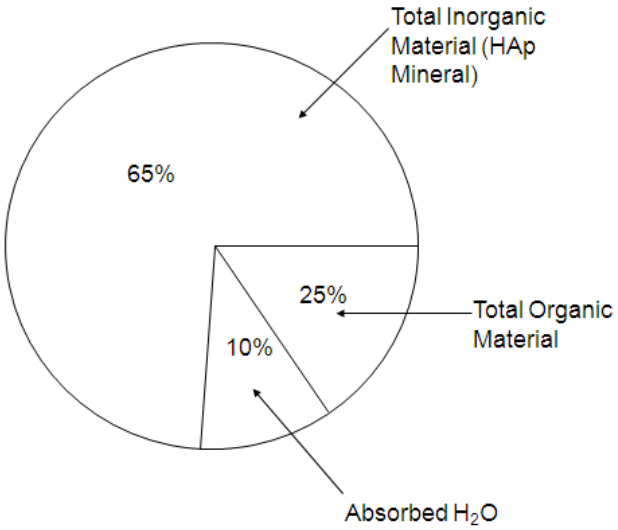

Figure 2-2: Chemical compositional analysis of human bone

As an estimate per weight, bone tissue is composed of 25% water, 43% mineral, 29% collagen and 3% of non-collagenous organic molecules (refer to Figure 2-3) [10]. Bone stores 99% of the total body calcium while the remaining 1% circulates in the blood [8].

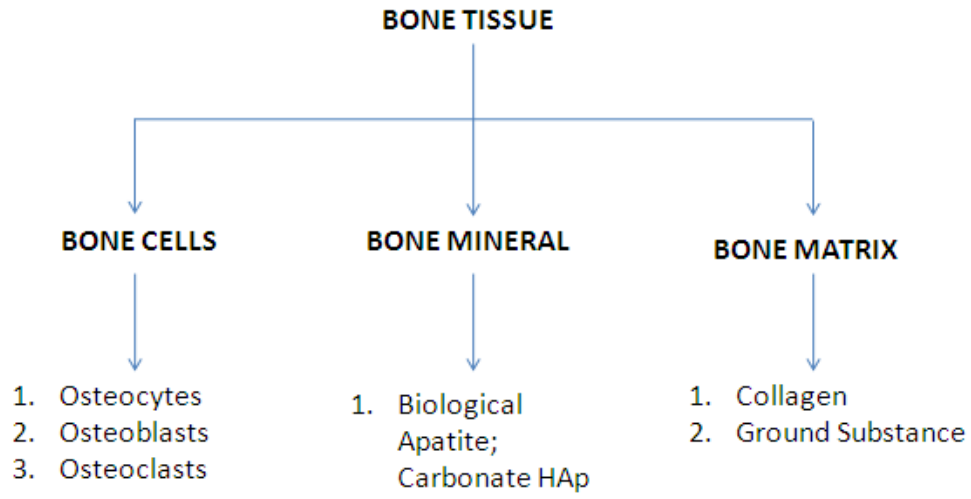

Figure 2-3: Comportments of human bone tissue

The inorganic component of human bone consists of calcium compound, as identical to synthetic carbonated HAp, made up of calcium ions, phosphate ions and hydroxyl ions in the ratio of the chemical formula, $Ca_{10}(PO_4)_6(OH)_2$. The constituent elements within bone mineral are given in Table 2-1. Mg, Na, K and carbonate ions are also present in bone salts, although they are not organised into specific crystals. Fluid Ca-P compounds in the matrix are transformed to HAp.

Table 2-1: Composition of the mineral phase in human bone. Adapted from [12 - 14]

Mineral Component	Chemical Formula	Enamel	Bone
Constituents (wt. %)			
Calcium	Ca^{2+}	36.0	24.5
Phosphorous	P	17.7	11.5
Ca/P molar ratio		1.62	1.65
Carbonate	CO_3^{2-}	3.2	5.8
Sodium	Na^{+}	0.5	0.7
Magnesium	Mg^{2+}	0.44	0.55
Potassium	K^{+}	0.08	0.03
Chloride	Cl^{-}	0.30	0.10
Fluoride	F^{-}	0.01	0.02
Total Inorganic (mineral)		**97.0**	**65.0**
Total Organic		**1.0**	**25.0**
Absorbed H_2O		**1.5**	**9.7**
Trace elements	Sr^{2+}, Pb^{2+}, Zn^{2+}, Cu^{2+}, Fe^{3+}		

While the main mineral components forming human bone are calcium (36.7 wt. %) and phosphorous (16.0 wt. %) with trace amounts of other minerals [15]; a significant amount of carbonate (7.4 wt. %), also appears to be present within the biological apatite, bone. Slosarczyk et al. [15] confirm that biological apatites present in; bone; dentin and enamel contain different amounts of carbonate 7.4: 5.6: 3.5 wt% respectively. The presence of CO_3^{2-} in their structure is of paramount importance; as it is the main source of lattice distortion, creating microstresses and crystalline defects in its vicinity which, in turn, play a fundamental role in its solubility. As a consequence, synthetic apatites aimed at emulating the biological scenario should exhibit small particle sizes and the presence of CO_3^{2-}[1]. The apatite crystals which form natural bone are smaller than 500 Å (nm) in size. This is a critical factor in understanding the solubility of biological apatites and the continuous bone regeneration due to constant dissolution–crystallisation cycles. [1]

On the other hand, the organic component of bone matrix comprises mainly of type I collagen; a fibrillar protein formed from three protein chains, wound together in a

triple helix. Collagen type I is laid down by bone forming cells (osteoblasts) in organised parallel sheets (lamellae) and subsequently the collagen chains become cross-linked by specialised covalent bonds (pyridinium cross-links) which help to give bone its tensile strength [12, 16]. When bone is formed rapidly, the lamellae are laid down in a disorderly fashion giving rise to "woven bone", which is mechanically weak and easily fractured. Bone matrix also contains small amounts of other collagens and several non-collagenous proteins and glycoproteins. Some of these, such as osteocalcin, are specific to bone, whereas others, such as osteopontin and fibronectin and various peptide growth factors are also found in other connective tissues. The function of non-collagenous bone proteins is unclear, but it is thought that they are involved in mediating the attachment of bone cells to bone matrix, and in regulating bone cell activity during the process of bone remodelling. The organic component of bone forms a framework upon which mineralisation occurs. During bone formation, osteoblasts lay down uncalcified bone matrix (osteoid) which contains the components described above and small amounts of other proteins, which are adsorbed from extracellular fluid. After a lag phase (~ 10 days), the matrix becomes mineralised, as HAp crystals are deposited in the spaces between collagen fibrils. Mineralisation confers upon bone the property of mechanical rigidity, which complements the tensile strength, and elasticity derived from bone collagen [16].

2.2.8 Human Bone Physiology

In any specimen of bone, three functionally distinct cell types are present; osteocytes, osteoblasts, and osteoclasts (refer to Figure 2-4). An overview for each cell type is described as follows [12, 17, 18]:

A. Osteocytes

Osteocytes are small, inactive cells, seemingly isolated from one another in individual lacunae. Inconspicuous cell processes extend out through tiny canaliculi and provide gap-junctional contact among neighbouring osteocytes as a means of communication and nutrient supply.

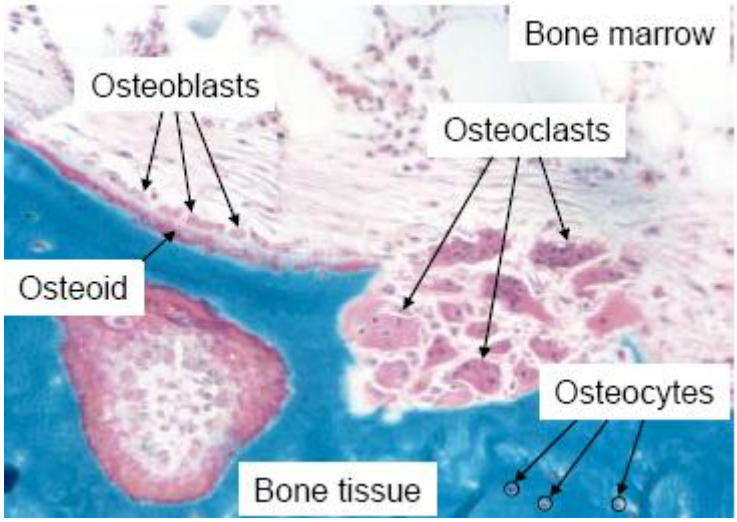

Figure: 2-4: Bone physiology. Osteoclasts are cells 20-100 μm in diameter that resorb old bone. Osteblasts are 10 μm in diameter and form new bone. Osteocytes are encased osteblasts that sense mechanical stimulus. Adapted from [18]

B. Osteoblasts

Osteoblasts (bone-forming cells) are small cuboidal cells, up to 10 μm in diameter, usually found lying adjacent to one another upon lamellae they have just secreted. Osteoblasts synthesise and deposit uncalcified new bone matrix (or osteoid). They are active in bone development and also in bone remodelling. During remodelling, these cells radially refill the gap open by the osteoclasts at a rate of about 1 μm per day (formation rate). Populations of osteocytes and osteoblasts may be interchangeable, reflecting different stages in the activity of individual cells. That is, active osteoblasts that become enclosed in bone may adopt the resting osteocyte form, while osteocytes which are released from their bony matrix (by osteoclast activity) may become active osteoblasts.

C. Osteoclasts

Osteoclasts (bone-removing cells) are large cells with multiple nuclei, typically 20 to 100 μm in diameter, each one typically sitting alone within a small hollow (Howship's lacuna) that it has just made by "eating" away the adjacent bone matrix. These cells secrete acids and enzymes to break down the mineralized bone matrix. Osteoclasts

remove pre-existing bone. They erode bone structure as they make their way through the bone matrix at a rate of about 40 μm per day (resorption rate) [18]. They are active in bone development and also in bone remodelling. Osteoclasts are more closely related to macrophages than to osteocytes or osteoblasts. They form a distinct cell population derived from the same precursor cells as macrophages.

2.2.9 Bone Remodelling By Human Bone Cells

Bone, as a living tissue, is continually adapting to changes in the physical environment. Throughout an individual's lifetime, old bone is removed (resorption) and new bone is added (formation). In human adults, 5% of cortical bone and 25% of trabecular bone is replaced every year by remodelling [10].

From a physiological standpoint, bone modelling can be defined as the reshaping of bone by independent action of osteoblasts and osteoclasts. The modeling and remodeling processes of human bone are not indifferent at cellular level. They are based on the separate actions of bone resorbing cells, called osteoclasts, and bone forming cells, called osteoblasts [17, 19]. The remodeling process begins at a quiescent bone surface with the appearance of osteoclasts. These are large multinucleated cells that form by fusion of mononuclear precursors of haemotopoetic origin. They attach to the bone tissue matrix and form a ruffled border at the bone/osteoclast interface that is completely surrounded by a "sealing" zone. Thus the osteoclast creates an isolated microenvironment. Subsequently the osteoclast acidifies the microenvironment and dissolves the organic and inorganic matrices of the bone. For a brief period after this resorptive process stops, osteoblasts appear at the same surface site. The osteoblasts derive from mesenchymal stem cells found in the bone marrow, periosteum and soft tissues. They deposit osteoid and mineralise it, so actually forming new bone. Some of the osteoblasts are encapsulated in the osteoid matrix and differentiate to osteocytes. Remaining osteoblasts continue to synthesize bone until they eventually stop and transform to quiescent lining cells that completely cover the newly formed bone surface. These lining cells are highly interconnected with the osteocytes in the bone matrix through a network of canaliculi. It appears that osteoclasts and osteoblasts closely collaborate in the remodeling process in what is

called a Basic Multicellular Unit (BMU) [17]. This indicates that a coupling mechanism must exist between formation and resorption. The nature of this coupling mechanism, however, is not known. The organisation of the BMU's in cortical and trabecular bone differs, but these differences are mainly morphological rather than biological. In cortical bone, the BMU forms a cylindrical canal of about 2000 mm long and 150-200 mm wide [17]. It gradually burrows through the bone with a speed of 20-40 mm/day [17]. In the tip, on the order of ten osteoclasts dig a circular tunnel (cutting cone) in the dominant loading direction. They are followed by several thousands of osteoblasts that fill the tunnel (closing cone) to produce a (secondary) osteon of renewed bone. In this way, between 2% and 5% of cortical bone is remodelled each year [17]. The remodeling process in trabecular bone is mainly a surface event. Due to the much larger surface to volume ratio, it is more actively remodelled than cortical bone, with remodeling rates that can be up to 10 times higher. Again osteoclasts come first in the process. They travel across the trabecular surface with a speed of approximately 25 mm/day, digging a trench rather than a tunnel, with a depth of 40-60 mm [17]. Like in cortical bone they are followed by osteoblast bone formation. Active remodeling sites cover areas of varying sizes from as small as 50×20 mm up to 1000×1000 mm [17] (refer to Figure 2-5). The trabecular BMU can be regarded as half a cortical BMU. The resulting structure that is formed is called a trabecular osteon or hemi-osteon. The cellular activities of osteoclasts and osteoblasts in modeling are basically similar to those in remodeling. However, in this case formation and resorption are not balanced, which causes changes in the micro-architecture. It can even occur that the activities of osteoclasts and osteoblasts are entirely uncoupled. Indeed, complete unloading may cause resorption not to be followed by formation. That bone formation is not necessarily preceded by resorption can be concluded from the observation that lining cells at the bone surface can transform back to bone forming osteoblasts.

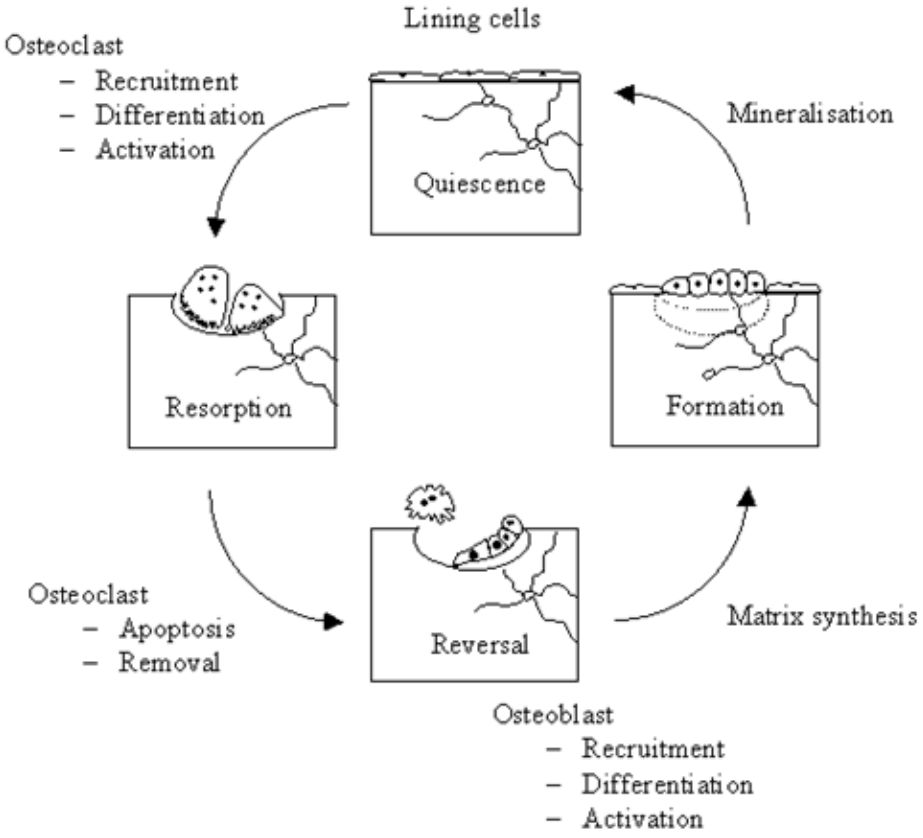

Figure 2-5: The bone remodeling cycle

2.2.10 Mechanical Properties Of Human Bone

The mechanical properties of the macrostructural form human bone (that is, trabecular and cortical) have been studied greatly; in terms of compressive strength, tensile strength, Young's modulus, hardness and fracture toughness. Overall, the differences between the mechanical properties in cancellous bone are much broader than those in cortical bone and indeed may vary by a factor of 2–5 from bone to bone [8]. To a great extent, differences between whole bones may be explained by the variance in their structure and mechanical function.

In cortical bone the mechanical properties are influenced greatly by the porosity, the mineralisation level and the organization of the solid matrix. The mechanical properties of human cortical bone from the tibia, femur, and humerus have been found to vary between subjects, although the density remains the same. In human cancellous

bone, by contrast, there is no difference in the mechanical properties of the humerus, the proximal tibia, and the lumbar spine. [8]

The mechanical properties are largely affected *in vivo*, with the orientation of bone specimen, which may be defined as longitudinal (running parallel to the predominant osteon ligaments), or transverse (through the osteon section) [12, 13]. An osteon defines a central long axis about which mineral-containing fibrils are arranged into lamellar sheets running helically with respect to the osteon. The mineral-containing fibrils are indeed the apatite-phase, forming needle-like crystals, which are orientated to the collagen fibre matrix [13].

Other factors, such as, humidity, mode of applied load, direction of the applied load and location of bone within the body also has an impact upon the mechanical properties of bone. Moreover, strength and other mechanical properties of bone depend upon bone density, porosity, and the molecular structure and arrangement of its constituent apatite crystals within their collagen matrix [13]. Typical mechanical properties of human bone are provided in Table 2-2.

Table 2-2: Mechanical properties of human femoral (cortical) bone tissue [12, 13]

Mechanical Properties	Test direction related to bone axis	
	Parallel	Normal
Tensile Strength (MPa)	124 - 174	49
Compressive Strength (MPa)	170 - 193	133
Young's Modulus (GPa)	17 – 18.9	11.5
Micro Hardness (VPN)	30-60	-
Fracture Toughness (MPa $m^{1/2}$)	2-12	8
Bending Strength (MPa)	160	
Shear Strength (MPa)	54	
Ultimate Tensile Strain (UTS)	0.014 – 0.031	0.007
Ultimate Compressive Strain	0.0185 – 0.026	0.028
Yield Tensile Strain	0.007	0.004
Yield Compressive Strain	0.010	0.011

2.3 SYNTHETIC APATITE

2.3.1 Hydroxyapatite (HAp) Calcium Phosphate

Calcium phosphate in the form of crystallized HAp and/or amorphous calcium phosphate (ACP) provides stiffness to the bone [20]. The mechanical properties of natural human bone depend largely on the humidity of its surrounding environment [20]. HAp ceramics do not exhibit any cytotoxic (cell-killing) effects; rather it shows excellent biocompatibility with hard tissues and also with skin and muscle tissues. Moreover, HAp can bond directly to bone [2, 12, 13, 20]. The benefits of HAp materials in coated implants have been widely acknowledged, but the occurrence of several poor performances such as improper melting of the feedstock after spraying, reproducibility and satisfying biomedical requirements has generated concerns over the consistency and reliability of thermally sprayed HAp coatings [21]. Recent investigations using HAp coatings have shown that process related variability has a significant influence on coating characteristics such as phase composition, structure and chemical composition, and performance such as bioresorption, degradation and bone apposition [2]. Variation in process parameters such as powder morphology can induce microstructural and mechanical inconsistencies that have an effect on the service performance of the coating [21, 22].

Ca/P ratios from 1.5 - 2.0, of HAp, are commonly used for orthopaedic applications in the form of bioceramic coatings [1]. The ideal Ca/P ratio for stoichiometric (that is, pure, single phase) HAp is 1.667 and the theoretical density is 3.156g cm^{-3} [12, 13, 23]. However, Suchanek et al. [24] reports that the Ca/P ratio does not significantly influence the grain growth of the HAp ceramics. Many studies conducted around the synthesis of HAp, show that a pH > 9.0 provides an appropriate environment for the formation of stoichiometric pure HAp powders [2]. HAp is the most stable calcium phosphate salt at physiological temperatures.

2.4 TECHNIQUES FOR PREPARING SYNTHETIC HAp

The various methodologies employed to produce synthetic HAp are discussed in this section to provide the necessary background information with respect to HAp powder production techniques, used to date. It is important to note that each method is greatly dependent on their synthetic starter / raw materials [23]. Bernard et al. [25] investigated the effect of purity of raw materials on the end HAp product. . It was established that the stoichiometry (that is, optimum concentration) of the HAp precipitate and its purity post thermal treatment, depends on the quality of the raw materials used. The production of synthetic ceramic HAp powders may be classified under four main headings:

i. Wet Chemical Synthesis (such as, Precipitation, Hydrothermal, Hydrolysis and Sol-Gel Techniques)
ii. Dry Chemical Synthesis (such as, solid-state reactions, mechanochemical synthesis)
iii. Vapour Phase Reactions (such as, spray and freeze-drying)
iv. Novel Techniques

Since the present research utilises the wet chemical precipitation method to synthesise phase pure HAp, this method is discussed in detail, with an overview of other possible synthetic routes for its synthesis. A comprehensive discussion of all of these techniques and the kinetics of precipitation are explained in Kehoe [26]. In this work, the advantages and disadvantages of each technique are considered, and compared against that of the wet chemical precipitation method.

The main advantage associated to the wet process, is that its by-product consists primarily of water and the probability of contamination during processing is very low. Low processing costs has also been reported. Its disadvantage is that the resulting product can be greatly affected by even a slight difference in the reaction conditions. The dry process, on the other hand shows high reproducibility in spite of the high risk of contamination during stages of milling and long heat treatment times [2, 13, 27].

2.4.1 Chemical Precipitation Route

In the precipitation route, HAp powders are obtained from a chemical reaction of inorganic oxide solutions [23]. The two most popular ways in precipitating HAp are described in the two reactions below [2, 23, 28]:

A. Reaction 1

The precipitation method for the reaction of orthophosphoric acid with calcium hydroxide:

$$10Ca(OH)_2 + 6H_3PO_4 \rightarrow Ca_{10}(PO_4)_6(OH)_2 + 18H_2O \qquad \textit{Equation (2-1)}$$

B. Reaction 2

The precipitation method for the reaction of diammonium hydrogen phosphate with calcium nitrate:

$$10Ca(NO_3)_2 + 6(NH_4)_2HPO_4 + 8NH_4OH \rightarrow Ca_{10}(PO_4)_6(OH)_2 + 20NH_4NO_3 + 6H_2O \qquad \textit{Equation (2-2)}$$

Reaction 1 is simple, cheap, suitable for large scale industrial production and non-polluting by nature, but often leads to the production of non-stoichiometric HAp, which creates subsequent problems during sintering (thermal decomposition of non-stoichiometric HAp leads to TCP when the Ca/P molar ratio < 1.67), or to CaO when the Ca/P molar ratio > 1.67. In contrast, Reaction 2 is expensive to produce and polluting by nature, in that it's by products must be removed. The quality of the initial reagents also play an important role in obtained high quality phase pure HAp. Synthesis, based on Reaction 1 has demonstrated that the purity and the properties of the chemicals and process parameters, such as, reagent addition flow rate, stirring rate, pH and reaction temperature all have a significant influence on the final quality of the HAp in relation to its crystallinity, crystallite size, morphology, particle size distribution, density and surface area. Another study has shown the effect of ripening time on crystallinity and sinterability and mechanical properties for dense HAp can be related to the initial reagent properties.

HAp synthesised by work conducted by Kweh et al. [2] using Reaction 2, have found that the reaction temperature, the reactant concentrations, rate of mixing the reactants

and the residence time can affect the overall characteristics of the HAp produced. The research also found that other phases can be produced with different reaction pH values.

HAp with a Ca/P molar ratio, ranging from 1.5 to 1.667 ($0 \leq x \leq 1$) using the conventional aqueous precipitation method from the addition of a diammonium phosphate solution ($(NH_4)_2HPO_4$) into a reactor containing a calcium nitrate solution was prepared by Raynaud et al. [22]. The device implemented was fully automated with the reactor placed in an argon atmosphere under dynamic flow in order to prevent any presence of CO_2, which could result in carbonate apatite formation. In this study, pH and temperature of synthesis were the preponderant parameters for the control of the precipitate composition.

Overall, precipitation techniques can produce small particle size and high-purity HAp powders, when the precipitation system and conditions are well controlled to obtain a reproducible precipitate. The important precipitation process variables include solution concentration (Ca/P ratio), pH, acid addition rate, stirrer speed, temperature, reaction time and atmospheric condition. [2]

The overall production routes for both precipitation reactions are outlined in Figure 2-6, while production routes concerning the hydrothermal [23, 28, 29], hydrolysis [30], sol-gel [31], solid-state [32 - 34], spray-drying [35] and freeze-drying [36, 37] techniques, as well as other various novel synthesis routes [38 – 42] for preparing HAp using novel precursor material [43], are outlined in Kehoe [26].

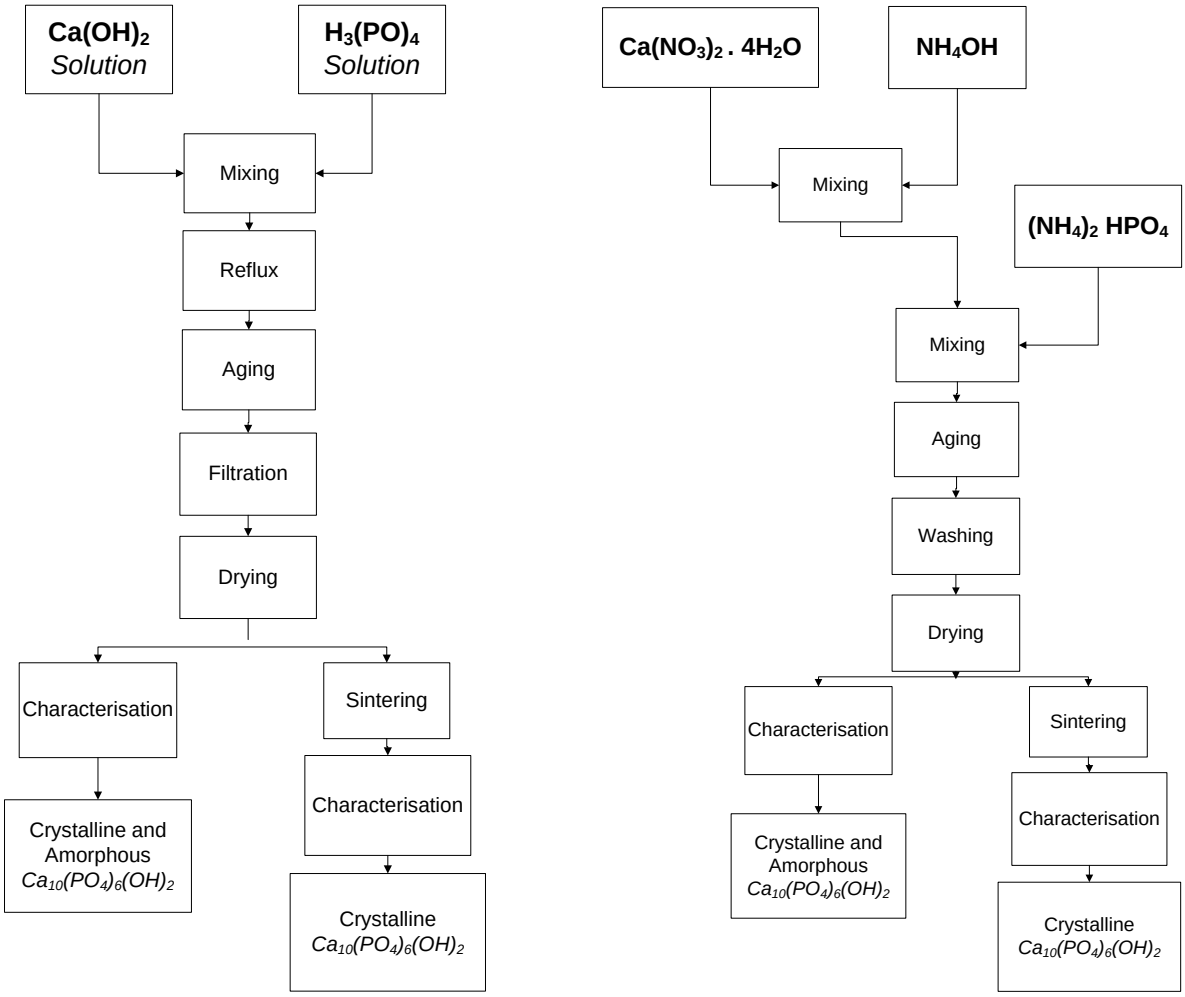

Figure 2-6: A flow chart for the synthesis of HAp powders via the precipitation route for Reaction 1 (left hand side) and Reaction 2 (right hand side)

2.5 PHYSICOCHEMICAL AND BIOLOGICAL PROPERTIES OF HAp

The present section will review the physical and mechanical properties of synthetic HAp powders yielded from the implementation of the various HAp powder production techniques (as discussed in the previous section). This section will aim to highlight the main differences between the HAp synthesised to-date against that of biological HAp (section 2.2).

2.5.1 Mechanical Properties Of HAp

To produce implant materials capable of withstanding mechanical loads, it is necessary to use densely sintered HAp, which surpasses porous HAp in strength. Ceramics should consist of fine grains because, according to the well-known Hall - Petch formula [12]:

$$\delta = \delta_0 + bd^{-1/2} \qquad \textit{Equation (2-3)}$$

where δ_0 and b are constants and d is the grain size, mechanical strength increases with decreasing grain size. The density of the HAp thus fabricated approaches theoretical density (3.156 g/cm^3) [13].

Tables 2-3 and 2-4 presents the values published for physical properties pertaining to HAp and the mechanical and physical properties of synthetic HAp, respectively. The key characteristics for highly dense HAp are its bending strength, tensile strength, and fracture toughness. The bending, compressive, and tensile strength values of HAp lie in the ranges 38–250, 120–150, and 38–300 MPa, respectively [12, 13, 45]. The large scatter is due to many factors, such as, the random strength distribution and the effects of residual microporosity, grain size and ion impurities. With increasing Ca/P ratio, the strength increases, reaches a peak at Ca/P of 1.67, and sharply decreases for Ca/P > 1.67 [24].

Weibull's modulus of dense HAp lies in the range 5–18, characteristic of brittle materials. The decelerated crack propagation coefficient ranges from 26 to 80 in a dry

atmosphere and from 12 to 49 in a humid atmosphere, indicating a high sensitivity to decelerated crack propagation [24, 46].

Young's modulus of dense HAp varies from 35 to 120 GPa [24], depending on the residual porosity and impurities. Young's modulus in bending is 44 to 88 GPa. The Vickers hardness of dense ceramics is 3 to 7 GPa. Dense HAp ceramics exhibit superplasticity at temperatures between 1000 and 1100°C due to grain boundary slip. The wear resistance and friction coefficient of dense HAp ceramics are comparable to those of enamel.

Table 2-3: Physical properties of synthetic HAp [12 - 15]

Physical Property	Metric Units
Density	3.00 - 3.219 g/cc
Porosity	0.1 - 3 %
Lattice Parameters (± 0.003nm)	
a lattice constant	9.432 – 0.9418 nm
b lattice constant	6.881 – 0.6884 nm
Crystallinity Index	33 - 37
Crystallite Size	0.0250 x 0.0030 (nm)
Ignition Products	HAp + CaO

Table 2-4: Mechanical properties of synthetic HAp [12, 13]

Mechanical Properties	Metric Units
Ultimate Tensile Strength (UTS)	38 - 48 MPa
Modulus of Elasticity	7 - 13 GPa
Flexural Strength	100 - 120 MPa
Compressive Strength	350 - 450 MPa
Fracture Toughness, K_{IC}	<1.0 MPa.m$^{1/2}$
Poisson's Ratio	0.27

It is evident that calcium phosphate in the form of crystallised HAp and/or amorphous calcium phosphate (ACP) provides stiffness to the bone [20]. The mechanical properties of bone, however, depend largely upon the humidity, mode of the applied

load, direction of the applied load and the location of the bone within the human body. Although HAp exhibits valuable properties as a biomaterial (regards biocompatibility, bioactivity, osteoconductivity, direct bonding with bones), its mechanical properties are poor, as indicated by its poor fracture toughness (K_{IC} is 0.8 to 1.2 MPa $m^{1/2}$), which is found to decrease almost linearly with increasing porosity. As a consequence, this severely restricts its field of application in orthopaedics. However, it still remains an excellent candidate for coating metallic prostheses or filling small bone defects. In the former application it would result in a combination of the good mechanical properties of metals and alloys with the excellent biocompatibility and bioactivity of HAp in guiding the bone growth to bond firmly from a mechanical point of view [1].

Mechanical integrity of natural bone is optimised with respect to weight minimisation and the ability to rapidly deliver calcium to support histological processes. The latter two factors require porosity. The mechanical disadvantages of the presence of pores in bone, which are regarded as flaws from the standpoint of fracture mechanics, are overcome by the incorporation of a large proportion of collagen reinforcement. The conflicting requirements of mechanical integrity and porosity, supports the unlikeliness that a single material would be capable of closely approximating the mechanical functional requirements of bone.

As natural bone consists of an inorganic/organic composite structure with grain size of 20 nm in diameter and 50 nm in length, from a bionics viewpoint, therefore HAp grains with a similar size would be more desirable for the application of implants [42]. Therefore, it is possible to consider a composite which can exhibit adequate mechanical properties. Kalita et al. [47] improved the densification, hardness and compression strength of synthetic HAp ceramics by introducing small quantities of MgO-CaO-P_2O_5-Na_2O-based sintering additives. Some compositions showed more than a 40% increase in Vickers microhardness compared to pure HAp processed under the same conditions. Adding HAp to a polymer matrix was also found to strengthen the material as a whole, often raising the tensile strength to within the range of cortical bone [48].

2.5.2 Crystal Structure Of HAp

It is generally accepted that slightly nonstoichiometric HAp has the hexagonal space group $P6_3/m$ structure, with a = 9.422 and c = 6.880 nm, while in the case of stoichiometric HAp the structure becomes monoclinic $P2_1/b$ [49]. This is characterised by ordering within OH^- ion columns to form a sequence $OH^-OH^-OH^-OH^-$, with an ordered arrangement of these columns, so that the *b*-axis is doubled giving lattice parameters a = 9.421(8), $b = 2a$, c = 6.8814(7) nm, γ = 1203 [32]. However, stoichiometric HAp may also be hexagonal, if OH^- are disordered. Normally, only those preparations that have a final high-temperature stage have the possibility of yielding monoclinic HAp. Other preparations are normally hexagonal, presumably because sufficient OH^- ions are missing, replaced by H_2O or impurity ions, so that the ordering is disturbed. Work carried out by the National Institute of Standards Technology (NIST) propose that the hexagonal form of HAp is formed by precipitation from supersaturated solutions at 25ºC to 100ºC, while the monoclinic form of HAp is primarily formed by heating the hexagonal form at 850ºC in air and then cooling to room temperature [50].

Recent theoretical studies by Calderin et al. [51] however, find the hexagonal and monoclinic structures both energetically acceptable for HAp, but Haverty et al. [52] finds that the $P6_3/m$ or the $P6_3$ hexagonal structural models are energetically unfavorable in comparison with a model based on the $P2_1/b$ symmetry or the newly proposed monoclinic $P2_1$ structural model (see Figure 2-10). They also conclude from Rietveld analysis of X-ray diffraction patterns from a NIST standard reference specimen that HAp (SRM-2910) crystallizes in a mixture of 23% $P2_1/b$ and 77% $P2_1$ monoclinic phases [50]. The overall XRD patterns of hexagonal and monoclinic HAp are almost identical; however the pattern of monoclinic HAp has additional weak lines whose intensities are less than 1% of the strongest hexagonal HAp line [50].

Figure 2-11 illustrates a half unit cell of a hexagonal HAp structure projected onto the ‘a’ and ‘b’ axes. The hydroxyl ions are located on the projection at the corners of the rhombic base of the unit cell forming columns of hydroxyls at the ‘c’ axis of ¼ and ¾

(or with a spacing of half the unit-cell height). There are two kinds of calcium-ion position contained in the lattice cell; hexagonal and columnar calcium.

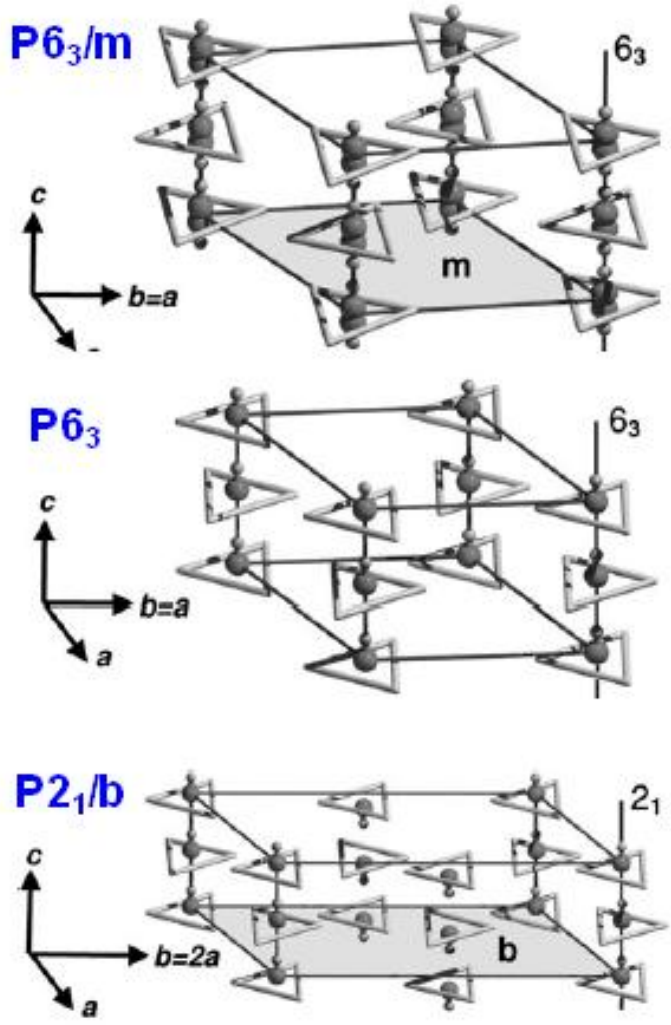

Figure 2-7: Various proposed HAp structures: Experimental HAp (Top: $P6_3/m$), Theoretical HAp (Middle: $P6_3$) and Monclinic (Bottom: $P2_1/b$). Adapted from [53]

Hexagonal calcium ions (or six-calcium ions) are associated with these hydroxyls, forming equilateral triangles centred on and perpendicular to the hydroxyl columns. Six of the PO_4^{2-}-tetrahedra are also on these planes. Columnar calcium ions being the net total of 4-calcium ions, are placed at the lattice points of [1/3, 2/3, 0] and [1/3, 2/3, 0] [13, 54]. Table 2-5 outlines the lattice coordinates for its unit cell.

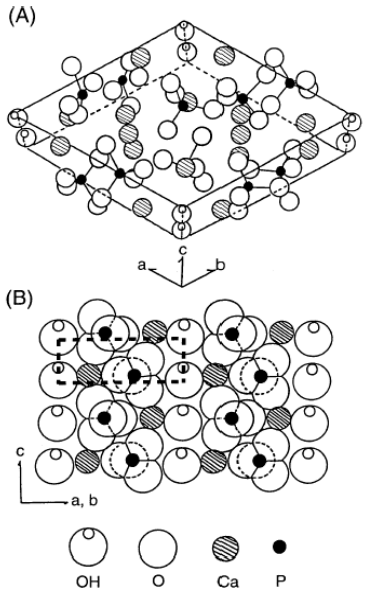

Figure 2-8: Illustration of (A) crystal structure and (B) ac or bc face of Calcium HAp. The area enclosed by dotted lines was 0.943 nm (a or b) x 0.688 nm (c) = 0.649 nm^2 [55]

Table 2-5: Unit-cell positions of the HAp lattice [13] where; α = 90^o, β=90^o, γ =120^o

Atom	x/a	y/b	z/c
Ca(I)	1/3	2/3	0.0010
Ca(II)	0.2464	0.9938	1/4
P	0.3999	0.3698	1/4
O(I)	0.3272	0.4837	1/4
O(II)	0.5899	0.4666	1/4
O(III)	0.3457	0.2595	0.0736
Hydroxyl	0.0000	0.0000	0.1930

2.5.3 Substitutions In HAp

An important consideration in the production and processing of HAp has been the control and the reduction in impurity levels (Table 2-6). These impurities may be classified as either substitutional or additional phases. Foreign elements obtained in HAp in the range of parts per million have not altered the overall biocompatibility response of the material [56].

Table 2-6: Impurity contents in HAp [13]

Trace element	HAp powder	
(ppm)	Laboratory (ppm)	Commercial (ppm)
Al	-	100 - 1000
Cu	8	1 - 10
Fe	30 - 40	100 - 1000
Ge	-	10 - 100
Mg	50	1000 - 2000
Mn	3 - 8	100 - 1000
Na	400	1000 - 3000
Pb	7	1 - 10
Si	200	100 - 1000
Ti	-	30 - 1000
Zn	20	10 - 100

HAp is capable of accommodating several substituents, while still maintaining its basic apatetic structure. Ca^{2+} can be substituted by various cations, such as, monovalent (Na^{+}, K^{+}) [57], divalent (Mg^{2+}, Sr^{2+}, Ba^{2+}, Pb^{2+}) [58] and trivalent (Y^{3+}) cations [58]. Significant anionic substitutions, include the replacement of OH by CO_3^{2-}, F^{-}, Cl^{-}, and PO_4^{3-} by CO_3^{2-} [59, 60], AsO_4^{3-} and VO_4^{3-} [61]. Some substitutions are coupled with others to maintain the charge balance in the apatite, such as, CO_3^{2-} for PO_4^{3-} coupled with Na^{+} for Ca^{2+}. The trivalent anionic phosphate sites cannot accept vacancies, as the trivalent anions are quite large and vacancies are believed to destabilise the lattice [62]. Adversely, the cationic sites can accept vacancies, up to a maximum of 2 sites out of the 10 existing in stoichiometric apatites [63]. The possible substitutions for each sublattice are indicated in Table 2.7.

Table 2-7: Summary of possible apatite structures

$M_{10}(ZO_4)_6X_2$	
M =	Ca, Sr, Ba, Cd, Pb, Mg, Na, K, H, D, …
Z =	P, CO_3, V, …
X =	OH, OD, CO_3, O, BO_2, F, Cl, Br, vacancies

Fluoride substituted apatites are less soluble than fluoride free synthetic and biological apatites [64]. Carbonate, CO_3, can substitute either as a type A or B substitution, dependent on its mode of carbonate substitution: $CO_3^{2-}$for OH^- (type A) or CO_3^{2-} for PO_4^{3-} (type B). Biological apatites are principally type B [59]. In synthetic powders prepared by wet methods, some fractions of PO_4^{3-} as well as OH^- groups are replaced by CO_3^{2-} groups (type AB). Among the variety of HAp-based bioceramics, CHAp seems to be a more promising material for bioresorbable bone substitution rather than bioactive coatings in orthopaedic application. Sintering time, temperature and the atmosphere are important parameters to control the level and type of carbonate substitution. The presence of CO_3^{2-} in HAp structure influences the decomposition, sinterability, solubility and biological reactivity of CHAp implantation materials [59]. The presence of CO_3^{2-} in the HAp structure influences decomposition, sinterability, solubility and biological reactivity of implantation material. Slosarczyk et al. [15] observed that the decomposition of HAp synthesised without any CO_3^{2-} additive did not occur. CO_3^{2-} ions, hence, are found to lower the thermal stability of HAp powders and produces CaO as a secondary phase, whose amount grows as treatment temperatures are increased to 1250ºC. CO_3^{2-} replacing PO_4^{3-} increase the Ca/P molar ratio of 1.667, resulting in non-stoichiometric solutions which are thermally less stable that those containing no substitutions. These results indicate that although carbonate can be found in natural bone, it is an undesirable impurity within synthetic HAp.

LeGeros et al. [59] have also demonstrated that the coupled CO_3 – for PO_4 and Na – for Ca substitution can alter the size and shape of the apatite crystal: from acicular to rods to equi-axed crystals with increasing carbonate content and in dissolution

properties, with the CO_3 substituted apatite being more soluble than CO_3-free synthetic apatites.

The magnesium content in raw materials used as precipitation precursors has also been found to have an adverse effect on the final HAp powder properties achieved [24, 65]. The presence of magnesium can alter the conditions of calcium phosphate precipitation and more precisely of HAp precipitation: it delays nucleation, growth and HAp maturation. It was also found to lead to the production of non-stoichiometric HAp decomposing upon subsequent calcinations [65]. Mg or Sr substitutions for Ca can cause an increase in the extent of dissolution of the apatite [64].

Differences in lattice parameters between substituted and unsubstituted HAp reflects the size and the amount of the substituting ions (see Table 2-8 and Table 2-9). Various substitutions in the apatite besides those of F^- or Cl^- for –OH or CO_3 for PO_4 mentioned above, also effect the crystallinity, thermal stability, and dissolution properties or solubility of the apatite crystal. When two or more substitutions are present, the substituents can have a synergistic or antagonistic effect on the properties of the apatite, such that Mg and CO_3 have synergistic effects on the crystallinity and dissolution properties of synthetic apatites: Mg and F or CO_3 and F have antagonistic, with F being the more dominant.

Table 2-8: Lattice parameters of aqueous and non-aqueous synthetic apatites. Adapted from [64]

Apatite	Major Substituent	Lattice Parameter, *a* , +0/-.003nm	Lattice Parameter, *c* , +/-0.003nm
Synthetic (non-aqueous)[a]			
OH-apatite	-	9.441	6.882
F-apatite	F	9.375	6.880
Cl-apatite	Cl	9.646	6.771
CO_3 apatite	CO_3	9.544	6.859
Synthetic (aqueous)[b]			
OH-apatite (Ca-deficient)	HPO_4^{**}	9.438	6.882
F-apatite	F	9.382	6.880
(Cl, OH)-apatite	Cl^{**}	9.515	6.858
CO_3-OH apatite	CO_3^{**}	9.298	6.924
CO_3-F apatite	CO_3^{**} , F	9.268	6.924
Sr-apatite	Sr	9.739	6.913
Pb-apatite	Pb	9.894	7.422
Ba-apatite	Ba	10.162	7.722

[a] Prepared at high temperatures (1000°C) by solid state reaction route
[b] Prepared at 100°C either by precipitation or by hydrolysis methods
[**] Maximum incorporation in case of Cl is less than one mole; in the case of CO_3 is 3 moles; in cases of H_3PO_4 is unknown. In these cases the substitutions are: F or Cl for OH; CO_3 for OH (Type A); CO_3 for PO_4 coupled with Na for Ca (Type B); HPO_4 for PO_4; Sr, Pb or Ba for Ca

Table 2-9: Qualitative effects of some substituents for Ca^{2+}, PO_4^{3-}, or OH in HAp on the lattice parameters and crystallinity of apatites. Adapted from [64]

Substituent	Ionic Rad (nm)	Lattice Parameter, *a* , +/-0.003nm	Lattice Parameter, *c* , +/-0.003nm	Crystallinity
for Calcium, Ca^{2+}	0.99	9.438	6.882	
Strontium, Sr^{2+}	1.12	(+)	(+)	(nc)
Barium, Ba^{2+}	1.34	(+)	(+)	(-)
Lead, Pb^{2+}	1.20	(+)	(+)	(-)
Potassium, K^+	1.33	(nc)	(nc)	(nc)
Sodium, Na^+	0.97	(nc)	(nc)	(nc)
Lithium, Li^+	0.68	(nc)	(nc)	(nc)
Magnesium, Mg^{2+}	0.66	(-)**	(-)**	(-)**
Cadmium, Cd^{2+}	0.97	(-)	(-)	(-)
Manganese, Mn^{2+}	0.80	(-)	(-)	(-)
Zinc, Zn^{2+}	0.74	(+)**	(+)**	(-)**
Aluminium, Al^{3+}	0.51	(+)	(+)	(-)
for OH				
Fluoride, F^-	1.36	(-)	(nc)	(+)
Chloride, Cl^-	1.81	(+)	(-)	(nc)
for PO_4^{3-}				
Carbonate, Co_3^{2-}		(-)	(+)	(-)
HPO_4^{2-}		(+)	(nc)	(nc)

(+) increase, (-) decrease, (nc) no change, **TCP formed in addition.

2.5.4 Solubility Of HAp In Relation To Other Calcium Phosphates

Various calcium phosphate compounds have been used in the field of biomedical engineering owing to the range of properties that they offer, from Tricalcium Phosphate (TCP) being resorbable to HAp being bioactive [66], while microscale HAp is typical highly phase stable and thus less bioresorbable [67].

Calcium phosphates (CaPs) contain the phosphate group PO_4^{3-}. Two different categories of CaP can be categorised as follows: (i) CaP obtained by precipitation from an aqueous solution at or around room temperature (low-temperature CaP) and (ii) CaP obtained by thermal reaction (high-temperature CaP). The most important property of CaP is its solubility in water, since the *in vivo* behaviour of CaPs can be predicted to a large extent by their solubility [68]. If the solubility of a CaP, (such as, HAp) is less than the mineral part of bone, it degrades extremely slowly if at all.

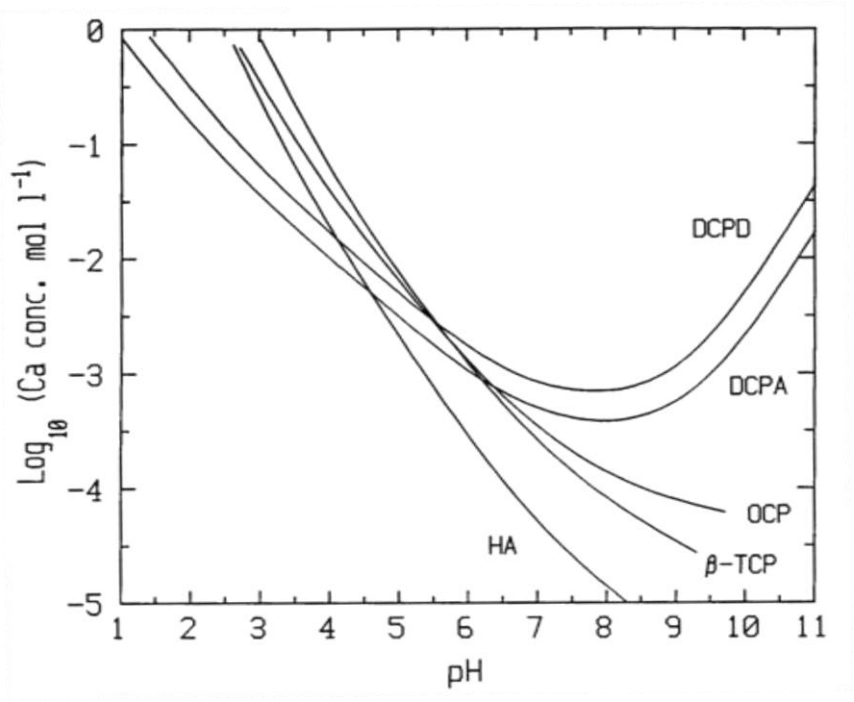

Figure 2-9: Solubility isotherms of CaP phases in the system $Ca(OH)_2$-H_3PO_4-H_2O at 37°C. The solubility is expressed in the total amount of calcium ions in solution [69]

If the solubility of a CaP is greater than that of the mineral part of bone, it is degraded. Therefore, using the different solubility isotherms of CaP, the in vivo degradation rate of CaP can be predicted to be in the order of (at pH 7.0):

MCPM > TTCP ≈ α-TCP > DCPD > DCPA > OCP > β-TCP > Ca-dHAp > HAp

However, the surface of a highly-soluble CaP can be reactive and may become covered with a poorly soluble CaP, hence reducing its degradation rate (refer to Figure 2-12).

In aqueous solutions and at ambient temperature (21ºC), the most important calcium phosphate salts may be identified. Factors affecting the solubility of HAp include the method of preparation, the resultant crystallinity, density and the extent of ionic substitutions into the apatite lattice [70]. While the forming method and exact stoichiometry will have an effect on solubility, the generally accepted order of solubility is as shown in Table 2-10.

Under normal physiological conditions (pH 7.2), HAp is the stable calcium phosphate compound [71]. This can drop to as low as a pH of 5.5 in the region of tissue damage, although this eventually returns back to a pH of 7.2 over a period of time. Even under these conditions HAp still remains a stable phase [71].

Table 2-10: Calcium phosphate compounds: chemical formulae, Ca/P molar ratios, dissolution rates and their acronyms

Ca/P molar ratio	Calcium Phosphate	Mineral Phase	Chemical Formula	Acronym
2.0	Tetracalcium phosphate	Hilgenstockite	$Ca_4O(PO_4)_2$	TTCP
1.67	Hydroxyapatite	Hydroxyapatite	$Ca_{10}(PO_4)_6(OH)_2$	HAp
1.67	Oxyapatite		$Ca_{10}(PO_4)_6O$	OXA
1.33 – 1.67	Calcium deficient hydroxyapatite		$Ca_{10-x}H_x(PO_4)_6(OH)_{2-x}$	*Ca-d*HAp
1.5	β – Tricalcium phosphate		β – $Ca_3(PO_4)_2$	β – TCP
1.5	α - Tricalcium phosphate		α - $Ca_3(PO_4)_2$	α - TCP
1.5	γ – Tricalcium phosphate		γ - $Ca_3(PO_4)_2$	γ – TCP
1.33	Octacalcium phosphate		$Ca_4H(PO_4)_3\,3H_2O$	OCP
1.00	Dicalcium phosphate anyhdrous	Monetite	$CaHPO_4$	DCPA
1.00	Dicalcium phosphate dihydrate	Brushite	$CaHPO_4.2H_2O$	DCPD
1.00	Calcium pyrophosphate (α, β, γ)		α - $Ca_2P_2O_7$ β - $Ca_2P_2O_7$ γ - $Ca_2P_2O_7$	CPP
1.00	Calcium pyrophosphate dihydrate		$Ca_2P_2O_7.2H_2O$	CPPD
0.7	Heptacalcium phosphate		$Ca_7(P_5O_{16})_2$	HCP
0.65	Tetracalcium dihydrogen phosphate		$Ca_4H_2P_6O_{20}$	TDHP
0.5	Monocalcium hydrate monohydrate		$Ca(H_2PO_4)_2.H_2O$	MCPM
0.5	Calcium metaphophate (α, β, γ)		$Ca(PO_3)_2$	CMP
	Amorphous calcium phosphate		$Ca_3(PO_4)_2 \cdot 3H_2O$[a]	ACP

a = an approximation [72]

2.5.5 Osseointegration Of HAp With Bone *In Vivo*

Since the clinical success of orthopaedic and dental implants depend on the osseointegration at the bone-implant interface; surfaces of bone-contacting devices would be desirable to be compositional, structural and functional analogous to that of human bone. Surface composition containing Ca and P; display good cytocompatibility *in vitro* and enhanced bone contact and greater new bone apposition, particularly Ca [16].

HAp coated implants have been shown to favour cell adhesion, differentiation and mineralization, and bone integration of the implant compared to uncoated titanium due to the osteoconductive properties of synthetic HAp [16]. The favourable effect of calcium phosphate coatings on bone response may be explained through the hypothesis that dissolution and reprecipitation of calcium ions from the coating stimulates osteogenic cells to differentiate and deposit a mineralised matrix. It is therefore expected that the new bone will form directly on the surface of the HAp coating. HAp coatings with high degrees of crystallinity show low-dissolution rates *in vitro* and less resorption and more direct bone contact *in vivo*. However, HAp coatings with a high amorphous content result in rapid weakening and disintegration of the coating and often promote inflammatory responses in the surrounding tissue. Okamoto et al. [73] reported that a significantly higher number of cells adhered to HAp than to uncoated titanium.

The crystallinity, composition, morphology and particle size of calcium phosphate effect its dissolution [16]. Synthetic HAp exhibits strong affinity to host hard tissue, promotes osseointegration and expedites the healing period required for titanium implants. It is known that human bone consists of roughly 70% HAp mineral and an organic matrix consisting largely of collagen type I, which is the principle collagen of skin and bone. Previous research has studied the coating of titanium alloy with collagen type I to investigate its beneficial effect in osseointegration [19]. It is demonstrated that the initial adhesion and spreading of osteoblasts have been accelerated. However, although collagen supports the adhesion of cells; enhanced bone mineral deposition still requires HAp.

The success or failure of HAp coated orthopaedic implants; depends on the control and consequences of cell behaviour post implantation [74]. Thus, the first and essential step for bone tissue-implant interface studies are *in vivo* tests using osteoblast cells due to the important role in which they play in the osteointegration of the implant. They have the ability to synthesise and produce extracellular matrix and to control its mineralization and thus regulate the ingrowth of bone to the implant.

Cell lines and primary human cells are commonly used for *in vitro* tests. But, primary human cell culture system does not exhibit reproducible results on account of differences between donors. An immortalised cell line is relatively easier to maintain over a long period of time with many passages without any loss of phenotypic expression. MG-63 cell line may be used to study the interactions between cells and biomaterial and to study the biocompatibility of the biomaterial [74].

2.5.6 Effect Of Surface Topography On Biological Response

The response of cells and tissues at implant interfaces can be affected by surface topography on a macroscopic as well as microscopic level. On the cell level, surface topgography plays a fundamental role in regulating cell behaviour, that is, the morphology, orientation and adhesion, proliferation and differentiation of mammalian cells [16]. The reaction of cells to topography of the substrate to which they are attached is one of the first phenomena observed in tissue culture and therefore plays a major role in the evolution and the properties of the implant-tissue interface (osseointegration).

A. Surface Roughness

Using MG63 (human osteoblast-like) culture cells, Martin et al. [75] demonstrated that cells cultured on rougher titanium surfaces exhibited decreased cellular proliferation and expressed more differentiated phenotype, which is a more osteoblastic phenotype. Also, cells on the rougher surfaces were found to release higher levels of prostaglandin E_2 (PGE_2) and latent transforming growth factor β (LTGF - β), both factors involved in regulation of bone formation. Thomas et al. [76] found that the surface texture (that is, a combination of topography and roughness)

significantly effect the interface response to the implant. An implant possessing a rough surface was found to yield both greater shear strength and direct bone apposition, whereas the implant with a smoother surface exhibited various degrees of fibrous encapsulation. Therefore, rough surfaces are assumed to produce better bone fixation than smooth surfaces. On the other hand, an *in vivo* study suggested that very different levels of rough surfaces of titanium exhibited a similar bony reaction and no significant difference in the interface length percentage covered by bone. Thus, the organisation of surface features also takes effect on bone formation at the implant-implant interface.

B. Surface Structures

Cells not only discriminate between various surface roughness levels, but also with surfaces of comparable roughness levels and different topologies. Micron and nano-topography present strong cues for cell behaviour and thus, the interactions of cells with topographic features of the substrate they attach to will affect a variety of cellular processes such as, cell adhesion, cytoskeletal organisation, cell motility, migration patterns and cell differentiation [16]. The reaction of cells to the topography of their substrate are assumed contact guidance, the phenomenon has been demonstrated by the organisation of surface roughness. The tendency of surface topography to influence cell spreading is otherwise termed ‘contact cue guidance’ [16].

2.6 PROCESS VARIABLES AFFECTING THE CHEMICAL PRECIPITATION METHOD

In this section, the process variable associated with the wet chemical precipitation method (reaction (1), Equation 2-1) will be discussed; in relation to the effect they impose upon the final physicochemical HAp powder particles obtained. Control over these process variables, in order to develop HAp powders of optimum quality; for plasma spray coating application onto femoral implants, will is also considered. This will ensure that reproducibility of the final HAp powder physicochemical characteristics is repeatedly obtainable. Table 2-11 highlights the variance between the precipitation process variables and the HAp powder properties achieved, through prior research investigations conducted in the fields of HAp synthesis. An explanation of the effects in varying these parameters on the final HAp powder properties (such as, stoichiometry, particle size, morphology, purity and crystallinity) will also be outlined.

2.6.1 Initial Reactant Concentration

Direct HAp formation has been reported, for low reactant concentrations (in the 10^{-3} M range and at pH 7.4), where the solution was undersaturated or slightly supersaturated with respect to the precursor phase [77, 78]. All the variance in results obtained for final HAp powder characteristics, define the complex role of chemical media in HAp formation; whose influence is evident not only through the super-saturation effect, but also through the nature and concentrations of ionic species. Difficulties encountered in preparing stoichiometric HAp from aqueous solution are caused by a high apatite affinity towards various impurities as well as the complex nature of the calcium phosphate system and the predominant role of kinetic parameters over thermodynamic ones during phase transformations [79].

Due to the low cost and simplicity of the wet chemical precipitation procedure, there is considerable interest in the HAp synthesis from aqueous solutions. However, most of the apatites obtained from this method are reported as non-stoichiometric [79]. During heating, non-stoichiometric apatites decompose and appear as either TCP or

CaO. Sintering of pure stoichiometric HAp powder, however, yields pure dense HAp powders with superior mechanical properties, while sintering of nonstoichiometric HAp, lead to the presence of other phases, such as: CaO if the Ca/P molar ratio exceeds 1.67 and TCP if Ca/P is below 1.67. Decomposition of calcium deficient apatites (Ca/P<1.67) in the temperature range 22–900°C takes place according to the following chemical reaction [71]:

$$Ca_{10-x}(HPO_4)_x(PO_4)_{6-x}(OH)_{2-x} \rightarrow xCa_9(PO_4)_6(\beta)+(1-x)Ca_{10}(PO_4)_6(OH)_2 \quad \textit{Equation (2-4)}$$

while in the reactant concentrations containing an excess of $Ca(OH)_2$ during thermal treatment; CaO is formed. A change in composition of HAp can decrease the strength of the final material, increase its dissolution rate, and consequently affect the rate and extent of biodegradation.

The substitution of phosphate ions PO_4^{3-} by hydrogen phosphate HPO_4^{2-} allows a continuous variation of the Ca/P atomic ratio between 9/6 and 10/6. This leads to calcium-deficient HAp (Ca-dHAp). Ca-dHAp powders can be precipitated from conventional wet chemical methods and decomposed into a mixture of HAP and tricalcium phosphate, $Ca_3(PO_4)_2$ (TCP) by thermal treatment above 700 °C, dependent upon the initial reactant (that is, Ca^{2+}) concentration. The resulting Ca/P molar ratio of the HA_P powder is one of the most crucial parameters in determining its thermal stability. In general, HAp prepared at low pH is highly Ca-deficient (Ca/P = 1.58), while the wet mechanochemical route is also known to produces powders with Ca/P ratio of 1.65 [80].

Since precipitated anions (PO_4^{3-}) are generated slowly in solutions containing the metal ion (Ca^{2+}) during chemical precipitation; this process entails adding the phosphate solution drops to the calcium ion-containing solution. The hydroxyl ions originally present in the calcium hydroxide suspension are readily exhausted by the phosphoric acid under a very high addition rate, lowering pH in the bulk apart from the calcium hydroxide particles. It is important that the reactants have the correct molar ratio of calcium and phosphorous and if the pH level falls below 9 or 7, it leads

to the production of calcium monophosphate and calcium dehydrates. They are more soluble in aqueous media and will resorb upon implantation.

Koutsopoulos [5] reported on the capacity for potassium ions of substituting calcium ions into the HAp crystal lattice and forming locally nonstoichiometric HAP islands within the bulk crystal. This finding is ambiguous and doubts arise from the different charges and the significant difference in the radii of the two ions (r_{Ca}^{2+} = 99 pm, r_{K}^{+} = 133 pm).

The control of pH is vital to the successful control of the chemical precipitation process. HAp, with a high crystallinity and with its primary particles in the submicron range and of finely divided precipitate was formed at a high pH in excess of 10 [5, 78]. Conn et al. [81] also confirm that the precipitation must be carried out at a pH above 10 in order to precipitate HAp powders with low bulk density and a high surface area. This research achieved this through implementing a two-stage reactor to produce HAp on a continuous basis with both stages under vigorous agitation. The phosphoric acid is added in the first stage in a manner suitable to disperse the acid so that high local concentrations of acid are avoided. It is important to hold the pH in stage one between about 9.5 to about 11. A pH of 9.5-10 indicates that the reaction in stage one is approaching 100% and the viscosity of the reaction mass approaches a maximum where agitation becomes less efficient. A pH above about 11 indicates that the extent of reaction is too low in stage one. Deviation from a pH of from about 9.5 to about 11, preferably from about 10 to about 11 and, more preferably, at about 10.5 indicates that either acid or lime flow is not correct and must be adjusted. Phosphoric acid delivery to the second stage is controlled in such a manner as to hold the pH at about 7.0 to about 7.4, preferably from about 7.2 to about 7.3.

Table 2-11: Comparative analysis of previous chemical precipitation process parameters investigated, where - denotes data unpublished

Source	Chemical Precipitation Reaction Method	PROCESS VARIABLES					POWDER CHARACTERISTICS				
		Ca/P molar ratio	Acid Addition Rate	Stirring Speed (rpm)	Temperature (°C)	pH	Density (g/cm^3)	Specific Surface Area (m^2/g)	Crystallite Size	Particle Size	Morphology
[82]	Reaction Method 1	1.67	-	-	-	10	$3.219 g/cm^3$	-	20 - 55nm	1 - 8μm	Spherical
[67]	Reaction Method 1	1.665	2mL/min	2000	40 - 65	10 - 11	-	-	-	-	-
[22]	Reaction Method 1	1.5 - 1.71	-	-	30 - 95	6.5 - 9	-	58 ± 1.5	-	-	-
[2]	Reaction Method 2	1.67	-	-	-	9	-	-	-	20 - 125μm	-
[21]	Reaction Method 2	-	-	-	-	-	-	-	-	53 - 75μm (Sintered HAp)	Spherical geometry (Sintered HAp)
[41]	Reaction Method 2	-	1.5L/h	-	40	8	-	-	20nm - Scherrer formula 250 nm - TEM image	-	-
[83]	Reaction Method 2	1.667	1 – 2 drops/s	500-2400	40 ± 2	7.5 - 9	-		-	-	-
[84]	Reaction Method 2	1.667	1 – 2 drops/s	2400	40 ± 2	7.5	-	54.5	-	50nm	Angular
[81]	Reaction Method 2	1.667	70.8kg/h	High	20 - 50	9.5 – 11; 7.0 – 7.4	-	-	-	-	-
[85]	Reaction Method 2	1.55 – 1.71	1 – 10mL/min	100 - 300	25 - 95	7.0	-	-	-	-	-
[71]	Reaction Method 2	1.667	-	-	22 - 95	9.5 - 12	-	-	-	-	-

Solids concentration also increases the collision frequency (since two particles are involved in each collision). pH has a very strong effect on the surface potential, for every compound there is a pH where the particle surface is electrically neutral (the isoelectric point). At this pH, particle-particle repulsion vanishes and agglomeration is highest [86]. A high ionic strength depresses the double layer, thus stimulating agglomeration. A high supersaturation decreases the time needed for binding particles together, thereby facilitating agglomeration [86].

2.6.2 Reaction Temperature

Temperature is found to affect predominantly the crystalline phase fraction, crystallite size and, as a consequence, specific surface area [71]. Controlling the reaction temperature during precipitation, Tampieri et al. [87] varied the degree of crystallinity (representing the fraction of completely crystallised phase) approximately from 20 to 80%. The resulting morphology of the two powders is shown in Figures 2-13(a) (80% crystalline) and 2-13(b) (20% crystalline). It is clear from these figures that increasing the precipitation temperature not only increases the crystallinity of the HAp powders but also induces an enhanced spherical morphology [41, 71, 79, 87]. A pure-phase HAp with the desired morphology could therefore be prepared by adjusting the reaction temperature and time [88].

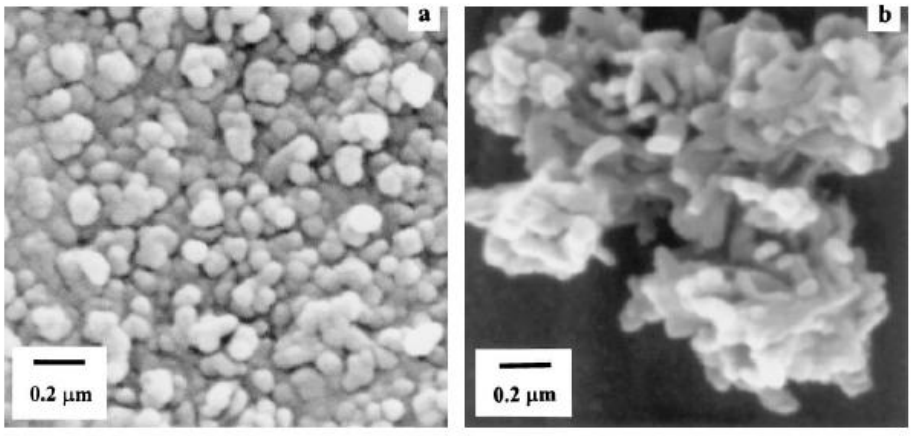

Figure 2-10: SEM micrographs showing morphologies of untreated HAp (a) 80% crystalline; (b) 20% crystalline [87]

The morphology of HAp crystals are strongly dependant on the temperature of the reaction [87, 88, 89]. Increasing the precipitation temperature from 20-100ºC induces a change in morphology from need-like precipitate to highly spheroidal precipitate respectively, for chemical precipitation reaction (2), Equation 2-2 [87]. However, the morphological change with temperature follows the reverse order when HAp is precipitated via the chemical precipitation reaction (1), Equation 2-1. Instead, it was reported that the morphology of the HAp particles changed from spheroidal to needle-like with increasing temperature [87]. In general, a needle-like morphology can be expected when the growth rate is faster and the aspect ratio decreases as the growth rate decreases. Thus, the growth rate of HAp should be expected to increase with increasing temperature when it is precipitated via chemical reaction (1), Equation 2-1 while decreasing with increasing temperature when precipitated via chemical reaction (2), Equation 2-2. An enhanced spherical morphology with larger particle size has elsewhere been reported with an increase in precipitation temperature. Kumar et al. [88] reinforces this evidence with Transmission Electron Microscopy (TEM) graphs of HAp powders (synthesised via the wet chemical using $Ca(OH)_2$ and H_3PO_4 revealed needle-shaped particles with a high aspect ratio at 40°C, which changed to spheroidal when the precipitation temperature was increased to 100°C. The changes in the morphology with temperature were analysed taking into account the driving force for the HAp precipitation and the supersaturation level of Ca^{2+} and PO_4^{3-} ions with respect to HAp [90]. The analysis indicated that the supersaturation level of the reactants, especially the concentration of Ca^{2+} ions, played a predominant role on the precipitate morphology for this classical acid-base reaction. Lazic et al. [71] also prove the stoichiometry of the non-matured HAp varied significantly with reaction synthesis temperature, such that samples precipitated at 95°C demonstrated properties of thermally stable stoichiometric HAp. The crystals precipitated at 22°C had the form of tiny needles with an average length of 110 nm and width of 11 nm. Maturation (that is, ripening time) under conditions of precipitation does not significantly affect crystal size. The crystals however become thicker and aggregation more pronounced. Crystals precipitated at high temperature are well-rounded. For studies conducted by Lazic et al. [71] at reaction synthesis temperatures of 15°C, the particle size of HAp was less than 10 nm, and at 60°C it became an acicular crystal

with a length of 100 nm. Figure 2-14 illustrates the aging / maturation time required at a particular precipitation temperature in order to obtain stoichiometric HAp [91].

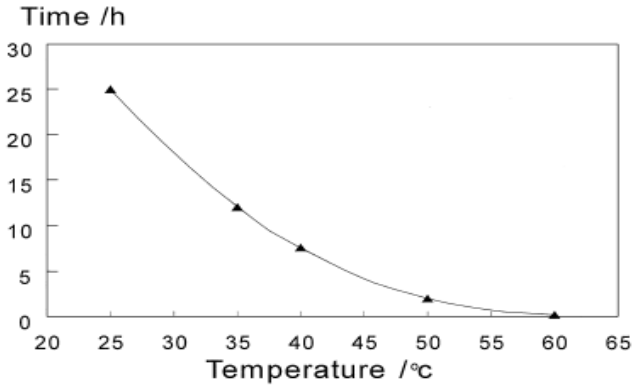

Figure 2-11: Time dependency of precipitation temperature to obtain phase pure HAp [91]

XRD analyses were carried out by Pang and Bao [90] with respect to HAp prepared by chemical precipitation through aqueous solutions of calcium chloride and ammonium hydrogenphosphate. Broad diffraction peaks were observed for the HAp powders synthesised at low temperature (15ºC). When the synthetic temperature was increased these diffraction peaks became sharper, indicating an increase in final HAp crystallinity. The crystallinity increased from 0.03% to 0.53% for the HAp powders prepared from 15 - 99ºC (refluxing) respectively, which indicated a strong synthetic temperature dependence of the crystallinity of prepared HAp. It was also noticed that the increase of the crystallinity with temperature was not linear. There was no significant change in crystallinity when the synthetic temperature was lower than 70ºC, however, a sharp increase in the crystallinity were observed at synthetic temperatures over 70ºC, as the crystalline activation energy of the HAp was overcome at that temperature. Kothappalli et al. [89] also indicate that when the reaction temperature is increased at a constant concentration, the diffraction peaks became more intense, indicating an increase in the crystallinity of the HAp powders. Smiciklas et al. [85] also find that increasing the reaction temperature, the crystallite size and the fraction of crystalline phase increases, while the specific surface area decreases [85]. The calculated crystallite size (X_s) for the HAp powders synthesised at different temperatures is listed in Table 2-12.

Table 2-12: The effect of synthetic temperature on the fraction crystallinity and crystallite size of HAp nanocrystals before and after calcination at 650ºC for 6 h [90]

Temperature (ºC)	Crystallinity, X_c		Crystallite Size, X_s, (nm)	
	Before calcination	After calcination	Before calcination	After calcination
15	0.03	0.39	20.8	35.1
50	0.06	0.58	27.8	37.3
70	0.10	0.63	34.9	42.7
80	0.32	0.65	45.9	44.0
90	0.48	0.71	50.0	46.5
99	0.53	0.72	52.7	47.4

Synthetic HAp occurs in two structural forms, hexagonal and monoclinic, which have minor structural differences. The hexagonal HAp form is usually formed by precipitation from supersaturated solutions at 25°C to 100°C and the monoclinic form of HAp is primarily formed by heating the hexagonal form at 850°C in air and then cooling to room temperature [92]. The overall XRD patterns of hexagonal and monoclinic HAp are almost identical; however the pattern of monoclinic HAp has additional weak lines whose intensities are less than 1 % of the strongest hexagonal HAp line. The main phase formed at room temperature was ACP, with minor amounts of HAp, whereas at 90°C HAP crystallized. This behavior cannot be explained from the supersaturations in these experiments, since the solubility of HAp is higher at low temperatures [78].

At a constant reactant concentration, as the reaction temperature is increased, the particle size and aspect ratio is also reported to increase [89]. However, with this increase of reactant temperature, the HAp agglomerate size decreased and it was observed that larger agglomerates were formed for relatively smaller particles, such as those synthesised at 25°C. Their sintering density also improved in spite of the decrease of the surface area with agglomerate size. Kothapalli et al. [89] also found that the density of the pre-sintered HAp increased with synthesis temperature in spite of the concentration of the reactants. The reactant temperature had more impact on the strength than the actual concentration. At a constant concentration, as the temperature increased, the flexural strength increased proportionally.

In the case of low temperature precipitation, stirring in the maturation stage has shown to play an essential role in obtaining required stoichiometry [71]. Also, raising the reaction temperature can also greatly shorten the reaction time for the formation of pure-phase HAp. Afshar et al. report a chemical precipitation reaction temperature of 40 °C is required to achieve a pure HAp product [83].

An investigation conducted by Conn et al. [81] reported that the temperature at which the chemical precipitation reaction is carried out has little effect on the product quality or on the efficiency of the process. Accordingly, temperatures from 35 to 90°C were stated as satisfactory in this study. Lower temperatures and aging time can extensively improve the yield and reduce the cost of the reaction. On the other hand, however, these parameters can also lead to heterogeneous compositions and morphology, and a calcium deficiency in the final product [85].

2.6.3 Reactant Addition Rate

A slow and controlled addition of phosphoric acid in an alkaline environment is necessary (as it controls the pH level) in order to fabricate pure stoichiometric HAp [2, 5, 83, 85]. A slow reactant addition rate is found to yield pure, well-crystallised HAp, due to low supersaturation and an avoidance of local inhomogeneity [96]. A high addition rate of phosphoric acid or in excess, leads to the formation of calcium deficient precipitate [2]. Afshar et al. [83] used extra acid solution to remove any extra calcium in the HA precipitate.

The rate of reactant addition effects the rate of HAp nucleation [5]. A slow addition rate ensures the absence of continuous nucleation. Addition times of 60 min or longer are found to result in a well crystallized HAp powder while an addition time of 30 min resulted in a biphasic mixture of HAp and ACP. For the latter case it is likely that the rate of addition of reactants was higher than the rate of their consumption due to HAp crystallization [78]. Therefore, the concentrations of calcium and phosphate ions in the solution built up during the addition period and eventually the solution became supersaturated with respect to ACP, which then formed preferentially. When the addition time was the longest (240 min), the crystallinity index was also the highest.

Although this result cannot be attributed exclusively to the addition time, it suggests ways to further improve the crystallinity.

Large HAp powder particle sizes are obtained when the addition rate of acid is lowered [84]. The order in which the reactants are added also play an important role in producing phase pure HAp. When the Ca solution is added to the P solution, a Ca-dHAp is produced at the beginning of the reaction and the final product can also be Ca- deficient, which is a common problem when employing wet methods of synthesis [93]. When P solution is added to a Ca solution, there exists a Ca-rich precipitate at the beginning, which progressively evolves into stoichiometric HAp towards the end of the reaction [93].

When the addition rate of the phosphoric acid is very high (2400 ml/min.), the synthesis reaction conversion decreases and there is some $Ca(OH)_2$ appears in the final product. When the acid addition rate is below 100 ml/min, the conversion rate of the reaction is 100% [94]. The addition rate of reactant, during the reaction synthesis therefore has a strong influence on the resulting composition. A higher addition rate of acid systematically results in an undesired increase of the $Ca(OH)_2$ content. This can be explained in terms of pH of the reaction media. When the acid is introduced at a very high addition rate, the pH of the reaction media decreases drastically (pH <7). Orthophosphoric acid is a weak triacid, in which the acidity potentials are as follows [94]:

$$H_3PO_4 \leftrightarrow H_2PO_4^- + H^+ \qquad pK_{a1} = 2.2 \qquad \textit{Equation (2-5)}$$

$$H_2PO_4^- \leftrightarrow HPO_4^{2-} + H^+ \qquad pK_{a2} = 7.2 \qquad \textit{Equation (2-6)}$$

$$HPO_4^- \leftrightarrow PO_4^{3-} + H^+ \qquad pK_{a3} = 12.3 \qquad \textit{Equation (2-7)}$$

If pH > pK_a then the dissociation of H_3PO_4 will occur according to the Le Chatelier principle [94]. In the other case the recombination will occur. Therefore when the acid is introduced in the reaction media at a high addition rate (2400ml/min) the pH decreases leading to an incomplete dissociation of orthophosphoric acid. In the absence of PO_4^{3-}, the formation of the HAp structure is compromised. This explains the presence of residual or unreacted $Ca(OH)_2$ which will further transform in lime

during heat treatment. In this condition, the synthesised HAp can contain a fraction of dihydrogenophosphate ($H_2PO_4^-$) or hydrogenophosphate ions (HPO_4^{2-}) substituted for phosphate ions (PO_4^{3-}) which can explain the residual $Ca(OH)_2$. Although hydrogenophosphated phases are quite difficult to detect by XRD, their presence induces small distortions in the unit cell. Those phases can be written by the following chemical expression [94]:

$$Ca_{10-x}(HPO_4)_x(PO_4)_{6-x}(OH)_{2-x}, \quad \text{with } 0 < x < 2 \qquad \textit{Equation (2-8)}$$

2.6.4 Stirring Speed

The chemical precipitation reaction requires mixing on a molecular level before actual precipitation of the crystallised product can proceed. The mixing procedure determines the final stoichiometry of HAp precipitate [93]. Since many precipitation processes are conducted at very high supersaturations, the characteristic reaction time can be of the same order of magnitude or even smaller than the mixing time [86]. When this situation prevails, the course of the mixing process helps to determine the course of supersaturation. Guilletti et al. [86] described these mixing conditions to affect crystal shape, purity, crystallinity, and even the phases that are formed. When large crystals of high crystallinity and purity are desired, precipitation should be conducted at low supersaturation. Therefore, reactants should be added near areas of high mixing intensity, and as far as possible from each other, (that is, a good dispersion of the concentrated reactant with the reactor contents should be stimulated). If fine particles with a narrow size distribution are desired, intense mixing should provide rapid contact between concentrated reactants [86]. Mixing effects have to be considered in order to extrapolate correctly a pilot reactor to the industrial scale [82]. The hydrodynamic factors which govern mixing and the initial contact between the reagents play an essential role on morphology and on crystal size distribution [78].

The stirring speed should be high enough to prepare a good homogenous media for precipitation of HAp. Both Monetite and Brushite formation occurs by insufficient mixing of calcium solution as the orthophosphoric solution is added [85]. The PO_4^{3-}

ion concentration builds up when it is not distributed homogeneously and a localised low pH is established. This part of the reaction vessel can be richer in PO_4^{3-} and provides conditions for the formation of soluble precipitates. A powerful and high-speed stirring device can be used to overcome this possibility [84]. Excellent agitation can be required to form a quality product [85], as poor agitation in the suspension contains entrapped unreacted $Ca(OH)_2$. High local concentrations of phosphoric acid must be avoided in order to prevent the formation of dicalcium phosphate which is impossible to convert to the desired HAp [81].

Lazic et al. [71] report that in the case of low temperature precipitation, stirring in the maturation stage is an essential role in obtaining the required stoichiometric Hap. Efficient agitation is very important to obtain equilibrium so that the pH of the final HAp slurry will not drift. Insufficient agitation will result in a rapid, wide change in pH as unmixed portions of different pH are carried through the chemical precipitation process.

Agglomeration is present in almost all precipitation processes and in some crystallisation systems, particularly during start-up, where higher supersaturations prevail [86]. When solid-liquid separation is critical, agglomeration is desired since it leads to larger, easy-to-filter particles. When products of high purity are required, agglomeration should be avoided since agglomerates trap impurities within their interstices [86]. The process of agglomeration starts with the transport of particles towards one another. When the particles have enough kinetic energy to overcome the repulsion due to their surface potential, they collide. If they remain in contact long enough for growth to take place and thereby bind the particles together; an agglomerate is formed [86]. Thus, the variables can affect agglomeration during industrial precipitation. Mixing intensity improves the particle collision frequency and thus agglomeration. However, a mixing intensity that is too high promotes particle disruption [86].

2.6.5 Ripening Time

During aging, the HAp crystals are subject to a process that includes dissolution and recrystallisation. During this stage the smallest crystals disappear in favour of the larger ones, which grow further. As a consequence the total number of crystals is reduced and the surface roughness of the crystals is reduced. Both phenomena result in a decrease of the specific surface area [5].

HAp crystallinity can be largely dependent upon ripening or maturation time allowed after the precipitation reaction [87]. Both the crystallinity and crystallite size of the HAp powders are found to increase very rapidly at the early ripening stages and gradually levelled off as ripening continues. Tampieri et al. found similar results were obtained when the synthetic temperature was raised to 99ºC [87]. The degree of crystallinity of HAp powders increased from 20 - 70% by increasing the maturation time to 24 h. Pang et al. [90] investigated the increase of crystallinity with the increase of the ripening time to observe a clear sharpening of the diffraction peaks (XRD) of the HAp powders. Both the crystallinity and crystallite size of the HAp powders increased very rapidly at the early ripening stages and gradually levelled off as ripening lasted. This profile of crystallinity increase with ripening time was also confirmed by FTIR analysis. The characteristic bands for HAp are exhibited in all the three patterns (1h, 96h and after calcination): 900–1200 cm^{-1} for phosphate stretching, 602 cm^{-1} for phosphate bending, 632 and 3571 cm^{-1} for hydroxyl vibrations [90]. The intensities of these two hydroxyl absorption bands and the band at 940 cm^{-1} for phosphate can be used as an indication of the HAp crystallinity. It is seen that the intensities of these three bands increase with the ripening time. In addition, the broad band at 2500–3700 cm^{-1}, which is a reflection of the combined water in HAp powders, also decreases with increasing the ripening time. The lower combined water content results from the higher crystallinity of HAp powder, implying the crystalline HAp powder is less hydrophilic than its amorphous counterpart.

Further evidence for the change of combined water with ripening time was provided by thermal gravimetric – dilatometry analysis (TG–DTA) measurements. The weight loss of HAp powders heated up to 750 °C is about 7.6 and 6% for 1- and 96-h ripening samples, respectively. The area of endothermic peak on DTA curve shows

the same result, too. The weight loss starts at about 100 °C and ends at about 500 °C based on the DTA curves. This weight loss comes from the elimination of combined water [90].

This crystalline behaviour as a function of ripening time can be explained by the mechanism of crystal growth in solution. It is well known that precipitation of particles involves nucleation and growth from a supersaturated solution. Chemical precipitation often experiences high reaction-induced supersaturation, leading to high nucleation rates [86]. In this case, a crystal nucleus usually has a rough surface due to the rapid production of insoluble materials. This rough surface provides energetically favourable conditions for crystal growth because the molecules adding on it has greater sticking probability. So the rough surface results in high growth rate. However, as the crystal continues to grow, its surface becomes smoother and as a result, the rate of crystal growth slows down. This is because the addition of molecules on the smooth surface has lower sticking probability.

TEM observations on the morphology changes of the HAp as a function of ripening time provide further evidence that this mechanism is controlling the rate of crystallisation. These TEM micrographs clearly show that the particles become increasingly regular and smooth with increasing ripening time [90].

Aging the suspension leads to the growth of the precipitate and changes the morphology to a more equiaxed status [84]. Leaving the suspension to settle after adding the acid solution causes completion of precipitation and more suitable properties as well as the process efficiency [84]. The thermodynamic stability of a solid compound arises from the ordered arrangement of its molecules in a crystal lattice in an infinite medium. For particles of finite size, the average particle stability is an average of its volume and surface contributions [86]. Since surfaces have a low stability, the smaller the particle, the lower its stability, (that is, the higher its solubility). This effect can be important for particles of 1 mm or less. In late stages of batch precipitation, when supersaturation is low, smaller particles tend to re-dissolve [86]. The residual supersaturation can slowly be consumed by larger particles. Aging can take days or even months, and in general, it helps to improve product quality as it

results in larger crystal sizes and improved product crystallinity. Further XRD analyses have also confirmed that performing calcinations after HA precipitation can significantly increase the resultant crystallinity of the HAp precipitate [89].

The formation of synthetic HA_P crystals from a highly supersaturated solutions proceeds via intermediate precursor phases, which have a transitory existence, such as TCP and OCP. Traces of precursors can be detected even after prolonged ripening times, therefore affecting the quality of the final HAp product. [5]

2.6.6 Atmospheric Environment

During the chemical precipitation route, adsorption of atmospheric CO_2 may occur, which in the form of CO_3^{2-} anion can be incorporated into the HAp crystal lattice, resulting in micro-stresses and distortion of the stoichiometric HAp lattice [59]. However, within Nitrogen (N_2) controlled environments, small percentages of CO_3^{2-} contamination was also found to arise as a consequence of subsequent sample handling steps [85].

Filtered inert gas should be continuously injected to both the reactor and the acid solution container during the precipitation process [83]. The filter should contain a sufficient amount of carbon dioxide absorber (such as, KOH or N_2). The HAp powder can be very hospitable in the substitution of carbon dioxide in its crystal structure. CO_3^{2-}ions can substitute hydroxyls or phosphates sites and based on this substitution, type A and type B of carbonated HAp are, respectively, formed. So, in order to reach a pure HAp precipitate without any carbon dioxide contamination, it is effective to use controlled atmosphere during precipitation process. Filtered inert gas shall be continuously injected to the reactor and the acid solution container during the precipitation process. The filter should contain a sufficient amount of carbon dioxide absorber.

2.7 HAp POWDER CHARACTERISTICS

The physicochemical properties for HAp powders prepared from the chemical precipitation technique vary considerably due to the process variable conditions and raw materials used. These properties are discussed with respect the optimum values required for HAp powder properties for plasma spray application as a coating onto orthopaedic implants. An overview of HAp powder properties, such as, its crystallinity, phase purity, crystallite size, lattice parameters, particle size and particle morphology are discussed in this section.

2.7.1 Crystallinity

Crystallinity depends on crystallite size and crystal strain and is the amount of crystalline phase present compared to its amorphous phase content. HAp crystallisation obeys the Ostwald rule of stages, so it is usually formed upon recrystallisation of precursor phases such as OCP, DCPD and ACP [78]. There are two different crystallisation processes involved in the crystallisation of HAp particles during synthesis and calcination. The crystallisation of HAp during synthesis follows a mechanism of solution crystallisation. Since the crystal growth proceeds through the packing of HAp molecules from the solution on the formed nuclei during the ripening process, the crystallites can freely grow on the surfaces of the precipitates in all directions. It is expected that the larger crystallites will be formed with longer ripening time until the crystallisation reaches to its equilibrium. During calcination, crystallisation of HAp experiences both the nucleation and crystal growth by the rearrangement of HAp molecules in amorphous phase. The nucleation and growth take place throughout the precipitates rather than on the surfaces only [78, 86, 90]. As more HAp molecules are available inside the precipitates for the nucleation and the crystal growth is in a confined environment, as well as the diffusion of the molecules in solid state is very slow, relatively smaller but more crystallites are expected to be produced in present calcination conditions. The dramatic increase in crystallinity after calcination indicates that the number of crystallites formed during calcination is large than that formed during synthesis, particularly for the "as prepared" HAp powders with lower crystallinity. As a result, the apparent crystallinity post sintering (X_c) is reduced after calcination for the "as prepared" samples with high crystallinity and

larger crystallites because a large amount of relatively smaller new crystallites are formed during calcination. On the other hand, the increased X_c for the "as prepared" samples with lower crystallinity and smaller crystallites comes from the growth of these smaller crystallites and new crystallites formed during calcination, which are relatively larger than "as prepared" smaller crystallites [90].

2.7.2 Phase Composition (Purity)

Deviation from the stoichiometry of HAp is due to the presence in the crystal lattice of vacancies and ion substitutes such as carbonates, hydrogen phosphates, potassium, sodium, nitrates, and chloride which are usually introduced into the precipitating system with the reactants [5]. Contamination of HAp with these ions or formation of deficient Hap's suffer from significant changes in their crystallographic characteristics and have different crystal morphology as compared to stoichiometric HAp.

The substitution of phosphate ions PO_4^{3-} by hydrogen phosphate HPO_4^{2-} allows a continuous variation of the Ca/P atomic ratio between 9/6 and 10/6. This leads to Ca-dHAp [80]. Ca-dHAp powders can be precipitated from conventional wet chemical methods and decomposed into a mixture of HAp and TCP by thermal treatment above 700 °C. This allows a direct processing of biphasic calcium phosphate ceramics HAp/TCP without the step of powder blending. Raynaud et al. [22] proved the reliability of the Ca/P atomic ratio of the initial HAp powder calculated by determining the phase proportions in calcined biphasic calcium phosphates. Thus, the percent of β-TCP and HAp in the sintered bodies can be determined from the Ca/P ratio of the precursor HAp powder. Considering the Ca-dHAp change with thermal treatment to stoichiometric HAp and β-TCP according to the following equation [80]:

$$Ca_{10-x}(HPO_4)_x(PO_4)_{6-x}(OH)_{2-x} \rightarrow (1-x)Ca_{10}(PO_4)_6(OH)_2 + 3x\beta\text{-}Ca_3(PO_4)_2 + xH_2O$$

Equation (2-9)

where x is the calcium deficiency, and thus, $Ca/P = (10 - x)/6$. The mole fraction of β-TCP to the mole fraction of HAp in the sintered bodies is given by: $X_{TCP}/X_{HAp} = 3x/(1 - x)$. Since;

$X_{HAp} = 1 - X_{TCP,}$ and $X_{TCP}/(1 - X_{TCP}) = 3x/(1 - x)$ *Equation (2-10)*

the percent of β-TCP can be calculated by knowing calcium deficiency (x) from the chemical analysis. During the precipitation of the crystalline material, a precursor phase is formed which is amorphous to XRD. This phase has been shown to be structurally and chemically distinct from HAp. Calculations assuming the amorphous phase consisted of individual or groups of individual HAp unit cells were incapable of explaining the observed diffraction pattern. Chemical analysis of the precursor phase indicated that this noncrystalline phase is a hydrated calcium phosphate of calcium to phosphorus ratio 3/2 as compared to the 5/3 ratio found in HAp [71]. This distinct amorphous phase converts, in the presence of water, to microcrystalline HAp. The lifetime of the metastable amorphous precursor in aqueous solution was reported to be a function of the presence of certain macromolecules and interfering ions, pH, viscosity, ionic strength, and temperature. A preliminary study of the kinetics of conversion of metastable ACP to HAp indicated that at high pH the rate of conversion was proportional to the amount of HAp already formed, suggesting that the conversion was proceeding autocatalytically [71].

Thermal heat treatment (T= 600ºC) of HAp synthesised at low temperature leads to the decomposition (dehydroxylation) of the calcium hydroxide ($Ca(OH)_2$) to form lime (CaO) with water. The addition rate of reactant during the reaction synthesis has also a strong influence on the resultant composition. A higher addition rate of acid systematically results in an increase of the $Ca(OH)_2$ content [94].

2.7.3 Crystallite Size

Very small crystallites in contrast to crystallinity may still be very crystalline. Stoichiometric HAp has the smallest crystallite size (as low as 57 nm) and Ca-dHAp have the largest ones [78]. These results agree well with the after-mentioned surface area measurements. Ca-dHAp has the largest crystallites, since it was prepared under acidic conditions. Many authors found that the crystallite size increases with increasing the acidity of the precipitation medium [78].

2.7.4 Lattice Parameters

Aizawa et al. [95] measured the lattice parameters of the *a*-axis and the *c*-axis. With increase of the Ca/P molar ratio of the resulting apatite, the lattice parameter of the *a*-axis slightly decreased, while that of the *c*-axis increased. In addition, the *a/c* ratio decreased with increasing Ca/P molar ratio of the resulting apatite. According to Elliott [69] the lattice parameters of crystalline Ca-dHAp increase in the *a*-axis direction with decreasing Ca/P molar ratio, but decrease in the *c*-axis direction. Thus, the *a/c* ratio increases with a decrease in the Ca/P ratio. The increase in the *a*-axis parameter with decreasing Ca/P ratio may be due to more incorporation of HPO_4^{2-} ion into Ca-dHAp structure.

2.7.5 Particle Size

The synthesis of small HAp powder particles (comprised of either smaller primary crystallites mentioned earlier or a mixture of primary crystallites with powder particles) are found to be attributed to the high supersaturations derived from the high pH and short reactant addition time. An increased carbonate concentration may also contribute to the formation of small particles [78].

HAp precipitated by Knowles et al. [96] at 60°C had a particle size of 61.06 nm and at 80°C, a particle size of 82.24 nm, measured by line broadening effects. Whilst the mean particle size for the HAp precipitated at 80°C is larger, there appears in the TEM to be some fine particulate, which would stay in suspension more easily.

2.7.6 Particle Morphology

Spherical powders, in general, have better rheological properties than irregular powders and, thus, produce better coatings for hip implants and chromatographic separation [82]. The powders morphology will depend on whether the powder particle or crystallite size is being assessed. The temperature synthesis effect on the HAp morphpology indicates that at low synthesis temperature the crystals carry a needle-shape [94]. Increasing the reaction temperature changes the crystal from as-needle shape to a more regular shape, close to circular. A shape factor can be defined by the

ratio length/width of the Hap crystals: Fs =L/1 (Fs: shape factor; L: particle length [m] and l: particle width [m]. The shape factor, Fs, of the HAp crystals decreases with an increase of the synthesis temperature. After heating at high temperature T= 850ºC/ 4 h and then at T=1250ºC/ 4 h, the particle shape are with a more regular shape. After heat treatment at 1250ºC all the particles become thicker with a shape factor close to 1, this is due to the sintering of all the particles. Transmission electronic diffraction provides information at a one particle scale. The main axis of the HAp particle with the needle shape corresponds to the c-axis of the HAp structure. This is true for nanocrystals synthesised at low temperature (T<45ºC). Moreover the crystal looks like a monocrystal. At higher synthesis temperature, nanocrystals are shown to lose their tendency to grow as a monocrystal following the c-axis of the apatitic structure. The crystallite size reaches a maximum value which corresponds to a temperature around 60ºC. This phenomenon can be explained by two temperature dependent effects which are concurrent. First of all, a temperature rise increases HAp crystallinity which is thermally activated. Secondly, the temperature increase limits the tendency to the monocrystalline HAp nanocrystals growth following the HAp c-axis, because from this critical temperature, particles become more regular and circular. Above this temperature, the tendency to grow stops. This explains the maximum size for the HAp crystallites at this temperature. HAp precipitated in work carried out by Knowles et al. [96] also confirms that the reaction temperature significantly affects the precipitate morphology.

2.7.7 HAp Rheology

The rheology of HAp was studied by Knowles et al. [96] where they found that the viscosity increased with the increase of the particle size with the behaviour ranging from newtonian to dilatant. No thixotropic properties were noticeable in any of the suspensions, due to the low solids content that was used in the experiments. In rheological tests conducted by Tian et al. [97], it was found that a second calcination at a higher temperature for a longer time produced a larger size which in turn reduced the viscosity of the suspensions over a wide range of shear rates.

2.8 THERMAL TREATMENT OF HAp

It is generally accepted that the heating of HAp leads to three concurrent processes which involve (i) the evaporation of water, (ii) dehydroxylation, and (iii) decomposition. Although there is agreement between researchers about the processes which occur during the thermal decomposition of HAp, it is difficult to predict the exact temperatures at which these reactions occur. This is because the reactions do not occur instantly but over a wide temperature range, which depends on a number of factors relating to both the environment and the composition of the HAp.

Upon heating to 700–800 °C, it is accepted that Ca-deficient apatite transforms to the low temperature polymorph of β-TCP with a loss of water as described in the following reaction [98]:

$$Ca_9(HPO_4)(PO_4)_5(OH) \rightarrow 3Ca_3(PO_4)_2 + H_2O$$ *Equation (2-11)*

Sintering beyond 1180 °C induces the phase transformation of β-TCP to the high-temperature polymorph, α-TCP [98]. Therefore, β-TCP is stable below 1180 °C, while α-TCP is stable in the temperature range 1180 – 1400 ° C and super α-TCP is observed above 1470 °C. This phase transformation is accompanied by density changes in the calcium phosphate material. The density decreases with phase transformation in the following sequence when heat-treated to higher temperatures, such that [98]:

HAp (3.156 g/cm^3) > β-TCP (3.07 g/cm^3) > α-TCP (2.77 g/cm^3)

Equation (2-12)

As previously discussed, the dissolution rate of β-TCP is indeed 3 – 12 times faster than that of stoichiometric HAp with *in vitro* studies conducted revealing that α-TCP exhibits a higher dissolution rate than β-TCP. Thus, the order of relative solubility follows the order: α-TCP > β-TCP >> HAp

The decomposition of phase pure HAp has been reported by Sridhar et al. [99] to occur from 1050°C onwards. Tampieri et al. [87] found that decomposition began to

occur from 1200°C. Liao et al. [100] found that HAp was stable 1000°C -1350°C. The highest thermal stability which has been found in the literature is that reported by Deram et al. [101]. They found that HAp powder samples didn't show any phase transformation up to a temperature of 1450°C.

The decomposition of HAp into, β-TCP, TTCP and α-TCP has been reported to begin at 1050°C by Sridhar et al. [99], 1200°C by Tampieri et al. [87] and 1400°C by Liao et al. [100]. A melting temperature of 1550°C was reported by Fazan [102] for phase pure HAp; 1630°C for TTCP and 1730°C for TCP. The temperature ranges in which reactions occur as HAp is heated from ambient temperature to 1730°C are summarised in Table 2-13.

Table 2-13: Thermal effects on HAp [103]

Temperature	Reaction(s)
25-200°C	Evaporation of absorbed water
200-600°C	Evaporation of lattice water
600-800°C	Decarbonation
800-900°C	Dehydroxylation of HAp forming partially or completely dehydroxylated oxyhydroxyapatite (OHAp)
1050-1400°C	HA decomposes to form β-TCP and TTCP
< 1120°C	β-TCP is stable
1120-1470°C	β-TCP is converted to α-TCP
1550°C	Melting temperature of HAp
1630°C	Melting temperature of TTCP, leaving behind CaO
1730°C	Melting of TCP

2.8.1 Calcination (Drying)

A. Oven Drying

The oven drying stage of HAp powder processing, otherwise known as a calcination processes; may be defined as endothermic reactions in which an oxysalt, such as a carbonate or hydroxide, decomposes leaving an oxide as a solid product and liberating a gas [104]. Finely divided and sinterable ceramic powders are produced via this process. The surface area and particle size are a strong function of the calcination temperature and therefore are carefully controlled throughout the process. Heating just above the decomposition temperature, produces very fine, high surface area powders. Heating at temperatures well above the decomposition temperatures reduces the surface area (by forming hard agglomerates and increasing the particle size) to any degree desired. Decomposition of coarse salt particles to small, high surface area oxide particles occurs during calcination [104]. Subdivision occurs as a result of the nucleation of many oxide particles within each salt particle, or by fracture associated with strains between the shrinking parent salt and growing product oxide particles. These strains arise, since the oxide always maintains an orientation relationship within the salt. The oxide lattice always attempts to maintain coherence with the salt along preferred orientations. However, the large difference between volume and lattice spacing of the salts and oxides leads to strains and fracture.

Calcined powders are invariably agglomerated often with several levels of porosity. These pores arise from the large shrinkage associated with transformation from high volume salt to low volume oxide. The largest agglomerates are usually porous relicts that are pseudomorphs (that is, possessing the same shape) of the salt particles. Finer agglomerates within the pseudomorph can arise from clusters of nucleated oxide particles within the salt resulting in a coral like structure.

The majority of the research employing the oven-drying step for the calcination of HAp powders generally implement a drying temperature; ranging between 65 – 105ºC [56, 71, 79, 83 - 85, 90, 94, 105].

B. Spray Drying

Spray drying is a process whereby the HAp slurry (produced via the wet chemical precipitation method) is sprayed into a warm drying medium to ideally produce spherical powder agglomerates of relative homogeneity. It is considered a relatively efficient process since the HAp is well dispersed in the drying medium, the diffusion path is shorter, and the high specific surface area contributes to a higher rate of evaporation per unit mass of HAp product. The large surface area-to-volume ratio of the droplets allows rapid water evaporation and the resulting dry powder once separated from the air can be stored for later use [106, 107].

Spray drying is a popular method for HAp powder production due to its control over the final HAp powder properties obtained, particularly with regards to its powder morphology [108, 109]. Its most important aspect is the first stage of the process; atomisation. The basic principles underlying spray drying have traditionally been used in the following sequence; (i) a liquid ceramic feed material is initially filtered, (ii) tray dried, (iii) rewet and (iv) crushed into a workable particle size. The spray dryer apparatus combines these steps into a single step process. The spray drying process sprays a liquid, (with the material content, such as, the HAp in its slurry form), into a heated chamber; the liquid then becomes evaporated and the powder can then be collected at its designated collection point. Batch mixing in slurry form (at the precipitation stage) along with atomising facilitate mixing and the achievement of mixedness [107]. Atomisation of the solution in a hot furnace can be implemented to combine drying and calcination all in the one step [106 - 111]. The main objective of atomisation is to produce a large number of small droplets from a liquid stream so that the droplets can be dried into particles.

2.8.2 Sintering

Sintering of the HAp powder post drying occurs within a controlled atmospheric environment raising the powder to a temperature below the melting point but sufficient to allow solid-state diffusion and to permit bonding of the particles. The first stage involves the combustion of air and volatisation of any thermal labile compounds that may interfere with good bonding [106]. The second stage (or high

temperature stage) involves solid-state diffusion and bonding between the powder particles to occur. Finally, a cooling period will be required to lower the temperature of the HAp product. The cooling period maintains the product in a controlled environment, serving to prevent oxidation that would occur upon direct discharge into air and possible thermal shock from rapid cooling [106].

The control of sintering behaviour in the production of HAp powders is very important [112 - 117]. Highly dense HAp is desirable to prevent the preparation of human fluid into the interfacial area between the HAp coating (described later) and Ti-alloys in hip joint replacements, while porous HAp are required for the replacement of fractured bone to allow ingrowth of the natural and artificial bones to occur and a strong bond between them to be readily attained [116]. HAp powders sintered by Sung et al. [114] at 1000ºC for 1h showed highly dense and almost pore-free morphology. The sintered density value for the sintered HAp was determined as 99.9% of the theoretical value for HAp, owing to the fine particle size produced during HAp synthesis. HAp powders, consisting of very fine particles have a much higher surface area, which is the driving force for solid-state sintering and the amount of surface energy decrease is proportional to the free energy decrease for the sintering reaction [114]. Therefore, sintering behaviour of HAp powders can be controlled by characterising powder particle size. Kim et al. [115] sintered HAp powders with a specific surface area of $68m^2/g$ at 1200ºC for 2h to improve the crystallinity of the final HAp product. It was also noted that prior calcinations at 900ºC for 4h in air with subsequent ball milling were effective in eliminating agglomerates in the HAp powder. Results from Juang et al. [116] showed that sintering treatments increased the average particle size and distribution. The sintering behaviours were investigated by dilatometry and density measurement. The fluidity of the HAp powders and the driving force for sintering were found to dominate the properties. Sintering at 1250ºC was found to result in a higher bending strength (about 55MPa) with a finer grain size. Work carried out by Ramesh et al. [117] supported this evidence, as scanning electron microscope (SEM) analyses of the sintered microstructure revealed an exponential increase in grain size with increasing sintering temperature.

Ramesh et al. [117] states that the HAp phase was stable when sintered below 1400ºC for 2h. However, sintering at temperatures ≥1400ºC resulted in the decomposition of HAp to form TCP, TTCP and CaO products. It was believed that the high humidity content present in the sintering atmosphere slowed down the decomposition rates by preventing dehydration of the OH^- groups from the HAp matrix [117].

Kim et al. [115] observed that substitutions into the HAp lattice (such as, carbonate, magnesium, silicon) inhibited apatite crystallisation in solution and destabilised the structure of HAp and favoured its thermal conversion into α- or β-TCP. An adverse affect on the sinterability of the HAp was identified. HAp decomposes to form other calcium phosphates at elevated temperatures. Two mechanisms have been proposed for the decomposition as follows [118]:

$$Ca_{10}(PO_4)_6(OH)_2 \Leftrightarrow 2\beta - Ca_3(PO_4)_2 + Ca_4P_2O_9 + \uparrow H_2O \qquad \textit{Equation (2-13)}$$

$$Ca_{10}(PO_4)_6(OH)_2 \Leftrightarrow 3\beta - Ca_3(PO_4)_2 + CaO + \uparrow H_2O \qquad \textit{Equation (2-14)}$$

Of these, the former is the more accepted mechanism. Further heating results in the transformation of β-tricalcium phosphate (β-$Ca_3(PO_4)_2$), forming α-tricalcium phosphate. This usually requires exposure to temperatures in excess of 1350°C for this phase transformation to take place. It is believed that phase pure HAp can be sintered without decomposition at temperatures of up to ~1300°C [12]. Regardless of which mechanism takes place, both result in the formation of soluble or resorbable calcium phosphates, which dissolve when exposed to physiological environments [118].

2.8.3 Factors Affecting Thermal Decomposition Of HAp

The factors affecting the thermal decomposition of HAp are as follows [118]:

A. Sintering Temperature and Atmosphere

The highest possible sintering temperature depends on the sintering atmosphere (partial pressure of water vapour) [12]: increasing the ambient humidity stabilizes HAp to higher temperatures. As discussed previously (section 2.8), increasing the temperature to 1500°C leads to rapid HAp decomposition, while, under ambient sintering conditions, decomposition is reported to begin in the range 1050-1100°C. Some researchers, however, have observed synthetic HAp to resist decomposition until 1200°C. Since a gaseous species exists on the products side of the decomposition reactions, sintering atmosphere is expected to influence the decomposition kinetics of HAp [118]. Consequently, sintering under vacuum conditions can induce decomposition at lower temperatures, favouring the formation of water vapour. On the other hand sintering in a moist atmosphere is found to counteract this effect and delay decomposition to some degree [94, 95, 118].

B. Ca/P Molar Ratio

HAp has a theoretical stoichiometric Ca/P molar ratio of 1.67, however this has been known to vary due to the HAp structure's willingness to undergo substitutions. Materials with Ca/P molar ratios different from 1.67 are known to be less thermally stable compared to stoichiometric HAp [98 - 103]. There is experimental evidence that HAp with a Ca/P molar ratio of 1.68 does not decompose at temperatures of up to 1450°C over a period of 3 h [12].

C. Initial Particle Size

Sintering of fine-particle HAp powder at 1300°C for 3 h ensures a nearly theoretical density. Sintering at higher temperatures is accompanied by secondary recrystallisation: as the sintering temperature is raised from 1300 to 1450°C, the grain size increases from 4 to 14 μm. The grain size as a function of heat-treatment

temperature exhibits Arrhenius behaviour with an apparent activation energy of 196 kJ/mol.

Clearly, the optimal sintering temperature and duration depend on the prior history and particle size of the powder, which influence its sintering behaviour and the phase composition of the resulting material. Increasing the particle size of the HAp powder from 1 to 4.2 mm markedly raises the shrinkage onset temperature [12]. In spite of the higher green density of coarse-particle compacts, the sintered density increases with decreasing particle size.

D. Initial HAp Synthesis Reaction

It is believed that the method used to synthesise the HAp powder can influence its thermal stability [114-116, 118, 119]. The belief is that HAp powders synthesised using hydrothermal methods are more stable compared to precipitated powders. This may be attributed to the presence of adsorbed HPO_4^{2-} ions.

E. Secondary Phases

Several researchers [118] have tried reinforcing HAp with secondary phases to improve its mechanical properties, which are not generally accepted to be suitable for load-bearing biomedical applications. In almost all cases, the presence of these phases reduced the temperature at which decomposition began. The same conclusion was applied to impurities in HAp powders.

2.9 POST-SINTERING PROCESSING OF HAp

2.9.1 Grinding

The next stage in the HAp powder processing is often the size reduction of the HAp powder particle agglomerates that have been produced upon sintering. Grinding and milling are extensively applied in the field of ceramics for size reduction [3]. The general phenomena during a solid state size reduction are based on fracture mechanics: the nucleation of cracks, followed by crack propagation and fracture, by which new surfaces are formed. A further decrease of mean particle size will only take place when these processes occur. The kinetic energy within the milling aggregate is partially transformed into mechanical stresses within the powder material to be disintegrated. The forces acting in these processes cause mainly compression and shear stresses, applied as impact. In ceramic materials, plastic deformation does not take place in coarse particles, but becomes significant for mean particle sizes in the micron range. The main process phenomenon for all grinding and milling processes, however, is crack propagation and fracture, which is accompanied by local, not well defined, temperature increase [3]. These are often defined as thermal ‘spikes’ and can result in anomalous structures [3]. The limit of the minimum obtainable particle size depends on the conditions of the mechanical process as well as on the material itself.

2.9.2 Sieving

Post sintering and grinding, the HAp powders are sieved through the desired mesh size (see Table 2-14) in order to ensure that the correct particle size distribution (>90% of the HAp powder particles are <100μm) can be achieved prior to plasma spraying the HAp powder as a coating onto orthopaedic implants.

Table 2-14: ASTM mesh sizes. According to ASTM B 214 – 07 [120]

Mesh Size	Microns	Inches
4	4760	0.185
6	3360	0.131
8	2380	0.093
12	1680	0.065
16	1190	0.046
20	840	0.0328
30	590	0.0232
40	420	0.0164
50	297	0.0116
60	250	0.0097
70	210	0.0082
80	177	0.0069
100	149	0.0058
140	105	0.0041
200	74	0.0029
230	62	0.0023
270	53	0.0021
325	44	0.0017
400	37	0.0015
625	20	0.0008
1250	10	0.0004
2500	5	0.0002

2.10 RHEOLOGICAL PROPERTIES OF HAp

Rheology is the most sensitive method for material characterisation because flow behaviour is responsive to properties such as molecular weight and molecular weight distribution. Rheology measurements are also useful in following the course of a chemical reaction [121]. Such measurements can be employed as a quality check during production or to monitor and/or control a process. Rheological measurements allow the study of chemical, mechanical, and thermal treatments, the effects of additives, or the course of a curing reaction.

2.10.1 HAp Precipitating Slurry

Tian et al. [97] made a comparative investigation on particle size, zeta potential and rheology behavior of suspensions of HAp powders produced by a wet-chemical synthesis method. Results showed that temperature and soaking time of the calcinations process significantly affected the HAp particle size and resulted in a reduction of the zeta potential and suspension viscosity. On this basis, it was concluded that the reduction in the viscosity was attributed to a higher repulsion barrier in interparticle potential.

According to Padilla et al. [122] HAp suspensions with high solids content were obtained through the wet chemical precipitation technique using $Ca(OH)_2$ and H_3PO_4. Powder calcinations temperatures were found to have an effect on phase composition, surface area, porosity and rheological behaviour [116]. HAp powders calcined at 1200ºC were capable of achieving 60% vol. of concentrated slurry.

2.10.2 HAp Powder Particles

A simple definition of powder flowability is the ability of a powder to flow [123]. Flow behaviour is multidimensional and depends on many powder characteristics and variables (See Table 2-15) [123]. Flowability is the result of a number of the combination of material physical properties that affect material flow and the equipment used to handle it. Equal consideration needs to be given to both the material and the equipment [123]. Powders are sometimes considered to be relatively

stable entities like the individual solid particles that make up their mass. This is not the case since the rheological properties of the mass are greatly influenced by the presence or absence of air [124].

The inherent changeability of powders means that processing and handling are not straightforward and predictable procedures [124 - 128]. Powder flowability is inherently complex due to the many physical and environmental variables that determine how it responds to being moved. Investigating flowability requires the use of a technique with exceptional sensitivity and repeatability of measurement.

Table 2-15: Variables affecting powder flowability [124]

Powder or Particle variables	**External Factors influencing Powder Behaviour**
Particle size	Flow rate
Size distribution	Compaction condition
Shape	Vibration
Surface texture	Temperature
Cohesivity	Humidity
Surface coating	Electro-static charge
Particle interaction	Aeration
Wear or attrition characteristic	Transportation experience
Propensity to electro-static charge	Container surface effects
Ability to recover from compaction	

There are no reliable quantitative relationships between primary properties like particle size and distribution, particle shape and secondary properties such as failure properties or bulk density [129]. Therefore, in order to reliably predict flow performance, an understanding of the impact and the interaction of all the above variables needs to be realised.

2.11 THERMAL SPRAY APPLICATION OF HAp POWDER FOR ORTHOAPEDIC COATING APPLICATION

2.11.1 Thermal Spray Method

Thermal spraying represents a group of processes which employ heat and velocity to coat the surface of one material with another, using powder or wire as feedstock. Thermal spray methods can be divided into two principal energy sources, chemical energy of the combustion gases that power the flame spray torch and electric currents providing energy for the plasma generators. Figure 2-15 highlights the principal thermal spray methods associated to both energy sources.

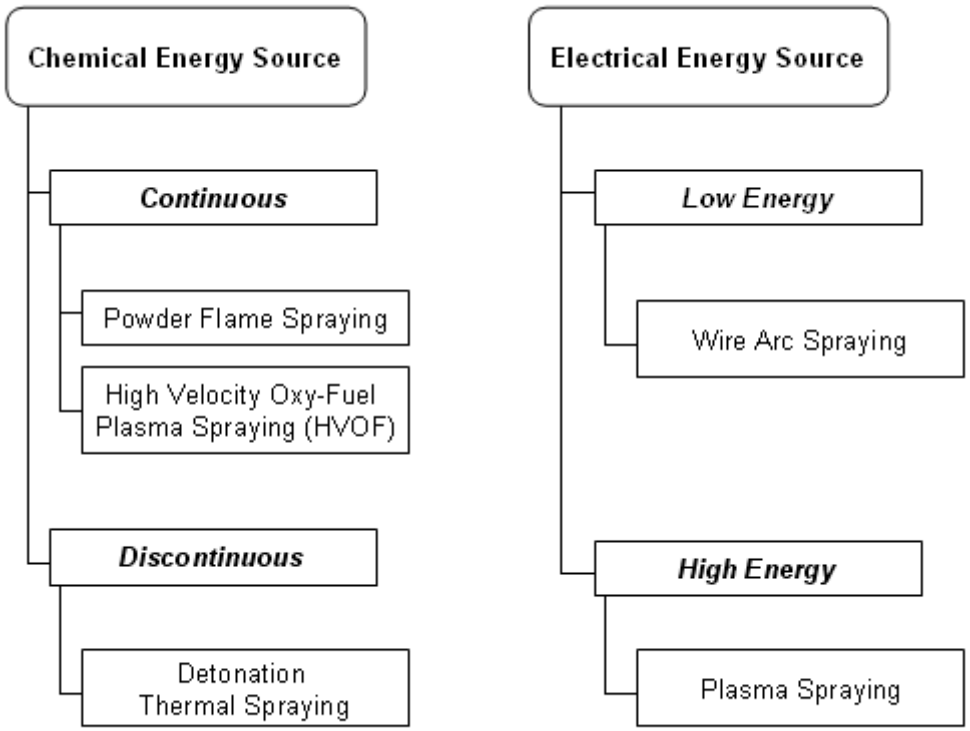

Figure 2-12: Thermal spray techniques divided by their principal energy sources

Many orthopaedic implant systems utilise osteoconductive surfaces, such as, HAp coatings to promote implant fixation to bone by direct bonding or osteointegration [2, 21, 131]. Of the many techniques used for depositing HAp onto orthopaedic implants, plasma spraying is the most commercially accepted and only FDA approved method

for producing HAp coatings [2, 21, 103, 131]. Plasma spraying has the ability to produce specialised coatings with functional properties such as, biocompatibility, fixation, corrosion and wear resistance that is beneficial to the field of biomedical engineering [132]. The principle of plasma spray operation is illustrated in Figure 2-16.

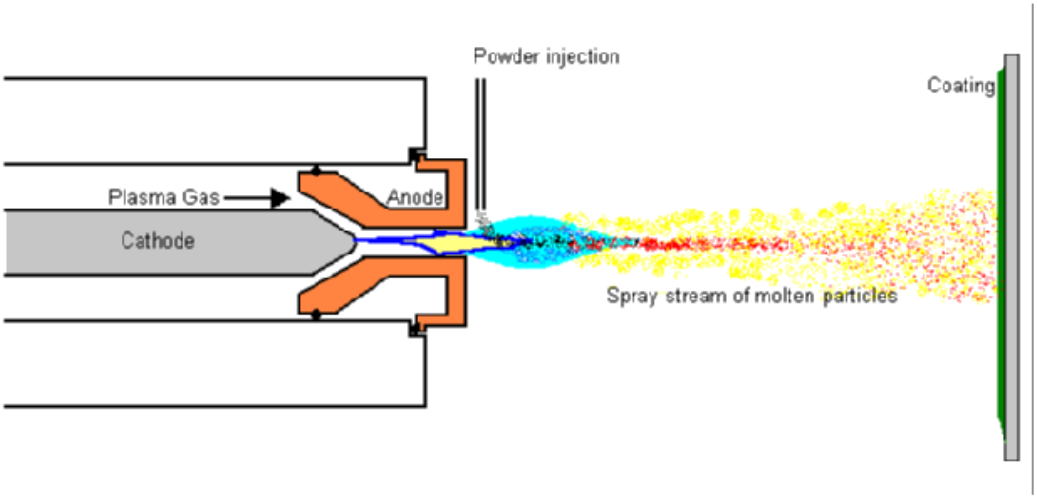

Figure 2-13: Schematic diagram of the thermal spray process [103]

2.11.2 Plasma Spray Operation

The plasma spray process is basically the spraying of molten or heat softened material onto a surface to provide a coating. Material in the form of powder is injected into a very high temperature plasma flame (caused by a mixture of high current arc and combustion gases), where it is rapidly heated and accelerated to a high velocity. The hot material impacts the substrate surface and rapidly cools forming a coating [103, 106, 109, 132-136].

The plasma spray gun comprises of a copper anode and tungsten cathode, both of which are water cooled. Plasma gas (inert gases; argon or nitrogen and combustion gases; hydrogen or helium) flow around the cathode and through the anode which are shaped in a nozzle shaped assembly. The combustion gas is not used for HAp production as this has chemical effects on resultant deposit. The plasma is initiated by a high voltage discharge which causes localised ionisation and a conductive path for a

DC arc to form between the cathode and anode [103, 132]. The resistance heating from the arc causes the (inert and combustion) gas to reach extreme temperatures as high as 30,000ºC, dissociate and ionise to form plasma [132, 136]. The plasma exits the anode nozzle as a free or neutral plasma flame (plasma which does not carry electric current) where the arc extends to the surface to be coated. When the plasma is stabilised (ready for spraying), the electric arc extends down the nozzle rather than shorting out to the nearest edge of the anode nozzle (arc instabilities are governed by the electrode design, gas injection mode, spraying parameters and the condition of the anode wall) [132]. This stretching of the arc is due to a thermal pinch effect [136]. The HAp powder is fed from a hopper unit using an inert gas (such as, Argon) into the plasma flame via an external powder port mounted near the anode nozzle exit [136]. The powder is rapidly heated and accelerated (velocity of 200-300 $m.sec^{-1}$) over spray distances of 25 to 150 mm [132]. Thermally sprayed coatings have a characteristic layered structure made of individual powder splats oriented parallel to the substrate surface producing high levels of anisotropy [102, 103, 132, 133, 136].

The plasma spray process is most commonly used in normal atmospheric conditions and referred to as Atmospheric Plasma Spraying (APS). A problem pertinent to the plasma-sprayed HA coating is the generation of an amorphous phase, along with other non-bioactive calcium phosphate phases following plasma spraying [132]. Calcium oxide is usually formed when HAp deposition is performed in air [132]. Coatings sprayed with large starting powders are found to undergo dramatic degradation after immersion *in vitro* [132]**.** The integrity of the coating produced in this environment ultimately depends on the amount of calcium oxide formed. Some plasma spraying have been conducted in protective environments using vacuum chambers normally back filled with a protective gas at low pressure; this is referred as Vacuum Plasma Spraying (VPS) or Low Pressure Plasma Spraying (LPPS) [132]. The different techniques distinguished by the surrounding atmosphere for plasma spraying are illustrated in Figure 2-17.

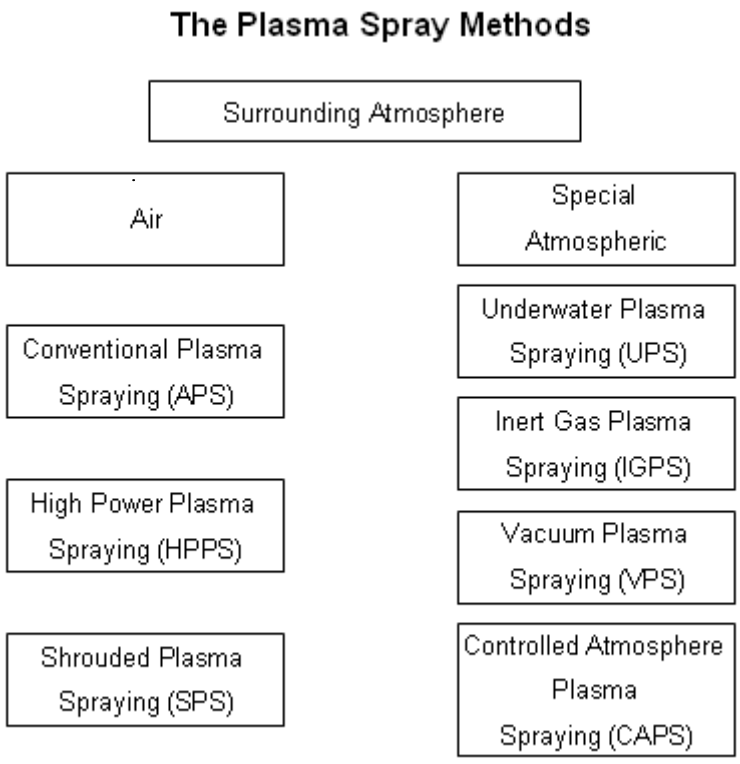

Figure 2-14: Plasma spray techniques divided by their surrounding atmospheres

Ideally, only a thin layer of each powder particle ends up in a molten plastic state, which undergoes phase transitions [132]. This plastic state, however, is necessary to ensure dense, adhesive and cohesive coatings. Subsequently, the properties of plasma sprayed coatings depend on the optimal relation between the particle size, particle chemistry, the gas used, the speed of the plasma, the distance between the plasma nozzle and the substrate (consisting of a Ti-alloy implant) and the cooling process for the desired composition and crystallinity [132]. Many of the parameters chosen in the control of the thermal spray techniques will have a dramatic influence on the final structure of the ceramic coating and must therefore be carefully controlled in order to optimise the performance of the HAp coating *in vivo*. In the plasma spray process, the main parameters include power, current, distance between nozzle and substrate (orthopaedic, Ti-alloy implant), plasma work gas rate, carrier gas rate and powder feed rate. The heat content of the plasma flame and thus the ability to increase the temperature of the powder particle depends on the type of gas used. Argon mixed with hydrogen gives a higher degree of crystallinity [132]. The combustion of the

inert and combustion gases has an effect on coating thickness and crystallinity [132]. The use of nitrogen gas as the carrier gas, as opposed to argon results in thicker coatings [132]. The plasma spray parameters commonly used to deposit the HAp powders onto orthopaedic implants are shown in Table 2-16.

Table 2-16: Optimum plasma spray parameters used for depositing dense HAp coatings onto orthopaedic implants. Adapted from [130]

Coating	Current (A)	Spray distance (mm)	Gas flow rate (scfh)	Carrier gas flow rate (scfh)	Powder feed rate (g/min)
HAp	750	70	114.59	10	20

Where scfh is standard cubic feet per hour

Plasma spraying has the advantage that it can spray very high melting point materials. Plasma sprayed coatings are generally much denser, stronger and cleaner than the other thermal spray processes with the exception of High Velocity Oxy-Fuel (HVOF) and detonation processes [133]. Plasma spray coatings account for the widest range of thermal spray coatings and applications, making this process the most versatile. Its main disadvantages owes to its relative high cost and complexity [96].

The deposition of HAp coatings on medical devices range between 50 to 100μm thick [102, 103, 134, 135]. Coatings with thicknesses greater than 80μm become brittle, whereas very thin coatings often resorb too fast [102]. Significant porosity of the HAp material lowers the mechanical strength and increases the resorption rate [102]. Optimum coatings consist of completely dense and pure HAp powders, with a Ca/P molar ratio close to that of natural bone (1.667) [2]. The optimum HAp powder particle size for plasma spraying generally does not exceed 160μm (Table 2-17). Hence the production and characterisation of HAp powder before thermal spraying will enhance the deposits performance in vivo.

Table 2-17: Properties of HAp applied onto Ti-Alloy substrates. [64]

Surface	Average Roughness (μm)	Initial Powder Size (μm)
HAp coating on Ti Substrate	4.96 ± 0.43	45 - 160

2.11.3 Thermal Stability Of HAp Coating

The ability to adapt to the harsh physiological environment depends very much on the degradation strength and thermal stability of a resultant HAp coating. Kweh et al. [2] noted that a pH of about 9 would produce the correct stoichiometric condition whereby only pure, single-phase HAp is formed. No other undesirable phases such TCP or CaO were found in the above research.

The use of precipitated HAp powder, subsequently spray dried has proven the ability to produce porous coating microstructures to aid in enhanced bone ingrowth. Flame-spheroidized powder however possesses the capability to produce dense, coherent HAp coatings with highly lamella structures, aiding in osteoconduction [1]. Spheroidized HAp (SHAp) powder provide better flowability and stability, which eventually affects the deposition and phase formation in the resultant coating [1]. This is achieved through an intermediate stage of flame spraying.

The level of crystallinity of the heat-treated SHAp powder was found to be much higher than that of the untreated powder. No undesirable phases of TCP and CaO were detected for both the SDHAp and SHAp powders [2]. This was identified by the increase in peak height and the narrow peak width. SHAp powder appears to inherit better particle characteristics than the former including, a spherical geometry, dense internal structure and a smooth glassy surface as mentioned earlier in this section.

2.12 STANDARDS AND REGULATORY REQUIREMENTS IN HAp POWDER PRODUCTION FOR ORTHOPAEDIC COATING APPLICATION

HAp coated titanium implants have been identified as Class III medical devices in accordance with the Food and Drug Authority (FDA) regulations [137]. The chemical and physical parameters for HAp as stated in the "Draft Guidance for Calcium Phosphate (Ca-P) Coatings for Preparation of FDA Submissions for Orthopaedic and Dental Endosseous Implants" [137] are in parallel to the American Standard for Testing of Materials, ASTM, F1609-08; "Standard specification for calcium phosphate coatings for implantable materials" [138]. These drafts outline the methods, regulations and standards (Table 2-18) associated to attaining optimum HAp powder properties with respect to elemental analysis, Ca/P ratio, density and solubility of HAp powders (Table 2-19).

Technical specifications for HAp, in its particulate form (that is, HAp powder) is outlined in ISO 13779-1, Implants for Surgery – Hydroxyapatite, Part 1 and ASTM F1185-03 [139, 140] is another specification, which covers the chemical and crystallographic requirements for HAp intended for surgical implants. In order for a material to be referenced as HAp, it must conform to this specification. The biological response to HAp in soft tissue and bone has been characterised by a history of clinical use and by laboratory studies. This specification includes powder, particulate, and forms intended for use as surgical implants, components of surgical implants, or as raw materials for manufacturing processes such as thermal spray coating, electrophoretic deposition, physical vapour deposition, while excluding HAp coatings, ACP, ceramic-glasses, tribasic calcium phosphate, whitlockite, and α- and β-TCP, which are alternatively covered under the standard specification for composition of Beta - Tricalcium phosphate for surgical implants, ASTM F1088-03 [141].

A highly pure, homogeneous, and highly crystalline HAp, produced and certified by the National Institute of Standards and Technology (NIST) is the standard reference material, SRM 2910 [50]. The contents of Ca^{2+}, PO_4^{3-}, OH^-, HPO_4^{2-}, H_2O, CO_3^{2-} and

trace constituents, the Ca/P molar ratio, crystal size and morphology, surface area, unit-cell parameters, crystallinity, and solubility of this HAp are also presented for this reference material.

2.12.1 Chemical And Crystallographic Analysis Of The Ca-P Powder

The FDA requires the following test data to be reported when using or proposing HAp products:

A. Elemental Analysis

An elemental analysis for the powder noting any impurities including, but not limited to, 50-ppm heavy metals, as identified in ASTM F1185 [140] is required. Characterisation of the protein present in the powder should also be included [138].

B. Calcium To Phosphorous (Ca/P) Ratio

The Ca/P ratios in atomic percent for the powder should be reported. In order to account for the deviation that may occur from the ideal stoichiometric ratio (Ca/P = 1.667); a sufficient number of samples are required for analysis in order to produce a statistically meaningful mean and variance (95% confidence interval) [138].

However, Table 2-19 indicates ranges for Ca/P ratio that have been found acceptable [120]. Therefore, the content of calcium and phosphorous ratio, Ca/P, shall have a value of $1.65 \leq Ca/P \geq 1.82$ for the atomic ratio in accordance to ISO 13779-1[139]. This must be determined using the specifications described in ISO 13779-3 [142].

C. X-Ray Diffraction (XRD)

Individually superimposed patterns of the formed HAp powder over the standard given for the relevant calcium phosphate compound (such as, HAp, JCPDS 9-342 [143]) in the powder diffraction files of the JCPDS (Joint Committee on Powder Diffraction Standards) must be determined.

Table 2-18: Relevant standards, methods and publications. Adapted from [137]

Guidance	Standard(s)	Method(s)	Publication(s)	Comments
Elemental Analysis	ASTM F1185 ASTM F1088	Atomic Absorption		
X-Ray Diffraction	JCPDS 9-342	Hanawalt Method for Powder	Cullinity [126]	Methods dependent upon starting material
	ASTM F4.2.3.8	Calculation of total area under curve (% amorphous material)		
Solubility			Ducheyne et al.[54]	
Density		Helium Pycnometer		

Table 2-19: Calcium Phosphate Powder Characteristics of Legally Marketed Devices. Adapted from [137]

Guidance	Maximum or Minimum Cleared	Range	Comments
Elemental Analysis	50 ppm heavy metals (MAX)		
Ca/P ratio		- Powder: 1.66 – 1.67 -Coating: 1.67 – 1.76	
Crystallinity	95% Crystallinity (MIN)		
Purity	95% Purity (MIN)		If the purity of the HAp powder is less than 95% or if the coating is less than 90%, the labelling of the implant should identify all major compounds present.
Density	- Powder: >3.00 g/cm^3 -Coating: >2.98 g/cm^3		

D. Infrared Spectrometry (IR)

The IR spectra of the HAp powder must also be indicated. Spectra must be plotted as percent transmittance versus wavenumber [137]. The characteristic absorption bands for HAp are as follows [137]:

$PO4^{3-}$: 570cm^{-1}, 962cm^{-1}, 1050cm^{-1}
OH-: 630cm^{-1}, 3540cm^{-1}

E. Solubility Of Ca/P Compound

A complete report regarding the solubility testing is required and should be conducted in a physiologically similar solution to tris-HCL buffered solution at 37°C, tested at a pH of 3.0 and 7.3 [137]. Room temperature and 100°C measurements are optional. Alteration in pH must also be recorder with the solubility product of HAp being based upon the normal stoichiometric formula $Ca_{10}(PO_4)_6(OH)_2$.

Xue et al. [135] examined the dissolution behaviour of HAp coatings in tris-buffer solutions. The results obtained indicated that the coating having the high crystallinity showed the lower dissolution as compared to the low crystallinity coating. Their crystallinity's were about 55% and 98%, respectively; indicating the significance in complying with FDA requirements of a 95% minimum with regards crystallinity obtained.

The HAp coated orthopaedic implant is required to satisfy the requirements for ISO 13779-2, ISO 13779-3 and ISO 13779-4, Implants for Surgery – Hydroxyapatite, Parts 2, 3 and 4 [142, 146, 147]. The chemical composition of the HAp coated orthopaedic implant is required to meet the specifications as outlined in ISO 13779-3, "Implants for surgery – hydroxyapatite: chemical analysis and characterization of crystallinity and phase purity". The practice ASTM F2024-00 [148] is for the determination, by the Reference Intensity Ratio (RIR) external standard method, of the percent by weight of the crystalline phases, HAp, β-TCP, and CaO in coatings deposited upon metallic substrates by plasma-spraying HAp. A major component in plasma-sprayed HAp coatings other than HAp is expected to be ACP. Crystalline

components other than HAp that may be present include α- and β-TCP, TTCP, CaO, and calcium pyrophosphates. Quantification of the minor crystalline components has proven to be very unreliable due to extreme overlap and confounding of XRD peaks. Therefore, this practice addresses the quantification of only HAp, B -TCP, and CaO. This practice was developed for plasma-sprayed HAp coatings with HAp contents of at least 50 % of the total coating.

Biocompatibility requirements are outlined in the ISO standard 10993, "Biological Evaluation of Medical Devices" [149] where part 1 of the standard aids in outlining the selection of tests required in order to assess its biological response *in vivo*. Part 5 outlines the tests for cytotoxicity through various *in vitro* methods [150] while parts 6, 9, 11 and 12 relate to tests for local effects after implantation, the degradation of the materials related to biological testing, tests for systemic toxicity, and sample preparation and reference materials, respectively [151 – 154].

2.13 SUMMARY

This literature survey highlights the great effect of the process parameters using the chemical precipitation technique for the synthesis of high HAp purity and crystallinity, which are in effect the deciding factors for its thermal stability and hence dissolution in a physiological environment. It also highlights the effect of varying these parameters on other HAp powder characteristics, such as, crystallite size, lattice parameters, particle size, morphology and its rheological properties. Therefore, in order to produce HAp powder with predictable powder characteristics, these parameters are required to be effectively designed. To evaluate the influence of these conditions on the final powder properties, various equipment and procedures were used and are described in the following chapter.

3 EXPERIMENTAL EQUIPMENT, PROCEDURES AND MATERIALS CHARACTERISATION

3.1 INTRODUCTION

This chapter outlines the experimental procedures, equipment, and material characterisation techniques used in the current research, in the preparation of high phase purity and crystalline HAp powders (both ≥95%), for application via plasma spraying onto orthopaedic implants in order to investigate the effect of the synthesis parameters on the final HAp powder properties obtained. The HAp was characterised at various stages of the production process ((i) post precipitation in slurry form and (ii) post sintering in powder form) to evaluate the various HAp properties, such as, phase purity, crystallinity, crystallite size, lattice parameters, particle size, density, specific surface area, porosity, morphology and rheological/viscous properties. The route used to prepare HAp powder in the initial stage of this investigation, was based on the process currently used in Irish industry (company name cannot be disclosed due to intellectual property rights) and reproduced in-house on a laboratory scaled version. The properties obtained for the powders produced in Irish industry and the current research were evaluated and compared against that of other marketed HAp powder producers (such as, CAMCERAM®, Tomito®, Plasma Biotal® and a sister company of the Irish based industrial company) to screen the powders of optimum quality for plasma spraying and identify the factors

affecting the final properties yielded. The observations aided in the selection of the process parameters for screening at the experimental design stages.

Two experimental designs were constructed: (i) screening experiments using a fractional factorial design to screen the factors which have a significant effect on the powder properties obtained and (ii) optimisation experiments using a box - behnken design to optimise the critical parameters controlling the powder properties obtained. A description of both the experimental designs used in the research is outlined in Section 3.6. The optimisation approach is outlined in Section 3.7.

The materials characterisation equipment used in the current investigation in order to characterise the HAp powders are described in Section 3.8, with respect to HAp powder phase purity, crystallinity, crystallite size, lattice parameters, particle size, specific surface area, powder density and powder morphology. The equipment and methods for observing the rheological properties of the HAp in a slurry and powder form are also presented.

An investigation to evaluate the *in vitro* behaviour of the powders produced was also conducted, through cell studies, such as, cell proliferation, cell viability and cell morphology. A description of these procedures is outlined in Section 3.9.

3.2 PREPARATION OF HAp POWDER

In order to replicate the HAp powder production process used by the Irish industry in-house on a laboratory scale, the following procedure was implemented (based on literature, industrial placement and practice), whereby the HAp was synthesised via the chemical precipitation method, using the precursor materials, calcium hydroxide, $Ca(OH)_2$ (produced in-house) and phosphoric acid, H_3PO_4 (JT Baker, Analyzed, 85% Pure) in the chemical reaction based on Equation 2-1. The initial stage of the process, involves the preparation of a $Ca(OH)_2$ slurry via the addition of 79.55g of CaO (JT Baker, Analyzed, 100% Pure) powders to 500mL of distilled water in a 1000mL-enclosed beaker, under vigorous agitation conditions with a vertical IKA mechanical overhead stirrer at 1000rpm, at an uncontrolled reaction temperature and without the control of the atmospheric environment (the latter two parameters were controlled in later studies). The next stage of the process involves neutralisation of the supersaturated solution by titration using 97.32g of 85% H_3PO_4 (JT Baker, Analyzed) at an addition rate of 1.5mL/min, controlled using a peristaltic pump. All chemicals used were reagent grade. 0.28 mol (9.94g) NH_4OH, was added to the HAp slurry after the 24h ripening period to stabilise the pH of the super-saturated solution to above pH 9. X-ray diffraction and pH readings obtained were used to follow the reaction and assess the composition, to determine when stoichiometric HAp was reached. Spray drying of the HAp slurry was then employed to evaporate the moisture content from the slurry. The spray dryer atomised the pre-HAp suspension via the controlled removal of water by temperature control and product collection into two different batch sizes (the parameter setting, of which are discussed in a later section). Analysing and correcting the viscosity of the final HAp slurry (to 2 – 3 cst) prior to spray drying ensured that dense, micron-sized powder particles were obtainable [82, 108]. The actual spray drying parameters were set to control the morphology of the particles to obtain powders of a spherical shape, with a view to enhancing the flowability of the powder particles. The dried powders were then sintered in a furnace at 1210ºC for 4h, ground using a mortar and pestle and sieved to eliminate any powders of particle sizes exceeding 100µm. A flow chart for this process is shown in Figure 3-1.

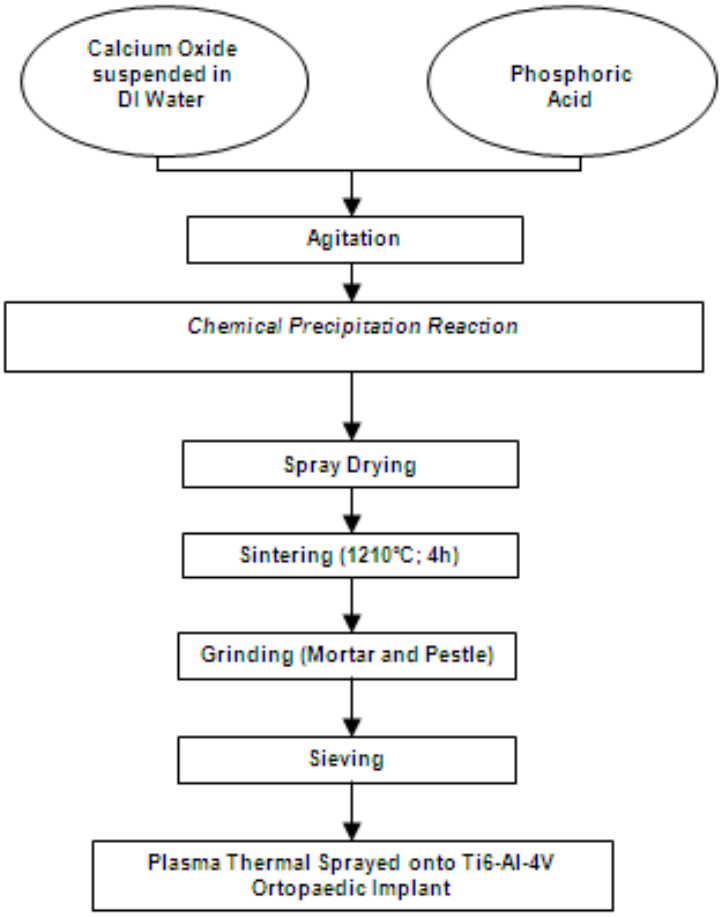

Figure 3-1: Flow chart of the HAp production process used in-house, as replicated on a laboratory scale, based on a current Irish based industrial process

The preliminary investigation of this study involved analysing the HAp powder characteristics of international suppliers and comparing these against the HAp powder properties currently being produced in industry in Ireland. HAp was synthesised in-house, within the Materials Processing Research Centre, under the same conditions as that disclosed by the HAp manufacturing company in Ireland; characterised and compared against that of the Irish HAp and also against those purchased by other various international suppliers. The HAp powders examined in this study were described in the following section.

3.3 CONTROL OF THE FACTORS AFFECTING CHEMICAL PRECIPITATION

3.3.1 Chemical Precipitation Equipment

A scaled down version of the chemical precipitation process, as used in Irish industry (see the experimental rig, Figure 3-2) was produced in the current research in order to examine the effect of the factors, which are considered to have a significant effect on the chemical precipitation process and thus the final HAp powder properties yielded. The drawings for this design can be referred to in Appendix A. The design of the experimental rig was developed by the author in order to accommodate the possibility in varying and ultimately controlling the factors, which affect the precipitation process (such as, temperature control, rate of reagent addition, stirring speed and atmospheric control).

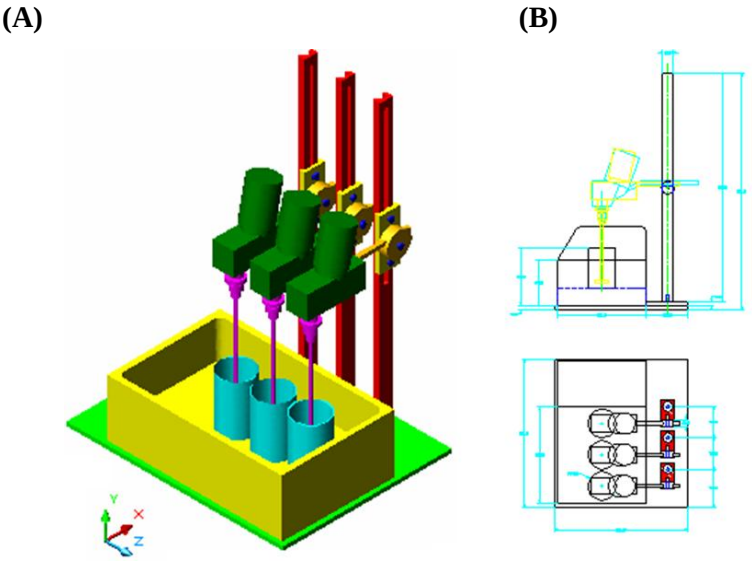

Figure 3-2: AUTOCAD 2005 Drawings of the chemical precipitation rig designed for the investigation of HAp synthesis (3-D view (A) and 2-D plan and elevation view (B)

Other important factors, controlling the process (such as, initial reagent concentrations and ripening/maturation time) did not influence the design of the rig, as these factors were considered to be independent of the rig design.

3.3.2 Temperature Control

Precipitation temperature was controlled using a temperature controlled water bath (NE4-28T Series) with precision as follows [155]:

- Temperature range: +5°C - 99°C
- Sensitivity/temperature stability: ±0.1°C at 45°C
- Temperature uniformity: ±0.01°C at 45°C

pH measurements were recorded via a Hanna HI 9813 Handheld pH, EC & TDS Meter with Probe (Hanna Instruments, Inc.) with an accuracy of pH: ± 0.2pH at ambient temperature. [156]

3.3.3 Rate Of Acid Addition

The rate of addition of acid reagent was controlled via a Watson Marlow 323D Series pump. Flow rates were obtained using silicone tubing with the pumphead rotating clockwise (15 – 220rpm). The range of flow rates may be controlled between 0.05 – 2000 ml/min [157].

3.3.4 Stirring Speed

Powerful mechanical Heidolph (RZR1) and IKA (RW20) overhead stirrers were used to agitate the aqueous suspension of HAp during chemical precipitation. A design for the stirrer stand was constructed with the capacity to ensure that the stirring alignment was centred within the reaction vessel, in spite of changes to the slurry viscosity (see Appendix A for related drawings of this design). However, the positions of the overhead stirrers within the precipitating reactor vessels are also considered to influence the overall reaction. The optimum set-up for off-bottom suspension of the impeller location within the reactor vessel was found to be one-third that of the impeller diameter from the tank bottom [158]. To ensure a uniformly mixed suspension is achieved, the impeller location can be as low as one-third the impeller diameter off-bottom, or higher, depending on the

need for agitating minimum slurry levels within the tank [158]. Handling minimum levels is an important consideration for batch rather than continuous flow operations. The parameters based on the study of optimum impeller location are shown in Table 3-1 and Figure 3-3.

Table 3-1: Impeller location parameters within the precipitating reactor (based on Figure 3-3)

Parameter	Ratio	Lower Limit	Upper Limit	Irish Industrial Setting	Setting
Impeller Diameter	D/T	0.1	0.8	0.5	0.75
Liquid Height Level	Z/T	0.6	0.7	1.5	0.7
Impeller Off-Bottom Clearance	C/T	0.3D	1D	0.75D	0.5D
Distance Between Multiple Impellers	S	0.5D	2D	1.1D	-

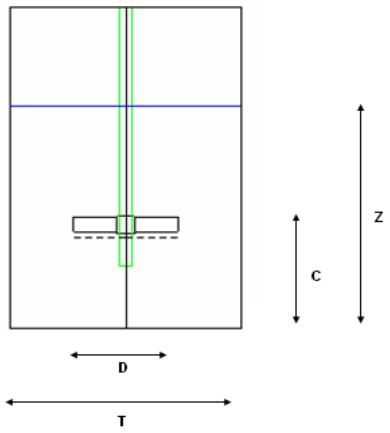

Figure 3-3: Schematic of important mixing and impeller location parameters. Adapted from [159]

3.3.5 Atmospheric Control

The precipitating reaction vessels were designed, to allow for the synthesis of HAp, under conditions of either an uncontrolled or inert atmospheric environment. To supplement a controlled atmospheric environment, the reactors were sealed, with a constant supply of N_2 continuously pumped into the reactor so as to eliminate contamination of the HAp product and the likelihood of carbonate substitutions into the end apatite lattice, thus leading to microstructural imperfections.

A schematic of the final chemical precipitation rig, with an overview of the control of the factors influencing the process and the methods for controlling them are shown in Figure 3-4.

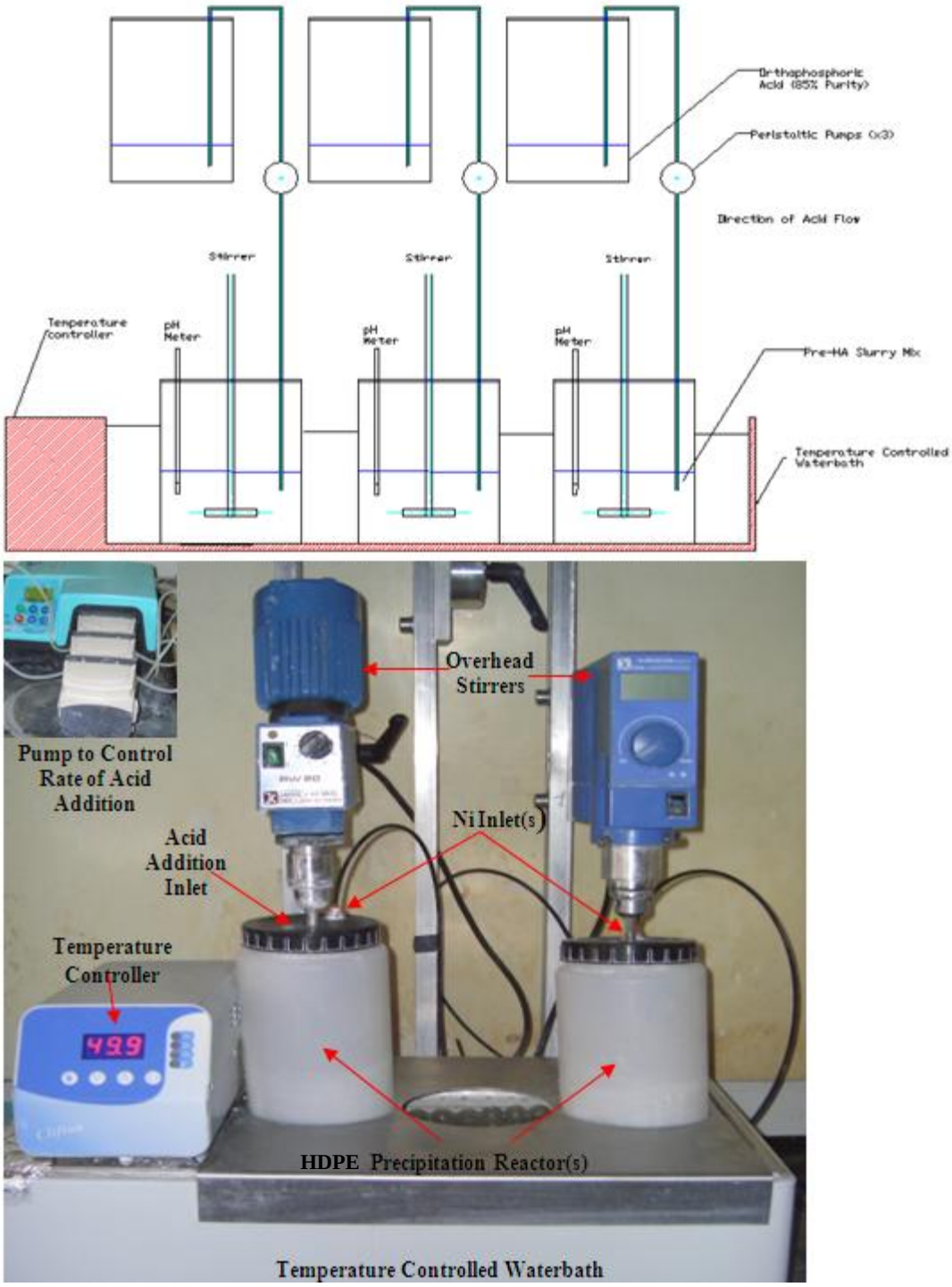

Figure 3-4: A 2-D schematic of the chemical precipitation rig (above) and an illustration of the rig in operation (below) using two precipitator reactors

3.4 MATERIAL CHARACTERISATION

Characterisation of the HAp (in slurry and powder form) was conducted throughout various stages of the production of HAp and in the current research itself, respectively. Characterisation of the HAp in its slurry form, was analysed, through measuring its final pH value, density and viscosity, while characterisation of the HAp powders was carried out using, XRD, SEM, PSA, Helium Pycnometry, Mercury Porisometry, the BET method and powder rheology equipment. A biological evaluation of the powders was also investigated at the experimental design stage of the investigation and the procedures used in this study, is discussed in a later section (3.9). An overview of the sequence of characterisation events is illustrated in Figure 3-5.

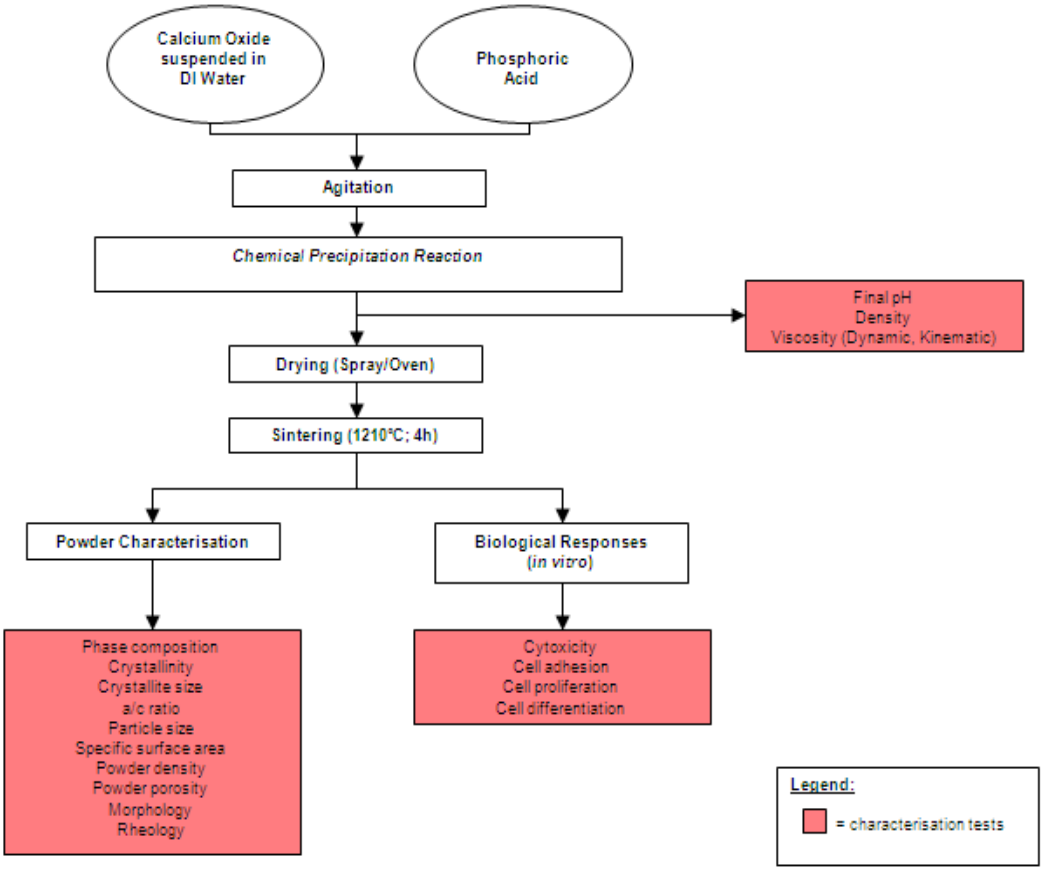

Figure 3-5: Overview of HAp synthesis route and materials characterisation

3.5 THERMAL TREATMENT OF HAp POWDERS

3.5.1 Spray Drying

The HAp slurry was transported to the spray drier (Niro P-6.3) at a rate of 1L/min for atomization into fine, micron sized powder particles of spheroidal morphology. Spray drying was performed in a co-current flow dryer, in which the flow of the droplets in the chamber travels in the same direction as the flow of the hot air. A straight vane rotary atomizer was used to optimise the desired powder characteristics. The powder particles were collected at the base of the drying chamber. Air borne particles were separated from exhaust air by a cyclone. The dried powder samples were collected at their respective collection points from the drying chamber. The parameters set for all spray drying operations of the powder samples are shown in Table 3-2 as proposed through a recent study concerning a critical investigation into the spray drying technique [109]. This technique was used to prepare a HAp powder (HAp6: refer to Section 4.1) on a laboratory scale version, via the same processing conditions as that used in Irish industry to (i) compare against other commercially available HAp and (ii) identify the effect of the various synthesis conditions on the respective powder characteristics for each of the HAp studied.

Table 3-2: Parameters used in the operation of the spray dryer

Parameter	Units	Settings
Inlet Temperature	^oC	170
Outlet Temperature	^oC	85
Cyclone Δ Pressure	mm H_2O	40
Av. Chamber Mass	gram	60
Av. Cyclone Mass	gram	38
Nozzle air Pressure	Bar	0.6
Nozzle air Flow	%	75
Slurry Feed	L/min	0.0456

3.5.2 Oven Drying

All other HAp powders prepared (excluding HAp6) in the present study were oven dried as opposed to the aforementioned technique of spray drying (see Section 3.5). This involved filtering of the HAp precipitate (that is, in slurry form) from suction via vacuum filtration using whatman filterpaper and dried at 105ºCfor 24h. This method was selected based on previous published literature as shown in Table 3-3 as follows:

Table 3-3: Previous settings implemented in published literature, for oven drying settings post chemical precipitation

Reference	Post precipitation steps and oven drying settings
Afshar et al. [83]	1. Filtered via centrifugation/whatman filter paper 2. Dried at 80ºC overnight
Saeri et al. [84]	1. Filtered via centrifugation/whatman filter paper 2. Washed by water and filtered again 3. Dried at 80ºC overnight
Santos et al. [56]	1. Supernatant decanted 2. Vacuum filtration 3. Washed repeatedly with DI water 4. Filtered again 5. Oven dried at 100ºC for 24h
Bernard et al. [93]	1. Precipitate washed with DI water 2. Vacuum filtration 3. Heated to 900ºC
Bouyer et al. [94]	1. Filtered via centrifugation 2. Heated at 80ºC while stirred
Lazic et al. [71, 79]	1. Washed with DDW 2. Filtered through black band filter paper in N2 atmosphere
Zhang et al. [28]	1. Filtered and washed with DDW & pure alcohol three times 2. Dried at 80ºC overnight
Smiciklas et al. [85]	1. Filtration via Buchner funnel 2. Dried at 105ºC for 24h
SRM 2910 [50]	1. Filtered 2. Washed with acetone 3. Dried at 105ºC for 24h

3.5.3 Sintering

All HAp powder samples in this research (spray/oven dried) were sintered in order to improve the crystallinity of the end product, so as to satisfy the minimum criterion (>95% crystallinity) as set out by the FDA [137], ASTM F1185 [140] and also in ISO 13779-1 [139]. The dried HAp powder samples were placed in a pre-programmed furnace, up to a maximum temperature of 1210ºC for a 30min period. The programme constituted of a ramping up and ramping down rate of 40ºC and 5ºC per min, respectively, as can been seen in Figure 3-6 to simulate the conditions used in Irish industry.

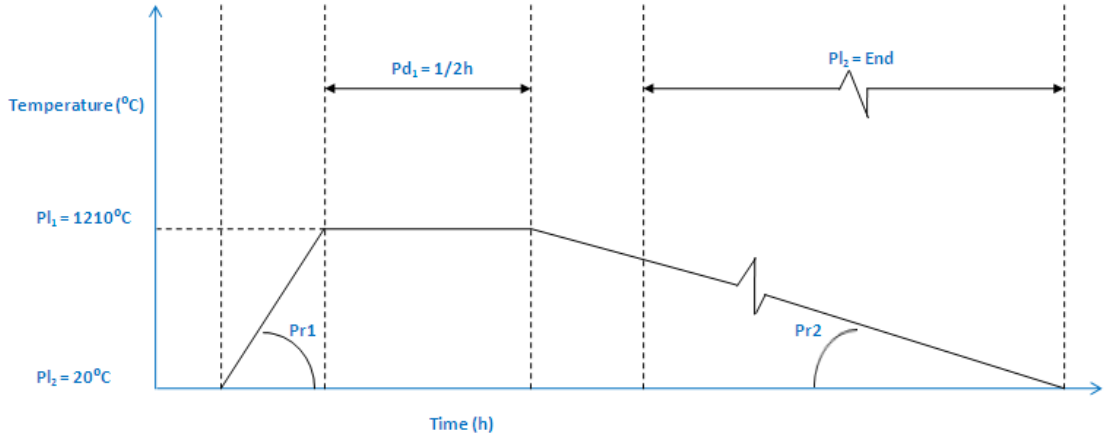

Control	Symbol	
Heating up rate	Pr1	2400 Degrees per hour
Temperature to stabilise at	Pl1	1210 Degrees
Time period to stabilise temperature at	Pd1	0.5 h
Cooling down rate	Pr2	300 Degrees per hour
Temperature to stabilise at	Pl2	Ambient (~20°C)
Time period to stabilise temperature at	Pd2	Ambient (~20°C)

Figure 3-6: Graphical display of the furnace programme (sintering times and temperatures) with legend

The final HAp powders obtained after sintering were then ground down using a mortar and pestle in order to eliminate the agglomerates that had formed during the sintering process. This helped to enhance the resulting powder flowability. The HAp powders were finally sieved through a standard mesh to ensure that no final HAp powder particles exceeded 100 µm for successful plasma spraying application [130].

3.6 EXPERIMENTAL DESIGN APPROACH

The approach to implementing experimental design in this study was investigated over two stages. The first stage involved preliminary screening experiments, used to identify a subset of the original process variables that have significant main and interaction effects on the final HAp powder properties obtained from synthesis via the chemical precipitation method. In the second stage, the variables that were found to be statistically significant were resubmitted to an optimised experimental design with narrower differences between the levels, chosen according to the results of the screening fractional factorial experimental design, and then optimised through response surface methodology. A brief overview of each experimental design is described in this section as follows:

Two-level *k* factors fractional factorial designs (2^{k-m})

Factorial designs involve testing several (*k*) factors at two levels (high and low). A Fractional Factorial experiment (2^{k-m}) uses only a half (2^{k-1}), a quarter (2^{k-2}), or some other division by a power of two of the number of runs that would be required for a Full Factorial Experiment. Thus, the number of runs required by full factorial designs increase geometrically as k is increased. It turns out, however, that when k is not small, the desired information can be often obtained by performing only a fraction of the full factorial design [160]. In practice, the number $n=2^k$ of experiments increases rapidly with the number of factors. Moreover, a lot of calculated coefficients corresponding to interactions of second (and higher) order can be supposed to be not significant. Consequently, the aim of the fractional 2^{k-m} factorial design is to extract the part of experiments from the full factorial design which enables to obtain the main effects and some first order interaction. To construct a 2^{k-m} matrix one may start with a 2^k one and replace some interactions with the variables.

A two-level fractional factorial design for n runs and m factors has an $n \times m$ design matrix, X, with each level equal to ±1. The aliasing properties of two-level designs depend heavily on their J-characteristics [161, 162], where:

$$Ji = J(i_1,....,i_k) = \sum_{p=1}^{n} Xpi_1 ... Xpi_k \qquad \textit{Equation (3-1)}$$

for $i = (i_1, i_2, \ldots, i_k)$. The J-characteristic J_i evaluates the degree of k-factor aliasing between factors $i_1, i_2, \ldots, i_k$. If $Ji = 0$, there is no aliasing, if $|Ji| = n$, there is complete aliasing, and if $0<|Ji|<n$, there is partial aliasing.

A key characteristic of a fractional factorial design is its resolution, that is, the degree to which main effects and interactions can be independently estimated and interpreted. In different words, the resolution of a design indicates the order of effects that can be estimated and are not confounded with each other. Box et al. [163] describe the hierarchy of resolution fractional designs. For designs with Resolution *I*, no effect is independently estimable. Therefore, designs with Resolution I are not interesting. Similarly, Resolution II is largely useless. Main effects would be confounded with other main effects. In the analysis of metric outcome variables, the most useful fractional factorial designs have Resolution III, IV, and V. At Resolution III, main effects can be estimated, but they are confounded with two way interactions. More interesting is often Resolution IV. At this level, main effects can be estimated, and they are not confounded with any of the two-way interactions. Two-way interactions, however, are confounded with each other.

Response surface methodology (RSM)

Relationship between the experimental response and factors are not always linear and the factors at multiple levels have to be used to determine quadratic $b_{ii}X_i$ 2 or cubic $b_{iii}X_i$ 3 terms using RSM methodology. One such design; the Box–Behnken design, includes all middle points of the edges of the k factors cube (replicated center points are needed for orthogonality and useful to estimate the global standard deviation). These designs developed by Box and Behnken in 1960 [164]. They are constructed by first combining two-level factorial designs with incomplete block designs and then a specified number of centre points are added.

3.6.1 Screening Experimental Design (Stage 1)

In order to obtain an optimised set of process conditions for HAp synthesis via the chemical precipitation technique, a fractional factorial experimental design was used to evaluate the preliminary significance of the process variables, as well as the interactions effects between them. The screening experimental plan was based on the fractional factorial (Res_{IV}^{4-1}) design (2^{k-n}, k=6 and n=2; size of the fraction used; that is a quarter of a full factorial design of 64 experimental runs) in 16 experimental runs, with main and interaction effects evaluated, using Design Expert 7.1.4 software (Stat-Ease) to investigate the optimum HAp synthesis process parameters using the chemical precipitation route. The factors were investigated at two levels (that is, +1(high) and -1(low)) and included, reaction synthesis temperature during precipitation, stirring speed, ripening time, acid addition rate, initial calcium concentration, and atmospheric environment (that is, synthesis with and without a controlled atmospheric environment). This experimental design was used to identify the factors which have the most significant effect on the resulting HAp powder properties, such as: phase purity, crystallinity, crystallite size (L_{002} and L_{300}), lattice parameters and particle size. This enabled a quantitative understanding of the relationship and interactions between the process parameters and their final HAp powder properties obtained.

The six experimental precipitation process parameters (found from literature and also in Irish industry), discussed above, were selected, each one at two levels, and these are indicated in Table 3-4. The minimum and the maximum possible level values selected for the screening experiments are also shown in Table 3-4 (denoted as -1 and +1), the levels of which are set outside the upper and lower range of that found in literature and industry.

Table 3-4: Experimental factors and level of factors

No	Variable	Symbol	Level -1	Level +1
A	Reagent Addition Rate	V_{ac}	0.005 mol/min	0.01 mol/min
B	Temperature	T_o	20°C	60°C
C	Stirring Speed	V_{st}	600rpm	1500rpm
D	Ripening Time	t_r	0.5h	48h
E	Initial Ca^{2+} Concentration	Ca^{2+}	0.1 mol/L	2 mol/L
F	Inert Atmosphere	atm.	without N_2	with N_2

Since the chemical precipitation route for the synthesis or phase evolution of HAp occurs in an aqueous suspension (analogous to that of room temperature, ~25°C); a lower synthesis temperature of 20°C was chosen as the minimum temperature of synthesis and 60°C as the maximum, in order to investigate a broad region outside of the optimum synthesis temperature, as highlighted in existing literature (40°C) [87 - 90]. The stirring speed was set according to limits previously published [85].

During precipitation, absorption of atmospheric CO_2 may occur, which in the form of CO_3^{2-} anion can be incorporated into the apatite crystal lattice. Experiments were performed with or without inert atmosphere to examine the significance of this parameter. Aging time plays an important role in the formation of highly crystallized products through phase evolution. During maturation, aggregation and crystal growth take place in the first 20h, after precipitation. After 20h, the crystal length and width are not significantly changed, and due to negative HAp solubility coefficient, this effect is more pronounced at room temperature [85]. Hence, an aging time of 48h was

investigated to examine whether any significant changes occur after this stage. The reaction yield and the reaction vessel capacity were taken into account in setting the minimum and the maximum molar concentrations of reagents: $Ca(OH)_2$ and H_3PO_4. The raw materials $Ca(OH)_2$ and H_3PO_4 react at a molar ratio of 5:3, according to the chemical equation 2.1 (as discussed in section 2.4.1):

$$10Ca(OH)_2+6H_3PO_4 \rightarrow Ca_{10}(PO_4)_6(OH)_2+18H_2O$$

A second order linear polynomial (regression) model for the six factors investigated was used to describe the relationship for each of the several responses and tested factors, as follows:

$$Y = b_0 + \sum b_j X_j + \sum b_{ij} X_i X_j + \varepsilon \qquad \textit{Equation (3-2)}$$

Where i, j vary from 1 to the number of process variables; coefficient b_0 is the mean of responses of all the experiment; b_i coefficient represents the effect of the variable X_i, and b_{ij}, are the coefficients of regression which represent the effects of interactions of variables X_iX_j and ε is the experimental error, such that:

$$\begin{aligned} Y_1 = {} & C_{st}+\beta_1T_o+\beta_2V_{ac}+\beta_3V_{st}+\beta_4t_r+\beta_5Ca^{2+}+\beta_6atm+\beta_7T_o.V_{ac} + \beta_8T_o.\ V_{st} +\beta_9T_o.\ t_r +\beta_{10}T_o.\ Ca^{2+} + \\ & \beta_{11}T_o.atm + \beta_{12}V_{ac}.\ V_{st} + \beta_{13}V_{ac}.\ t_r + \beta_{14}V_{ac}.\ Ca^{2+} + \beta_{15}V_{ac}.atm + \beta_{16}V_{st}.\ t_r + \beta_{17}V_{st}.\ Ca^{2+} \\ & + \beta_{18}V_{st}.atm + \beta_{19}t_r.\ Ca^{2+} + \beta_{20}t_r.atm + \beta_{21}\ Ca^{2+}.atm + \text{experimental error} \end{aligned}$$

Equation (3-3)

Where Y_1 is response 1, β_1-β_{21} is the regression co-efficient, T_0 is the reaction synthesis temperature, V_{ac} is the acid addition rate, V_{st} is the stirring speed, t_r is the ripening time, Ca^{2+} is the initial calcium concentration and atm. is the atmospheric control.

This model was used to evaluate all the responses ($Y_1 - Y_6$) such as Y_1 the phase purity, X_p (%), Y_2 the crystallinity, X_c (%), Y_3 the crystallite size in the 002 plane, X_s, L_{002} (nm),

Y_4 the crystallite size in the 300 plane, X_s, L_{300} (nm), Y_5 the a/c ratio and Y_6 the particle size, P_s, (μm). The responses were measured in sequential order for each experiment and performed in triplicate. As discussed earlier, the fractional factorial experiment is generated from a full factorial experiment by choosing an alias structure. The alias structure determines which effects are confounded with each other, and the confoundings generated for the above model are represented in Table 3-5.

Table 3-5: Alias structure for the screening factorial experimental design, confoundings

Term	Generator	Confounded with	Confounded with
Vac	a		
T0	b		
Vst	c		
tr	d		
cal	abc		
atm	bcd		
Vac*T0		Vst*cal	
Vac*Vst		T0*cal	
Vac*tr		cal*atm	
Vac*cal		T0*Vst	tr*atm
Vac*atm		tr*cal	
T0*Vst		Vac*cal	tr*atm
T0*tr		Vst*atm	
T0*cal		Vac*Vst	
T0*atm		Vst*tr	
Vst*tr		T0*atm	
Vst*cal		Vac*T0	
Vst*atm		T0*tr	
tr*cal		Vac*atm	
tr*atm		Vac*cal	T0*Vst
cal*atm		Vac*tr	

The design matrices of experiments, in coded and real values, obtained according to the fractional factorial design, resolution IV, are shown in Table 3-6 and Table 3-7, respectively. The run order of experiments was run in a completely randomized order in order to assure that uncontrolled factors did not affect the final results obtained.

Table 3-6: Design matrix for screening fractional factorial design, expressed as coded values

Exp No	Run No	H_3PO_4 addition rate (mole/min)	Temperature (°C)	Stirring speed (rpm)	Ripening time (h)	calcium concentration (mol/L)	atmosphere
1	15	-1	-1	-1	-1	-1	+
2	4	1	-1	-1	-1	1	+
3	10	-1	1	-1	-1	1	-
4	8	1	1	-1	-1	-1	-
5	5	-1	-1	1	-1	1	-
6	3	1	-1	1	-1	-1	-
7	16	-1	1	1	-1	-1	+
8	1	1	1	1	-1	1	+
9	6	-1	-1	-1	1	-1	-
10	2	1	-1	-1	1	1	-
11	12	-1	1	-1	1	1	+
12	14	1	1	-1	1	-1	+
13	11	-1	-1	1	1	1	+
14	13	1	-1	1	1	-1	+
15	7	-1	1	1	1	-1	-
16	9	1	1	1	1	1	-

Table 3-7: Design matrix for screening fractional factorial design, expressed as real values

Exp No	Run Order	H3PO4 addition rate (mole/min)	Temperature (°C)	Stirring speed (rpm)	Ripening time (h)	calcium concentration (mol/L)	Inert atmosphere
N1	15	0.005	20	600	0.5	0.1	yes
N2	4	0.01	20	600	0.5	2	yes
N3	10	0.005	60	600	0.5	2	no
N4	8	0.01	60	600	0.5	0.1	no
N5	5	0.005	20	1500	0.5	2	no
N6	3	0.01	20	1500	0.5	0.1	no
N7	16	0.005	60	1500	0.5	0.1	yes
N8	1	0.01	60	1500	0.5	2	yes
N9	6	0.005	20	600	48	0.1	no
N10	2	0.01	20	600	48	2	no
N11	12	0.005	60	600	48	2	yes
N12	14	0.01	60	600	48	0.1	yes
N13	11	0.005	20	1500	48	2	yes
N14	13	0.01	20	1500	48	0.1	yes
N15	7	0.005	60	1500	48	0.1	no
N16	9	0.01	60	1500	48	2	no

Figure 3-7 illustrates an overview of the complete production process implemented, so as to obtain the HAp in powder form from its aqueous suspension form at the chemical precipitation stage. The factors and responses are presented for the stages of the process, in which they are controlled and evaluated, respectively.

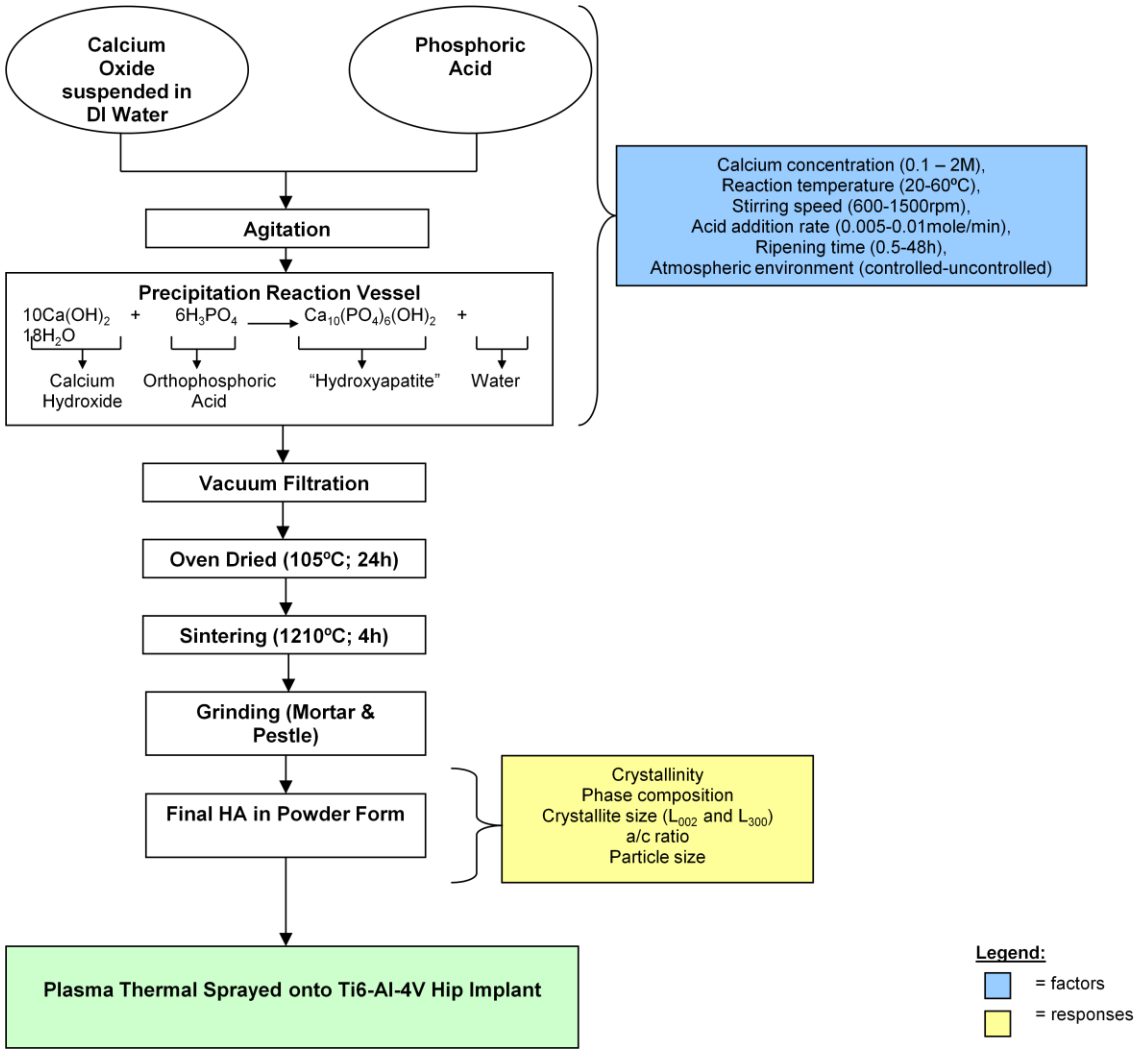

Figure 3-7: Overview of the production process in obtaining HAp in powder form and the process variables and responses evaluated at the screening fractional factorial design stage

0.1 - 2M $Ca(OH)_2$ solutions were prepared by adding CaO powders to 500mL of distilled water in a 1000mL-enclosed reactor and vigorously stirred with a vertical mechanical overhead stirrer between 600 - 1500rpm at the reaction temperature (20 - 100ºC) maintained by a thermostat-controlled water-bath. The H_3PO_4 acid was added to the $Ca(OH)_2$ solution at an addition rate of 0.005 - 0.01mol/min using a peristaltic pump. Ripening periods of between 0.5 - 48h were investigated to monitor the maturation of HAp in the reaction vessel, while kept under continuous stirring conditions and reaction

temperature (as dictated by the experimental design). At the end of this ripening period, the aqueous suspension of HAp was filtered from suction via vacuum filtration and oven dried at 105ºC for 24h. Finally, all of the samples were sintered at 1210ºC for 4h to increase the final crystallinity obtained (ideally, >95%), ground using a mortar and pestle and sieved for particle size not exceeding 100µm (to suit plasma spraying application).

3.6.2 Optimisation Experimental Design (Stage 2)

A Box-Behnken experimental design (see Figure 3-8), with three levels on the three most influential factors was used to allow the estimation of a full quadratic polynomial model, including interaction effects in 17 experimental runs, with main and interaction effects evaluated using Design Expert 7.1.4 software to investigate an optimised set of conditions for HAp synthesis using the chemical precipitation route. Box-Behnken designs have two parts [165]; (i) centerpoints, and (ii) points lying on one sphere, equally distant from the centerpoint. The latter points consist of small two-level full factorials where some factors are fixed at their centre values. The number of centerpoints (five) was chosen to establish rotatability. The levels selected for the screening experiments are shown in Table 3-8 (denoted as -1, 0 and +1 for minimum, centerpoint and maximum values, respectively).

The three key controllable process factors investigated, were selected, based upon the evaluation of the significant main and interaction effects of the preliminary screening phase, involving the screening experimental design and comprise of T_o: reaction synthesis temperature (40 - 60°C), V_{st}: stirring speed (900 – 1500rpm) and t_r: ripening time (24 – 48h). The processing region for the three process factor was limited to the region over which existing published literature has indicated as desirable values and was also selected based on the results as obtained at the preliminary screening stage of the design of experiments. The other parameters (Ca^{2+} conc. (2.0M), acid addition rate (0.01 mol/min) with atmospheric control) were kept constant in all cases.

Table 3-8: Design optimisation of experiments: experimental factors and level of factors

No	Variable	Symbol	Level -1	Level 0	Level +1
A	Temperature (°C)	T_o	40°C	50°C	60°C
B	Stirring Speed (rpm)	V_{st}	900rpm	1200rpm	1500rpm
C	Ripening Time (h)	t_r	24h	36h	48h

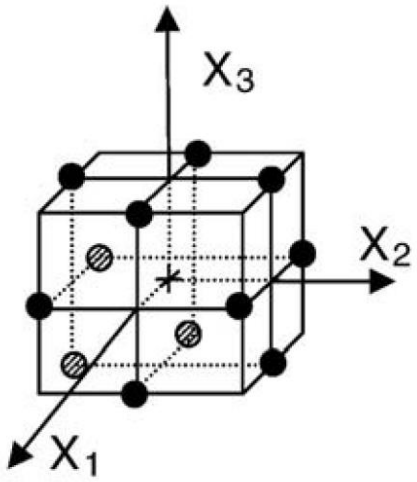

Figure 3-8: Graphical representation of the matrices of a box-behnken design [166]

To optimise fully the responses ($Y_1 - Y_6$) evaluated, an appropriate approximation for the true functional relationship between the independent variables and the response surface was identified, using the following second order quadratic polynomial model for RSM box-behnken design, as follows:

$$Y = b_0 + \sum b_i X_i + \sum b_{ij} X_i X_j + \sum b_{ii} X_{ii}^2 + \varepsilon \qquad \textit{Equation (3-4)}$$

Where i, j vary from 1 to the number of process variables, coefficient b_0 is the mean of responses of all the experiment, b_i coefficient represents the effect of the variable X_i, and b_{ij}, are the coefficients of regression which represent the effects of interactions of

variables X_iX_j ,and b_{ii}, are the coefficients of regression which represent the effects of interactions of the variable X_iX_i , and ε is the experimental error.

This model was used to evaluate the same responses ($Y_1 - Y_6$) as that evaluated in the screening stages of the design, such as Y_1 the phase purity, X_p (%), Y_2 the crystallinity, X_c (%), Y_3: crystallite size in the 002 plane, X_s, L_{002} (nm), Y_4 the crystallite size in the 300 plane, X_s, L_{300} (nm), Y_5 the a/c ratio and Y_6 the particle size, P_s, (μm). The responses were measured in sequential order for each experiment and performed in triplicate. The design matrix of experiments, in coded and real values, obtained according to the optimised box-behnken design, are shown in Tables 3-9 and 3-10, respectively.

Table 3-9: Design matrix for optimisation box-behnken design, expressed as coded values

Exp No	Run No	Temperature (°C)	Stirring speed (rpm)	Ripening time (h)
1	5	-1	-1	0
2	14	1	-1	0
3	2	-1	1	0
4	10	1	1	0
5	4	-1	0	-1
6	16	1	0	-1
7	3	-1	0	1
8	15	1	0	1
9	12	0	-1	-1
10	13	0	1	-1
11	17	0	-1	1
12	7	0	1	1
13	1	0	0	0
14	6	0	0	0
15	8	0	0	0
16	11	0	0	0
17	9	0	0	0

Centerpoint runs were interspersed among the RSM experimental design setting runs for two purposes: (i) to provide a measure of process stability and inherent variability and (ii) to check for curvature. In an unblocked RSM design, the number of centerpoints controls other properties of the design matrix. The number of centre points can make the design orthogonal or have "uniform precision." Uniform precision ensures that the variance of prediction is the same at the centre of the experimental space as it is at a unit distance away from the centre.

Table 3-10: Design matrix for optimisation box-behnken design, expressed as real values

Exp No	Run No	Temperature (°C)	Stirring speed (rpm)	Ripening time (h)
N1	5	40	900	36
N2	14	60	900	36
N3	2	40	1500	36
N4	10	60	1500	36
N5	4	40	1200	24
N6	16	60	1200	24
N7	3	40	1200	48
N8	15	60	1200	48
N9	12	50	900	24
N10	13	50	1500	24
N11	17	50	900	48
N12	7	50	1500	48
N13	1	50	1200	36
N14	6	50	1200	36
N15	8	50	1200	36
N16	11	50	1200	36
N17	9	50	1200	36

Figure 3-9 illustrates an overview of the complete production process implemented, so as to obtain the HAp in powder form from its aqueous suspension form at the chemical precipitation stage. The factors and responses are presented for the stages of the process, in which they are controlled and evaluated, respectively. The factors which remained constant are also presented. These factors were considered to exert a lower level of significance over the effects of the responses studied, as identified at the screening stage of the investigation.

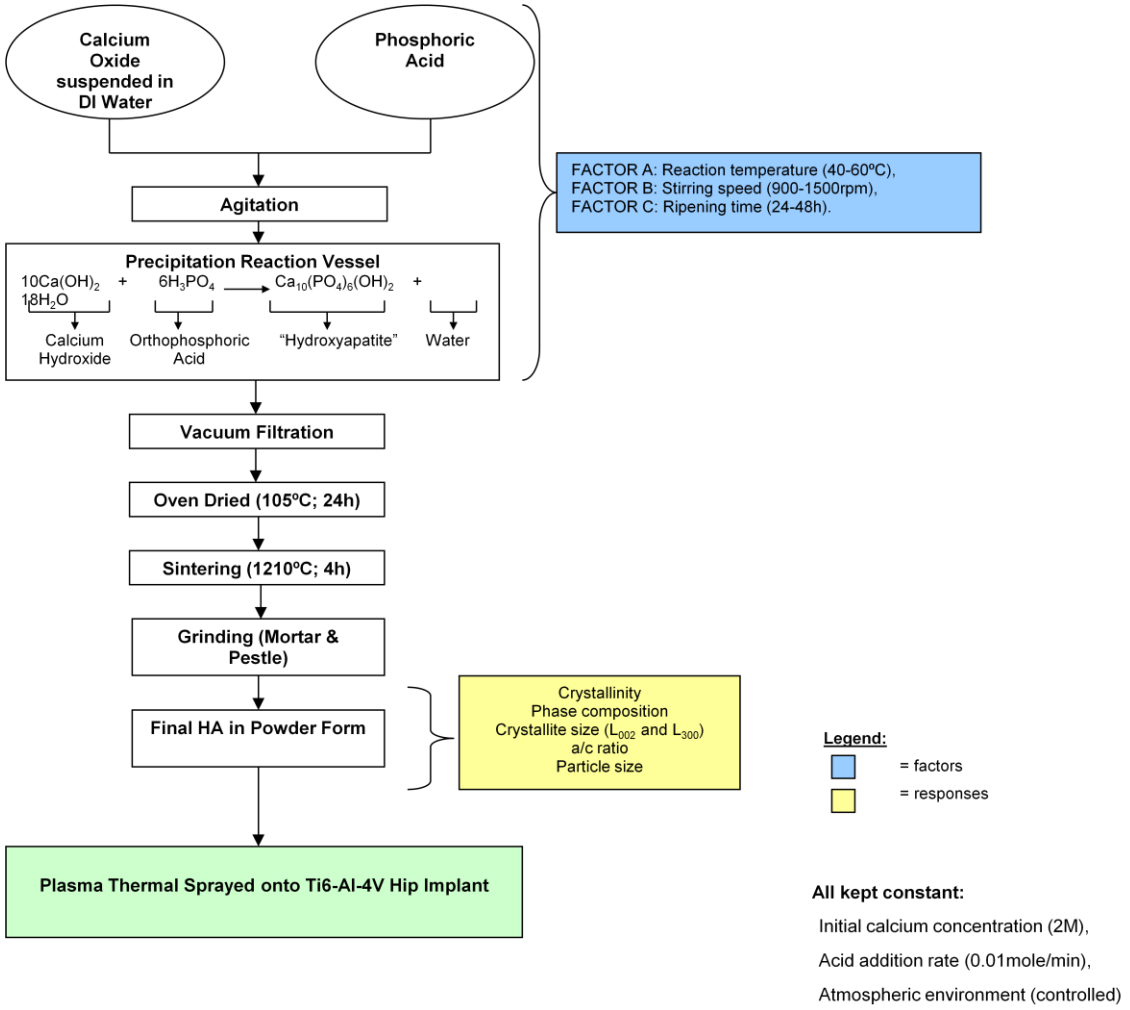

Figure 3-9: Overview of the production process in obtaining HAp in powder form and the process variables and responses evaluated at the optimisation box-behnken design stage

2M $Ca(OH)_2$ solutions were prepared by adding CaO powders to 500mL of distilled water in a 1000mL-enclosed reactor and vigorously stirred with a vertical mechanical overhead stirrer between 900 - 1500rpm at the reaction temperature (40 - 60ºC) maintained by a thermostat-controlled water-bath. The H_3PO_4 acid was added to the $Ca(OH)_2$ solution at an addition rate of 0.01mole/min using a peristaltic pump. Ripening periods of between 24 - 48h were investigated to monitor the maturation of HAp in the reaction vessel, while kept under continuous stirring conditions and reaction temperature (as dictated by the experimental design). At the end of this ripening period, the aqueous suspension of HAp was filtered from suction via vacuum filtration and oven dried at 105ºC for 24h. Finally, all of the samples were sintered at 1210ºC for 4h to increase the final crystallinity obtained (ideally, >95%), ground using a mortar and pestle and sieved for particle size not exceeding 100µm.

The average length of time, (inclusive of the ripening time, t_r) to conduct the 16 and 17 experimental runs for the screening (Fractional Factorial) and optimisation (Box-Behnken) designs are outlined in Figure 3-10. The times are indicative of that allotted to each processing step in producing the HAp powder.

Refer to Appendix B for a detailed overview on the model fitting, methods for determining the significance of the regression co-efficients (experimental factors), a description of the charts and plots presented in the following chapter and numerical optimisation using the numerical approach [160, 167].

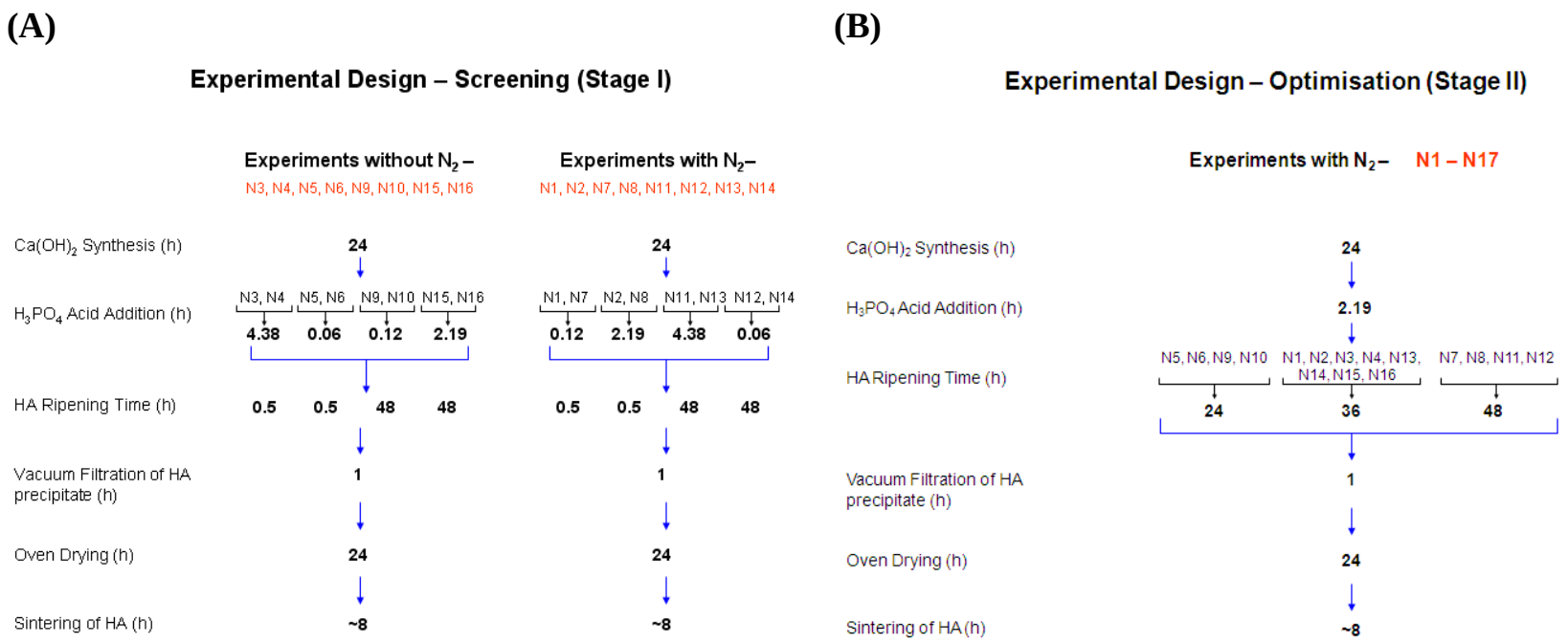

Figure 3-10: Graphical presentation of the time factored for each process step in the production of HAp powder via the chemical precipitation method

3.7 POWDER CHARACTERISATION METHODS AND EQUIPMENT

3.7.1 X- Ray Diffraction

All powder samples were analysed by conventional powder X-Ray diffractometry. X - Ray Powder Diffraction (XRPD) analysis is a powerful method by which X-rays of a known wavelength are passed through a powder sample to fully investigate its crystal structure. The wave nature of the X-rays means that they are diffracted by the lattice of the crystal to give a unique pattern of peaks of 'reflections' at differing angles and of different intensity, just as light can be diffracted by a grating of suitably spaced lines. The diffracted beams from atoms in successive planes cancel unless they are in phase, and the condition for this is given by the BRAGG relationship [5, 13, 15, 50, 136, 144]:

$$n\lambda = 2d\sin\theta \qquad \textit{Equation (3-5)}$$

where λ is the wavelength of the x-rays, d is the distance between different plane of atoms in the crystal lattice and θ is the angle of diffraction. The x-Ray detector moves around the sample and measures the intensity of these peaks and the position of these peaks (diffraction angle 2θ). The highest peak is defined as the 100% x peak and the intensity of all the other peaks are measured as a percentage of the 100% peak.

X-ray diffraction studies on the powder samples were carried out using a high resolution Bruker Advance D8 XRD (See Figure 3-11) diffractometer in Bragg-Brentano geometry, with a CuKα monochromated beam (λ = 0.15406Å) produced at 40kV and 40mA. The scanning range (2θ) was performed from 20º to 60º with a step size of 0.02° 2 theta/s [65]. XRD was used to assess the phases present, crystallinity and purity of the HAp powders as well as its crystallographic properties (such as, crystallite size and lattice parameters) in order to ensure compliance to regulatory requirements.

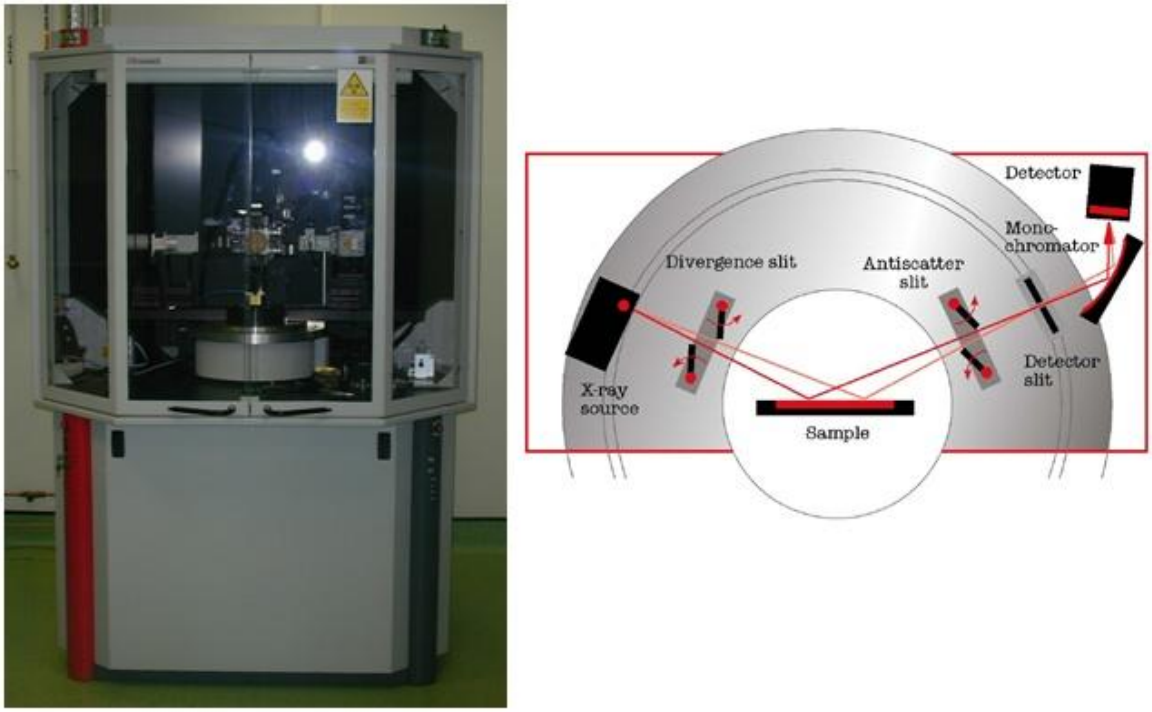

Figure 3-11: Bruker AXS D8 Advance XRD in the Materials Research Processing Centre, MPRC (left hand side) and typical features of the XRD equipment (right hand side)

3.7.2 Phase Identification

Phase identification was performed with reference to the library database supplied by the International Centre for Diffraction Data (ICDD) by directly comparing the X-ray diffraction patterns to the Joint Committee for Powder Diffraction Standards (JCPDS) files for HAp (JCPDS, Card No. 9-432) and also the common phases present within calcium phosphate based powders, such as, α-TCP (9-348), β-TCP (9-169), DCPA (9-80), DCPD (9-77), OCP (26-1056), TTCP (25-1137) and CHAp (19-272) in order to obtain an indication of the relative proportions of phases present in the powders analysed. The list of peaks for HAp and the most important peaks of other calcium phosphates are given in Tables 3-12 and 3-13, respectively. The phases identified were also checked against that of the database supplied by the ICDD, using the software, Crystallographica-Search-Match (CSM) (Oxford Cryosystems).

Table 3-11: ASTM Card No.9-432 for Hydroxyapatite

d (Å)	I/Ii %	Miller Indices
5.250	5	(101)
4.720	3	(110)
4.070	9	(200)
3.880	9	(111)
3.510	1	(201)
3.440	40	(002)
3.170	11	(102)
3.080	17	(210)
2.814	100	(211)
2.778	60	(112)
2.720	60	(300)
2.631	25	(202)
2.528	5	(301)
2.296	7	(212)
2.262	20	(310)
2.228	1	(221)
2.148	9	(311)
2.134	3	(302)
2.065	7	(113)
2.040	1	(400)
2.000	5	(203)
1.943	30	(222)
1.890	15	(312)
1.871	5	(320)
1.841	40	(213)
1.806	20	(321)
1.780	11	(410)
1.754	15	(402), (303)
1.722	20	(004), (411)
1.684	3	(104)
1.644	9	(322), (223)
1.611	7	(313)
1.587	3	(501), (204)
1.542	5	(420)
1.530	5	(331)
1.503	9	(214), (421)
1.474	11	(502)
1.465	3	(510)

Table 3-12: List of most important peaks for β-TCP; α-TCP, DCPA, DCPD, CHAp and DCP

β - TCP[a]			α - TCP[b]			DCPA[c]			DCPD[d]			CHAp[e]			OCP[f]		
d (Å)	I/I_i %	Miller Indices	d (Å)	I/I_i %	Miller Indices	d (Å)	I/I_i %	Miller Indices	d (Å)	I/I_i %	Miller Indices	d (Å)	I/I_i %	Miller Indices	d (Å)	I/I_i %	Miller Indices
6.49	15	(006)	7.31	25	(111)	6.74	13	(010), (110)	7.57	100	(020)	3.46	25	(002)	18.68	300	(100)
5.21	20	(110)	4.00	20	(150)	3.48	13	(121)	4.24	100	(021)	2.78	100	(211), (112)	9.36	45	(200)
4.05	15	(204)	3.91	40	(202)	3.37	70	020	3.05	75	(111), (041)	2.68	40	(300)	9.05	40	
3.45	25	(1.1.10)	3.88	40	(241)	3.35	75	(110), (220)	2.93	50	(221)	2.23	16	(310)	5.52	25	
3.21	55	(214)	3.69	40	(132)	3.33	17	(210)	2.62	50	(220), (151)	1.93	16	(232), (401)	3.66	30	
3.01	15	(300)	3.66	17	(151), (222)	3.13	20	(111)	2.60	30	(202)	1.84	16	(213)	3.44	60	
2.88	100	(2.1.10), (217)	3.01	20	(510)	2.96	100	(112), (112)	2.17	20	(151)				3.42	50	
2.76	20	(218)	2.95	20	(113)	2.94	35	(102)	2.15	17	(242)				3.21	25	
2.61	65	(220)	2.92	35	(402), (023)	2.75	20	(230)	1.82	20	(241)				2.87	30	
1.93	20	(4.1.10), (327)	2.91	100	(441), (170)	2.72	35	(200), (102)							2.83	100	(260)
1.90	15	(328)	2.86	30	(511)	2.25	15	(030)							2.82	95	(320), (241)
1.73	25	(2.2.20)	2.62	50	(043), (352)	2.50	15	(231), (022)							2.78	45	
			2.59	30	(080)	2.20	13	(003)							2.75	35	
															2.71	25	
															2.67	50	(700)
															2.64	35	

[a]A.S.T.M. card file No. 9 – 169; [b]A.S.T.M. card file No. 9 – 348; [c]A.S.T.M. card file No. 9 – 80; [d]A.S.T.M. card file No. 9 – 77; [e]Caronated apatite; A.S.T.M. card file No. 19 – 272 and [f]A.S.T.M. card file No. 26 – 1056

3.7.3 Phase Purity

The phase purity of the prepared HAp samples in this research were measured directly from the X-ray diffraction patterns. The equation used to calculate the percentage purity (X_p) of the HAp powders is represented as follows [142, 148]:

$$X_p\ (\%) = \frac{\sum A_C - \sum I_{impurity}}{\sum A_C} \times 100 \qquad \textit{Equation (3-6)}$$

Where ΣA_C is the sum of the area under all the HAp crystalline peaks and $\Sigma I_{impurity}$ is the sum of the area under all of the impurities present in the sample between 20º to 60 º.

Another method used to quantify each of the phases present was the Rietvled refinement method, based on approach that the experimental powder diffraction data is utilised without extraction of the individual integrated intensities or the individual structure factors, and all structural and instrumental parameters are refined by fitting a calculated profile to the observed data. The method relies on the simple relationship [168]:

$$W_p = S_p (ZMV)_p / \sum_{i=1}^{n} S_i (ZMV)_i \qquad \textit{Equation (3-7)}$$

where *W* is the relative weight fraction of phase p in a mixture of n phases, and *S, Z, M,* and *V* are the Rietveld scale factor, the number of formula units per cell, the mass of the formula unit (in atomic mass units) and the unit cell volume (in nm^3), respectively.

Rietveld analysis was undertaken using TOPAS R (Bruker-AXS) and the atomic structural models acquired from the ICDD. In these analyses, the amorphous component was described using an atomic model fixed to that of stoichiometric HAp but with a crystallite size similar in magnitude to that of the lattice parameters. This produced a diffraction pattern with the appearance of that from an amorphous material, that is,

significantly broadened and overlapped diffraction maxima. To provide appropriate and precise values of crystallite size, these parameter values were refined against diffraction data from an amorphous CaP phase. For all analyses of mixed phases, all the parameters (except for the scale factor) of the amorphous phase were fixed to these values. This may simplify the precise shape of scattering from the amorphous component, but can provide an approximate value for the density of the non-crystalline phase. An influential parameter in this analysis for accurate quantification is the appropriate choice of background which was determined empirically and represented by a 1st order Chebchev polynomial.

The fitting methodology was assessed for accuracy and reliability by repeated, independent determinations of known mixtures of amorphous and crystalline phases. The atomic model parameters (such as, atomic positions, thermal parameters and occupancies) were fixed throughout. This effectively fixed the absorption co-efficients for each phase present. The scale factors, lattice parameters, crystallite size and peak shapes were refined for all crystalline phases. The main advantage associate to this approach is that preferred orientation (PO) can also be included and accounted for in the fitting process based on spherical harmonics.

3.7.4 Crystallinity

The crystallinity is a complex concept integrating the effects on the XRD of crystal strain, diffraction domain size and crystal defects. However, in order to compare the 'crystallinity' of the synthetic HAp the following calculations were made based on the XRD patterns obtained between 20º to 60º (2θ). The percentage crystallinity (X_c) was determined using the following equation [5, 169]:

$$X_c\,(\%) = \frac{\sum A_C}{\sum A_C + \sum A_A} \times 100$$

Equation (3-8)

Where $\Sigma A_C + \Sigma A_A$ give the sum of the area under all the HAp crystalline and amorphous peaks and ΣA_C yields the sum of the areas under the crystalline peaks present in the scan range between 20 º to 60º.

3.7.5 Crystallite Size (L_{002} And L_{300})

The crystallite size, in two reflection planes (L_{002} and L_{300}) were calculated based on the extraction of information from the X – ray diffraction patterns. Based on Scherrer's formula, crystallite size can be calculated from the XRD peak broadness [5, 85]:

$$D = 0.9\alpha \text{ FWHMcos } \theta \qquad \textit{Equation (3-9)}$$

where D is the crystallite size (nm), α the wavelength of monochromatic X-ray beam (0.15406 nm for Cu Kα radiation), FWHM is the full width at the half maximum of the diffraction peak under consideration (rad), and θ the diffraction angle (º).

3.7.6 Lattice Parameter Determination

Theoretically, the lattice parameters (a and c) for the hexagonal crystal structure of HAp, are determined from the relationship between the distance, d, of two adjacent net planes and the (h k l) Miller Indices of the reflection planes and is given by the equation [5, 13]:

$$d = \frac{1}{\sqrt{\frac{4(h^2 + hk + l^2)}{3a^2} + \frac{l^2}{c^2}}} \qquad \textit{Equation (3-10)}$$

Where d is the lattice spacing, h, k, l is the Miller indices, a , c is the lattice parameters, λ is the wavelength (CuKα: λ = 0.15405nm) and 2θ is the diffraction angle. For the hexagonal unit cell, a = b, α = β = 90º, and γ = 120º and using Bragg's Law [5, 13] Equation (3-19) now takes the form:

$$\eta\mu^2\theta_d = \frac{\lambda^2}{4}.\left(\frac{4(h^2+hk+l^2)}{3a^2}+\frac{l^2}{c^2}\right) \qquad \textit{Equation (3-11)}$$

Where the diffraction angle, θd, is given as a function of the Miller indices.

The lattice parameters were evaluated in this investigation in order to assess the microstructural differences between the HAp samples evaluated and were determined by least square refinements from the well determined positions of the most intense reflections, which are processed using the least squares refinement software package CelRef 3.0. CelRef is a crystal cell parameters refinement program for powder X-rays or neutron diagram, using the least squares refinement method as follows [170, 171]:

The expression of the measured Bragg angle θ is:

$$\theta = \Delta\theta + \text{Arcsin}(\lambda/2d) \qquad \textit{Equation (3-12)}$$

where d is the interplanar distance for (h,k,l), λ is the wavelength, and Δθ is the zero angular shift. This shift can be constant (goniometer error) or can vary with θ, if the *a* sample displacement *e* exists, such that:

$$\Delta\theta = e/R * \cos(\theta) \qquad \textit{Equation (3-13)}$$

Where R is the diffractometer radius.

If a*, b*, c*, α*, β*, γ* are the reciprocal cell parameters then [171]:

1/d**2= (ha*)**2+(kb*)**2+(lc*)**2+2hka*b*cosγ*+2klb*c*cosα*+2lhc*a*cosβ*

Equation (3-14)

The above expression depends on N unknown values, belonging to the group (Δθ, l, a*, b*, c*, α*, β*, γ*) according to the crystal system and the parameters to be refined, (for example N can be 1 to 3 for cubic crystal or 6 to 8 for triclinic system). This expression is fitted on M observed values (M>N) by a non linear Least Square method (Gauss). From the reciprocal fitted parameters a*, b*, c*, α*, β*, γ*, the direct parameters a, b, c, α, β, γ are calculated. This is an iterative method, starting from raw values. The parameters standard errors are calculated as well as a mean square deviation [171]:

$$R=\mathrm{sqrt}[(\theta_{obs} - \theta_{calc})^{**}2]/(N-M) \qquad \textit{Equation (3-15)}$$

3.7.7 Powder Morphology

Scanning Electron Microscopy (SEM) was used in the present research due to the high resolution and depth of field generated by its images. The image is an artificial map of the surface, that is, there are no direct ray paths linking the specimen to the projected image, as is the case in optical and transmission microscopes. Instead, the area under observation is irradiated with a finely focused electron beam of between 10 – 25kV, which may be static or swept in a raster across the surface of the material in synchronism with a spot on a cathode ray tube (CRT). A detector monitors the scattered electron (SE) (including back scattered electron (BSE)) signals and the brightness of the spot on the CRT is controlled by an amplified version of the detected signal. The scan of the CRT is fixed and the effect of reducing the area scanned on the specimen is to increase the magnification of the map. The intensities of the SE and BSE generated are dependent on the angle of incidence between the beam and the specimen. This factor accounts for the contrast in topographical features for the specimen examined. The angle of incidence will vary because of the roughness of the material, leading to the development of contrast, which relates to the physical nature of the specimen. The surfaces facing the light source appear bright while those facing away range from grey to black. Hence, only the surfaces which face the detector provide a strong enough signals to obtain a useful image, while black are indicative of a tilted surface.

A Cambridge/Leica Stereoscan 440 Scanning Electron SEM with image analysis and quantitative EDX capabilities (see Figure 3-12) was used in the present research to study the surface morphology and characteristics of the powder at an accelerating voltage of 1.5kV [136]. These instruments allowed the examination of topography (that is, surface morphology of the powders) and overall elemental uniformity. The surface morphology of the HAp powders were of interest as their topology provides a good indication as to the type of reaction kinetics that may have been involved during synthesis via chemical precipitation and ultimately determines its capability to flow (that is, the HAp powder flowability) pre-plasma spraying.

The HAp powder samples are non-conducting, by nature. In order to prevent charging from occurring during examination, sample preparation for each HAp powder sample was undertaken. The first stage involved suspending HAp powder particles (~0.2g) in glue on an aluminium stub. The samples were allowed a sufficient period to dry (10min). after which, any excess powder was eliminated with an air hose at low pressure prior to the carbon coating process. The Edwards Scancoat six sputter coater (see Figure 3-12(a)) was used to apply a layer of carbon onto the HAp samples (2 – 3 min), in order to increase the electrical conductivity of the specimen sample during SEM operation (see Figure 3-12(b) and hence provide a clear analysis of the individual HAp powder particles and/or particle aggregates morphological properties.

(A) **(B)**

Figure 3-12: The edwards scancoat six sputter coater (left hand side) and the stereoscan 440 scanning electron microscopy (right hand side)

3.7.8 Mean Particle Size and Particle Size Distribution Analysis

Particle size analysis was performed in this research, via a single lens laser diffraction system, using a small helium neon laser of the order of 2 mW power to measure the size of particles. It operates on the principle of laser scattering using Mie theory and Fraunhofer analysis [172]. The light from the low power Helium-Neon laser is used to form a collimated and monochromatic beam of light (typically, 18 mm in diameter). This beam of light is known as the analyser beam and any particles present within it, scatter this laser light. The particles are introduced to the analyser beam by the sample presentation modules or by direct spraying through the measurement area [173]. Laser scattering consists of a two-stage process aimed at measuring the low angle scattering characteristic of the sample particles. The measurement is in two stages since the sample measurement also contains light picked up from other sources (such as, daylight and flare off optical surfaces). Separate measurement of these non-sample scattering sources make it is possible to subtract out this contribution from the sample measurement [173]. Figure 3-13 illustrates the Fourier Optics optical configuration employed by the Malvern Mastersizer. The scattered light data is then transferred to the software running on the PC. The knowledge gained from the scattering theory and particle properties was used to transform the scattered light data to a distribution of particle size information.

Particle size analysis using the wet method for powder sample preparation can be achieved in either two ways: (i) low-interfacial tension liquid/gaseous by wetting agents and (ii) low-interfacial tension solid/liquid by hydrophillizing agents. The determination of mean particle size and particle size distributions were carried out using a Malvern Mastersizer Type S Laser Diffractometer (see Figure 3-14) in order to analyse the various HAp samples for their powder; mean particle sizes at production stages post thermal treatment, through spray drying. The Malvern Mastersizer S offers the widest dynamic range at 0.05 to 3500 microns, excellent repeatability, and flexibility in sample handling. Wet and dry powder analysis methods are available using this instrument. Wet methods

of sample dispersion are preferred as this avoids segregation errors associated with the dry method of powder analysis [173].

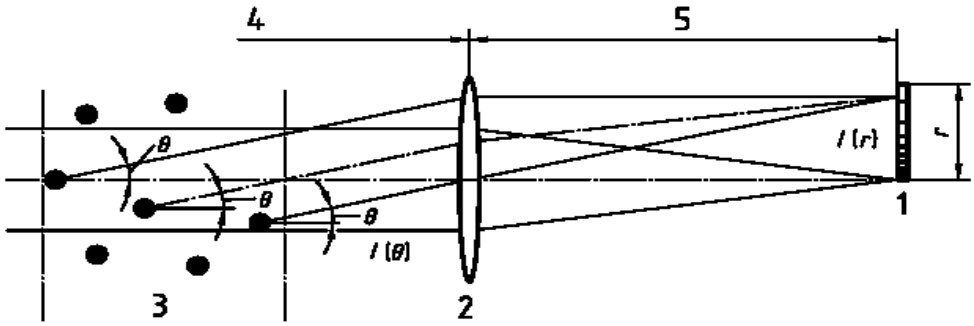

Figure 3-13: Optical Set-Up: Particles are in parallel beam before and within working distance where 1 is the Detector, 2 is the Fourier Lens, 3 is the Particle ensemble, 4 is the working distance and 5 is the focal distance [173]

The following procedure was used to prepare the HAp powder particle samples as dispersed solutions for examination in the Malvern Mastersizer. The dispersant agent was selected in accordance to ISO 14887 [174] and the method used in the sample preparation for analysing the particle size analysis via the wet method, is as follows:

1. 1 g of sodium hexametaphosphate was mixed intensively via a magnetic stirrer in 1000ml of deionised water to act as a dispersant.
2. 0.5 g of the HAp powder sample was dispersed in 30ml of the above prepared dispersant in an 80 - 100ml heavy-duty beaker.
3. The suspension was then stirred again using a magnetic stirrer for a period of more than 2 min to ensure that the HAp powder and dispersant had formed a suspension.
4. The stirred suspension was then placed in an ultrasonic bath for a 5 min period (see Figure 3-15).

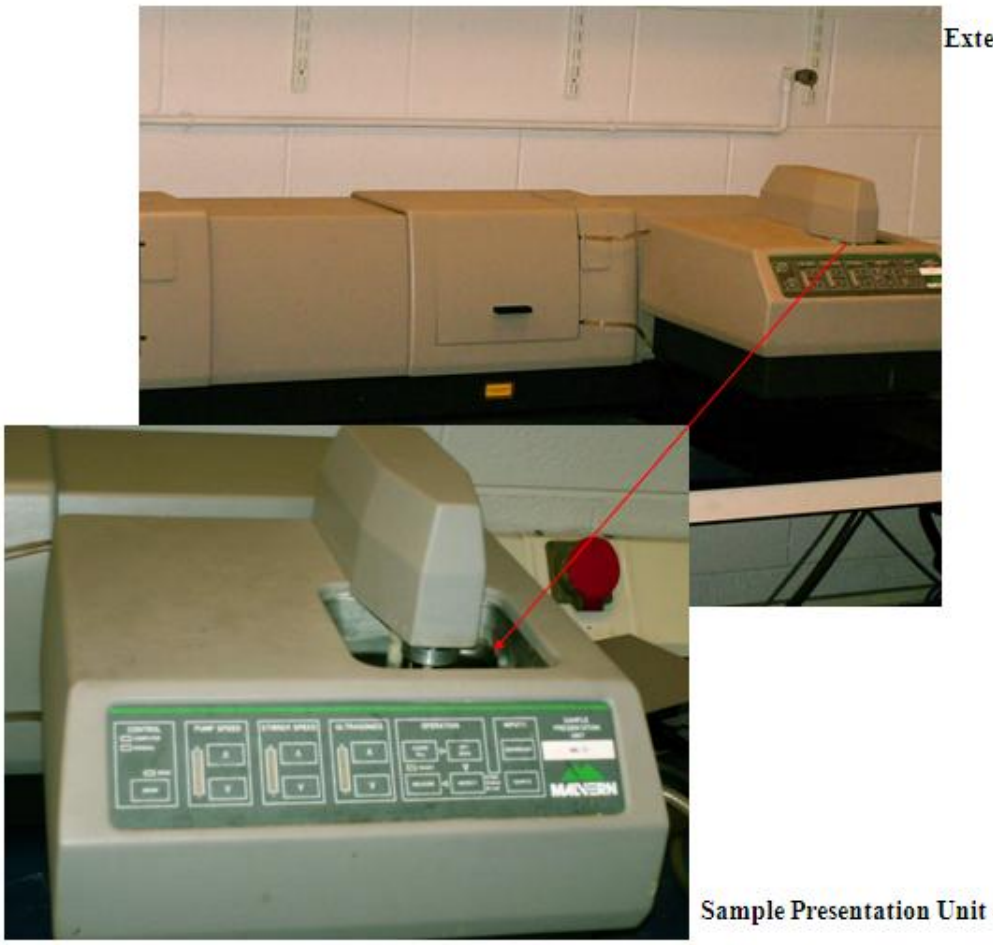

Figure 3-14: External view of the Malvern Mastersizer particle size analyser and sample preparation unit

According to ISO 14887 [174], complete dispersion occurs in a liquid when the individual particles that made up the original clumps have become separated, move independently of one another and remain separated. Successful particle size analysis has a number of pre-requisites, such as: (i) representative samples and delivery of samples to the sample system, (ii) transportation and dispersion of the sample to the laser in a statistically representative manner, (iii) material analysis using the appropriate optical presentation model and (iv) correlation of data to historical data from alternative techniques [175].

Figure 3-15: Ultrasonic waterbath

3.7.9 Surface Area Measurement Of HAp Using The Brunnauer Emett Teller (B.E.T.) Method

Brunnauer Emett Teller (B.E.T.) surface area analysis is considered the standard technique in evaluating the specific surface area of a material, which utilises low temperature gas adsorption or the uptake of a gas on the powders surface. The specific surface area of the HAp powders were measured using a Gemini 2375 Analyser, (Micromeritics Instruments Inc., Norcross, GA) (see Figure 3-16) with liquid nitrogen used as coolant. This standard method for measurement of specific surface area is based on the physical adsorption of nitrogen on the solid surface using the B.E.T. method [176].

Figure 3-16: Micromeritics Gemini 2375 Analyzer

The total surface area (S_t), of a solid material can be expressed as the product of the number of molecules of adsorbate in a monolayer, N_m, and the effective cross – sectional area of the adsorbate molecule, A_{CS}, that is [176]:

$$S_t = N_m A_{CS} \qquad \textit{Equation (3-16)}$$

As the pressure is increased during the B.E.T. process, adsorption of a vapour (nitrogen) onto a solid surface occurs until the surface becomes progressively coated with the adsorbate. The BET theory was originally proposed in 1938 [176] and is still the most generally used method for calculating the weight of adsorbant on a monolayer, Wm. Nitrogen is the most commonly used as it adsorbs easily onto most solid surfaces and its cross sectional area is well established. The determination of the surface area using BET theory requires the application of the B.E.T. equation [176]:

$$\frac{1}{W[(P_0/P)-1\}} = \frac{1}{W_m C} + \frac{C-1}{W_m C}\left(\frac{P}{P_0}\right) \qquad \textit{Equation (3-17)}$$

In which W is the weight of vapour adsorbed, P/P_0 is the B.E.T. constant, and Wm is the weight of adsorbate in a monolayer [176]. A plot of 1/W (Po/P-1) versus P/Po, will yield a straight line in the range $0.05 \leq P/Po \leq 0.35$ with slope [176]:

$$s = \frac{C-1}{W_m C} \qquad \textit{Equation (3-18)}$$

and intercept, i

$$i = \frac{1}{W_m C} \qquad \textit{Equation (3-19)}$$

Solving equations 3-18 and 3-19 gives:

$$W_m = \frac{1}{s+i} \qquad \textit{Equation (3-20)}$$

In establishing W_m, the sample surface area can be calculated using the following equation:

$$S_t = \frac{W_m \overline{N} A_{CS}}{\overline{M}}$$

Equation (3-21)

Where A_{CS} is the cross-sectional area of a molecule of adsorbate, $\overline{M}$ is the molecular weight of an adsorbate molecule, and $\overline{N}$ is Avogrado's number. The specific surface area can be determined by dividing S_t by the weight of the sample.

The HAp powder samples were prepared by out-gassing the material at a temperature of 200ºC to remove any surface organic or moisture contaminants present. This ensured maximum accuracy and reproducibility. Additionally, out-gassing prevents contaminants entering the detector causing noise and erroneous signals. The specific surface area was calculated as per unit weight of the powder. This analysis complements the particle size distribution providing information about the presence of internally finer particles. It is accepted that the smaller the particle size, the greater the specific surface area. However, the specific surface area is also dependent on the particle shape, size and its distribution and surface conditions [177]. The B.E.T. method is used amongst the vast majority of works due to its ease of use, its definitiveness and its ability to accommodate each of the five isotherm types.

3.7.10 Density Measurements

The density of the HAp powder samples were measured using a Helium Pycnometer, Micromeritics AccuPyc 1330 He-pycnometer, Micromeritics Instruments Inc., Norcross, GA (see Figure 3-17). The AccuPyc works by measuring the amount of displaced gas. The pressures observed upon filling the sample chamber and then discharging it into a second empty chamber allow computation of the sample solid phase volume. Gas molecules rapidly fill the tiniest pores of the sample; only the truly solid phase of the sample displaces the gas with an accuracy of +/- 0.03% [178]. The sample size of HAp powder required is between 1 - 5g of dry substance with a preferable volume size of between 7.5 - 75 cm^3. The instrument automatically purges water and volatiles from the sample and then repeats the analysis until successive measurements converge upon a consistent result.

The acceptable limits of density (g/cm^3) for the HAp (both, in powder and coating form) are reported in accordance to the "Calcium Phosphate (Ca-P) Coating Draft Guidance for Preparation of FDA Submissions for Orthopaedic and Dental Endosseous Implants" [137]. Acceptable ranges of HAp powder densities are quoted in Table 2-19 [50, 137]. These values are found to correlate well with that of the theoretical density value of hexagonal HAp (3.156 g/cm^3), which is calculated based on its crystal structure parameters [143].

Particle size, particle size distribution (PSD), average porosity size, overall pore volume and the total surface area of the HAp powder also provide for additional information required in accordance to the 510(K) Information needed for HAp coated orthopaedic implants [137].

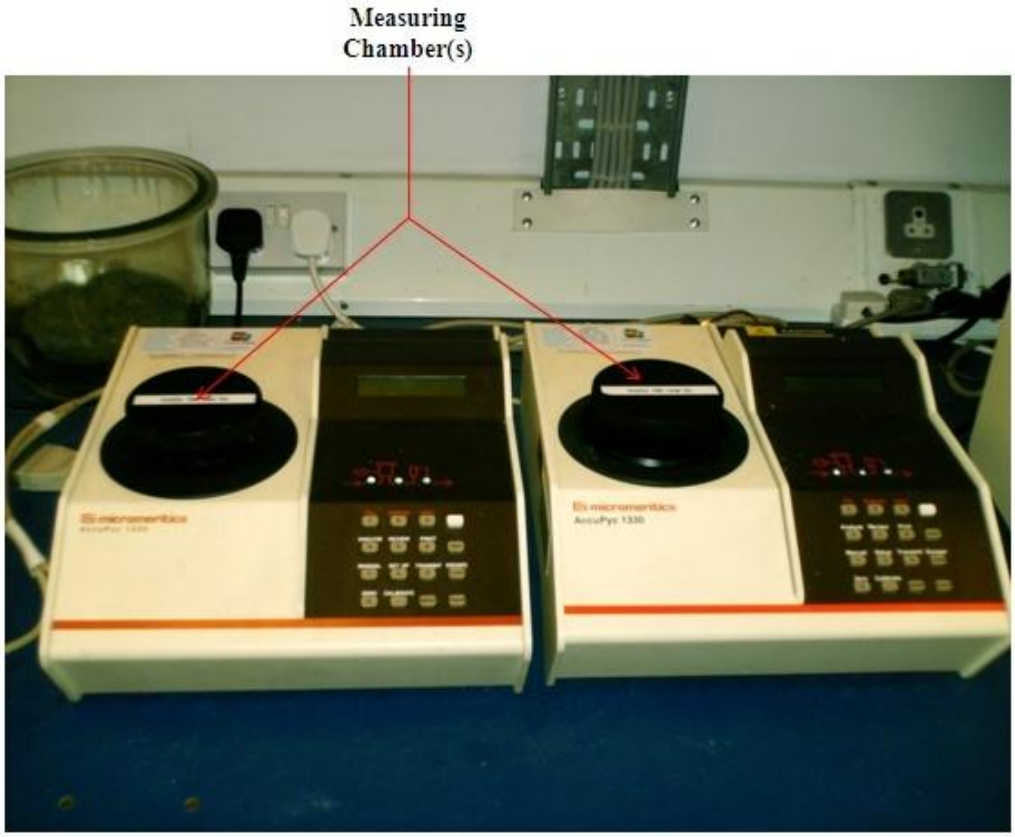

Figure 3-17: Micromeritics AccuPyc 1330 Helium Pycnometer for small sample volume (left hand side) and large sample volume (right hand side)

3.7.11 HAp Rheology

A. HAp Slurry Density

The bulk density of the HAp in slurry form (that is, post chemical precipitation) was measured, using a beaker of a known volume and mass. An average of three readings was recorded for every sample, with the results calculated in g/cm^3.

B. HAp Slurry Rheology

Rheology is a science of deformation and flow of materials. The principal theoretical concepts are kinematics, dealing with geometrical aspects of deformation and flow; conservation laws, forces, stress and energy interchanges; constitutive relations special to classes of bodies. The constitutive relations, namely, the relations between stress, strain and time for a given test sample, serve to link motion and forces to complete the description of the flow process, which may then be applied to solve complex engineering problems. There exists, the Newtonian and non-Newtonian fluids, based on the constitutive relations. For the fluids, the viscosity η, is defined as [179]:

$$\eta = \frac{\text{Shear stress}}{\text{Rate of Shear strain}} \qquad \textit{Equation (3-22)}$$

In the case of Newtonian fluids, η is constant. For non-Newtonian fluids, η is variable, which means that the shear stress (s) varies with the rate of shear strain (c). It is generally accepted, however that most semisolids, such as slurries, exhibit properties of non-Newtonian fluids [179, 180]. The information for characterization of the rheology of non-Newtonian slurries is outlined in Figure 3-18(a). However, time-dependent non-Newtonian fluids are usually encountered in fine and concentrated aqueous suspensions. Time-dependent non-Newtonian fluids may be characterised according to viscosity with time under conditions of shear rate and sub-divided into two categories, such as, thixotropic and rheopectic. A thixotropic fluid undergoes a decrease in viscosity with

time, when subjected to constant shear, whereas a rheopectic fluid's viscosity increases with time as it is sheared at a constant rate (Figure 3-18(b))

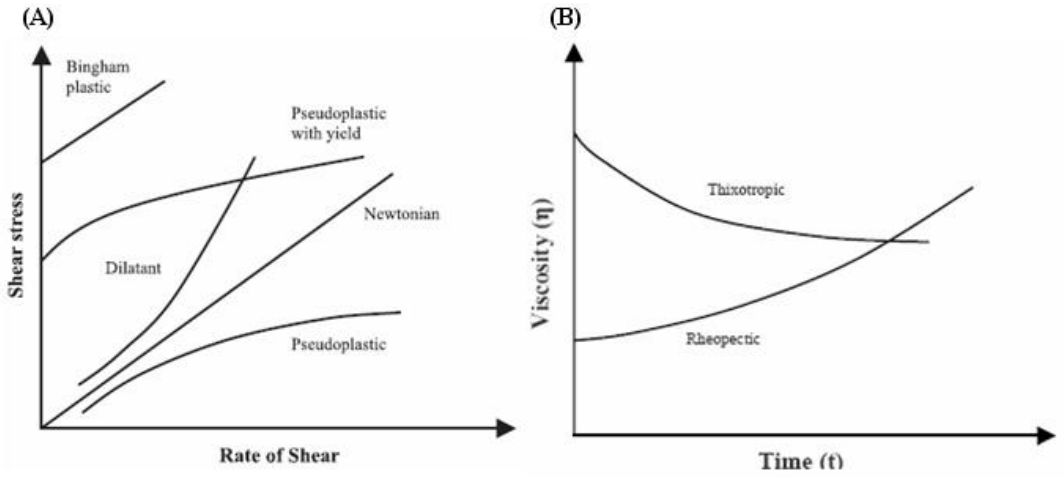

Figure 3-18: Shear stress versus shear rate curves for time-independent non-Newtonian slurries (A) and Viscosity versus time curves at a given shear rate for time – dependent non-Newtonian slurries (B)

The behaviour of HAp aqueous suspensions is quite complex as a result of the changes in the concentration of the hydroxylic groups on the surface due to the suspension parameters. However, rheology is the most sensitive method for material characterisation, since flow behaviour is responsive to properties, such as molecular weight and molecular weight distribution. As a consequence, rheology measurements are useful in following the course of a chemical reaction. Such measurements can be employed as a quality check during production or to monitor and/or control a process. The rheological behaviour of a HAp slurry may also be indicative of interparticle interaction or aggregation in the slurry itself, further enhancing the requirement to control this parameter within industrial processes (such as, the transportation of the HAp slurry into a spray dryer). However, the rheological properties for aqueous suspensions of HAp are highly complicated and there is no singular parameter that can explain it. The physical and chemical properties of the HAp slurry, such as solids content, particle size and distribution, particle shape, pH value, shear rate, slurry temperature, all have a significant

effect on slurry rheology due to the change or modification in surface property [179, 180]. As known, fine particles (<1 micron) in a suspension attract each other by van der Waals attractive forces to form aggregates, which evidently increase the resultant velocity of the HAp suspension. In general, the HAp slurry flowability can be improved by decreasing the slurry viscosity and by reducing or eliminating the shear yield stress in order to increase the product fineness.

Rheological characteristics of aqueous suspensions of HAp slurry (such as, slurry viscosities and flow behaviour) were conducted using the RI-2-M Rheometer, Rheology International Series 2 (see Figure 3-19) with cone and plate measuring geometry; with diameter 25 mm and 0.1 rad cone angle. Pre-shearing was done for 1 min prior to recording of all measurements (that is, each shear rate was given a time lag of 1 min to establish an equilibrium). All measurements were performed at 25 (+/-0.2°C) and conducted in triplicate.

(i) Cone And Plate Viscometer

As previously identified, the present investigation utilised the cone and plate rotational type viscometer in order to measure the absolute viscosities of various HAp slurries. A schematic representation of the cone and plate geometry is illustrated in Figure 3-20. The cone and plate geometry is particularly suitable for advanced rheological analysis of non-Newtonian fluids.

The absolute viscosity for HAp slurry samples (0.5mL) were measured under conditions of defined shear rate and shear stress, where shearing of the fluid is achieved by the action of the rotating cone spindle. The RI-2-M model has the capacity to generate shear rates in the range of 0.2 sec-1 to 3,750 sec-1, and measure viscosities ranging from 103 mPa.s to 513,345 mPa.s [181].

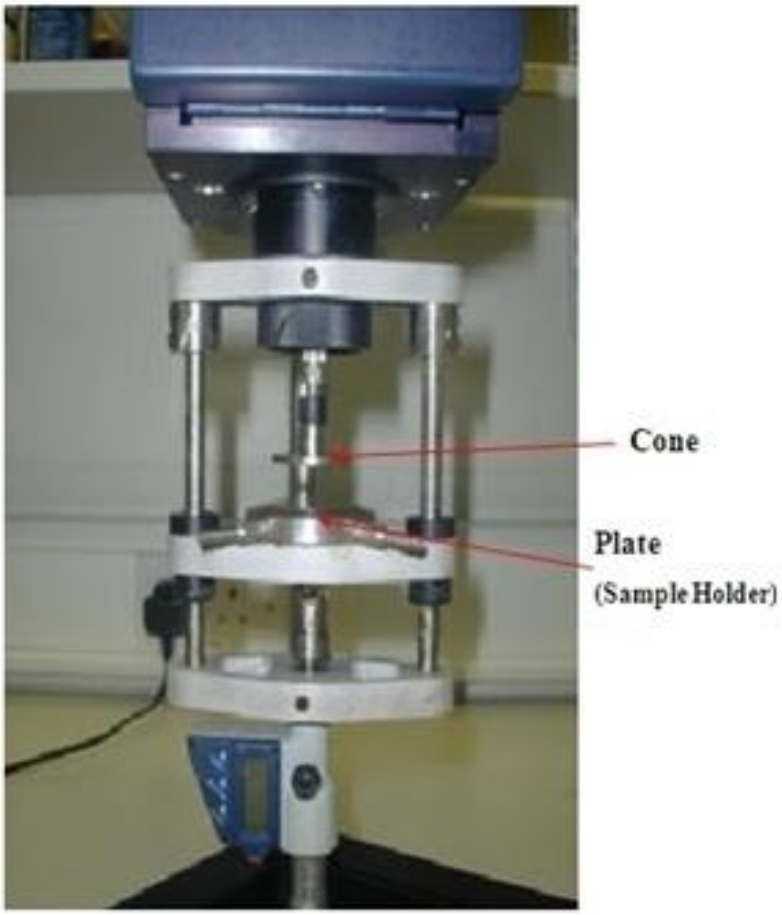

Figure 3-19: Methods of measuring the viscosity for the HAp slurries using the cone and plane rotational viscometer

The equipment is calibrated prior to recording each viscosity measurement, through using the inbuilt autozero function; after setting the minimum distance between the cone and plate sample (0.1mm). The value which displays after Autozero (0.0mm) is an electronic value within the transducer arising from the test, and is either added or subtracted from all test values until the next autozero calibration is performed. This ensures that complete instrument accuracy was sustainable over long operating periods.

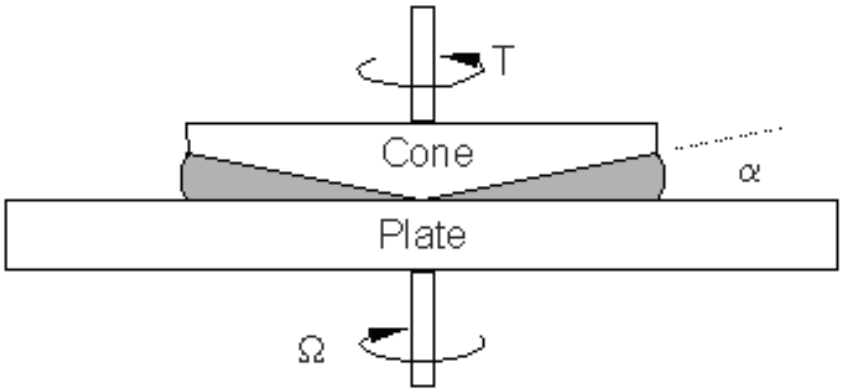

Figure 3-20: Cone and plate geometry – rotational type viscometer

The absolute viscosity of the HAp slurry, determined using a cone and plate geometry can be calculated using the following equation [182]:

$$\mu_a = \frac{3T}{2\pi R^3}\frac{\alpha}{\Omega} \qquad \textit{Equation (3-23)}$$

Where;	R	cone radius	m
	α	cone angle	radians
	$\dot{\gamma}$	shear rate	s^{-1}
	τ	shear stress	Pa
	Ω	angular velocity of cone	rad/s

C. HAp Powder Rheology

A Hall flowmeter (designed and manufactured by the author) was used to determine the flowability of the HAp powders, post thermal treated (that is, post - sintering), in accordance with ASTM B213-03 [183].

The ability of the HAp powder to flow is a function of interparticle friction. As interparticle friction increases, the flow is disturbed (that is, slowed). Extremely fine powders may not flow. Factors affecting the flow rate are humidity and moisture content, such that, wet or moist powders may not flow. The Hall flowmeter funnel consists primarily of a calibrated orifice of 2.54mm in diameter and the distance between the orifice and the top of the beaker is 125.4mm. Blocking the discharge orifice (of the HAp powder) at the bottom of the funnel with a dry finger, a pre-measured mass of HAp powder (10.0g) as sampled into a clean weighing dish (beaker), was carefully poured into the centre of the flowmeter funnel, without any tapping, vibration or movement of the funnel. The empty beaker was then placed under the funnel orifice. The stopwatch was started; simultaneous to removing the finger from under the orifice. The time was recorded, to the instant of the last powder exiting the funnel orifice, to the nearest 0.1s.

The measurements were recorded in triplicate. A schematic of the Hall flowmeter manufactured for this investigation with the drawings pertaining to the required dimensions, as specified in ASTM B213- 03 is illustrated in Figure 3-21 (Refer also to Appendix C)

(A) **(B)**

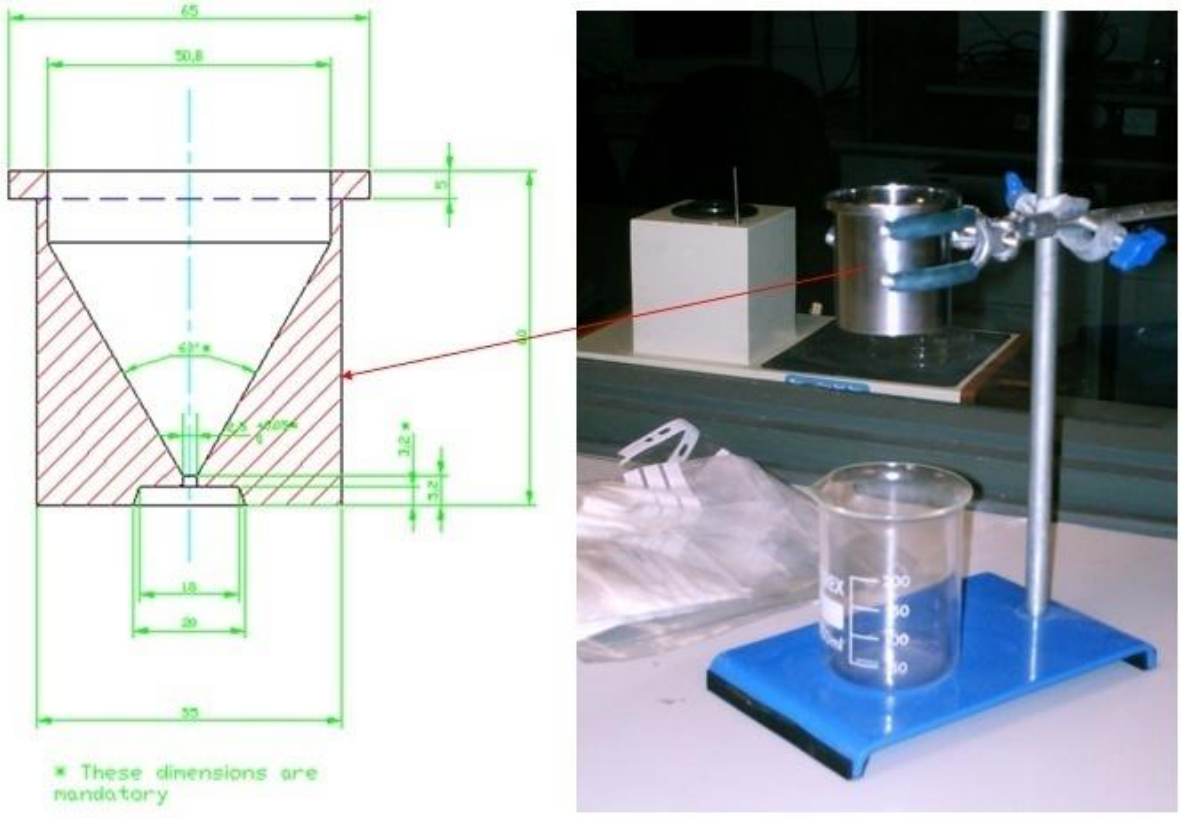

Figure 3-21: Autocad 2005 Drawing of the Hall Flowmeter (A) and a photographic illustration of the apparatus in use (B)

3.8 BIOLOGICAL RESPONSE OF HAp POWDERS

3.8.1 Osteoblast Cells

MG-63 osteoblast-like cells, originally isolated from a human osteosarcoma [184], were used for these experiments. MG63 have been well characterised, and widely used for the testing of biomaterials. MG-63 (American Type Culture Collection: ATCC number CRL 1427) cells were cultured in Dulbecco's modified Eagle medium (DMEM, Invitrogen, France) supplemented with 10% Fetal calf serum (FCS, Invitrogen, France) and 0.5% antibiotics (penicillin-streptomycin, Invitrogen, France). Cells were maintained at 37ºC in a fully humidified atmosphere (see Figure 3-22) at 5% CO_2 in air. At confluence (that is, the state in which cells have grown to full capacity and no additional surface area space is present), cells were harvested with 0.1% trypsin-EDTA solution in phosphate-buffered saline (PBS, pH 7.4) at 37ºC for 5min, centrifuged to pellet the cells, and resuspended in DMEM with the FCS and antibiotics.

Figure 3-22: Humidified Incubator

After cell passaging (a technique whereby cells are maintained under cultured conditions for an extended period of time, at 90-100% confluency), HAp was added to the cell culture medium and seeded in to a 24-well plate, in order to study the cell proliferation and viability. The HAp/Cell Culture medium was also fixed onto Thermanox® (a cell culture plastic specially made for cell culture and SEM observation) to investigate the resulting cell morphology (see Figure 3-23).

3.8.2 Cell Proliferation

2mg of HAp powder particles were added to 2mL of cell culture medium and seeded at a density of 20,000 cells per well. As a control measure; two commercially available powders (HAp1 and HAp5) were added to the cell culture plates and evaluated against the HAp produced in-house under various synthesis conditions. The plates were incubated at 37ºC with 5% CO2 for 1, 4, 7, 14, and 28 days. At each culture period, cells were detached with 0.1% trypsin-EDTA solution in phosphate buffered solution (PBS, pH 7.4) at 37ºC for 5min.

Figure 3-23: 24-well plate and optical microscope

Before counting, the cell suspension was stained with 0.1mL of Trypan Blue solution and allowed to stand at 37ºC for 5 min. Trypan Blue is a vital dye. The reactivity of Trypan blue is based on the fact that the chromopore is negatively charged and does not interact with cells unless their membranes damaged. Therefore, cells which exclude the dye are viable.

The cell number was determined by counting with a Malassez hemacytometer (see Figure 3-24) under phase contrast microscope (see Figure 3-23), and all counting's were run in triplicate. As outlined previously, the non-viable cells were denoted by the presence of a stained while the viable cells excluded this stain.

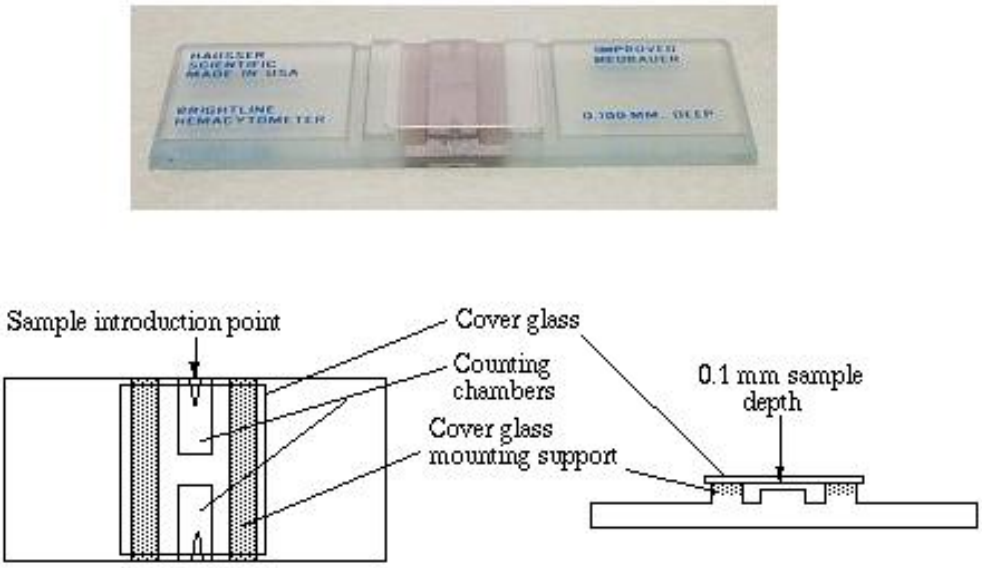

Figure 3-24: Malassez hemacytometer

3.8.3 Cell Viability

The cell viability was performed with the Cell Titer 96® Aqueous One Solution Cell Proliferation Assay (Promega, France), according to manufacturer's instructions [185]. The concept is based on an enzymatic reduction of a tetrazlium salt. This test is a colorimetric method for determining the viability of cells. The conversion of methyl thiazol sulphate (MTS) into aqueous soluble formazan is accomplished by dehydrogenase enzymes found in metabolically active cells. The intensity of the colour is proportional to the number of living cells in culture and can be measured at a wavelength of 490nm. Briefly, supernatant of each condition was cultured for 48h with cells on 96 wells plate. After 48h, the medium was replaced by freshly prepared MTS for 5h, the plate was incubated at 37ºC to develop the colour, and the plate was read at 490nm in an enzyme-linked immunosorbent assay (ELISA) plate reader (see Figure 3-25) for absorbence measurements [74].

Figure 3-25: ELISA plate reader

3.8.4 Cell Morphology

SEM observations were performed to evaluate the morphology of the cells. Assays were run in triplicate and the data were analyzed using Student *t* test and significance was considered to be achieved at $p < 0.05$.

3.9 SUMMARY

The experimental equipment, procedures and characterisation techniques outlined in this chapter were then used to assess the HAp powder characteristics in the next chapter, with a view to investigating the optimisation of HAp powder for orthopaedic application via the thermal spraying technique.

4 RESULTS AND DISCUSSION

4.1 INTRODUCTION

HAp coatings have been widely used in orthopaedic applications to improve the biocompatibility of metallic implants. Studies have shown that essential properties for good coating performance include a high degree of crystallinity, a low porosity level, a high coating purity, high cohesion strength and a high degree of adhesion. However, it is difficult to achieve these properties by varying the spraying parameters alone. In addition to these process parameters, the HAp powder characteristics have a major influence over the final coating quality.

The present study aims to investigate the physico-chemical and biological powder properties of HAp synthesised via the chemical precipitation method using $Ca(OH)_2$ and H_3PO_4, as precursor materials: with the aim to produce HAp powder of optimum properties, pertinent to highly successful coating application via the plasma spraying method onto orthopaedic implants. The optimised powders were also aimed at satisfying criterion as set out by ISO 13779-1 [139], ASTM F1185 [140] and the Food and Drug Administration [137], in the US, to ensure the potential marketability of the produced powders.

The preliminary investigation of this study involved analysing the HAp powder characteristics of international suppliers and comparing these against the HAp powder properties currently being produced by industry in Ireland. HAp was synthesised in-

house, within the Materials Processing Research Centre, under the same conditions as that disclosed by the HAp manufacturing company in Ireland: characterised and compared against that of the Irish HAp and also against those purchased by other various international suppliers. The HAp powders examined in this study were as follows:

HAp1: Irish HAp (Undisclosed Company)
HAp2: American HAp (Undisclosed Company)
HAp3: Japanese HAp (Tomito®)
HAp4: Netherlands HAp (CAMCERAM®)
HAp5: British HAp (Plasma Biotal®)
HAp6: In-house HAp

(HAp3 – HAp5 are commercially available powders, while HAp1 and HAp2 are applied as orthopaedic coatings at their respective industrial site).

The preliminary characterisation of the above HAp powders is presented, with the results obtained grouped into the following categories:

HAp Physicochemical Powder Properties:

1. XRD Diffraction
    a. Phase Composition and Purity
    b. Crystallinity
    c. Lattice Parameters and Crystallite Size

2. Particle Size and Specific Surface Area Analysis
    a. Particle Size and Specific Surface Area
    b. Particle Size Distribution

3. HA Powder Density

4. SEM Micrographs
    a. Powder Morphology
    b. Particle Size

Rheological Evaluation of HAp:

1. HA Slurry Density
2. HA Slurry Rheology
3. HAp Powder Flowability

A rheological evaluation of the HAp (in slurry form) was investigated during the course of the chemical precipitation reaction to examine the influence of the slurry viscosity on the spray drying stage of HAp powder production.

The review of literature and the preliminary investigation of this study were used to identify the most important synthesis parameters of chemical precipitation influencing the final HAp powder characteristics. These critical parameters were investigated further using design of experiments. A Fractional-Factorial (Res IV) screening design (2^6) with main and interaction effects, with the six critical variables, at two levels, was used to screen a large number of the precipitation process variables in order to determine their effect on the final HAp powder characteristics (16 experiments). The six factors investigated were: T_0 synthesis temperature (ºC), V_{st} stirring speed (rpm), V_{ac} acid addition rate (mol/min), t_r ripening time (h), Ca^{2+} initial calcium concentration (M) and a qualitative factor examining the presence of a controlled/uncontrolled environment. This experimental design highlighted the factors that have the most significant affect on HAp precipitation process parameters, which was then used to build an optimisation experimental design based on the Box-Behnkhen optimisation model (17 experiments). Linear and quadratic polynomial equations for predicting the phase composition, crystallinity, crystallite size, lattice parameters and particle size were developed for both the screening and optimisation designs, enabling the final determination of a set of

idealised precipitation process parameters to obtain reproducible, highly desirable HAp feedstock specific for plasma spraying application. To validate the results obtained from both the screening and optimisation experimental designs, three extra confirmatory tests were conducted and the HAp powders yielded were characterised and compared against the previous results as obtained from both experimental designs.

An investigation was also conducted to study the possible mechanism of various HAp with different crystallinity, morphology and particle size on a well studied osteoblast-like cell line (MG-63) commonly used to test *in vitro* bone - biomaterials biocompatibility. The HAp properties were controlled via modulating the chemical precipitation experimental parameters (such as, synthesis temperature, stirring speed, acid addition rate, ripening time, and initial calcium concentration) of the synthesis process. Eight variations of HAp powders were used in this study. The cell morphology was assessed using the scanning electron microscope (SEM), the cell proliferation and viability by biological techniques.

4.2 ANALYSIS OF HAp POWDER CHARACTERISTICS

In order to determine an optimum set of precipitation process parameters capable of synthesising HAp possessing ideal physicochemical powder characteristics; the most influencing reaction parameters must firstly be identified. A comparative analysis of the HAp powder characteristics amongst international (commercial) suppliers of HAp was undertaken with a view to benchmarking HAp1 and HAp6 powders against each other. To characterize these powders, XRD analyses were performed to determine: the phase composition, purity, crystallinity, lattice parameters and crystallite size. In addition, the powder particle size, particle size distribution and specific surface area were measured using Laser Diffraction and BET method, respectively. The final HAp powder density, prior to plasma spray coating application onto orthopaedic implants was measured using Helium Pycnometry, while the morphology of the powders were observed using SEM.

4.2.1 Phase Identification And Phase Purity

The XRD patterns of the final sintered HAp powders (HAp1 – HAp6) are illustrated in Figure 4-1 (refer to Sections 3.8.1 – 3.8.3). Details of the process parameters used in producing HAp2 – 5 are unknown. However, what is known is discussed in the following section. The diffraction patterns are found to typically agree with those published in literature [2, 5, 13, 56, 85]. All the XRD patterns obtained have characteristic peaks consistent with the International Centre for Diffraction Data (ICDD) files for calcium phosphates. The predominant phase, as expected, was confirmed with JCPDS file no. 9-432 (refer to section 3.8.2) for stoichiometric HAp. This suggest that no foreign elements, such as sodium (Na^{2+}), ammonium (NH_4^+), potassium (K^+), chloride (Cl^-) and nitrate (NO_3^-) ions were involved in the reaction synthesis, since there is strong evidence to suggest that these ions are easily incorporated into the crystal lattice leading to the formation of non-stoichiometric HAp [5]. The absence of such elements may be attributed to the purity of the raw precursor materials used in the reaction synthesis. It is known that chloride ions enter the crystal lattice substituting hydroxyl groups, while potassium ions are found to substitute calcium ions into the HAp crystal lattice forming locally non-stoichiometric HAp islands in the bulk crystal. In order to avoid

contamination of the product, the use of calcium nitrate and phosphoric acid instead of calcium chloride salts and potassium dihydrogen phosphate, respectively are advantageous as the presence of potassium ions is avoided and the nitrate ions are too large to substitute hydroxyl groups in the crystal lattice of HAp. These substitutions were avoided in the preparation of HAp1, HAp2 and HAp6, since the reactants used were $Ca(OH)_2$ and H_3PO_4.

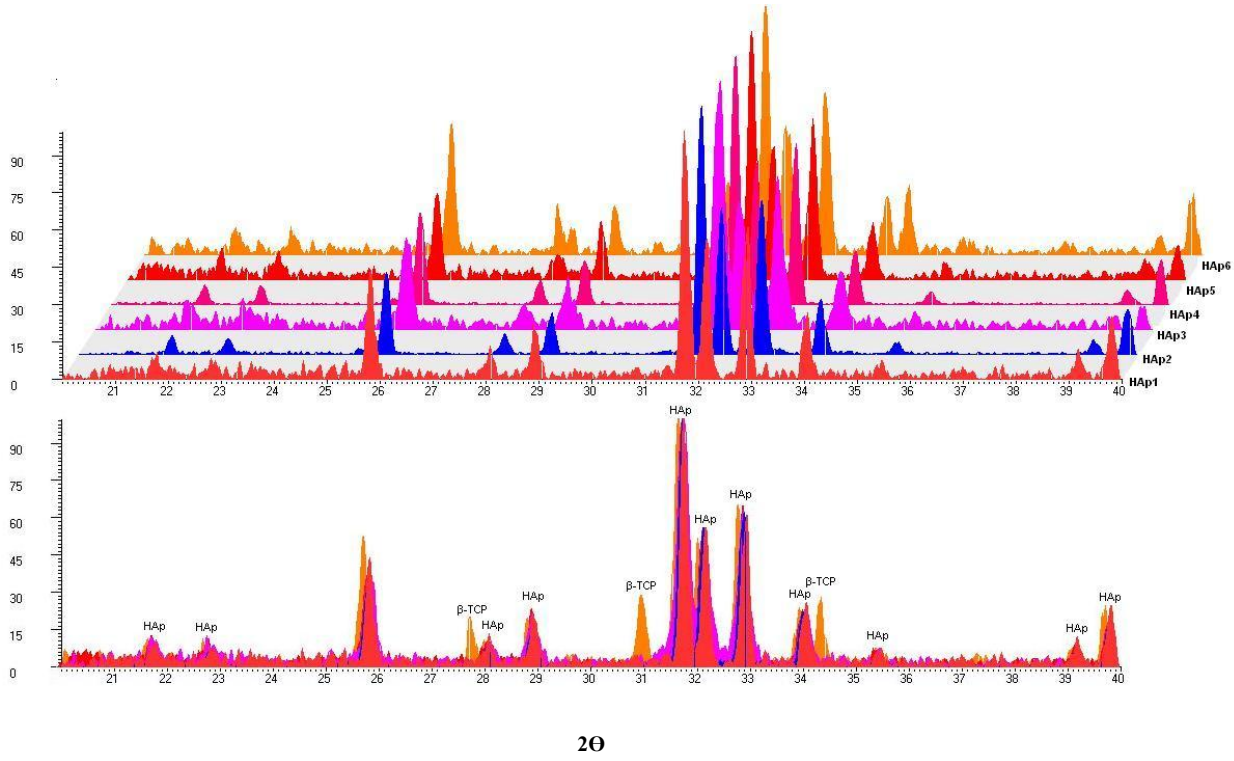

Figure 4-1: Comparison of x-Ray diffraction patterns for HAp1 – HAp6 powders in 2-D (below) and 3-D (above)

For all HAp powders studied, no trace elements of CaO were observed. This indicates that either a small level or no carbonation of the HAp occurred during the reaction synthesis [5, 7]. For all the HAp powders analysed, no significant amounts of foreign elements were observed. However, one such secondary phase (β – TCP) was observed [186]. The diffraction patterns show that the amount of this phase varies with the HAp origin. HAp6 contains the highest content of β-TCP, while HAp1, HAp3 and HAp5

contain only minor traces of this phase. The apparition of β-TCP can be attributed to (i) a high sintering temperature (>1200ºC), as it has been reported that stoichiometric HAp can readily decompose to TCP, ACP and/or CPP at this sintering temperature [87] and (ii) the Ca-deficient nature of the HAp resulting in the production of secondary phases post sintering, at temperatures, starting as low as 700ºC [98]. The obtained degrees of purity are listed in Table 4-1. According to purity, the HAp powders can be classified as follows: HAp2 = HAp4 > HAp5 > HAp3 > HAp1 > HAp6. The synthesis of Ca-deficient HAp1, HAp2 and HAp6 can be explained by:

Low reaction synthesis temperature (~20ºC): implemented at ambient temperature. Numerous researchers have studied the effect of this parameter on the HAp stoichiometry. Increasing the reaction temperature has had a favourable effect on the end stoichiometry of phase pure HAp [79, 87 - 90], and at a critical temperature, pure HAp can be formed.

Insufficient stirring speed (1000rpm): In cases of low temperature synthesis, stirring in the maturation stage has shown to play an essential role in obtaining the required stoichiometry [78]. Insufficient stirring has been shown to produce thermally unstable HAp, where decomposition occurs into a mixture of HAp and TCP. Afshar et al. [83] found that increasing the stirring speed from 500 to 2000rpm, decreased significantly the amount of CaO present in their sintered HAp samples, producing Ca-dHAp. Both Monetite (DCPA) and Brushite (DCPD) formation is favoured by insufficient mixing of calcium solution as the orthophosphoric solution is added.

Reactant addition time: HAp crystallisation obeys the Ostwald rule of stages [78], so it is usually formed upon recrystallisation of precursor phases such as OCP, DCPA, DCPD and ACP. Direct HAp formation is only found for low reactants concentration where the solution was undersaturated or slightly supersaturated with respect to the precursor phase. The HAp obtained through precursor phases is Ca-dHAp and requires long maturation times to approach stoichiometry. The supersaturation may be kept low by ensuring that the rate of addition of reactants is lower than the rate of crystallisation.

Table 4-1: Results for XRD analysis of HAp1 – HAp6 powder samples

HAp Powder	Phases Present	Crystallinity, (%)	Purity, (%)	Crystallite Size (nm)		Lattice Parameters (nm)	
		X_c	X_p	L_{002}	L_{003}	*a*	*c*
HAp1	HAp + β-TCP + α-TCP	93.94(±2)	97.36(±2)	62.23(±0.04)	81.17(±0.04)	9.4050(±0.04)	6.7943(±0.04)
HAp2	HAp	95.47(±2)	100.00(±2)	63.86(±0.04)	76.86(±0.04)	9.4294(±0.04)	6.9022(±0.04)
HAp3	HAp + β-TCP + α-TCP	98.85(±2)	98.21(±2)	45.06(±0.04)	48.42(±0.04)	9.4286(±0.04)	6.8877(±0.04)
HAp4	HAp	98.75(±2)	100.00(±2)	66.72(±0.04)	74.63(±0.04)	9.4263(±0.04)	6.8944(±0.04)
HAp5	HAp + β-TCP	97.31(±2)	99.56(±2)	66.24(±0.04)	69.27(±0.04)	9.4312(±0.04)	6.8875(±0.04)
HAp6	HAp + β-TCP + α-TCP	95.49(±2)	90.44(±2)	62.23(±0.04)	81.17(±0.04)	9.4642(±0.04)	6.8822(±0.04)
Stoichiometric HAp [13]	HAp	100%	100%		-	9.4420	6.8800

Addition times of 60min or longer are required to obtain a well crystallised HAp product. Addition times of 30min, adversely have been found to result in a mixture of HAp and ACP. The measured pH at the end of the synthesis, is strongly linked to the reactant addition rate; a key parameter which can be used to determine the purity of the as synthesised and also for the stabilisation of the suspension. Bouyer et al. [94] state that when the addition rate of the phosphoric acid is very high (V_{add} = 2400mL/min, the synthesis reaction conversion decreases and there is some $Ca(OH)_2$ appearing in the product, while below 100mL/min, the conversion rate of the reaction is 100%.

Sintering Temperature: The effect of the sintering temperature on the phase purity of HAp6 was investigated in this study and can be seen in Table 4-2. The results indicate that the purity of the spray dried HAp is lower than the sintered HAp, while a significant level of β-TCP was only evident in the post sintered HAp powder (see Figure 4-2).

Table 4-2: Effect of sintering on the crystallinity and phase purity of HAp

HAp6	Crystallinity, Xc (%)	Purity, Xp (%)
Spray Dried Chamber	33.45 (±2)	97.08(±2)
Spray Dried Cyclone	38.32(±2)	96.07(±2)
Sintered (2:1 ratio; Chamber: Cyclone)	95.49(±2)	90.44(±2)

It has been reported that TCP appears, as a result of sintering temperatures reaching in excess of 1000ºC [2]. The sintering of pure stoichiometric HAp powder yields pure dense HAp ceramics with superior mechanical properties; whereas the sintering of non-stoichiometric HAp causes other phases to be formed: TTCP and/or CaO if the Ca/P molar ratio exceeds 1.67 and α- and/or β-TCP if the Ca/P molar ratio is below 1.67 [79]. OCP (Ca/P = 1.33) formed at the beginning of the precipitation reaction is so unstable that it quickly transforms to ACP (Ca/P = 1.5) very quickly [91]. ACP then transforms to Ca-dHAp gradually to become stable HAp. ACP is composed of free radicals of OH^-

and HPO_4^{2-} and DAP had radicals of OH^- and HPO_4^{2-}, while HAp had no radicals of HPO_4^{2-} but higher peaks of OH^-. Figure 4-2 illustrates that sintering parameters have a significant effect on the final purity of the HAp. This behaviour can be due to the fact that the decomposition of Ca-dHAp in the temperature range 22-900ºC takes place according to the following reaction [79]:

$$Ca_{10-x}(HPO_4)_x(PO_4)_{6-x}(OH)_{2-x} \rightarrow xCa_9(PO_4)_6(\beta) + (1-x)Ca_{10}(PO_4)_6(OH)_2$$

Equation (4-1)

Samples with an excess of $Ca(OH)_2$ during thermal treatment, result in the presence of CaO. At higher temperatures of 1200ºC further decomposition occurs according to the following reaction [79]:

$$Ca_{10}(PO_4)_6(OH)_2 \rightarrow 2Ca_3(PO_4)_2(\alpha) + Ca_4P_2O_9 + H_2O$$

Equation (4-2)

The extent of the reaction is dependent on the initial stoichiometry of the HAp. Ca-dHAp shows high degradation tendency, while in the case of stoichiometric HAp some loss of OH^- groups occur. In order to eliminate contamination during synthesis of the HAp, the use of calcium nitrate and phosphoric acid instead of calcium chloride salts and potassium dihydrogen phosphate, respectively are advantageous because the presence of potassium ions is avoided and the nitrate ions are too large to substitute hydroxyl groups in the crystal lattice of HAp. The synthesis route has a great effect on the final HAp purity [26]. The purity of HAp3 was greater than that of HAp1 and 6 (see Table 4-1). The elevated temperature at which the HAp was synthesised via the hydrothermal method may be accounted for in respect to the high purity obtained. The preparation route for HAp3 and 4, internationally marketed powders are undisclosed.

4.2.2 Crystallinity

The calculated crystallinity for the various HAp powders are outlined in Table 4-1 (refer to Sections 3.8.1 and 3.8.4). All powders, except for HAp1 and 6 have crystallinity's greater than 95%, the minimum requirement as set out by the FDA [137]. HAp4 and HAp5 appear to possess a greater degree of crystallinity than HAp3 since narrower peaks are indicative of a more crystalline HAp (larger crystallite size) whereas broad peaks represent lower levels of crystallinity [2].

The effect of heat treatment on crystallinity can be seen in Figure 4-2 where the sintering of spray dried HAp particles at 1210ºC resulted in a considerable increase in crystallinity. Spray dried HAp possessed a crystallinity of 71.06(±2)%, while sintered HAp attained levels of crystallinity of 92.60(±2)%; an increase of up to 21%. The sintered HAp powder

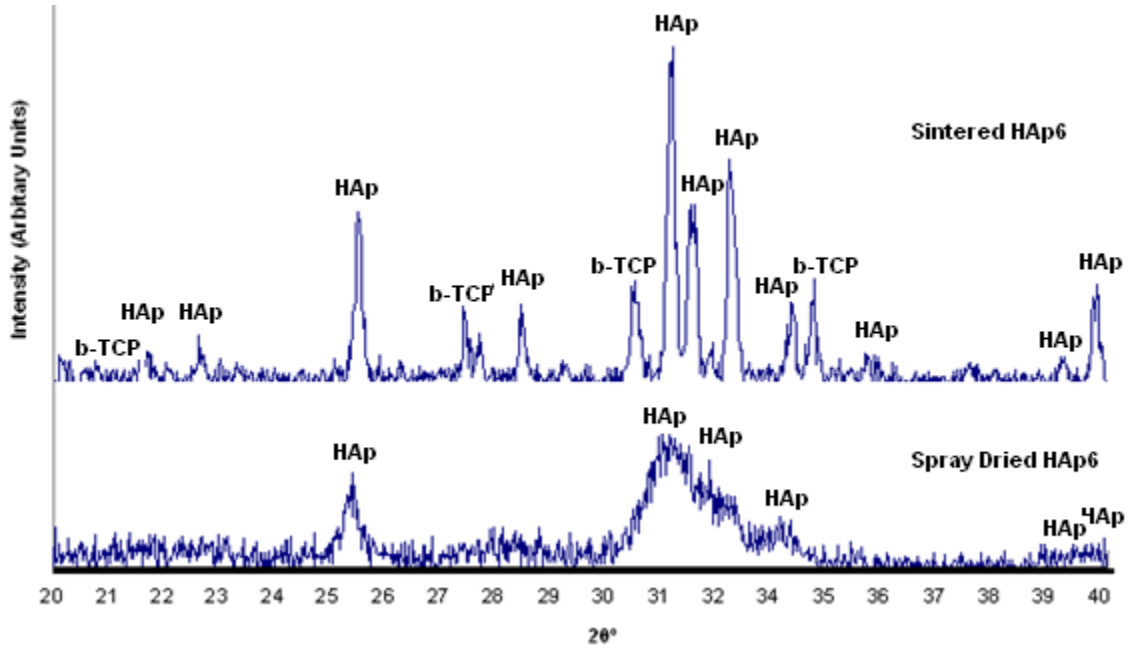

Figure 4-2: HAp6: Spray dried and final sintered HAp xrd patterns

also showed a substantial increase in peak height and an associated drop in peak width, corresponding to its increase in crystallinity. These results illustrate the significance of the sintering stage in increasing crystallinity to that as specified by ASTMF1185-03 and the FDA. Figure 4-3 illustrates the purity as a percentage versus crystallinity as a percentage. Although the purity of HAp6 is lower than the minimum requirement of 95% purity, it has a high level of crystallinity (95.59±2%). The order of crystallinity according to Table 4-1 follows the order: HAp3 > HAp4 > HAp5 > HAp6 > HAp2 > HAp1

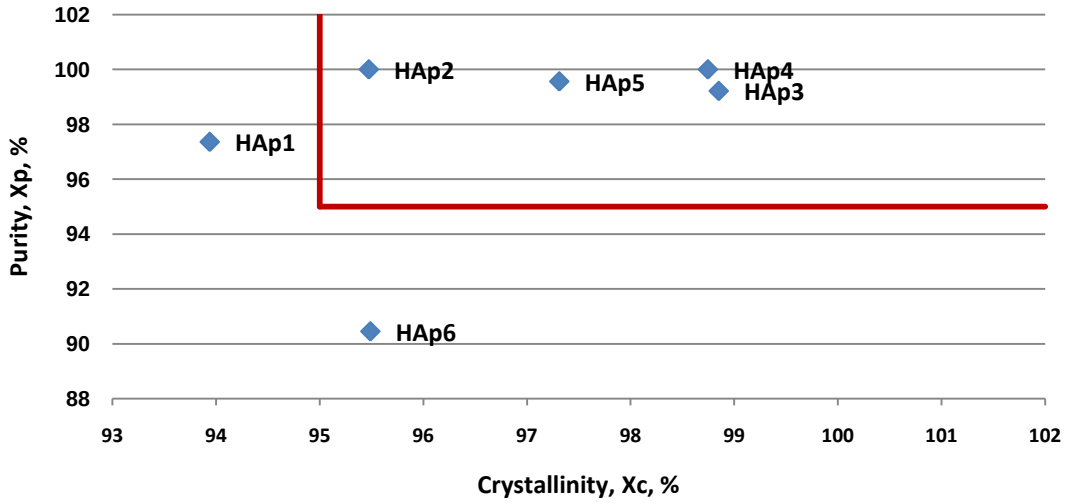

Figure 4-3: Purity versus crystallinity for HAp1 – HAp6

The only powder failing to reach the required level of crystallinity is HAp1. Adversely, HAp6 is the only powder failing to satisfy the minimum requirement of 95% purity, with HAp1 meeting this requirement (97.36±2%). HAp2-5, on the other hand all meet the minimum requirements of 95% purity and crystallinity.

4.2.3 Lattice Parameters And Crystallite Size

The crystallographic characteristics of the HAp, with regards their lattice parameters and crystallite size were analysed and are presented in Table 4-1, which summarises the lattice parameters for the HAp powders analysed in this study (refer to Sections 3.8.5 and 3.8.6). It is well known that changes in lattice parameters indicate a possible deviation from stoichiometry. It is suggested elsewhere that an increase in the lattice parameter *c* with a reduction in lattice parameter *a* indicates either (i) a change in the Ca/P ratio in the HAp; (ii) a change in the Ca/OH ratio in the HAp, or (iii) a substitution of OH groups by CO_3 groups [13]. Cases (i) and (ii) suggest the occurrence of an altered composition on account of precipitation of the impure phases present in the HAp. Case (iii), suggests that the HAp may have reacted with CO_2 in the air, indicative of an uncontrolled atmospheric environment. The highest lattice parameter in the a-axis of HAp6 in comparison to the pure HAp2 and HAp4 confirms the Ca-deficient nature of this powder. Similar results were reported by Aizawa et al. [95], demonstrating that the lattice parameters for Ca-dHAp increases in the *a*-axis direction with decreasing purity, but decrease in the *c*-axis direction. Figure 4-4 illustrates the increase of the a/c ratio increases with decreasing HAp purity.

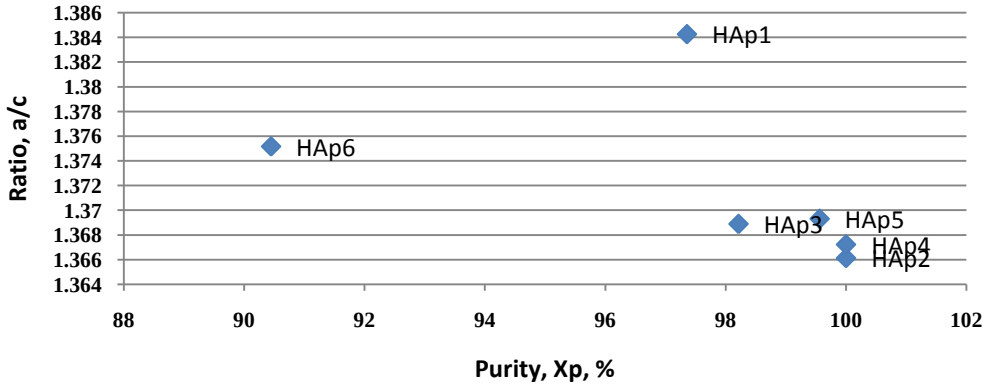

Figure 4-4: a/c ratio against HAp purity for HAp1 – HAp6

Table 4-3 evaluates the deviation from stoichiometric HAp of the HAp powders studied. HAp2 to 5 demonstrate a contraction in the *a*-axis and an expansion in the *c*-axis HAp.

HAp1 demonstrates a contraction of both the *a*- and *c*-axis, while HAp6 demonstrates an expansion in both axes. It has been reported that a decrease in the a-axis coupled with an increase in the c-axis may be attributed to either F or CO_3 substitution for PO_4^{3-}, on account of the atmospheric environment [69]. The increase in the *a*-axis of HAp6 with decreasing purity may be due to incorporation of HPO_4^{2-} into the Ca-dHAp structure.

Table 4-3: Evaluation of deviation from the lattice parameters associated to stoichiometric HAp (a: 9.442nm and c: 6.889nm [64]), + expansion, - contraction

	Lattice Parameter Change	
	a-axis	**c-axis**
HAp1	-	-
HAp2	-	+
HAp3	-	+
HAp4	-	+
HAp5	-	+
HAp6	+	+

Pang and Bao [90] state that the crystallite sizes of as-prepared HAp increase with the increase of the reaction synthesis temperature, the higher the reaction synthesis temperature, the larger the crystallite size of the crystal formed. This theory is also confirmed in studies conducted by Smiciklas et al. [85]. This explains the similar crystallite sizes obtained for the HAp1, HAp2 and HAp6 powders, since all three HAp were prepared at ambient temperature of same synthesis route as opposed to the other HAp with unknown processing parameters. Spray dried HAp with a crystallite size (L_{300}) of ~41nm was found to increase to ~81nm post sintering. Pang and Bao [90] found that the crystallite size values increase for HAp with lower crystallinity and smaller crystallite sizes but decreased for those with high crystallinity and larger crystallite sizes since a large amount of relatively smaller new crystallites are formed during calcinations. This phenomenon has also been shown by other researchers for Ca-dHAp.

4.2.4 HAp Particle Size (PS) And Specific Surface Area (SSA)

There are many advantages to reducing the granule size of HAp powder particles (refer to Section 3.8.8). In general, the smaller the granule size, the higher the specific surface area and the higher the bonding capacity. Powder particle size is larger than its primary crystallite size due to the processing conditions of the precipitate to produce the powder. Particle size is dependent upon reaction synthesis temperature [89], acid addition rate [83], and ripening time [90]. Table 4-4 outlines the average of three results recorded for mode, mean particle sizes and the percentage (10, 50 and 90%) of powder particles within a specific range for the several powders analysed (HAp1 – HAp6) prior to plasma spraying application and also post spray drying (HAp1 and HAp6). Figure 4-5 graphically compares the mean particle sizes obtained for the micron sized HAp powders analysed. The order of mean particle size and specific surface area from the largest is as follows:

Particle Size (μm) = HAp5 → HAp4 → HAp2 → HAp1 → HAp3 → HAp6

SSA (m^2/g) = HAp5 → HAp1 → HAp6 → HAp3 → HAp2 → HAp4

All the HAp powder particles analysed have 90% of their particles <100μm, which is a requirement for successful coating application via thermal plasma spraying onto orthopaedic implants [87, 113]. The difference between the observed and reported values for HAp particle size in literature can be attributed to the different synthesising routes and conditions implemented. The absence of particles with diameters less than their calculated crystallite size suggests that there is no suspended single crystallite of HAp in any of the samples analysed. The results for the particle sizes obtained may be accounted for by:

Synthesis (Reaction) Temperature

The smallest particle size of HAp1, HAp2 and HAp6 can be attributed to the low reaction temperature (T = 20ºC). Similar results reported [22, 89, 94] have indicated that an increase of the synthesis temperature results in a decrease of the SSA of the powder particles and hence, an increase in particle size. It is known, in this study, that HAp5 is produced via the hydrothermal method and subsequently

Table 4-4: Particle size analysis results and specific surface area of HAp1 – HAp6

HA Powder	*Diameter (µm) on:*			*Mean*	*Mode*	*Specific Surface Area*
	10%	*50%*	*90%*	*(µm)*	*(µm)*	*(m^2/g)*
HAp1	5.70	18.86	41.83	21.94	21.26	0.63
HAp2	8.38	23.09	52.13	27.48	52.13	0.02
HAp3	0.83	16.74	36.70	18.28	24.31	1.28
HAp4	12.27	31.59	61.15	36.31	41.43	0.01
HAp5	3.38	36.83	69.22	37.91	48.27	0.53
HAp6	4.33	11.64	24.91	13.39	26.20	1.63
HAp1: Spray Dried HAp Powder						
Chamber Powder	3.36	12.45	27.44	14.33	16.18	-
Cyclone Powder	4.61	10.78	19.31	11.51	10.90	-
HAp6: Spray Dried HAp Powder						
Chamber Powder	1.68	6.55	20.49	9.22	7.72	1.42
Cyclone Powder	2.39	8.10	19.23	9.76	12.21	1.24

synthesised at a high reaction synthesis temperature (≤300ºC). This may be attributed to its larger mean particle size of 37.91µm. The higher the reaction synthesis temperature, the higher the particle size obtained as a result of the increase in temperature, activating its subsequent particle growth.

Reactant Concentration

The large particle size of HAp4 and HAp5 can be attributed to the high reactant concentration. It has been observed that when the reactant concentration is high, the precipitates selectively grow quicker along the c-axis compared to the a-axis resulting in high aspect ratio HAp particles [89].

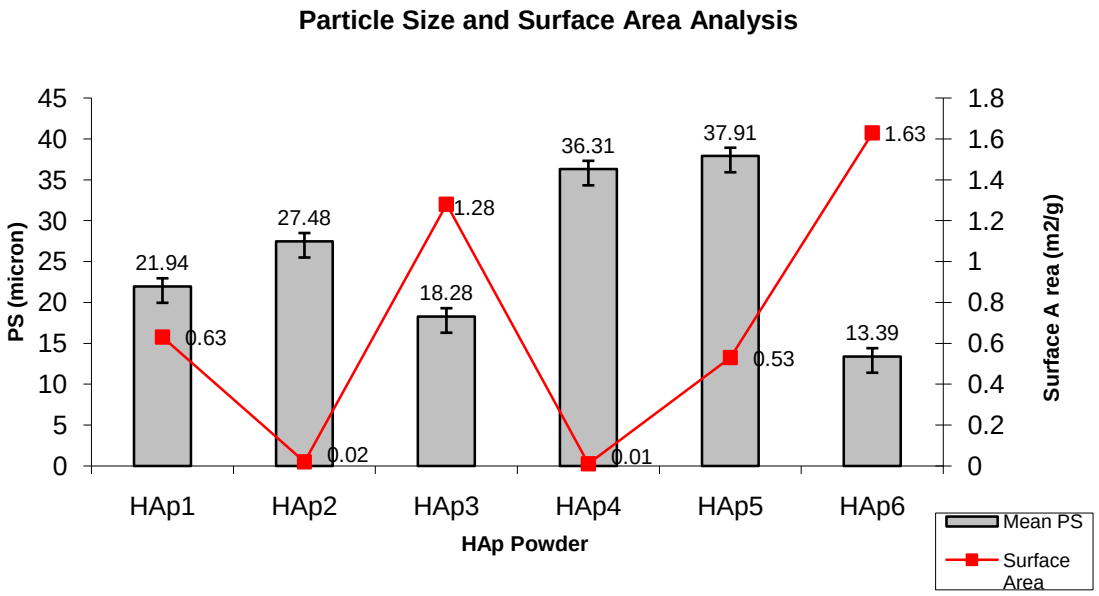

Figure 4-5: Comparison of mean particle size and specific surface area for HAp1 – HAp6

Reactant Addition Rate

The large particle size of HAp4 and HAp5 can be attributed to the low rate of acid. Bouyer et al. [94] show that a low reactant addition rate seems to give an opposite effect on the HAp particle SSA. This is also confirmed by Afshar et al. [83] who state that the particle size of HAp increases as the acid addition rate is lowered.

Sintering Temperature

The sintering temperature is also found to have an impact on the final HAp powder particle size obtained. Sintering carried out on HAp6 at 1200ºC, increased the average particle size from ~9.22μm to ~13.39μm, while HAp1 increased its particle size from between 11 – 14μm up to ~21.94μm. These results are in agreement with Kothappli et al. [89] since both HAp1 and HAp6 are found to possess the highest SSA as opposed to HAp2, HAp4 and HAp5. A high initial SSA (therefore, low particle size) and chemical purity are thought to favour sinterability of HAp [89] and hence the results obtained for HAp6 appear favourable. The Herring law of sintering [89] suggests that the sintering rate at a given temperature is inversely proportional to the square of the powder particle size. Thus, the smaller the agglomerate size, the easier for the powder to achieve high density at the same sintering temperature. Due to a large SSA, small precipitates are more likely to form large agglomerates so as to minimize their surface energy [89]. This is also in agreement with Gibson et al. [187] who also reported that smaller particles appeared to form into large agglomerates with rough surfaces, which is indicative of high surface areas.

4.2.5 Particle Size Distribution (PSD)

A graphical comparison of the particle size distributions attained for HAp powders (HAp1 – HAp6) analysed in this study is shown in Figure 4-6 (refer to Section 3.8.8). A comparison of the PSD for HAp3, HAp4 and HAp5 is illustrated in Figure 4-7(a). Both HAp4 and HAp5 demonstrate a unimodal distribution, while HAp3 demonstrates a bimodal distribution. This can be explained by the agglomeration of this powder on account of its extremely fine particle size [89].

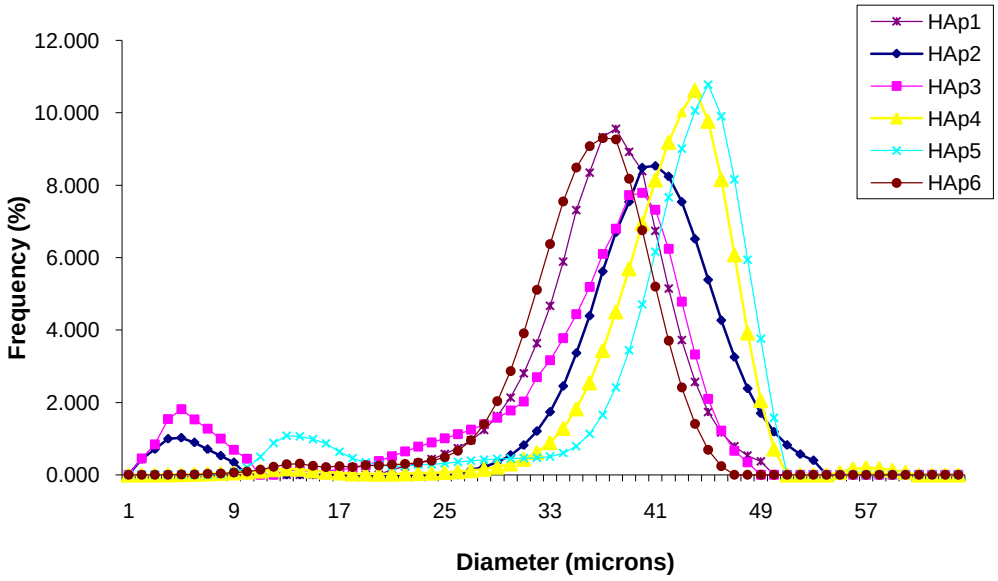

Figure 4-6: Comparison of particle size distributions obtained for HAp1 – HAp6

A comparison of the PSD for HAp1, HAp2 and HAp6 is illustrated in Figure 4-7(b). Again, HAp1 and HAp2 exhibit a unimodal distribution, while HAp6 exhibits a bimodal distribution. This result obtained for HAp6 correlates well with the result of HAp3 as established above, where the low particle sizes of both these HAp are attributable to the significance of their bimodal PSD.

(A)

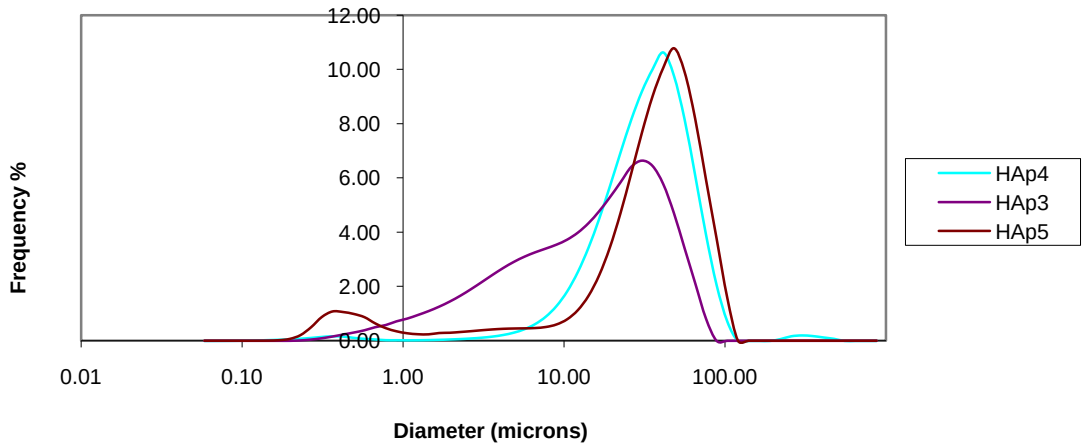

(B)

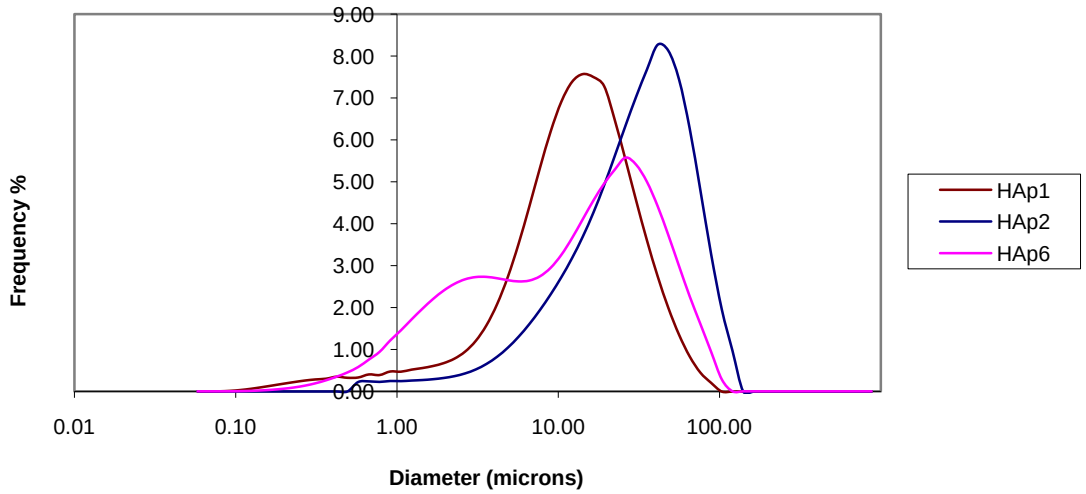

Figure 4-7: Comparison of PSD for HAp3, 4 and 5 (A) and comparison of PSD for HAp1, 2 and 6 (B)

Figure 4-8 illustrates the effect of sintering on PSD for both chamber and cyclone spray dried HAp powder particles. The cyclone spray dried HAp6 powder presents a unimodal distribution before and after sintering, while the chamber spray dried HAp6 powder attains a bimodal distribution post sintering. Prior to sintering, the cyclone spray dried

HAp6 powder possessed a mean particle size of 9.76µm while its chamber spray dried powder had a mean particle size of 9.22µm. The finer particle size of the chamber spray dried HAp signifies that agglomeration of its fines resulted (accounted for by its bimodal distribution).

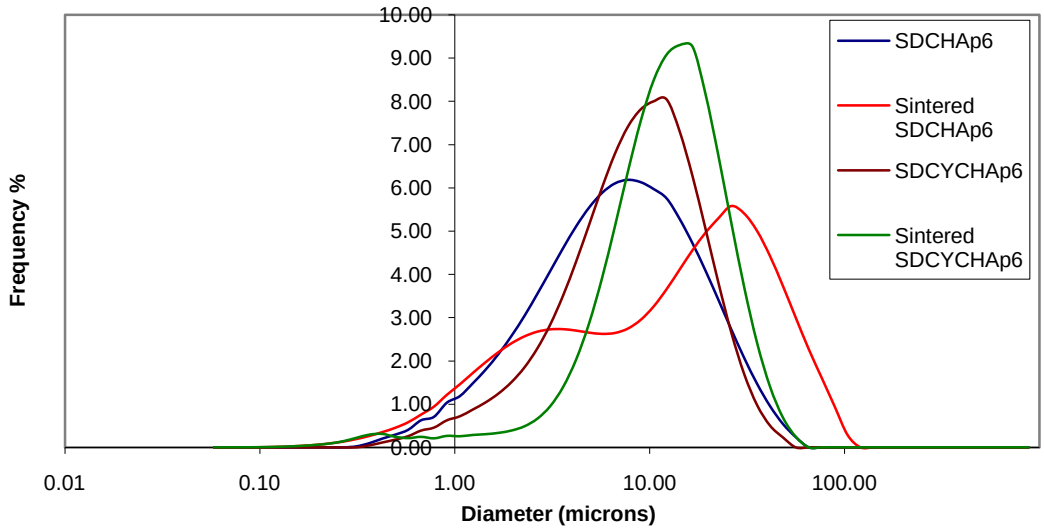

Figure 4-8: Effect of sintering on particle size distribution for spray dried chamber HAp6 (SDCHHAp6) and the spray dried cyclone HAp6 (SDCYCHAp6) powders

Figures 4-9 and 4-10 show the PSD distribution of the six HAp powders (HAp1 – HAp6) analysed along with their cumulative frequency curves in accordance to ISO 9276 – 1 [188].

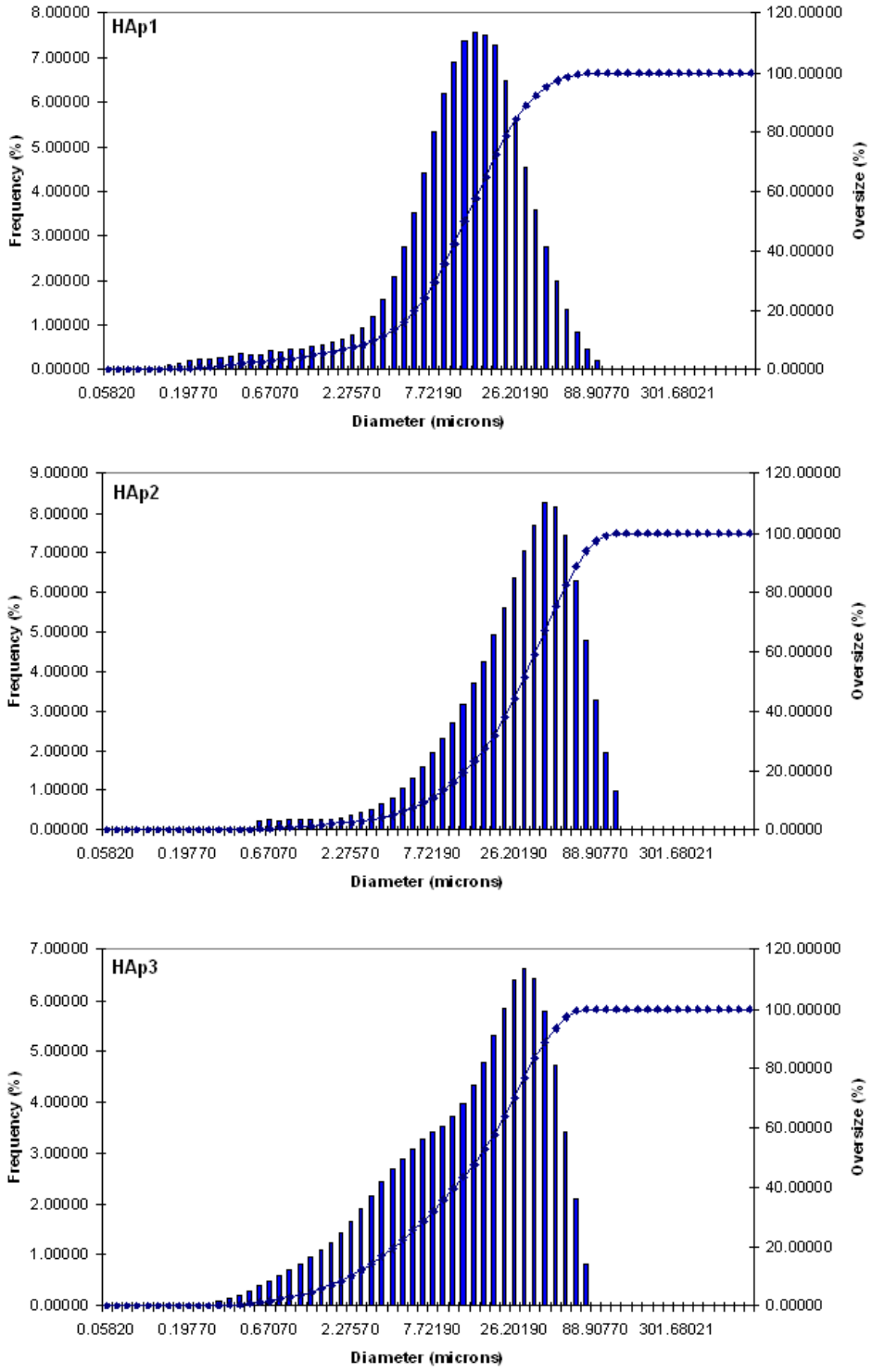

Figure 4-9: Particle size distribution graphs: histogram and cumulative distribution for HAp1 - 3

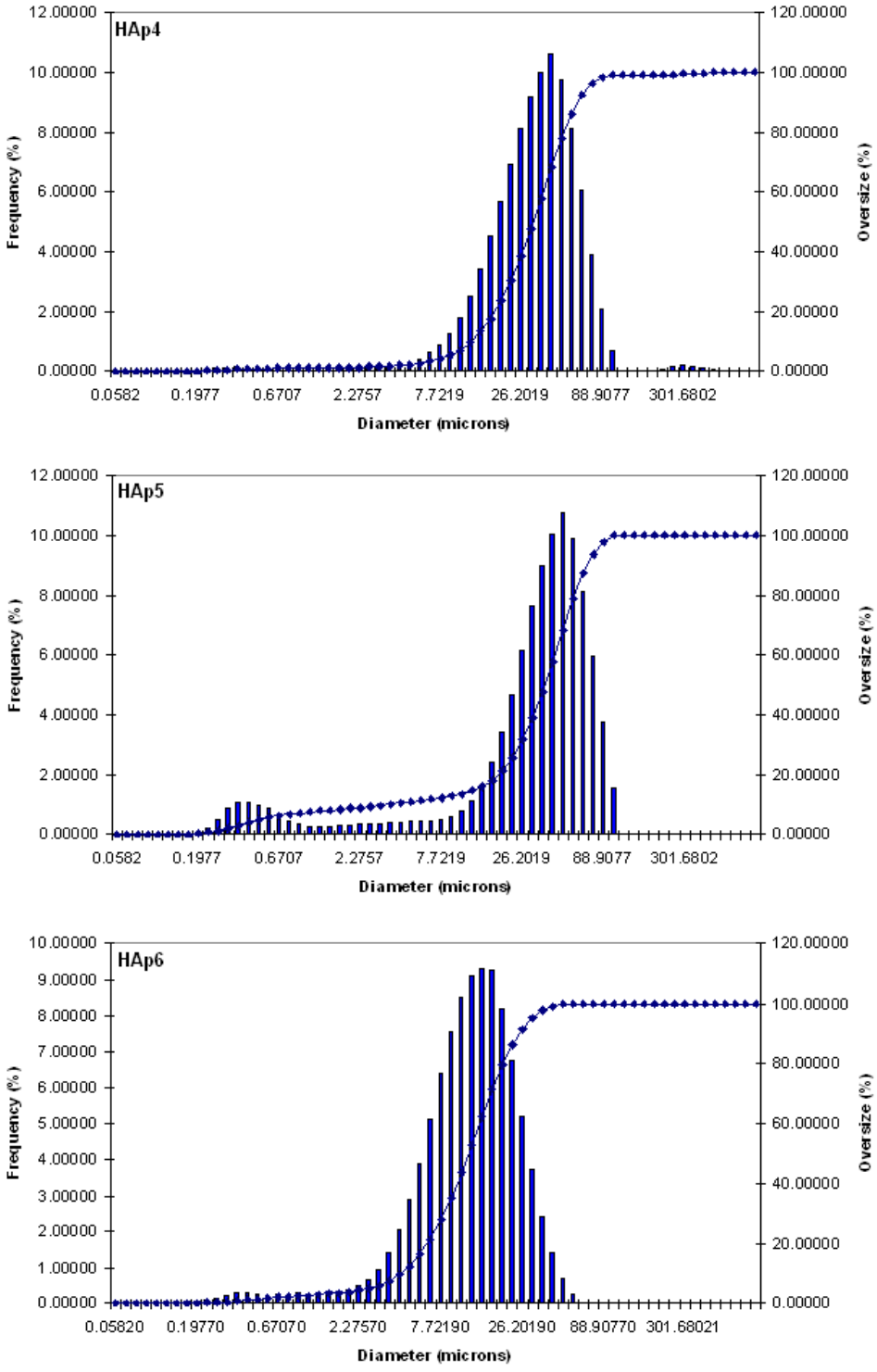

Figure 4-10: Particle size distribution graphs: histogram and cumulative distribution for HAp4 - 6

4.2.6 HAp Powder Density

Highly dense HAp powders are desirable to prevent the preparation of human fluid into the interfacial area between the HAp coating and Ti-alloys in the hip joint replacement [189]. The theoretical value for dense HAp is calculated as 3.16g/cc (see section 3.8.10). FDA [137] regulations, however, require a minimum density of 3.05g/cc for HAp powders for coating application onto orthopaedic implants. Therefore, all the HAp powders analysed in this study are within these required specifications.

All the HAp powders (see Table 4-5), appear to exceed the theoretical value for HAp density, with the exception of HAp1 and HAp. HAp3 and HAp6 exhibit highly dense sintered powders. This may be accounted for by their finer particle size.

Table 4-5: Comparison of HA powder density measurements using helium pycnometry

HAp Powder	***Pycnometric Density (g/cm^3)***
HAp1	3.08
HAp2	3.11
HAp3	3.47
HAp4	3.20
HAp5	3.28
HAp6	3.33

Figure 4-11 illustrates the comparison of HAp density obtained for all HAp powders analysed. The low density values observed for HAp1 and HAp2 correspond well with the argument set above, since the particle sizes for these powders are 21.94μm and 27.48μm, respectively. HAp3 and HAp6, alternatively, demonstrate a higher sintered density with particle sizes of 18.28μm and 13.39μm, respectively.

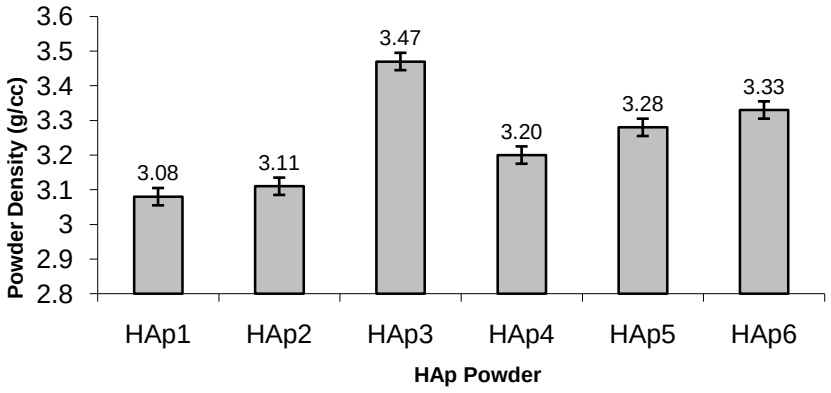

Figure 4-11: Comparison of powder density for HAp1 – HAp6

The green density (pre-sintered) for HAp is compared against sintered density in Table 4-6 for HAp6 (that is, in-house HAp) and may also be viewed graphically in Figure 4-12. Sung et al. [114] suggests that HAp consisting of finer particle size have a much higher SSA, which is the driving force for solid state sintering and the amount of surface energy decrease is proportional to the free energy decrease for the sintering reaction. The chamber spray dried powder studied in HAp6 exhibits a higher increase in density than the cyclone spray dried powders post sintered. The green density of the spray dried HAp can be increased with increased solids concentration of the feed slurry. However, sintering behaviour can be controlled by varying the particle size, which may be realised by altering the reaction process parameters.

Table 4-6: Effect of sintering treatment on the resulting HAp6 powder density

Post Spray Dry Chamber HAp6 *(g/cm^3)*	**Post Sintering Cyclone HAp6 *(g/cm^3)***
2.91	3.47
3.23	3.33

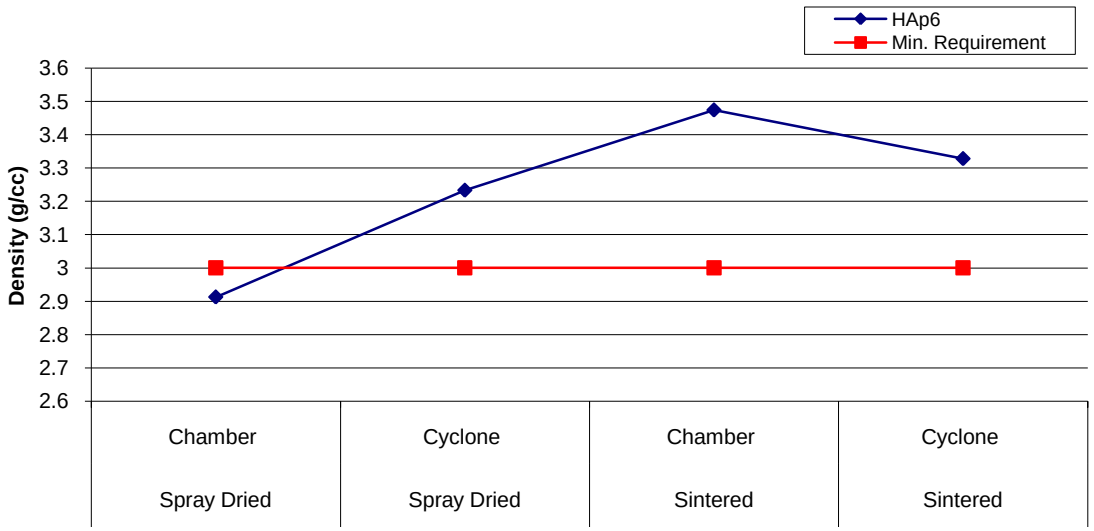

Figure 4-12: Effect of heat treatment (1200ºC) on the resulting density obtained for HAp6

4.2.7 HAp Powder Morphology

It is known that spherical powders, in general, have better rheological properties than irregular powders and, thus, produce better coatings for hip implants [2]. In order to produce dense, high-quality materials for special-purpose, it is very important to predict or control granule morphology (refer to Section 3.8.7) [110].

Table 4-7 and Figure 4-13 compare the morphological properties for each of the six HAp analysed. HAp4 is found to possess the most ideal spherical and regular shaped particles indicative of enhanced rheological properties. HAp3 also appears to posses this attribute, although its surface morphology appears less smooth and regular in comparison to HAp4. This may also be attributed to the fact that the powders may have been synthesised at a higher reaction synthesis temperatures, endured longer maturation/ripening times, lower initial calcium concentrations and idealised spray drying condition (if implemented).

Table 4-7: Comparison of HAp morphology in terms of regularity and smoothness (- indicates highly irregular/smooth, + indicating regular/smooth, ++ indicating increased regularity/smoothness and +++ indicating highly desirable levels of regularity/smoothness)

HAp Sample	*Purity (%)*	*Regularity*	*Smoothness*
HAp1	97.36(±2)	+	+
HAp2	100.00(±2)	++	+
HAp3	98.21(±2)	++	++
HAp4	100.00(±2)	+++	+++
HAp5	99.56(±2)	-	++
HAp6	90.44(±2)	+	+

(A) HAp1

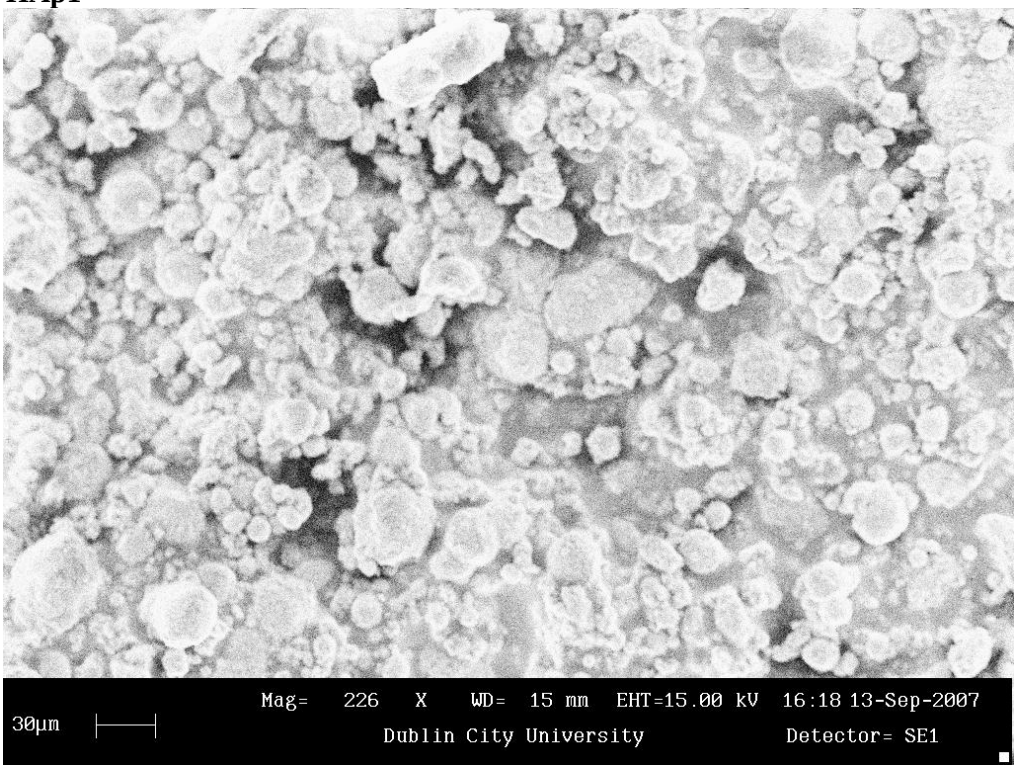
Mag= 226 X WD= 15 mm EHT=15.00 kV 16:18 13-Sep-2007
30µm
Dublin City University
Detector= SE1

HAp2

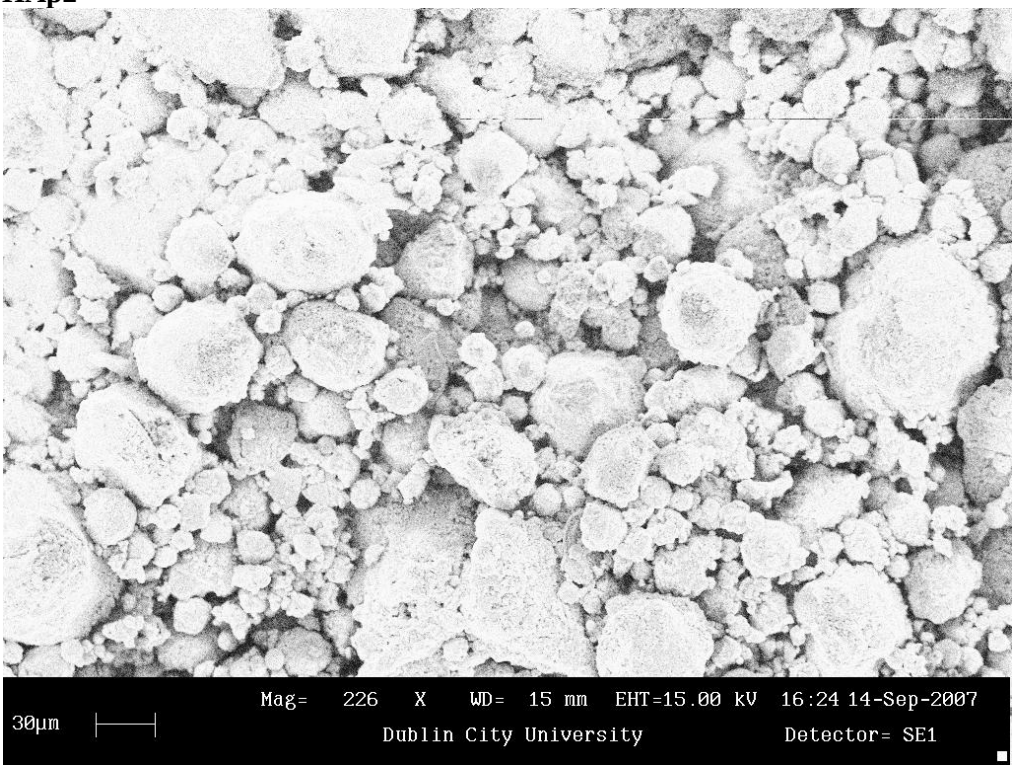
Mag= 226 X WD= 15 mm EHT=15.00 kV 16:24 14-Sep-2007
30µm
Dublin City University
Detector= SE1

(B) HAp3

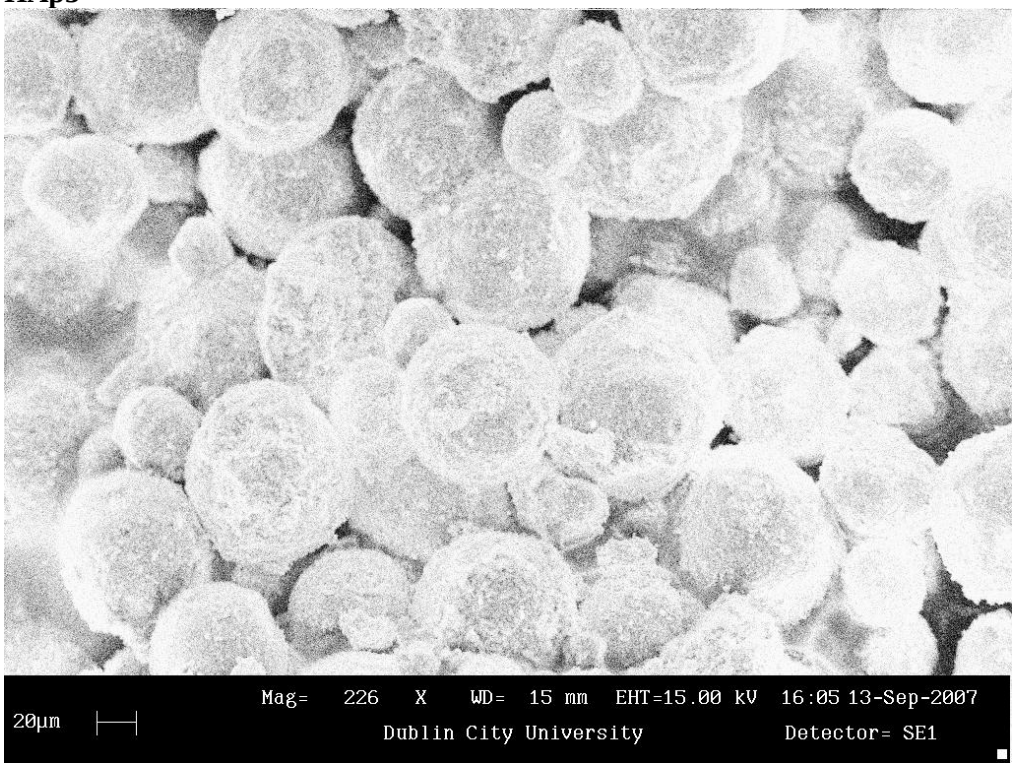
Mag= 226 X WD= 15 mm EHT=15.00 kV 16:05 13-Sep-2007
20µm
Dublin City University
Detector= SE1

HAp4

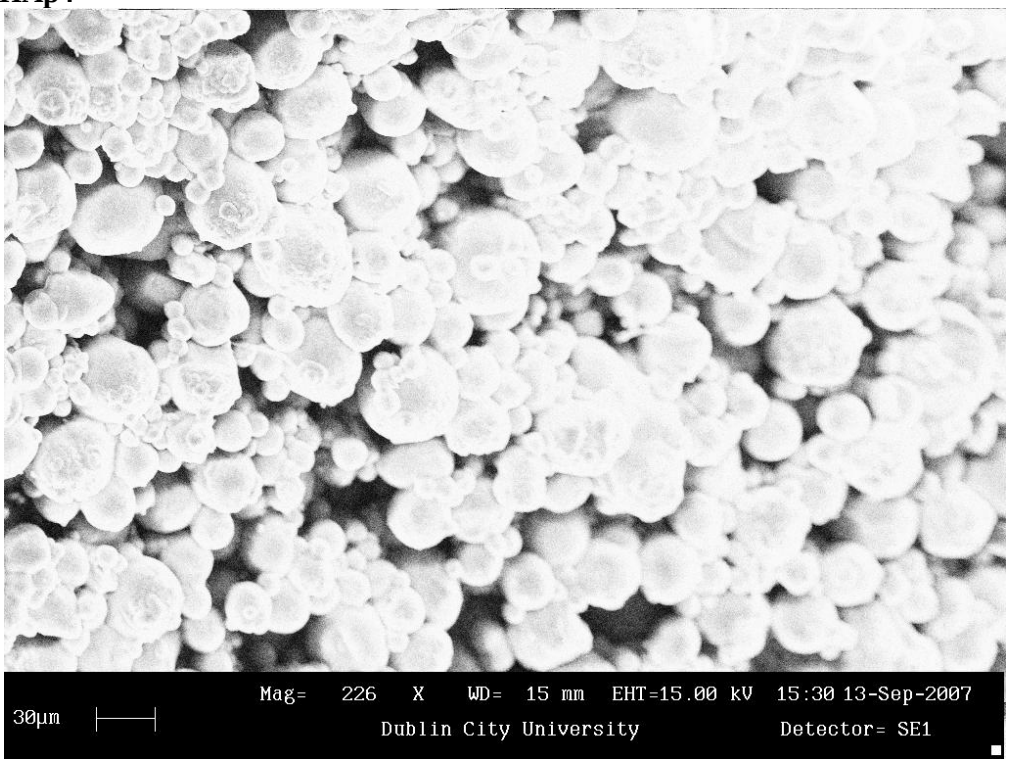
Mag= 226 X WD= 15 mm EHT=15.00 kV 15:30 13-Sep-2007
30µm
Dublin City University
Detector= SE1

(C) HAp5

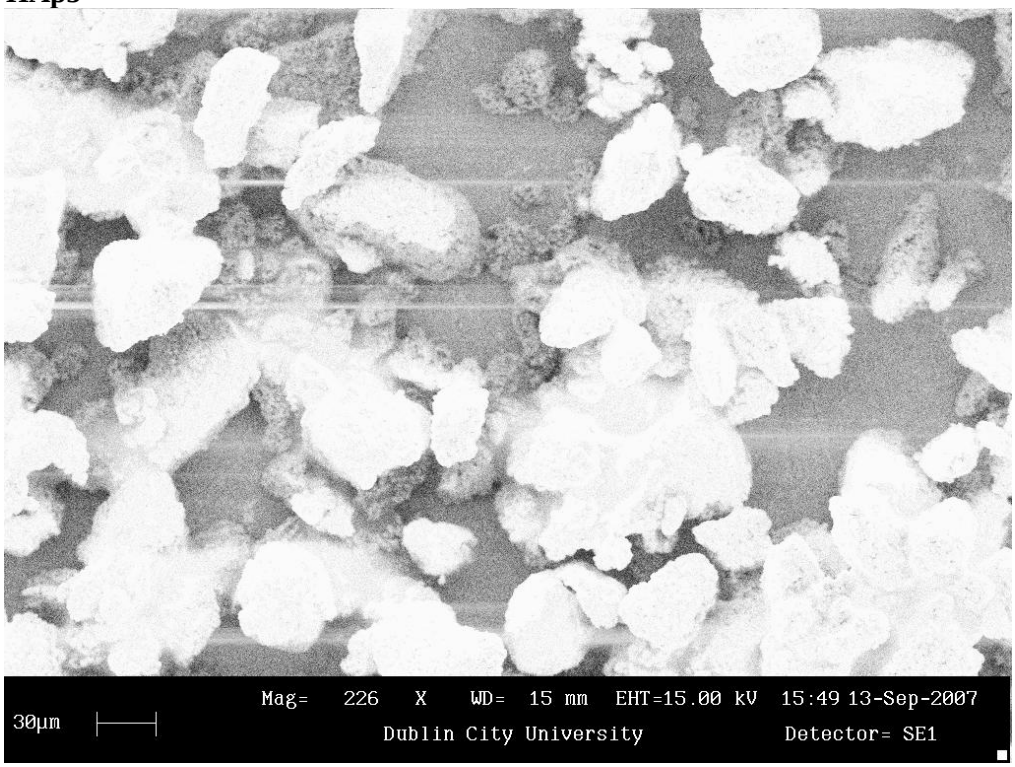

HAp6

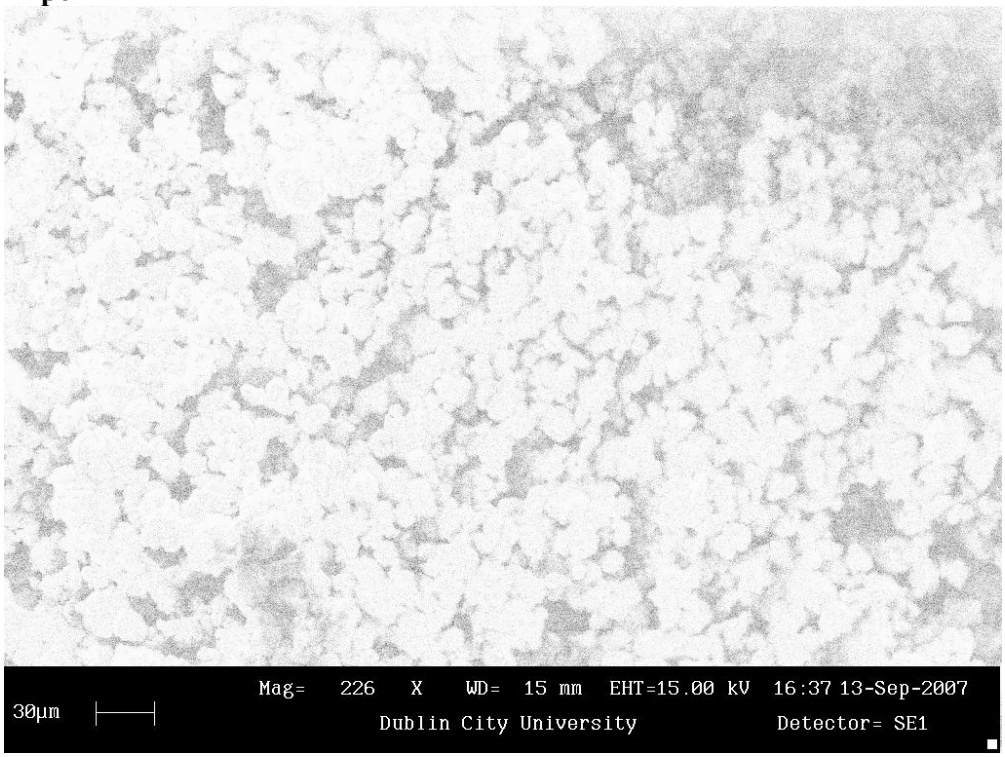

Figure 4-13: SEM micrographs of HAp1 – HAp2 (A), HAp3 – HAp4 (B) and HAp5 – HAp6 (C)

Post heat-treatments (such as, flame spheroidisation) may also have been implemented in order to enhance its spherical nature. HAp5 appears the most irregular in shape. This may be explained by the hydrothermal route in which the powders were prepared, since it is well known that this synthesis method produces needle shaped particles [23]. HAp1 and HAp6 have similar morphology, with regular shape agglomerated particles, but with a lower surface smoothness than that of HAp3 and HAp4. An increase in the synthesis temperature, ripening time and decrease in calcium concentration may thus be required in order to increase the surface smoothness. The effect of sintering on the powder morphology for HAp1 and HAp6 is demonstrated in Figures 4-14 and 4-15, respectively. This processing step has a significant effect on altering the final morphology of the powders prior to spray drying.

Kothapalli et al. [89] also demonstrate that an increase in synthesis temperature increases the size of HAp precipitates. At a high reaction synthesis temperature, the rate of particle ripening was high and the precipitates grew large during the allotted time. For irregular shaped (rod-like) particles, the length and the breadth of the HAp particles are found to increase with the temperature, while the aspect ratio is also found to increase. The key factors to controlling the HAp aspect ratio are (i) reaction synthesis temperature, (ii) pH and (iii) initial reactant concentrations. A low synthesis temperature, is found to result in needle-shaped particles [94]. Increasing the synthesis temperature changes the particles from a needle-shaped morphology to a more regular shaped with a lower aspect ratio, closer to 1 (ideal).

The key factors controlling the morphology of the powders can vary with:

Spray Drying Conditions

Spray drying process conditions, such as droplet size, initial solid concentration, viscosity of liquid and drying temperature can have an impact upon the end morphology of the spray dried powder. Luo et al. [108] controlled the morphology of HAp powders, with spray drying as the controlling step to produce solid spheres by varying the atomization pressure and the concentration of the feed slurry.

Reaction Synthesis Temperature

It is known that the precipitation reaction temperature is found to induce an enhanced spherical morphology [87 - 90] for wet chemical precipitation reactions involving raw chemicals such as, $Ca(OH)_2$ and H_3PO_4. It has been shown that needle-shaped particles are likely to form at low reaction temperatures attaining a high aspect ratio, which changes to spheroidal when the precipitation temperature is increased to temperatures reaching 100 °C [88, 94]. Kumar et al. [88] accounted the change in the morphology by

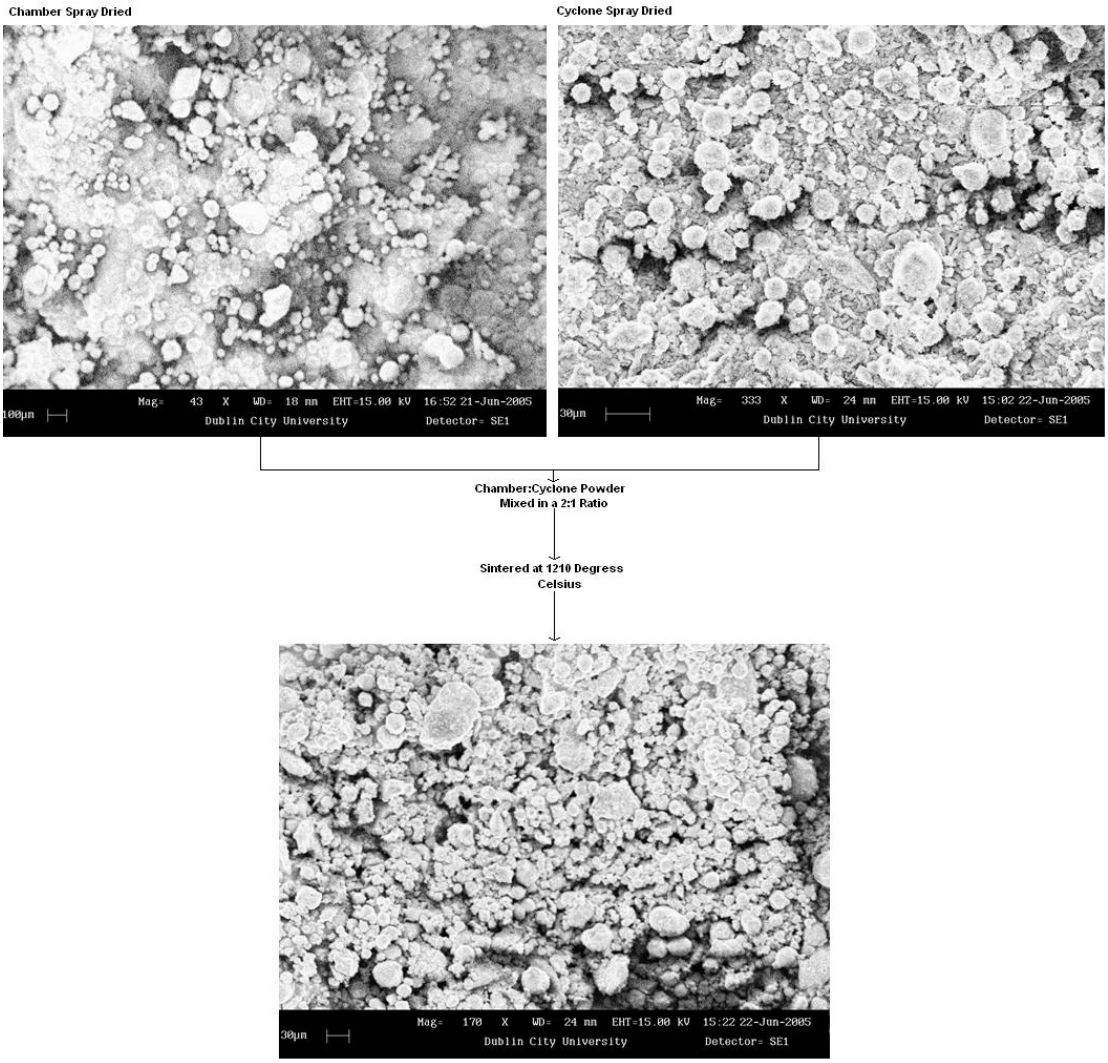

Figure 4-14: Effect of heat treatment on HAp1 powder morphology

the reaction temperature as the driving force for the HAp precipitation and the supersaturation level of Ca^{2+} and PO_4^{3-} ions with respect to HAp. The analysis indicated that the supersaturation level of the reactants, especially the concentration of Ca^{2+} ions, played a predominant role on the precipitate morphology for this classical acid-base reaction. Pang et al. [90] also suggests that an increase of reaction temperature produce more regular shapes particles and clearer contours with less aggregation.

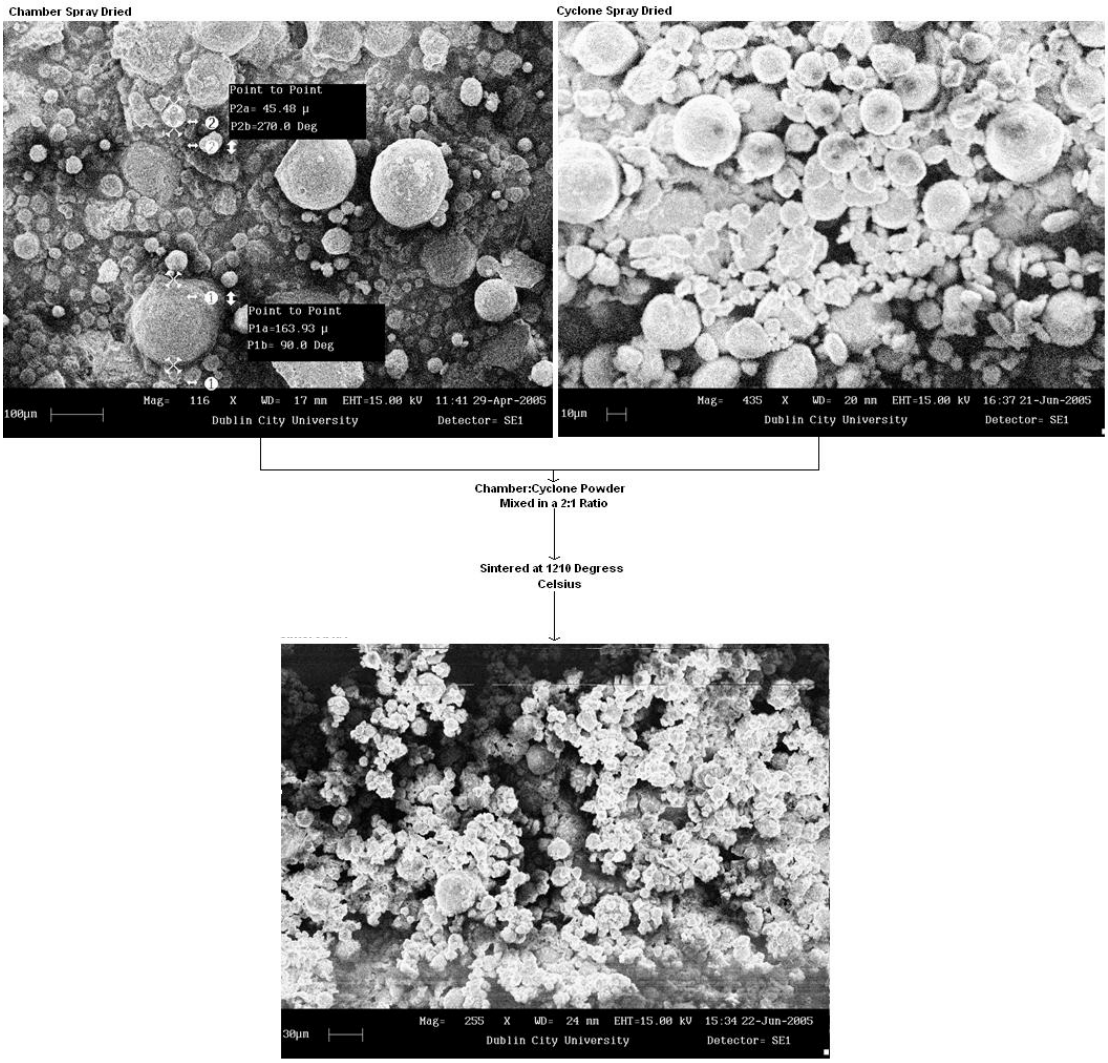

Figure 4-15: Effect of heat treatment on HAp6 powder morphology

Ripening Time

Ripening time (maturation phase of HAp during chemical precipitation) is another factor controlling the morphology of HAp particles synthesised. Pang et al. [90] observed that increased ripening times have an effect on HAp morphology enhancing a more regular and smooth-like appearance. This is explained by the mechanism of crystal growth in solution. Chemical precipitation often experiences high-reaction induced supersaturation leading to high nucleation rates. In this case, a crystal nucleus possesses a rough surface due to the rapid production of insoluble materials. This rough surface favours conditions for crystal growth as the molecules adding on it has greater sticking probability. However, as the crystal continues to grow, it attains a smoother surface resulting in the slow down of crystal growth.

Reactant Concentration

The reactant concentration has also been proven to affect the morphological properties for HAp powder particles. Kothapalli et al. [89] observed that high reactant concentrations resulted in particles with higher aspect ratios. The purity of the powders is also thought to control the morphological properties of HAp.

4.2.8 HAp Powder Flowability

The flowability of the HAp powders was determined according to ASTMB213-03 [183] and can be seen in Figure 4-16 (refer to Sections 3.8.11). There exists a direct correlation between the particle size and the resulting powder flowability. For large powder particles (HAp3, HAp4 and HAp5) the flow rate of the powders ranges between 0.17 to 0.20g/s, whereas the finer powder particles (HAp1, HAp3 and HAp6) demonstrate a flow rate ranging between 0.12 to 0.15g/s. All powder flows were observed to flow in a discontinuous flow (that is, a pulsating manner), the degree of which was dependent on the morphology of the tested powder. These results show a good correlation between those published in previous work undertaken by Kweh et al. [2] where the effect of spray drying was examined with respect to powder flowability. The poor flowability of HAp3 may be attributed bimodal particle size distribution as its mean particle size and morphology appear to favour an enhanced flowability.

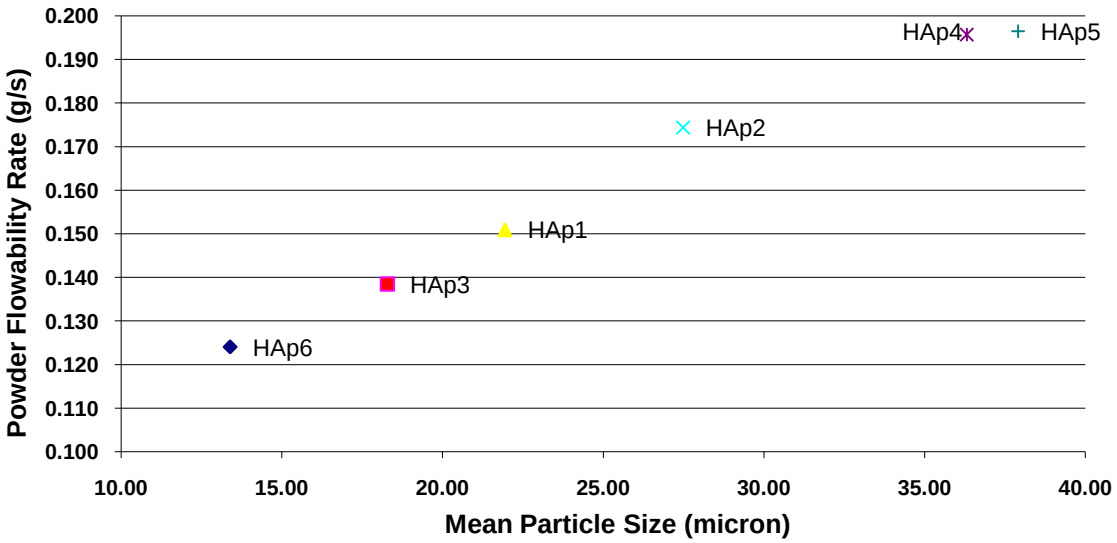

Figure 4-16: Powder flowability measurements recorded using the Hall flowmeter device

4.3 HAp SLURRY RHEOLOGICAL PROPERTIES

In addition to the HAp synthesis reaction conditions, the final quality of the HAp powder is also influenced by the spray drying conditions. However, the rheological properties of the HAp slurry pre spray drying is also found to have an effect on the final spray dried powder properties yielded. In order to ensure, an optimum viscosity is achieved prior to the spray drying stage, the evolution of the suspensions rheology during HAp synthesis was studied. Rheology measurements are a useful tool in following the course of a chemical reaction. The results obtained in this study are presented in Table 4-8 and Figure 4-17, respectively. A marked increase of the HAp1 slurry viscosity throughout the stages of its synthesis is observed during the course of the Irish industry's chemical precipitation reaction method. The dynamic viscosity was found to increase from around 16 – 18 mPa.s, during calcium hydroxide formation to 38 mPa.s after a 24h maturation phase. Similar results were reported by Tian et al. [97] who demonstrated how viscosity is a function of particle size.

Table 4-8: Rheological properties obtained for HAp1 during chemical precipitation

	CaO & H_2O Mix	**H_3PO_4 Addition**	**24h Maturation**
Density (kg/m^3)	1075.59	1107.60	1118.95
Viscosity (mPa.s)	16 - 18	24 - 29	26 - 38
Temperature (^oC)	31 - 33	44 - 47	31 - 32
pH	12 - 12.6	12.5 - 11.3	11.3 – 11.4

The pH and the synthesis temperature of the chemical reaction were also observed at three stages; stage 1: calcium hydroxide formation; stage 2: orthophosphoric acid addition and stage 3: post 24 maturation of acid addition. As expected, the initial pH of the HAp1 slurry at stage 1 was found to stabilise between 12 – 12.6, decreasing to between 12.6 – 11.2 with subsequent additions of acid and finally stabilised at pH 11 for stage 3. While the synthesis temperature was uncontrolled, the temperature of the HAp1

slurry was found to alter during the course of the chemical reaction, varying between 31 - 33ºC, with a slight increase resulting from acid additions by up to 14ºC. Figure 4-17 presents a graphical illustration of the rheological results, suggesting a linear relationship between the dynamic viscosity of the HAp1 slurry was achieved through the three stages of the synthesis route.

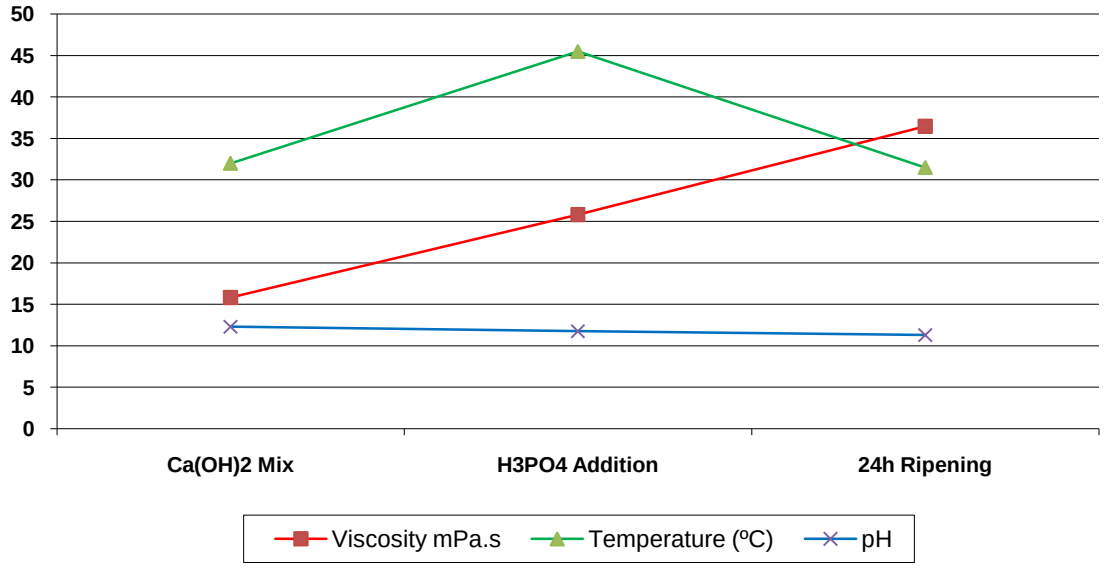

Figure 4-17: Graphical results of rheology (viscosity, temperature & pH) for HAp1

Appendix D illustrates the flow curves of the HAp slurry throughout the stages of HAp1 synthesis, using the chemical precipitation technique. The flow curves describe the variability of viscosity with solids concentration and particle size distribution. This comportment has already been described by Chow et al. [35]. Time-dependent behaviour was exhibited for all HAp1 slurry analyses during HAp synthesis. During calcium hydroxide formation dilatent behaviour of the HAp slurry was most evident, while additions of orthophsophoric acid exhibited a thixotropic behaviour.

4.3.1 HAp Slurry Density

In order to calculate the kinematic viscosity of the HAp slurry, and compare against desirable levels, as reported elsewhere by Luo et al. [82, 108]; the HAp slurry density was measured during the wet chemical synthesis of HAp1 and HAp6 (see Table 4-8 and Figure 4-18). The results indicate the increase of density during the preparation of HAp.

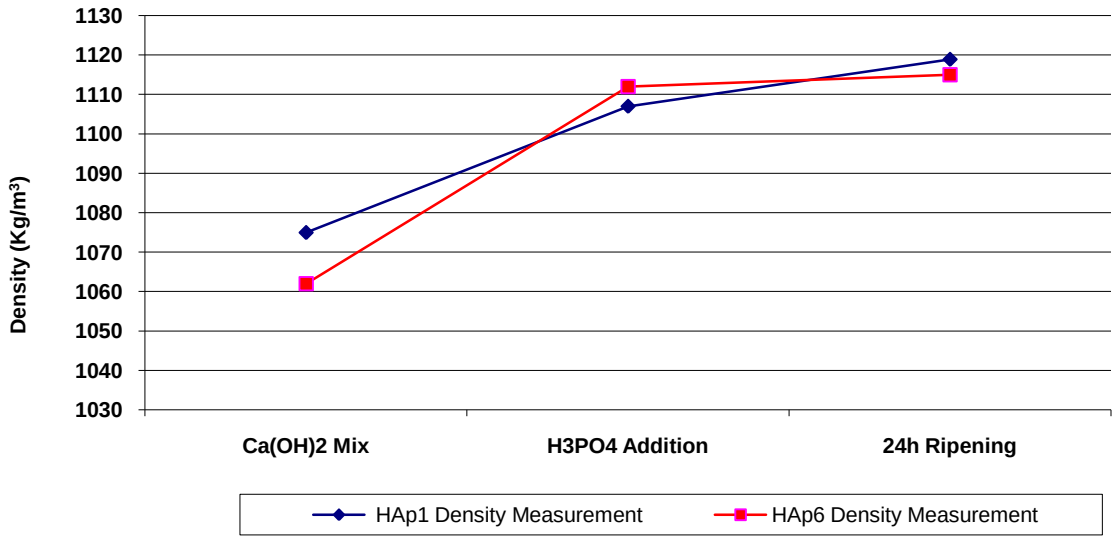

Figure 4-18: Comparison of slurry density for HAp1 and HAp6

The density obtained at the initial stage (that is, stage 1), where calcium hydroxide is produced, varies at 1.06 g/cc for HAp6 slurry and 1.08 g/cc for HAp1 slurry (the initial density of the CaO is 1.99g/cc while that of DI water is 1.00g/cc). Thus, the density for this first stage of HAp synthesis is similar to that of pure DI water, while additions of the acid and subsequent stages of the maturation stage of HAp resulted in a slight increase of density for both HAp slurries to 1.14 g/cc and 1.16 g/cc for HAp6 and HAp1 slurries, respectively (the initial density of H_3PO_4 (85% purity) between 25 ºC to 40ºC, ranges between 1.69 g/cc to 1.69 g/cc, respectively). This behaviour is due to the increase of the powder particle size. Previous research has demonstrated that the density of the HAp slurry significantly impacts upon the final HAp powder particle size obtained.

4.3.2 HAp Slurry Rheology

The kinematic viscosities (that is, the ratio of dynamic viscosity to density) of HAp1 and HAp6 are calculated and compared against the range of kinematic viscosities, proposed in work carried out by Luo et al. [108] to aid in producing highly dense HAp powder particles of a controlled (spherical) morphology, in the desired micron range for plasma spray onto orthopaedic implants (see Table 4-9 and Figure 4-19).

Table 4-9: Kinematic viscosity calculations for HAp1 and HAp6

		HAp1 slurry	HAp6 slurry
Density (g/cc)	CaO & H_2O Mix	1.08	1.06
	H_3PO_4 Addition	1.11	1.09
	24h Maturation	1.12	1.11
	Pre-Spray Dry Mix	1.16	1.14
Dynamic Viscosity (mPa.s)	CaO & H_2O Mix	16	16
	H_3PO_4 Addition	26	26
	24h Maturation	36	34
	Pre-Spray Dry Mix	75	57
Kinematic Viscosity (cst)	CaO & H_2O Mix	14.65	14.87
	H_3PO_4 Addition	23.26	23.36
	24h Maturation	32.56	30.21
	Pre-Spray Dry Mix	64.66	49.91

The results indicate that both HAp1 and HAp6 slurries are within the optimum range after the maturation phase of 24h. However, further mixing of the HAp slurry prior to spray drying was found to significantly increase the kinematic viscosity of both HAp1

and HAp6. An unexpected high kinematic viscosity of the HAp1 pre – spray dry slurry mixture was observed at ~75cst and outside the range recommended by Luo et al. [108]. This may be attributed to the fact that the HAp1 slurry was not spray dried immediately post 24h maturation, but instead allowed to continue its chemical reaction under agitation.

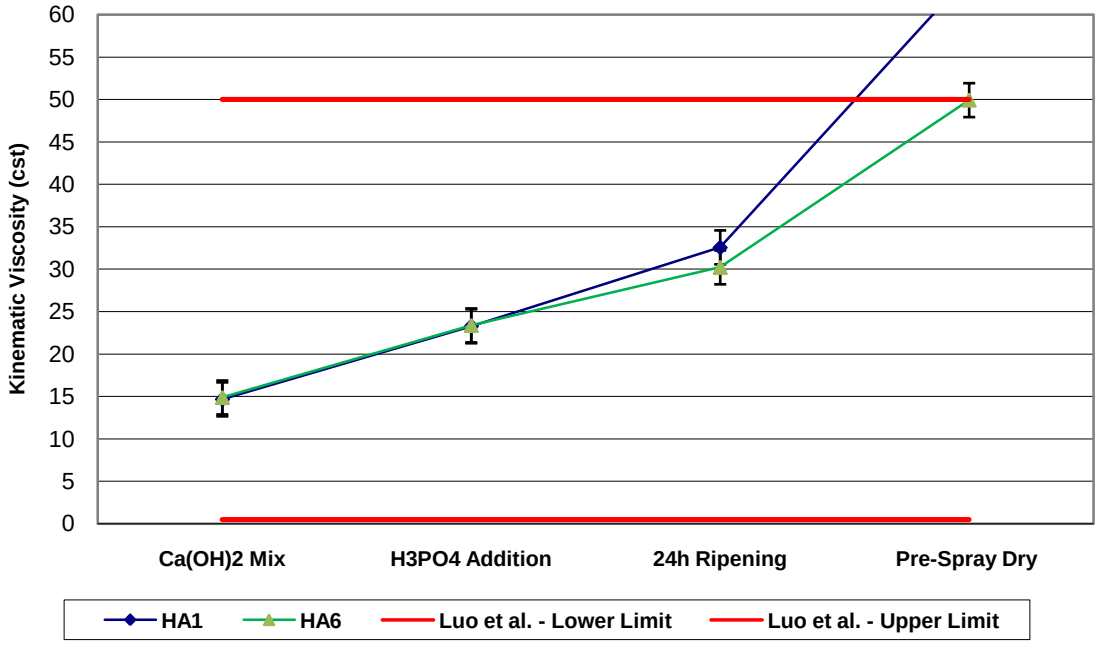

Figure 4-19: Kinematic viscosities for HAp1 and HAp6

Figure 4-19 highlights the requirement to control the kinematic viscosity of the HAp slurry (0.5 – 50cst) prior to spray drying in order to ensure that highly dense HAp of a spherical morphology is produced [108]. This is achieved through additions of distilled water to the HAp slurry mixture before the spray drying process [109].

4.3.3 Summary

A summary of the findings for this study are outlined in the list below and demonstrates how each powder characteristic varies for each case of response investigated. This can be attributed to the variance in the powder synthesis route used in obtaining each of the powders. While the routes used to synthesise HAp3 and HAp4 are unknown, it is known that the hydrothermal route was used to produce the commercial powder HAp5, while the chemical precipitation technique was used in producing the remaining HAp powders (HAp1, HAp2 and HAp6).

(A)	**Phase Purity**	HAp2 =	HAp4 >	HAp5 >	HAp3 >	HAp1 >	HAp6
(B)	**Crystallinity**	HAp3 >	HAp4 >	HAp5 >	HAp6 >	HAp2 >	HAp1
(C)	**a/c ratio**	HAp1 >	HAp6 >	HAp5 ~	HAp3 >	HAp4 >	HAp2
(D)	**Mean Particle Size**	HAp5 >	HAp4 >	HAp2 >	HAp1 >	HAp3 >	HAp6
(E)	**Particle Surface Area**	HAp5 >	HAp1 >	HAp6 >	HAp3 >	HAp2 >	HAp4
(F)	**Powder Density**	HAp3 >	HAp6 >	HAp5 >	HAp4 >	HAp2 >	HAp1
(G)	**Powder Morphology**						
	(Regularity)	HAp3 =	HAp4 >	HAp2 >	HAp1 =	HAp6 >	HAp5
	(Smoothness)	HAp3 =	HAp4 >	HAp5 >	HAp1 =	HAp6 =	HAp2
(H)	**Powder Flowrate**	HAp5 =	HAp4 >	HAp2 >	HAp1 >	HAp3 >	HAp6

However, comparing the powders of the same synthesis route (HAp1, HAp2 and HAp6) also shows a significant variance between the responses obtained and for this reason, the variance of the process parameters can have an effect on altering the final powder characteristics. To ensure that HAp possessing all of the optimum responses required (phase purity and crystallinity, both >95%, particle size <100µm, ↑density, ↑powder flowrate, ↑surface smoothness, where ↑ denotes that a high results is desired) are obtained, it is critical to control the process parameters which have an effect on one or more of each of these responses and hence the requirement for an optimisation study, which is investigated in the following sections.

4.4 SCREENING OF CHEMICAL PRECIPITATION PROCESS PARAMETERS

In this section, the experimental design used, the range of each chemical precipitation process parameter and experimental layout are presented. This section demonstrates the results for the screening of the most significant chemical precipitation process parameters, in terms of the ANOVA analysis for each response investigated, and the validation of the models produced. The effects of the process parameters on each response are described and discussed. Furthermore, the results of the phase purity, crystallinity, crystallite size, lattice parameters and particle size are illustrated and discussed to distinguish the effects of the process parameters on the final HAp powder properties obtained.

To screen the most significant chemical precipitation process parameters, the design of experiments was based on a fractional-factorial design, (2^6), with main and interaction effects, with the six influencing variables, at two levels, in sixteen runs used to identify how influential the process parameters are in terms of satisfying regulatory requirements and the synergism between these factors and hence the optimal conditions. Six experimental precipitation process parameters were selected, each one at two levels, and these are indicated in Table 4-10. The minimum and the maximum possible level values were selected for the screening experiments and are shown in Table 4-10 (denoted as -1 (min. level) and +1 (max. level).

Table 4-10: Experimental factors and level of factors

No	*Variable*	*Level -1*	*Level +1*
A	Reagent Addition Rate, V_{ac}	0.005 mol/min	0.01 mol/min
B	Reaction Temperature, T_o	20°C	60°C
C	Stirring Speed, V_{st}	600rpm	1500rpm
D	Ripening Time, t_r	0.5h	48h
E	Initial Ca2+ Concentration, Ca^{2+}	0.1 mol/L	2 mol/L
F	Inert Atmosphere, (atm)	without N_2	with N_2

The experiments were carried out according to the design matrix shown in Table 4-11 in a fully randomised order to avoid any systematic error. For this screening evaluation, several mathematical models were developed successfully to predict the following responses: phase purity (X_p), crystallinity (X_c), crystallite size (X_s, L_{002} and L_{300}), lattice parameters (*a* and *c*) and the powder particle size (P_s). The responses obtained were calculated according to the experimental design matrix, characterized as per experimental methods outlined in Chapter 3 and are discussed in the following sections. The averages for three measurements for each response are presented in Table 4-12. Also refer to Appendix E for a detailed analysis of the repeated results.

Table 4-11: Fractional-Factorial (Res IV) experimental design, real values

Sample	V_{ac} (mol/min)	T_o (°C)	V_{st} (rpm)	t_r (h)	Ca^{2+} (mol/L)	atm
N1	0.005	20	600	0.5	0.1	yes
N2	0.01	20	600	0.5	2	yes
N3	0.005	60	600	0.5	2	no
N4	0.01	60	600	0.5	0.1	no
N5	0.005	20	1500	0.5	2	no
N6	0.01	20	1500	0.5	0.1	no
N7	0.005	60	1500	0.5	0.1	yes
N8	0.01	60	1500	0.5	2	yes
N9	0.005	20	600	48	0.1	no
N10	0.01	20	600	48	2	no
N11	0.005	60	600	48	2	yes
N12	0.01	60	600	48	0.1	yes
N13	0.005	20	1500	48	2	yes
N14	0.01	20	1500	48	0.1	yes
N15	0.005	60	1500	48	0.1	no
N16	0.01	60	1500	48	2	no

Table 4-12: Phase purity (X_p), crystallinity (X_c), crystallite size (X_s, L_{002} and L_{300}), lattice parameter ratio (a/c) and mean particle size (P_s) of the different HAp samples for various conditions of acid addition (V_{ac}), temperature (T_o), stirring speed (V_{st}), ripening time (t_r), calcium conc. (Ca^{2+}) and atmospheric control (atm)

Sample	Purity, X_p, (%)	Crystallinity, X_c, (%)	Crystallite Size, X_s, L_{002} (nm)	Crystallite Size, X_s, L_{300} (nm)	Lattice Parameter, *a*	Lattice Parameter, *c*	Mean Particle Size, P_s (µm)
N1	44.25	72.23	61.47	56.09	9.4243	6.8953	58.60
N2	21.15	80.62	59.44	66.91	9.4625	6.8965	38.03
N3	83.19	45.69	90.48	126.35	9.4805	6.9049	23.28
N4	65.02	67.38	54.50	86.23	9.4828	6.8814	48.82
N5	44.01	54.85	98.79	139.70	9.4072	6.8817	54.94
N6	42.29	57.68	76.03	82.49	9.4168	6.8570	57.77
N7	63.59	76.49	59.04	87.96	9.4312	6.8890	19.96
N8	50.21	61.29	51.44	64.35	9.4462	6.8961	22.65
N9	86.37	58.50	41.60	58.84	9.4264	6.8749	63.83
N10	44.88	73.21	54.77	10.73	9.4871	6.8882	30.81
N11	74.85	71.74	60.82	73.91	9.4255	6.8820	20.74
N12	53.77	79.65	44.28	75.14	9.4300	6.8819	50.69
N13	38.14	80.58	52.20	70.61	9.4150	6.8808	34.38
N14	100.00	86.32	57.11	64.25	9.4145	6.8805	53.48
N15	44.27	90.95	69.45	76.04	9.4173	6.9009	36.15
N16	98.89	95.19	107.92	90.53	9.4296	6.8723	15.38

Statistical analysis of the obtained data was performed using the Design Expert 7.1® (Stat-Ease, Inc.) software. Analysis of the regression coefficients of the linear polynomial models describing the relationship between the responses of purity (X_p), crystallinity (X_c), crystallite sizes (X_s, L_{002} and L_{300}), lattice parameters (*a* and *c*) and mean particle size (P_s) against the six factors (V_{ac}, T_o, V_{st}, t_r, Ca^{2+}, atm) are presented in the following section.

4.4.1 Development Of Phase Purity Model

As a result of analysing the measured responses using the Design Expert software, the test for significance of the regression models and the test for significance on individual model co-efficients were performed using the same statistical software package for all responses. By selecting the backward regression method, the insignificant model terms ($P<0.05$), were automatically eliminated. The resulting ANOVA table (Tables 4-13) for the reduced linear phase purity model outlines the analysis of variance for this response and show the significant model terms affecting the phase purity. This table also shows other adequacy measures, such as, R^2, Adjusted R^2 and Predicted R^2. All the adequacy measures should converge close to 1, which is in reasonable agreement in indicating adequate models [160]. The Adequate Precision in this case is 34.562. An Adequate Precision ratio of greater than 4 indicates adequate model discrimination [160].

The analysis of variance, indicates, that for the phase purity model, all of the chemical precipitation parameters have an effect on the resulting phase purity model, either as a main or interaction effect with another parameter. The main effects of the reaction synthesis temperature (T_o), ripening time (t_r), calcium concentration (Ca^{2+}), presence of an atmospherically controlled environment (atm.) and the two way interaction effects of acid addition rate and stirring speed (V_{ac}* V_{st}), acid addition rate and ripening time (V_{ac}* t_r), acid addition rate and calcium concentration (V_{ac}* Ca^{2+}), reaction temperature and ripening time (T_o* t_r), reaction temperature and a controlled environment (T_o* atm.) and the three way interaction of acid addition rate, reaction temperature and controlled environment (V_{ac}* T_o* atm.) are the most significant model terms associated with phase

purity. The final mathematical models in terms of coded and actual factors, for an atm. (with or without) as determined by the design expert software are shown in Equations 4-3 to 4-5.

Table 4-13: ANOVA table for phase purity reduced linear polynomial model

Source	Sum of squares	d.f.	Mean Square	*F* value	Prob >*F*
Model (Significant)	7979.02	10	797.90	101.49	<0.0001 Significant
T_o	794.03	1	794.03	101.00	0.0002
t_r	1015.50	1	1015.50	129.17	<0.0001
Ca^{2+}	122.31	1	122.31	15.56	0.0109
atm.	247.69	1	247.69	31.50	0.0025
V_{ac} * V_{st}	2632.28	1	2632.28	334.81	<0.0001
V_{ac} * t_r	760.05	1	760.05	96.68	0.0002
V_{ac} * Ca^{2+}	142.06	1	142.06	18.07	0.0081
T_o * t_r	728.09	1	728.09	92.61	0.0002
T_o * atm.	76.18	1	76.18	9.69	0.0265
V_{ac} * T_o * atm.	1460.82	1	1460.82	185.81	<0.0001
Residual	39.31	5	7.86		
Corrected total	8018.33	15			

R^2 = 0.9951; predicted R^2 = 0.9498; adjusted R^2 = 0.9853; adequate precision = 34.562

Phase Purity, X_p, (%) = 59.68

+ 7.04 *T_o

+ 7.97 *t_r

– 2.76 *Ca^{2+}

+ 3.93 *atm.

+ 12.83 *V_{ac}* V_{st}

+ 6.89 *V_{ac}* t_r

– 2.98 *V_{ac}* Ca^{2+}

– 6.75 *T_o* t_r

+ 2.18 *T_o* atm.

+ 9.56 *V_{ac}* T_o* atm. *Equation (4-3)*

For an uncontrolled atmospheric environment:

Phase Purity, = +70.50227

X_p, (%)	+1.96035	* Reaction Temp	
	+0.032905	* Ripening Time	
	+6.49911	* Ca^{2+} Conc.	
	+11.40128	* H_3PO_4 addition rate * Stirring Speed	
	+116.08032	* H_3PO_4 addition rate * Ripening Time	
	-1254.60263	* H_3PO_4 addition rate * Ca^{2+} Conc.	
	-0.014202	* Reaction Temp * Ripening Time	*Equation (4-4)*

For a controlled (inert) atmospheric environment:

Phase Purity, = +188.45472

X_p, (%)	-0.68800	* Reaction Temp	
	+6.49911	* Ca^{2+} Conc.	
	+0.032905	* Ripening Time	
	+11.40128	* H_3PO_4 addition rate * Stirring Speed	
	+116.08032	* H_3PO_4 addition rate * Ripening Time	
	-1254.60263	* H_3PO_4 addition rate * Ca^{2+} Conc.	
	-0.014202	* Temp * Ripening Time	*Equation (4-5)*

Figure 4-20 shows the relationship between the actual and predicted values of phase purity. This figure indicates that the developed model is adequate, since the residuals in the prediction of each response are small, with the residuals tending to be close to the diagonal line.

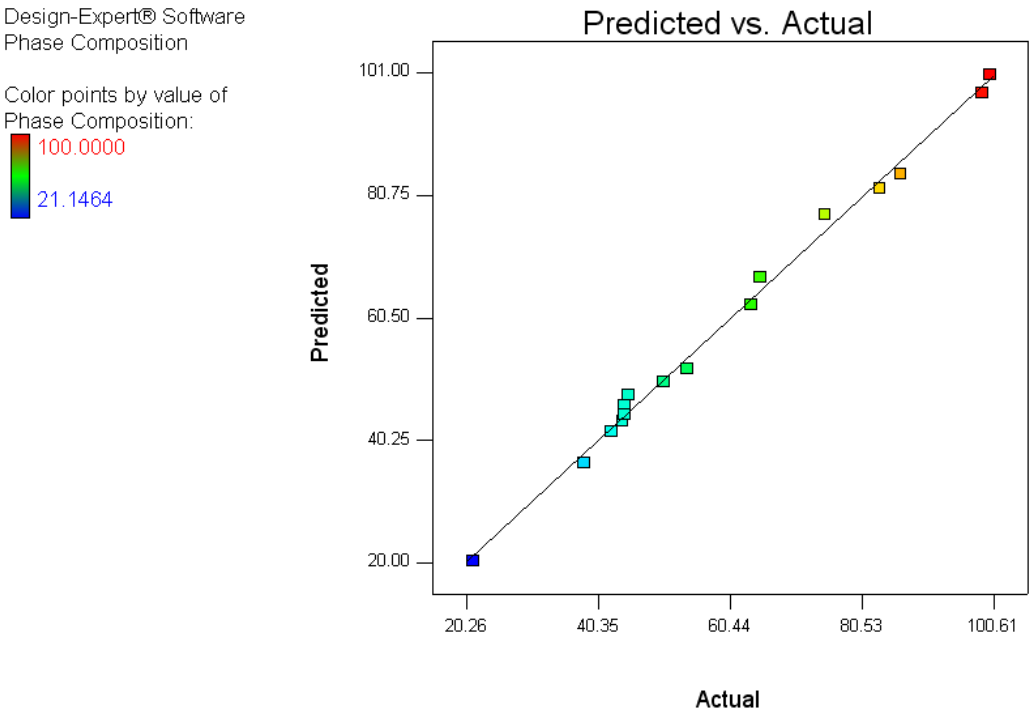

Figure 4-20: Scatter diagram for phase purity

4.4.2 Effect Of Process Parameters On Phase Purity

Deviation from stoichiometric HAp is due to the presence in the crystal lattice of vacancies and ion substitutes, such as carbonates and hydrogen phosphates, which are usually introduced into the precipitating system with the reactants. Ca-dHAp suffers from significant changes in its crystallographic characteristics, in comparison to pure stoichiometric HAp. Since, it is well known that the neutralisation of calcium hydroxide with orthophosphoric acid leads to non-stoichiometric HAp, control of the process parameters affecting the purity is critical in obtaining high levels of purity (>95%). This section discusses the effect of the process variables (using the crystallinity model developed in the previous section) on the final phase purity of HAp.

The phase purity is directly related to all of the process variables investigated, either as a main or as part of an interaction effect, as stated earlier. The reason for predicting the phase purity is to develop a model, to aid in the selection of an appropriate range for the optimisation stage (at a later stage). The pareto chart for the phase purity model, as illustrated in Figure 4-21, highlights the order of the significant main and interaction parameter effects, which ultimately affect the phase purity model.

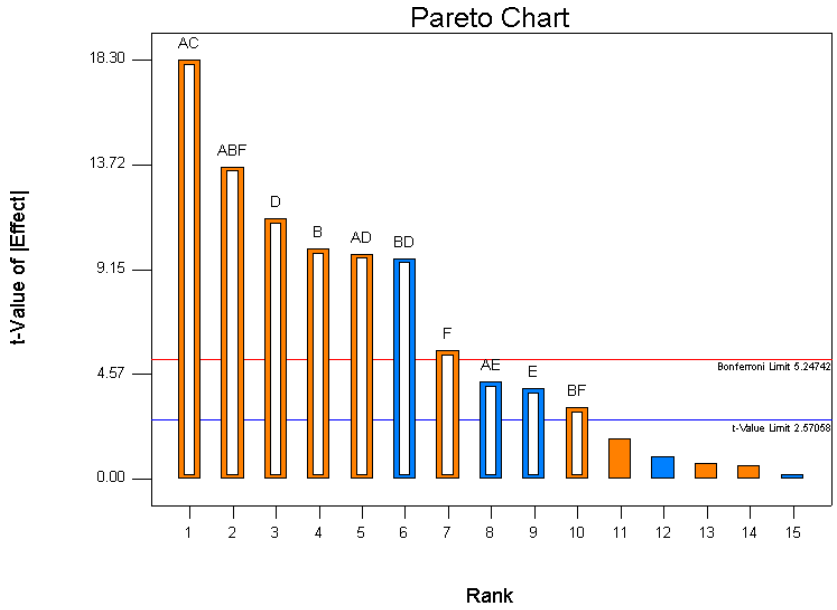

Figure 4-21: Pareto chart, examining the level of main and interaction effects (orange: positive effect and blue: negative effect) of the process parameter on the phase purity: where A is V_{ac}, B is T_o, C is V_{st}, D is t_r, E is Ca^{2+} conc. and F is atm.

The order of the level of significance of the positive effects of the chemical precipitation process parameters on the phase purity follows the order: $(V_{ac}* V_{st}) > (V_{ac}* T_o* atm.) > (t_r) > (T_o) > (V_{ac}* t_r) > (atm.) > (T_o* atm.)$ while the order of the level of significance of the negative effects on the phase purity is as follows: $(T_o* t_r) > (V_{ac}* Ca^{2+}) > (Ca^{2+})$. Hence, if high levels of phase purity are to be obtained, the top four most influencing effects for control are as follows:

1.	Acid addition rate * Stirring Speed↑	(Two-way interaction effect)
2.	Acid addition rate * Reaction temperature * atmospheric control↑	(Three-way interaction effect)
3.	Ripening time↑	(Main effect)
4.	Reaction temperature↑	(Main effect)

Where ↑ denotes a high level and ↓ denotes a low level is required.

The primary factor most affecting the phase purity appears to be the two-way interaction effect between the acid addition rate and the stirring speed. The stirring speed should be high enough to prepare a good homogeneous media for preparation of HAp [83], with both monetite and brushite formation favoured by sufficient mixing of the calcium solution as the orthophosphoric solution is added. When it is not distributed homogenously, the PO_4^{3-} ion concentration can build up and a localized low pH will be established. This part of the reaction vessel is richer in PO_4^{3-} and provides conditions for the formation of soluble precipitates. The model indicates therefore, that with an increase in acid addition rate, it is imperative to also increase the stirring speed to obtain a high level of HAp purity.

The second factor most affecting the phase purity is a three-way interaction effect between the acid addition rate, the reaction temperature and the atmospheric control. Seckler et al. [78] have reported that the main phase formed at room temperature is ACP with minor amounts of HAp, while the amounts of HAp present increased with an increase in temperature. The model indicates that use of a controlled inert environment and acid addition rate is favoured by use of a high reaction temperature to ensure impurities incorporated into the reaction vessel are kept at a minimum.

The ripening time and reaction temperature are the third and forth most significant effects (main), respectively and correlate well with evidence provided by Liu et al. [91] in demonstrating the significance of the ripening time with respect to purity, for the full conversion of precursor phases, such as: OCP, DCPD and ACP to phase pure HAp, while the lifetime of the metastable amorphous precursor in aqueous solution has been reported to be a function of the reaction synthesis temperature.

Figure 4-22 shows a perturbation plot highlighting the effect of all parameters on the phase purity. The perturbation plot allows the effect of all the factors at a particular point in the design space to be compared. This type of display does not show the effect of interactions. Instead, the lines represent the behaviours of each factor while holding the others in a constant ratio (centre point by default). In the case of more than one factor this type of display could be used to find those factors that most affect the response. The significant interaction (between the rate of acid addition and the stirring speed) most affecting the phase purity is shown in Figure 4-23, under an uncontrolled and controlled (inert) atmosphere. 3-D and 2-D contour plots are presented in Figure 4-24(a) to (c), and highlight the positive influence of increasing both the reaction synthesis temperature and the ripening time. However, a decrease in the calcium concentration is required in order to ensure high levels of phase purity are attained. A ripening time of at least 24h proved difficult in attaining a minimum of 95% purity at ambient reaction temperatures. Instead, higher levels of a reaction temperature are necessary in order to correct this. It is also evident that the presence of a controlled (inert) environment has a positive effect on the final purity obtained.

(A) **(B)**

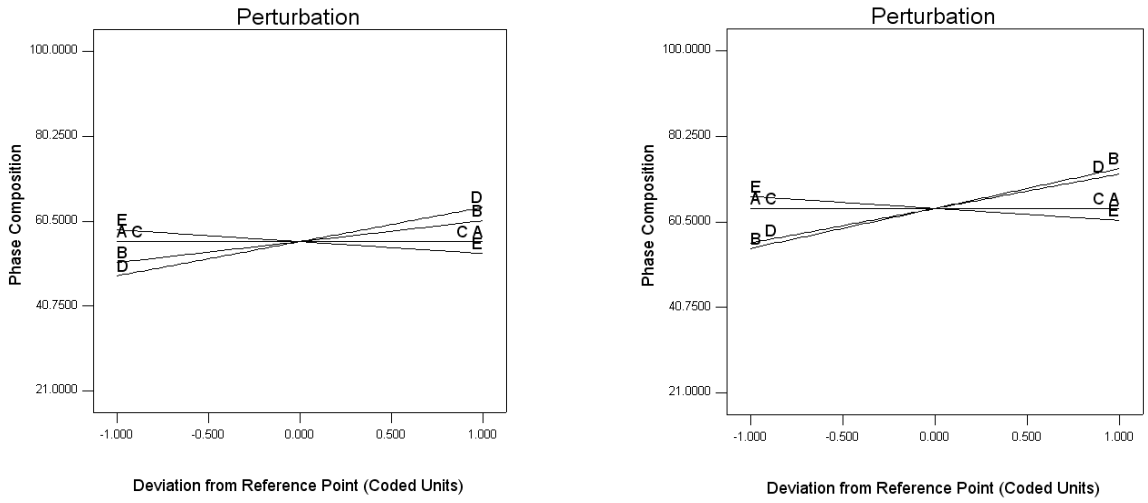

Figure 4-22: Perturbation plot showing the effect of all the parameters on the phase purity under (A) an uncontrolled environment and (B) a controlled (inert) environment

(A) Uncontrolled atmosphere

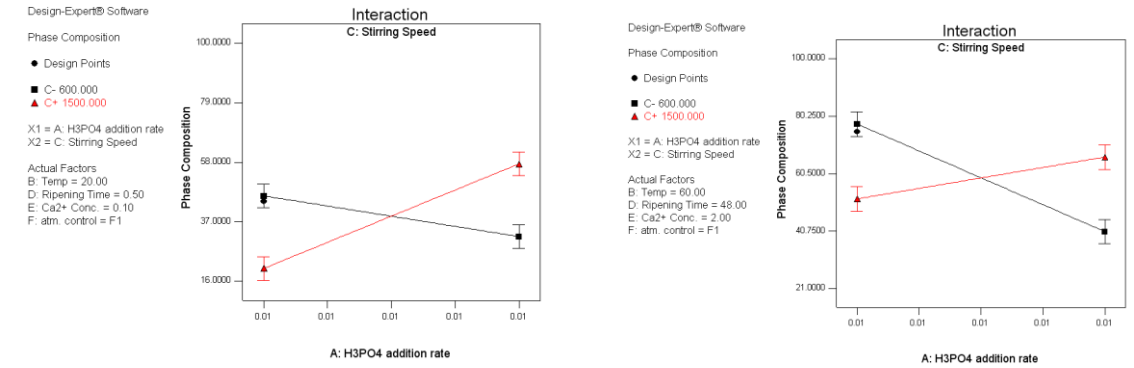

(B) Controlled atmosphere

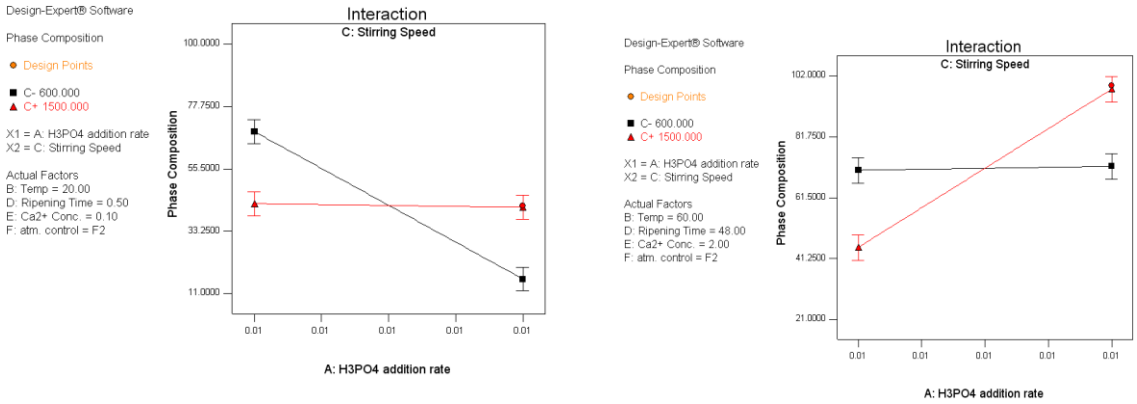

Figure 4-23: Interaction plot showing the most significant interaction effects of V_{ac} and V_{st} on the phase purity for (A) an uncontrolled atmospheric environment and (B) a controlled inert environment for low (left hand side) and high (right hand side) remaining factors

The model also demonstrates that low temperature synthesis at a low stirring speed results in low levels of HAp purity (that is, a mixture of HAp and β-TCP), while using a high synthesis temperature and stirring speed can increase the final purity.

A comparison of the effect of the chemical precipitation parameters between the powders obtained at lowest (N2) and highest purity (N14 and N16, with a minimum of 95% purity, as required per regulations reviewed in section 2.12) is reviewed in Table 4-14.

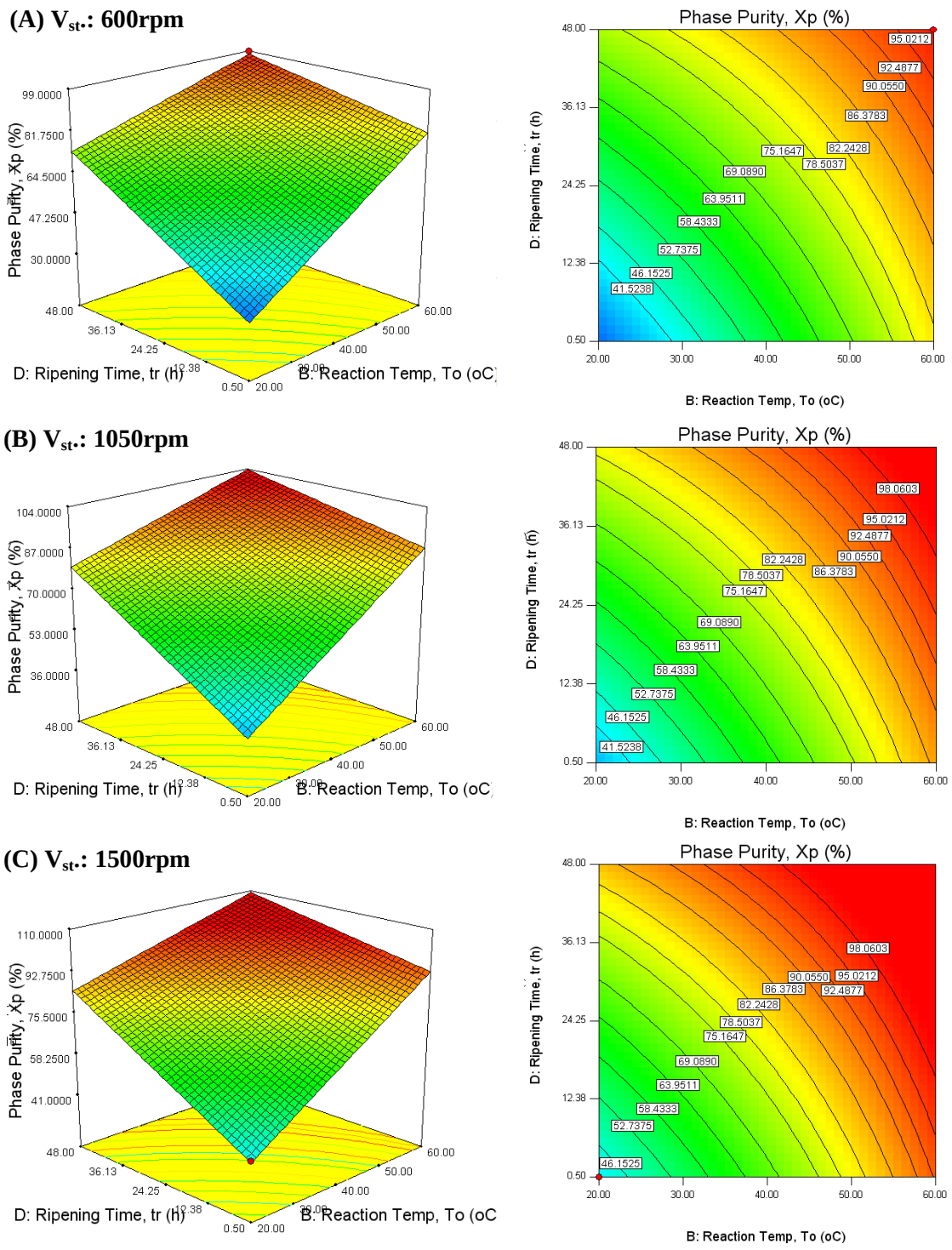

Figure 4-24: 3D surface and 2D contour plots of phase purity at (A) a stirring speed of 600rpm; (B) a stirring speed of 1050rpm and (C) a stirring speed of 1500rpm (under a controlled environment at t_r = 48h and Ca^{2+} = 2.0M)

The purity values obtained have been verified by Rietveld refinement and shows N14 as the only powder to have attained 100 wt. % purity. The second highest level of purity obtained was for N16: with 98.89 wt. % HAp and 1.11 wt% CaO. The lowest level of purity obtained, however, was for N2: with only 21.15 wt. % HAp evident. Instead, its predominant phase consists of 65.54 wt. % β-TCP. Comparing the chemical precipitation parameters of N2 against the more pure HAp powders (N14 and N16) therefore, demonstrates the requirement of a higher stirring speed and ripening time in obtaining increased levels of phase purity. This concept has been previously discussed in relation to studies conducted by Afshar et al. [83] confirming that the stirring speed should be high enough to prepare a good homogeneous media for preparation of HAp. Comparing N14 with N16 shows how a low calcium concentration is favoured for high levels of purity, which correlates well with that proposed by Guilietti et al. [86] who maintain that high purity levels can be attained, when precipitation is conducted at low supersaturation levels. Comparing the effect of the atmospheric control on the final purity also confirms that the presence of a controlled (inert) environment can also have a positive influence on the final phase purity.

Table 4-14: Effect of the chemical precipitation parameters (factors) studied on the purity (response)

	Factors						**Response**
Sample	**V_{ac} (mol/min)**	**T_o (°C)**	**V_{st} (rpm)**	**t_r (h)**	**Ca^{2+} (mol/L)**	**atm.**	**X_p (%)**
N2	0.01	20	600	0.5	2	+	21.15
N14	0.01	20	1500	48	0.1	+	100.00
N16	0.01	60	1500	48	2	-	98.89

Figure 4-25 shows 2-D and 3-D illustrations of the comparison between the XRD patterns obtained for the three powder samples, N2, N14 and N16 under discussion. With respect to purity, the only two samples in this study to satisfy regulatory requirements (min. 95%) in the order of most pure is N14 > N16. Refer to Appendix F for XRD patterns relating to all 16 sets of conditions outlined in the design matrix (see Table 3.7).

(A)

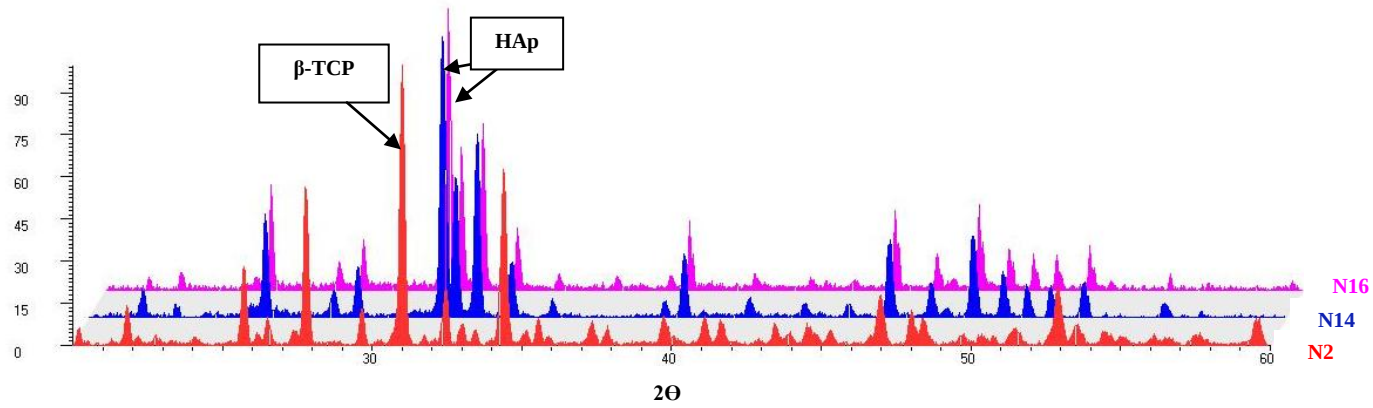

(B)

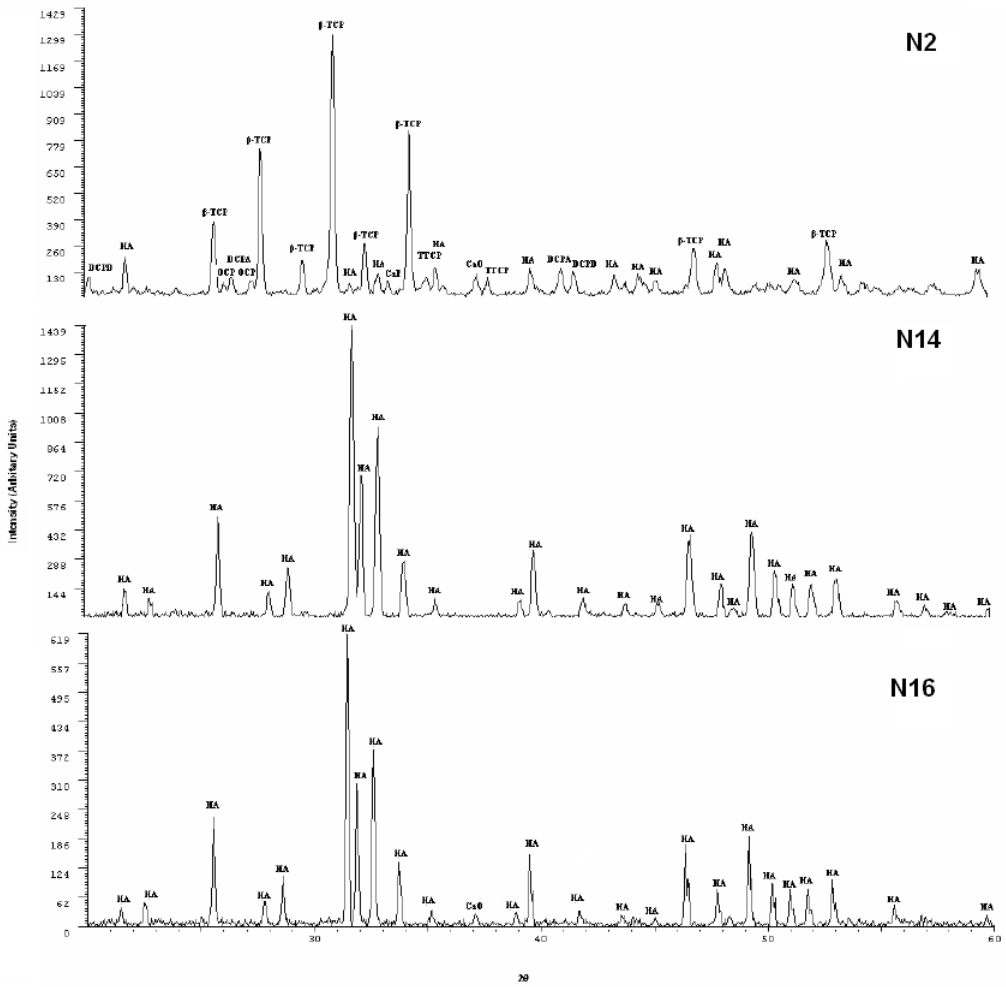

Figure 4-25: (A) 3-D illustration and (B) 2-D illustration comparing XRD patterns obtained for N2, N14 and N16

4.4.3 Development Of Crystallinity Model

As a result of analysing the measured responses using the Design Expert software, the fit summary selects the highest order polynomial where the additional terms are significant and the model is not aliased. By selecting the manual regression method, the insignificant model terms ($P<0.1$), with less than a 5% contribution were eliminated. The precent contribution is obtained from adding up the total sum of squares and then taking from each term's sum of squares and dividing by the total to get a percentage. Table 4-15 presents the ANOVA results for the crystallinity and shows the significant model terms. The same tables show also the other adequacy measures R^2, Adjusted R^2 and Predicted R^2. All the adequacy measures are close to 1, which is in reasonable agreement and indicate adequate models [160]. The Adequate Precision is 9.805. An Adequate Precision ratio of greater than 4 indicates adequate model discrimination [160].

The analysis of variance for the crystallinity model indicates that all of the chemical precipitation parameters have an effect on the resulting crystallinity model, either as a main or interaction effect with another parameter. The main effects of the acid addition rate (V_{ac}), stirring speed (V_{st}), ripening time (t_r), controlled atmosphere (atm.) and the two way interaction effects of acid addition rate and stirring speed (V_{ac}* V_{st}), acid addition rate and calcium concentration (V_{ac}* Ca^{2+}), reaction temperature and ripening time (T_o* t_r), reaction temperature and a controlled environment (T_o* atm.) are the most significant model terms associated with achieving high levels of crystallinity (>95%). The final mathematical models in terms of coded and actual factors (with and without atmospheric control) as determined by the Design Expert software are shown in Equations 4-6 to 4-8.

Figure 4-26 shows the relationship between the actual and predicted values of crystallinity. This figure indicates that the developed model is adequate, since the residuals in the prediction of each response are small, with the residuals tending to be close to the diagonal line.

Table 4-15: ANOVA table for crystallinity reduced linear polynomial model

Source	Sum of squares	d.f.	Mean Square	*F* value	Prob >*F*
Model (Significant)	2596.23	8	324.53	9.31	0.0041 Significant
V_{ac}	158.20	1	158.20	4.54	0.0707
V_{st}	184.57	1	184.57	5.29	0.0549
t_r	898.69	1	898.69	25.77	0.0014
atm.	268.06	1	268.06	7.69	0.0276
V_{ac} * V_{st}	189.81	1	189.81	5.44	0.0524
V_{ac} * Ca^{2+}	260.83	1	260.83	7.48	0.0291
T_o * t_r	178.59	1	178.59	5.12	0.0581
T_o * atm.	457.48	1	457.48	13.12	0.0085
Residual	244.10	7	34.87		
Corrected total	2840.33	15			

R^2 = 0.9141; predicted R^2 = 0.5510; adjusted R^2 = 0.8158; adequate precision = 9.805

Crystallinity, = 72.02

X_c, (%) +3.14 $*V_{ac}$

+ 3.40 $*V_{st}$

+ 7.49 $*t_r$

– 4.09 *atm.

– 3.44 $*V_{ac}* V_{st}$

+ 4.04 $*V_{ac}* Ca^{2+}$

+ 3.34 $*T_o* t_r$

+ 5.35 $*T_o*$ atm. *Equation (4-6)*

For an uncontrolled atmospheric environment:

Crystallinity, = +37.69018

X_c, (%) +4509.69603 * H_3PO_4 addition rate

+0.030509 * Stirring Speed

+0.11365 * Ripening Time

-3.06155 * H_3PO_4 addition rate * Stirring Speed

+35.51526 * H_3PO_4 addition rate * Ca^{2+} Conc.

+5.04780E-003 * Reaction Temp * Ripening Time *Equation (4-7)*

For a controlled (inert) atmospheric environment:

Crystallinity, = +8.11504

X_c, (%) +4509.69603 * H_3PO_4 addition rate

+0.030509 * Stirring Speed

+0.11365 * Ripening Time

-3.06155 * H_3PO_4 addition rate * Stirring Speed

+35.51526 * H_3PO_4 addition rate * Ca2+ Conc.

+5.04780E-003 * Reaction Temp * Ripening Time *Equation (4-8)*

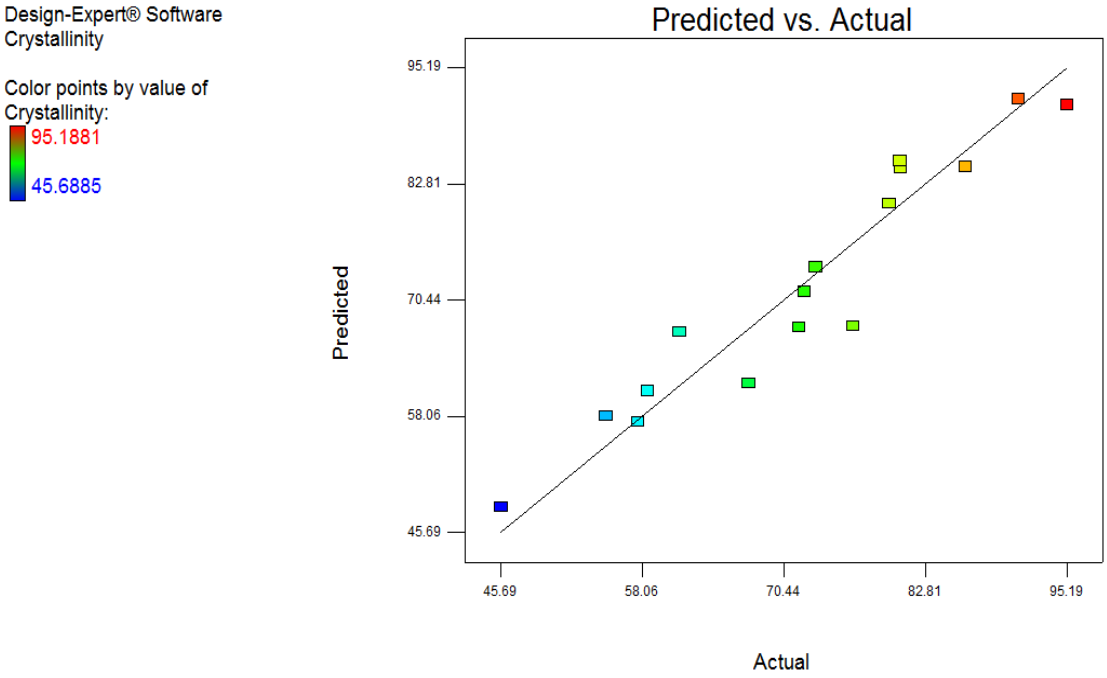

Figure 4-26: Scatter diagram for crystallinity

4.4.4 Effect Of Process Parameters On Crystallinity

The crystallinity of the HAp is one of the deciding factors for (i) producing thermally stable HAp and (ii) determining its rate of dissolution in its physiological environment. Difficulties in preparing synthetic HAp crystals from aqueous solutions are primarily caused by the high affinity of the material to some ions, the complex nature of the calcium phosphates system, and the role of the kinetic parameters. Therefore, in order to produce HAp with predictable crystallinity; reactant concentrations, reaction synthesis temperature, stirring speed, ripening time and the presence of an inert environment should be effectively designed to obtain high levels of crystallinity (>95%). This section discusses the effect of the most significant process variables (using the crystallinity model developed in the previous section) on the final crystallinity obtained for HAp. The crystallinity is directly related to all of the process variables investigated in this study, either as a main or included in an interaction effect, as stated earlier. The reason for predicting the crystallinity, at this stage, is to develop a model, to aid in the selection of an appropriate range for the optimisation stage (at a later stage). The pareto chart for the crystallinity model, as illsutrated in Figure 4-27, highlights the order of the significant main and interaction parameter effects, which ultimately affect the crystallinity model.

The order of the level of significance of the positive effects of the chemical precipitation process parameters on crystallinity follows the order: $(t_r) > (T_o * \text{atm.}) > (V_{ac} * Ca^{2+}) > (V_{st}) > (T_o * t_r) > (V_{ac})$ while the order of the level of significance of the negative effects on the phase purity is as follows: $(\text{atm.}) > (V_{ac} * V_{st})$.

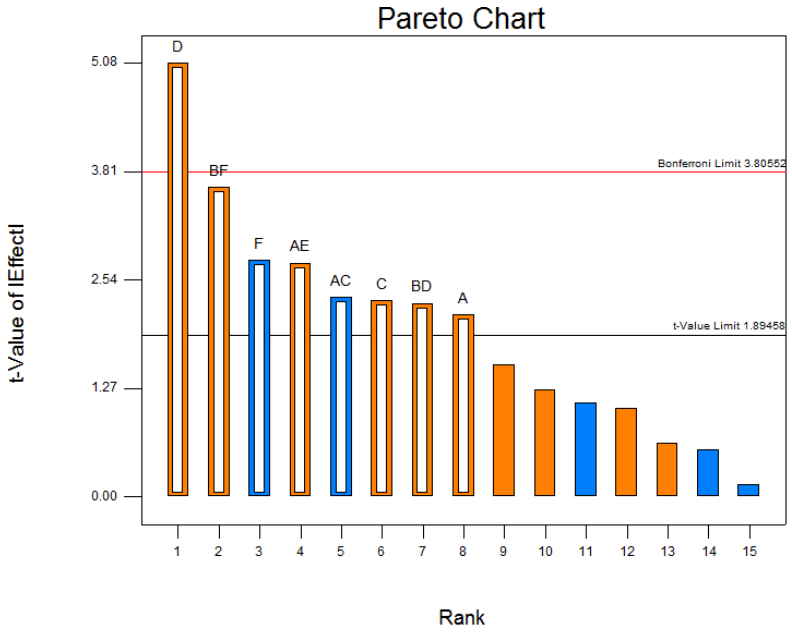

Figure 4-27: Pareto chart, examining the level of main and interaction effects (orange: positive effect and blue: negative effect) of the process parameter on the crystallinity; where A is V_{ac}, B is T_o, C is V_{st}, D is t_r, E is Ca^{2+} conc. and F is atm.

Hence, if high levels of crystallinity are to be obtained, the top four most influencing effects for control are as follows:

1. Ripening time↑ (Main effect)
2. Reaction temperature * atmospheric control↑ (Two-way interaction effect)
3. Atmospheric control↓ (Main effect)
4. Acid addition rate * Calcium concentration↑ (Two-way interaction effect)

As expected, the primary factor most affecting the crystallinity, confirms the ripening time as the most critical factor for controlling the resultant percentage crystallinity. The crystalline behaviour as a function of ripening time is attributed to the mechanism of crystal growth in solution, since it is well known that the precipitation of particles involves nucleation and growth from a supersaturated solution.

The second most important effect involves a two-way interaction effect between the reaction temperature and atmospheric control. An increase in precipitation reaction temperature has elsewhere been reported [71, 85, 90] to further enhance the final crystallinity. In order for an increase in this parameter to take effect in this model, however, requires the simultaneous use of a controlled inert environment. Although, as a main effect, this parameter is found to decrease the crystallinity. The fourth most significant factor effecting the crystallinity is the two-way interaction effect involving both reagents: the acid addition rate and the calcium concentration, showing that an increase in both parameters can favour an increase in crystallinity.

Comparing the models for phase purity and crystallinity, it is clear that they both share the same dependency on the main effect of ripening time (t_r) and a controlled environment (atm.) to reach optimal levels for each response. The interaction effects of the acid addition rate and stirring speed (V_{ac}* V_{st}), acid addition rate and calcium concentration (V_{ac}* Ca^{2+}), reaction temperature and ripening time (T_o* t_r), and reaction temperature and controlled environment (T_o* atm.) are also common interaction effects for both phase purity and crystallinity models which were found to significantly affect end result for both responses. Figure 4-28 shows a perturbation plot highlighting the effect of all parameters on the crystallinity. The most significant interaction effect (between the reaction synthesis temperature and the presence of an inert environemnt) affecting the crystallinity is shown in Figure 4-29. Contour plots examining the main interaction effects are shown in Figure 4-30. This figure shows that the crystallinity (synthesised under a controlled inert environment) increases directly, with an increase in the acid addition rate, stirring speed and ripening time.

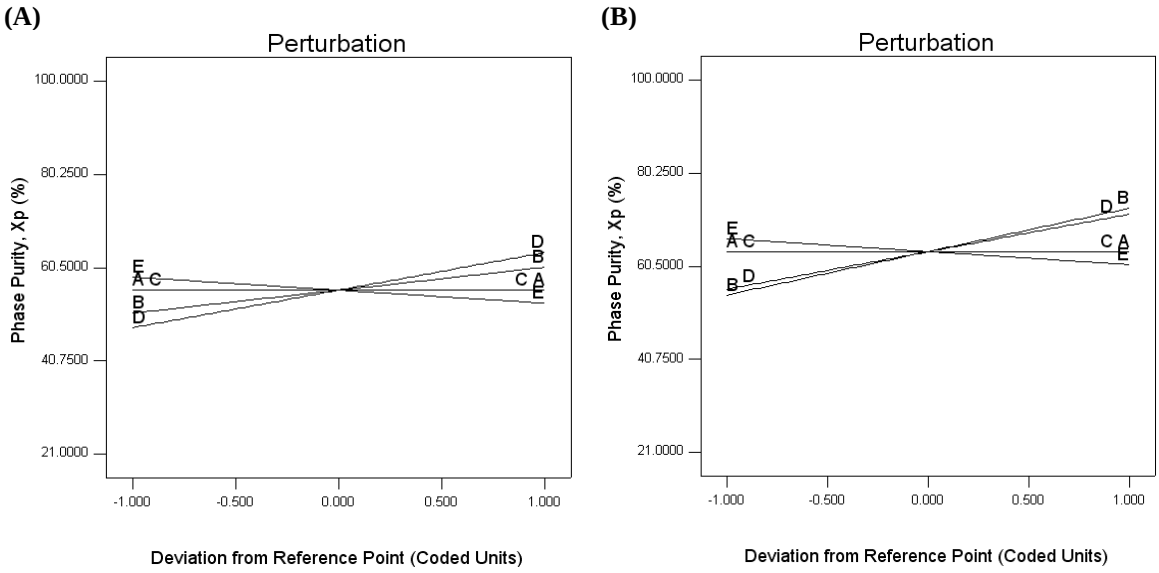

Figure 4-28: Perturbation plot showing the effect of all the parameters on the crystallinity under (A) an uncontrolled environment and (B) a controlled (inert) environment

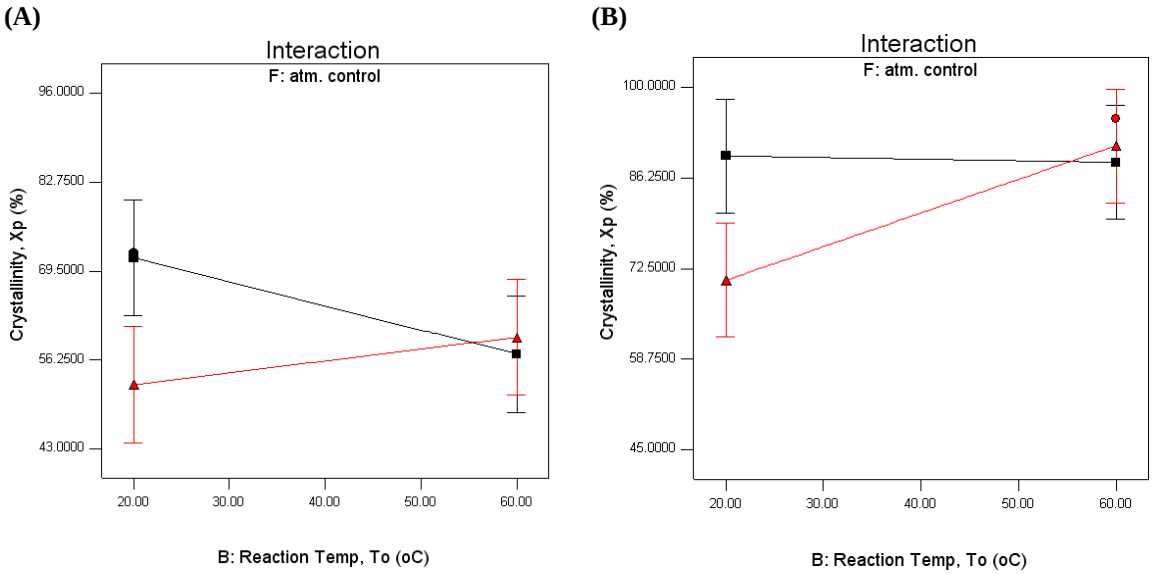

Figure 4-29: Interaction plot showing the most significant interaction effects of T_o and atm. on the phase purity for (A) an uncontrolled atmospheric environment and (B) a controlled inert environment (all other factors at upper level)

(A) Ripening Time: 0.5h

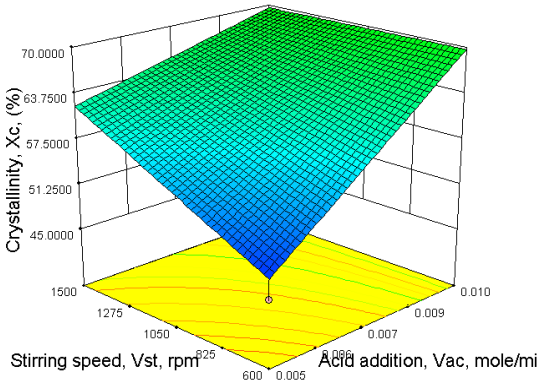

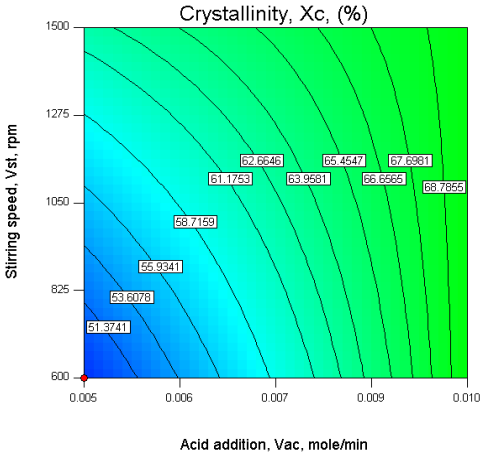

(B) Ripening Time: 24h

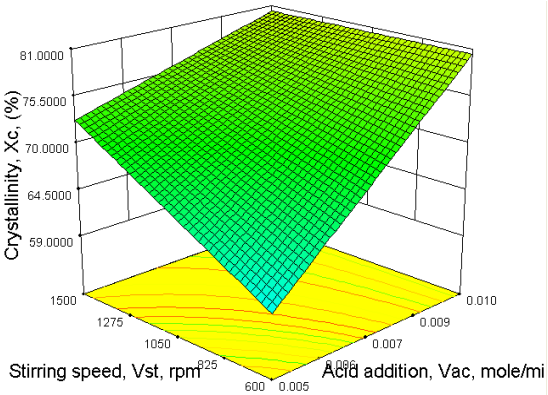

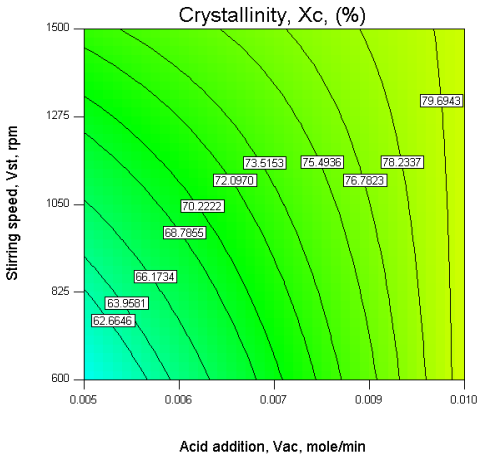

(C) Ripening Time: 48h

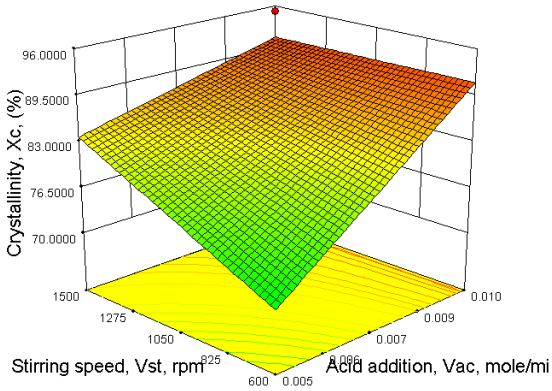

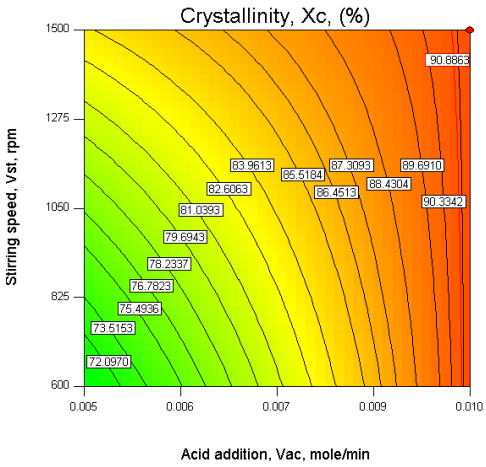

Figure 4-30: 3D surface and 2D contour plots of crystallinity at (A) a ripening time of 0.5h; (B) a ripening time of 24h and (C) a ripening time of 48h (under a controlled environment at T_o = 60°C and Ca^{2+} = 2.0M)

Synthesis under an inert environment, as found to have a positive interaction effect with the reaction temperature influencing the final crystallinity, is shown in Figure 4-31. The crystallinity model dictates that an increase in the ripening time is the most significant parameter to enhance the end crystallinity of HAp and that this effect is more significant under a low reaction synthesis temperature (that is, its dependency for an increased ripening time is promoted). The interaction effect between the synthesis temperature and ripening time is small in comparison to the effect of the ripening time on the final crsyatllinity. However, it may be explained by the fact that an increase in temperature results in both a shortening of the induction time and an increase in the rate of crystal proliferation.

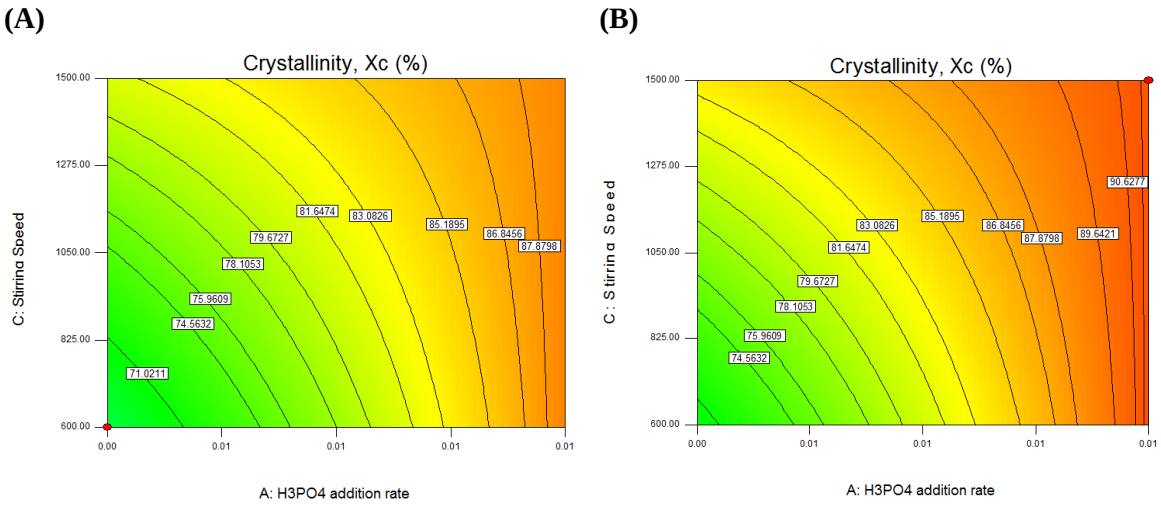

Figure 4-31: 2D contour plots of crystallinity under (A) an uncontrolled environment and (B) an inert environment (at T_o = 60°C, Ca^{2+} = 2.0M and t_r = 48h)

A comparison of the effect of the chemical precipitation parameters between the powders obtained at lowest (N3) and highest crystallinity (N14 and N16) is reviewed below in Table 4-16. However, it is evident that the only powder synthesised in this study meeting the required minimum of 95% crystallinity is N16. Comparing the chemical precipitation parameters of N3 against the more crystalline HAp powders (N14 and N16) demonstrates the requirement of a higher stirring speed (V_{st}), reactant concentration (Ca^{2+} and V_{ac}) and ripening time (t_r) in obtaining increased levels of crystallinity. Comparing N14 and N16

also confirms that an increase in the reaction synthesis temperature may exert a positive influence on the final crystallinity, while the presence of a controlled environment is found to have an insignificant effect on achieving a high level of crystallinity. However, while the calculated crystallinity value for N14 is lower than N16, its XRD pattern (refer to Figure 4-26) is indicative of a highly crystalline HAp. This may be attributed to its calculation based upoon aggregates of its crystallites (mean powder particle size, Table 4-23) as opposed to its primary crystallite size.

Table 4-16: Effect of the chemical precipitation parameters (factors) studied on the crystallinity (response)

	Factors						Response
Sample	**V_{ac} (mol/min)**	**T_o (°C)**	**V_{st} (rpm)**	**t_r (h)**	**Ca^{2+} (mol/L)**	**atm.**	**X_c (%)**
N3	0.005	60	600	0.5	2	-	45.69
N14	0.01	20	1500	48	0.1	+	86.32
N16	0.01	60	1500	48	2	-	95.19

Figure 4-25 shows a 2-D illustration of the comparison in crystallinity between the XRD patterns obtained for the least and most crystalline powder samples synthesised in this study (that is, N3 and N16).

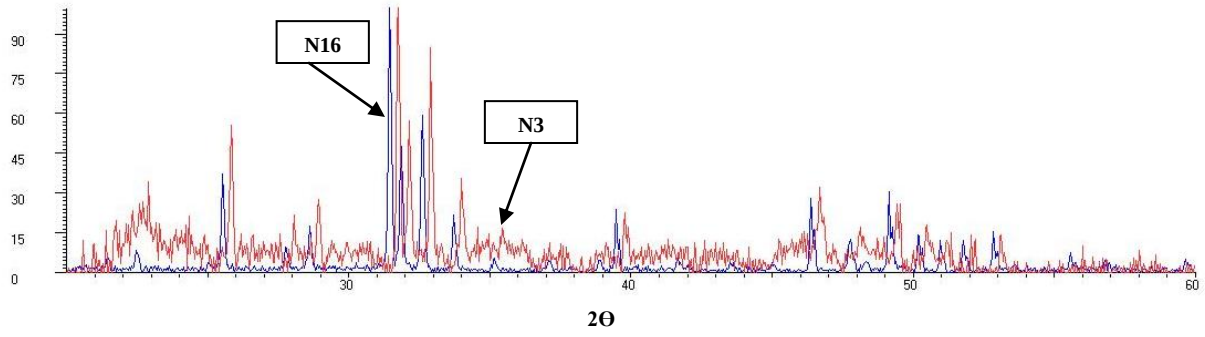

Figure 4-32: 2-D illustration comparing XRD diffraction patterns obtained for N3 and N16

4.4.5 Development Of Crystallite Size Models (L_{002} and L_{300})

The same steps and adequacy tests, which were outlined earlier, were followed and performed at this point. The manual regression method was used to eliminate the insignificant model terms ($P<0.1$) with less than a 5% contribution. A logit power transformation was used to develop the L_{300} model, where the response is bounded between a lower and upper limit of 10 and 140, respectively, since it possessed a ratio of maximum to minimum responses of 13.0181. A ratio greater than 10 indicates that a transformation is required. Therefore, a ratio of 2.5945 for the L_{002} model suggested that a transformation would have little effect and was not used in this case. Tables 4-17 and 4-18 presenting the resulting ANOVA tables and the other adequacy measures for the crystallite size models in the 002 and 300 (that is L_{002} and L_{300}) planes, are considered here. The analysis of variance, indicates, that for the crystallite size model for the L_{002} plane, all of the chemical precipitation parameters have a significant effect on the resulting a/c ratio model, either as a main or interaction effect with another parameter. The main effects of the stirring speed (V_{st}), ripening time (t_r), calcium concentration (Ca^{2+}), atmospheric control (atm.) and the two way interaction effects of acid addition rate and ripening time (V_{ac}* t_r), reaction temperature and ripening time (T_o* t_r) and reaction temperature and atmospheric control (T_o* atm.) are the most significant model terms associated with affecting the resulting crystallite size in the 002 plane. On the other hand, the significant main effects on the crystallite size in the 300 plane is the acid ripening time (t_r), acid addition rate (V_{ac}) and stirring speed (V_{st}), while two way interactions between the acid addition rate and the reaction temperature (V_{ac} * T_o), acid addition rate and calcium concentration (V_{ac}* Ca^{2+}), acid addition rate and atmospheric environment (V_{ac} * atm.) and reaction temperature and ripening time (T_o * t_r) is also found to be an influencing factor for this response. A three way interaction effect between the acid addition rate, reaction temperature and the atmospheric environment (V_{ac} * T_o * atm.) was also noted. The final mathematical models for the crystallite size response, L_{002} in terms of coded and actual factors as determined by the Design Expert software are shown in Equations 4-9 to 4-11. While, the final mathematical models in terms of coded and actual factors for L_{300} are presented in Equations 4-12 to 4-14.

Table 4-17: ANOVA table for crystallite size, L_{002} reduced linear polynomial model

Source	Sum of squares	d.f.	Mean Square	*F* value	Prob >*F*
Model (Significant)	4947.74	7	706.82	10.76	0.0016 Significant
V_{st}	684.52	1	684.52	10.42	0.0121
t_r	248.46	1	248.46	3.78	0.0877
Ca^{2+}	789.42	1	789.42	12.02	0.0085
atm.	1364.26	1	1364.26	20.76	0.0019
V_{ac} * t_r	734.29	1	734.29	11.18	0.0102
T_o * t_r	856.21	1	856.21	13.03	0.0069
T_o * atm.	270.58	1	270.58	4.12	0.0769
Residual	525.61	8	65.70		
Corrected total	5473.35	15			

R^2 = 0.9040; predicted R^2 = 0.6159; adjusted R^2 = 0.8199; adequate precision = 11.085

Table 4-18: ANOVA table for crystallite size, L_{300} reduced linear polynomial model

Source	Sum of squares	d.f.	Mean Square	*F* value	Prob >*F*
Model	64.90	8	8.11	13.29	0.0014 Significant
V_{ac}	9.57	1	9.57	15.68	0.0055
V_{st}	6.86	1	6.86	11.24	0.0122
t_r	11.67	1	11.67	19.11	0.0033
V_{ac} * T_o	4.31	1	4.31	7.06	0.0326
V_{ac} * Ca^{2+}	12.63	1	12.63	20.70	0.0026
V_{ac} * atm.	7.95	1	7.95	13.03	0.0086
T_o * t_r	5.65	1	5.65	9.26	0.0188
V_{ac} * T_o * atm.	6.25	1	6.25	10.23	0.0151
Residual	4.27	7	0.61		
Corrected total	69.17	15			

R^2 = 0.9382; predicted R^2 = 0.6773; adjusted R^2 = 0.8676; adequate precision = 19.161

Crystallite Size, = 64.96

L_{002} (nm)	+ 6.54	$*V_{st}$	
	- 3.94	$*t_r$	
	+ 7.02	$*Ca^{2+}$	
	+ 9.23	*atm.	
	+ 6.77	$*V_{ac}* t_r$	
	+ 7.32	$*T_o* t_r$	
	+ 4.11	$*T_o*$ atm.	*Equation (4-9)*

For an uncontrolled atmospheric environment:

Crystallite Size, = +44.94738

L_{002} (nm)	+0.014535	* Stirring Speed	
	- 0.87066	* Ripening Time	
	+7.39386	* Ca^{2+} Conc.	
	+40.94013	* H_3PO_4 addition rate * Ripening Time	
	+9.94218E-003	* Reaction Temp * Ripening Time	*Equation (4-10)*

For a controlled (inert) atmospheric environment:

Crystallite Size, = +46.96590

L_{002} (nm)	+0.014535	* Stirring Speed	
	- 0.87066	* Ripening Time	
	+7.39386	* Ca^{2+} Conc.	
	+40.94013	* H_3PO_4 addition rate * Ripening Time	
	+9.94218E-003	* Reaction Temp * Ripening Time	*Equation (4-11)*

Logit (Crystallite Size, L_{300} (nm)) =

Ln[(Crystallite Size, L_{300} – 10.00)/(140.00 – Crystallite Size, L_{300})] =

$$
\begin{aligned}
&+0.15 \\
&-0.77 \quad *V_{ac} \\
&+0.65 \quad *V_{st} \\
&-0.85 \quad *t_r \\
&+0.52 \quad *V_{ac} * T_o \\
&-0.89 \quad *V_{ac} * Ca^{2+} \\
&-0.71 \quad *V_{ac} * atm. \\
&+0.59 \quad * T_o * t_r \\
&+0.62 \quad *V_{ac} * T_o * atm.
\end{aligned}
$$

Equation (4-12)

For an uncontrolled atmospheric environment:

Logit (Crystallite Size, L_{300} (nm)) =

Ln[(Crystallite Size, L_{300} – 10.00)/(140.00 – Crystallite Size, L_{300})] =

$$
\begin{aligned}
&+1.81027 \\
&-235.26182 \quad * H_3PO_4 \text{ addition rate} \\
&+1.45519E\text{-}003 \quad * \text{Stirring Speed} \\
&-0.071007 \quad * \text{Ripening Time} \\
&-1.73988 \quad * H_3PO_4 \text{ addition rate} * \text{Reaction Temp.} \\
&-12.33184 \quad * H_3PO_4 \text{ addition rate} * Ca^{2+} \text{ Conc.} \\
&+8.76279E\text{-}004 \quad * \text{Reaction Temp.} * \text{Ripening Time}
\end{aligned}
$$

Equation (4-13)

For a controlled (inert) atmospheric environment:

Logit (Crystallite Size, L_{300} (nm)) =

Ln[(Crystallite Size, L_{300} – 10.00)/(140.00 – Crystallite Size, L_{300})] =

+1.81027

-349.78734 * H_3PO_4 addition rate

+1.45519E-003 * Stirring Speed

-0.071007 * Ripening Time

-1.54575 * H_3PO_4 addition rate * Reaction Temp.

-12.33184 * H_3PO_4 addition rate * Ca^{2+} Conc.

+8.76279E-004 * Reaction Temp. * Ripening Time *Equation (4-14)*

The validity of the models developed can be drawn also from Figures 4-33(a) and (b), which present the relationship between the measured and predicted values of the crystallite sizes in the two planes 002 and 300. These scatter diagrams indicate that the above mathematical models show a good agreement between the measured and estimated values of the above mentioned responses.

(A)

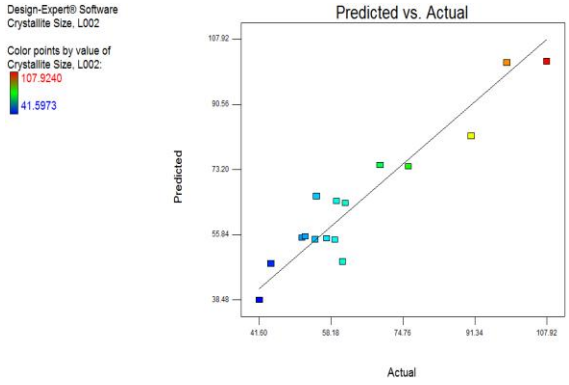

(B)

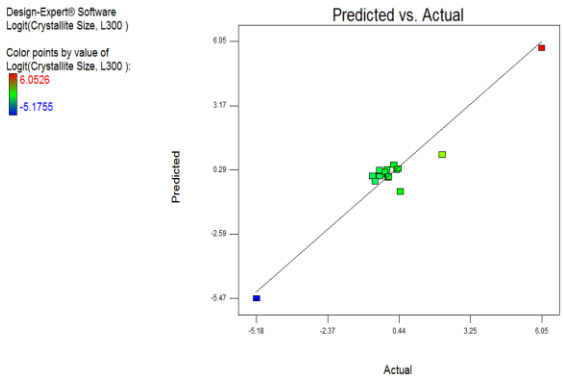

Figure 4-33: Scatter diagram for (A) crystallite size, L_{002} and (B) crystallite size L_{300}

4.4.6 Effect Of The Process Parameters On The Crystallite Size

The pareto charts for the crystallite size models for both the L_{002} and L_{300} planes, as illustrated in Figure 4-34(a) and (b), highlight the most significant parameters with either a positive or negative effect on each model. The order of the level of significance of the positive effects on the L_{002} model, from the most significant, follows the order: (atm.) > (T_o* t_r) > (Ca^{2+}) > (V_{ac}* t_r) > (V_{st}) > (T_o * atm.), while the only negative effect to significantly affect the L_{002} model is the ripening time (t_r). The order of the level of significance of the most significant positive effects on the L_{300} model follows the order: (V_{st}) > (V_{ac} * T_o * atm.) > (T_o * t_r) > (V_{ac} * T_o), while the order of the level of most significant negative effects follows the order: (V_{ac}* atm.) > (t_r) > (V_{ac}) > (V_{ac}* atm.) for the L_{002} model.

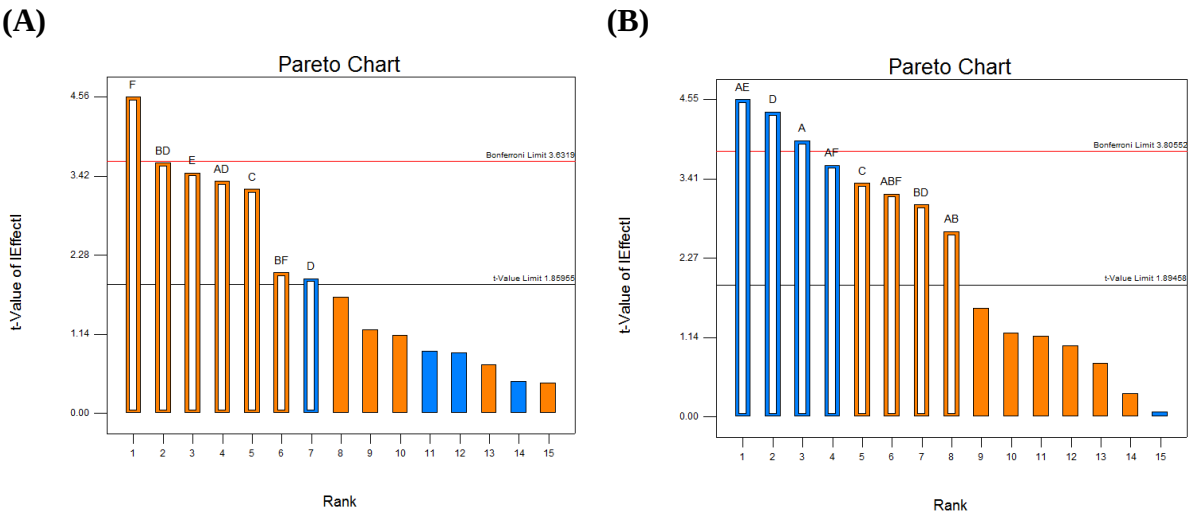

Figure 4-34: Pareto chart, examining the level of main and interaction effects (orange: positive effect and blue: negative effect) of the process parameter on (A) crystallite size in the 002 plane and (B) crystallite size in the 300 plane; where A is V_{ac}, B is T_o, C is V_{st}, D is t_r, E is Ca^{2+} conc. and F is atm.

Hence, if high levels of crystallite size in both planes are to be obtained, the top four most influencing effects for controlling both responses are as follows:

For Crystallite Size, L_{002} -

1.	Atmospheric Environment↑	(Main effect)
2.	Reaction temperature * Ripening time↑	(Two-way interaction effect)
3.	Calcium concentration↑	(Main effect)
4.	Acid addition rate * Ripening time↑	(Two-way interaction effect)

For Crystallite Size, L_{300} -

1.	Acid addition rate * Calcium concentration↓	(Two-way interaction effect)
2.	Ripening time↓	(Main effect)
3.	Acid addition rate↓	(Main effect)
4.	Acid addition rate * Atmospheric environment↓	(Two-way interaction effect)

Firstly, the top four most influencing effects are not similar in both cases of crystallite size for the two plane investigated. The factor most affecting the crystallite size in the 002 plane is the use of a controlled inert environment. The model dictates that the implementation of this parameter will increase the crystallite size in this plane. This theory is in good agreement with a similar finding by Smiciklas et al. [85] where a resulting increase of crystallite size for this plane was also reported, from the use of an inert atmosphere. The second most influencing factor for this plane is the two-way interaction effect between the reaction temperature and the ripening time. Smiciklas et al. [85] examined the effect of both factors as a main effect and reported that an increase in both contributed to an increase in the crystallite size for this plane. The third most influencing factor is the calcium concentration, for which an increase of this parameter can also produce a larger crystallite size for this plane. However, in comparison an increase of calcium concentration (interacting with the acid addition rate) can reduce the crystallite size in the 300 plane. Both results agree well with findings reported in a similar study [85]. The fourth most influencing factor is the two way interaction between the acid addition rate and the ripening time. Again, it has reported that both of these factors investigated as main effects can increase the crystallite size for this plane.

In contrast, a reduction of all four most influencing factors can acquire a larger crystallite size for the 300 plane. These findings correlate well with those reported by Smiciklas et al. [85], with the exception of ripening time, where it was reported that an increase was required for an increase in crystallite size for the 300 plane. The stirring speed is not found to be included as one of the four most influencing factors for both responses. However, it is shown to be the fifth for both, with a similar magnitude of positive influence (refer to Figures 4-34(a) and (b)).

Figure 4-35 and 4-36 show the perturbation plots highlighting the effect of all the parameters on the crystallite size in the 002 and 300 plane, respectively.

(A) **(B)**

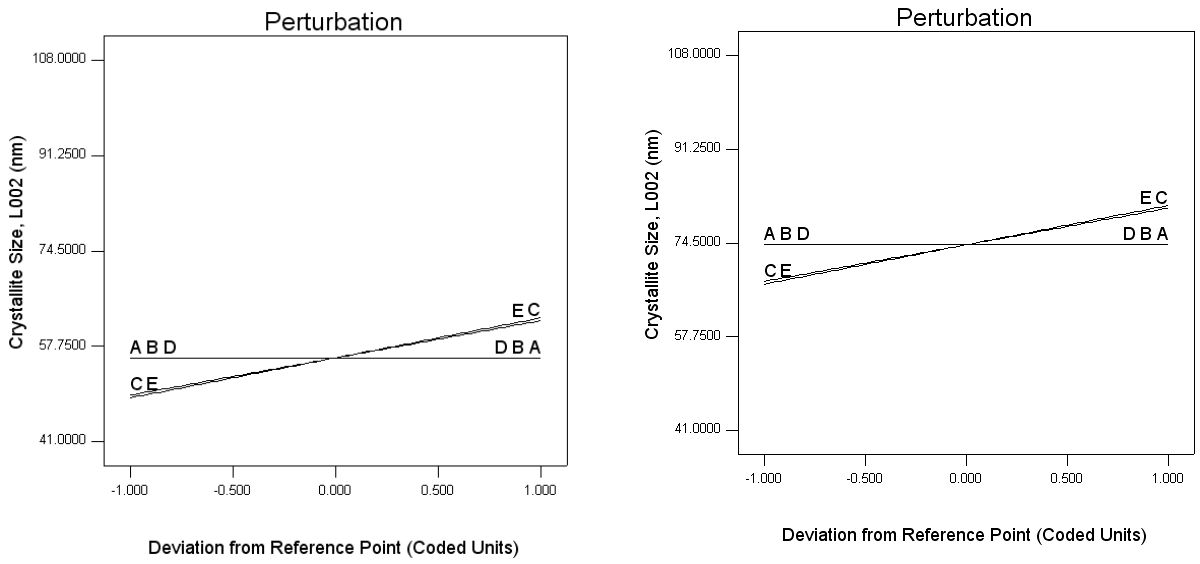

Figure 4-35: Perturbation plot showing the effect of all the parameters on the crystallite size, L_{002} under (A) an uncontrolled environment and (B) a controlled (inert) environment

(A) **(B)**

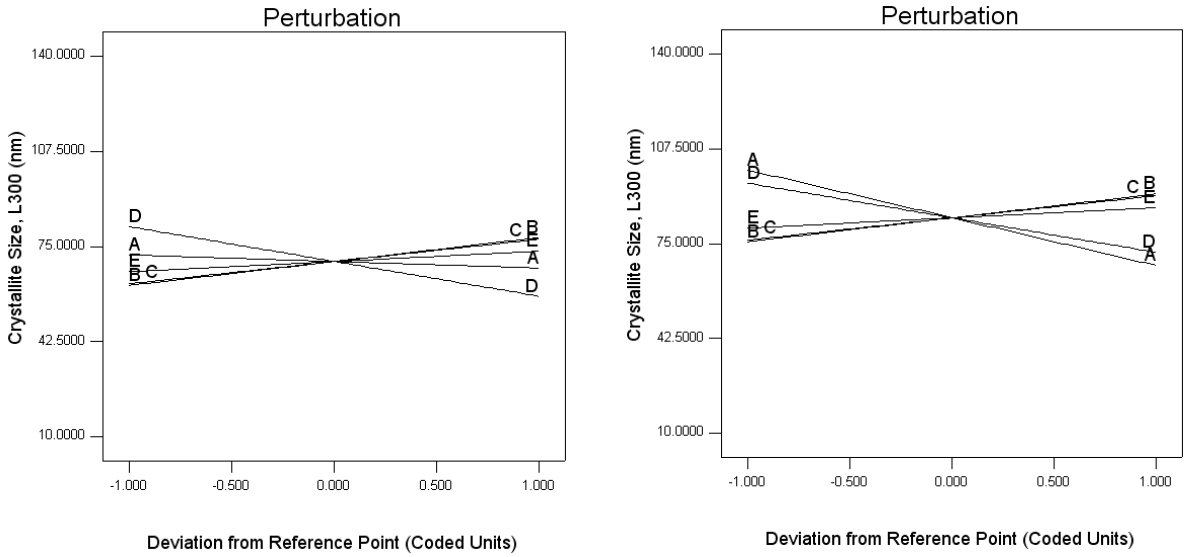

Figure 4-36: Perturbation plot showing the effect of all the parameters on the crystallite size, L_{300} under (A) an uncontrolled environment and (B) a controlled (inert) environment

4.4.7 Development Of Lattice Parameter Ratio Model

As indicated earlier, the test for significance of the regression models and the test for significance on individual model coefficients were performed using the Design Expert statistical software. Selecting the backward regression method allowed for the elimination of the insignificant model terms, automatically. The ANOVA table for the reduced linear model relating to the response of the lattice parameter ratio (a/c) was abstracted and is presented in Table 4-19. For this model, the 'Prob. > F' value does not exceed 0.1, which indicates that the models are statistically significant. Also the terms in this model has a significant effect on the response being investigated. The same tables show also the other adequacy measures such as the R^2 (the measure of the amount of variation around the mean explained by the model), adjusted R^2 (the measure of the amount of variation around the mean explained by the model adjusted for the amount of terms) and predicted R^2 values (the measure of the amount of variation in new data explained by the model). The entire adequacy measures are close to 1.00, which is in reasonable agreement and indicates adequate models are found for each response. The adequate precision compares the range of the predicted value at the design points to the average prediction error. In this case, the value of adequate precision is 16.042. An adequate precision ratio above 4 indicates adequate model discrimination.

The analysis of variance, indicates, that for the lattice parameter ratio (a/c) model, all of the chemical precipitation parameters, with the exclusion of atmospheric control have a significant effect on the resulting a/c ratio model, either as a main or interaction effect with another parameter. The main effects of the reaction temperature (T_o), stirring speed (V_{st}), ripening time (t_r), calcium concentration (Ca^{2+}) and the two way interaction effects of acid addition rate and reaction temperature (V_{ac}* T_o), acid addition rate and stirring speed (V_{ac}* V_{st}), acid addition rate and calcium concentration (V_{ac}* Ca^{2+}) are the most significant model terms associated with altering the lattice parameter ratio. It is clear that all the significant interaction effects included in the model involve the acid addition rate as an influencing variable to affect the resulting a/c ratio and hence it's crystallographic structure.

The final mathematical model for the lattice parameter ratio response in terms of coded factors, as determined by the Design Expert software is shown in Equation 4-15. While, the final mathematical models in terms of actual factors are presented in Equations 4-16.

Table 4-19: ANOVA table for a/c ratio reduced linear polynomial model

Source	Sum of squares	d.f.	Mean Square	*F* value	Prob >*F*
Model	0.0001630	7	0.00002329	25.93	<0.0001 Significant
T_o	0.0000092	1	0.00000915	10.19	0.0128
V_{st}	0.0000480	1	0.00004796	53.40	<0.0001
t_r	0.0000851	1	0.00008510	94.75	<0.0001
Ca^{2+}	0.0000054	1	0.00000541	6.02	0.0397
V_{ac} * T_o	0.0000041	1	0.00000410	4.57	0.0651
V_{ac} * V_{st}	0.0000039	1	0.00000390	4.34	0.0707
V_{ac} * Ca^{2+}	0.0000074	1	0.00000743	8.27	0.0207
Residual	0.0000047	8	0.00000090		
Corrected total	0.0001702	15			

R^2 = 0.9578; predicted R^2 = 0.8312; adjusted R^2 = 0.9209; adequate precision = 16.042

a/c ratio = 1.37

$$
\begin{aligned}
&- 7.563e\text{-}004 && * T_o \\
&- 1.731e\text{-}003 && * V_{st} \\
&- 2.306e\text{-}003 && * t_r \\
&+ 5.812e\text{-}004 && * Ca^{2+} \\
&+ 5.063e\text{-}004 && * V_{ac} * T_o \\
&- 4.937e\text{-}004 && * V_{ac} * V_{st} \\
&- 6.812e\text{-}004 && * V_{ac} * Ca^{2+}
\end{aligned}
$$

Equation (4-15)

a/c ratio = +1.38138

-1.26577E-004	* Reaction Temp
-1.22065E-006	* Stirring Speed
-9.71053E-005	* Ripening Time
+2.61393E-003	* Ca^{2+} Conc.
+0.011835	* H_3PO_4 addition rate * Reaction Temp
-3.50210E-004	* H_3PO_4 addition rate * Stirring Speed
-0.26694	* H_3PO_4 addition rate * Ca^{2+} Conc.

Equation (4-16)

Figure 4-37 shows the relationship between the actual and predicted values of the lattice parameter ratio. This figure indicates that the developed model is adequate, since the residuals in the prediction of each response are small, with the residuals tending to be close to the diagonal line. The range of values appears to lie in three clusters between a minimum of ~1.369, an average of ~1.374 and a maximum value of ~1.378.

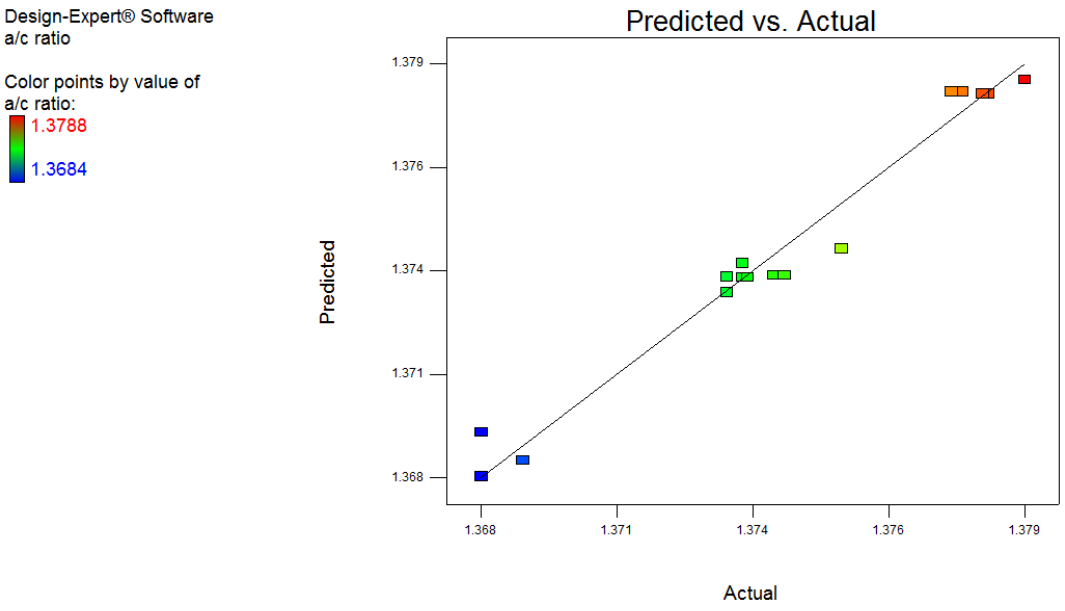

Figure 4-37: Scatter diagram for lattice parameter ratio

4.4.8 Effect Of The Process Parameters On The Lattice Parameter Ratio

The pareto chart for the lattice parameter ratio model, as illustrated in Figure 4-38, highlights the most significant parameters affecting the model. The order of the level of significance of the positive effects of the chemical precipitation process parameters on the a/c ratio follows the order: $(Ca^{2+}) > (V_{ac} * T_o)$ while the order of the level of significance of the negative effects on the lattice parameter ratio is as follows: $(t_r) > (V_{st}) > (T_o) > (V_{ac} * Ca^{2+}) > (V_{ac} * V_{st})$.

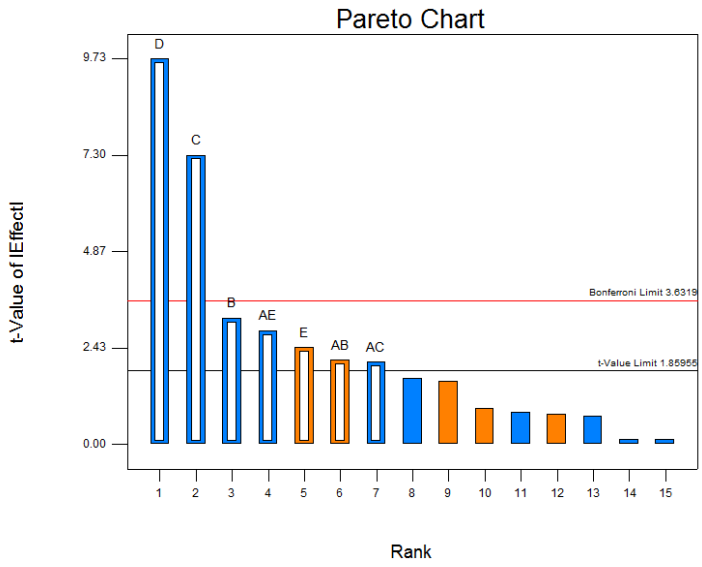

Figure 4-38: Pareto chart, examining the level of main and interaction effects (orange: positive effect and blue: negative effect) of the process parameter on the lattice parameter ratio; where A is V_{ac}, B is T_o, C is V_{st}, D is t_r and E is Ca^{2+} Conc.

Although, if a low lattice parameter ratio is required, the top four most influencing effects for controlling this response are as follows:

1. Ripening time↑ (Main effect)
2. Stirring speed↑ (Main effect)
3. Reaction temperature↑ (Main effect)
4. Acid addition rate * Calcium concentration↑ (Two-way interaction effect)

The factor most affecting the lattice parameter ratio is the ripening time. Increasing the ripening time indicates that a decrease in the ratio can be achieved, representing a contraction in the *a* direction and an expansion in the *c* direction. On the other hand, β-TCP is promoted with an expansion in the *a* direction and a contraction in the *c* direction [64]. The second and third highest factors most affecting the lattice parameter ratio is the stirring speed and reaction temperature, respectively. Increasing both parameters can result in a decrease of the lattice parameter ratio response. The fourth highest significant effect involves a two-way interaction between the acid addition rate and the calcium concentration. A combined increase of both these parameters can also result in a decrease of the lattice parameter ratio.

Figure 4-39 shows a perturbation plot highlighting the effect of all parameters on the lattice parameter ratio. Contour plots examining the main interaction effects are shown in Figure 4-40. A study of the qualitative effects of the chemical precipitation parameters on the resulting crystal structure (see Table 4-20) for each experimental conditions, with regards the resultant changes in lattice parameters on account of some substitutions for Ca^{2+}, PO_4^{3+} or OH^- of the calcium phosphate apatite, yielded the following conclusions: (i) eleven of the experiments (N1-N6, N8-N9 and N11-N13) resulted in an expansion in the *a*-axis and a contraction in the *c*-axis on account of undesirable ionic substitutions, (ii) four of the experiments (N7, N14-N16) resulted in a contraction of both the *a*- and *c*-axis and (iii) one experiment (N10) accounted for an expansion in both the *a*- and *c*-axis. Both an expansion in the *a*-axis and a contraction in the *c*-axis and a contraction in both the *a*- and *c*-axis may be accounted for by the following heterionic exchanges / ionic substitutions outlined in Table 4-21.

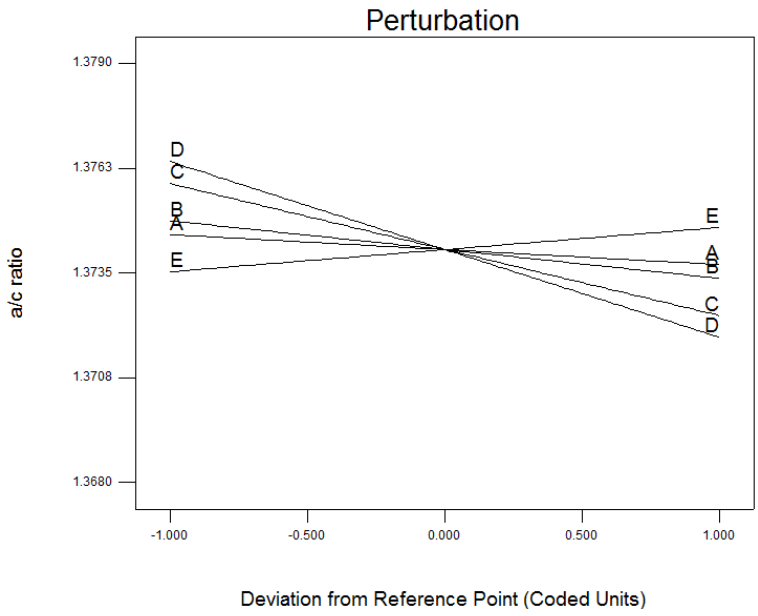

Figure 4-39: Perturbation plot showing the effect of all the parameters on the lattice parameter ratio

Table 4-20: Study of the qualtitative effect of the chemical precipitation process parameters on changes in the lattice parameters (*a*- and *c*-)

	Lattice Parameter Change	
	***a*-axis**	***c*-axis**
N1	+	-
N2	+	-
N3	+	-
N4	+	-
N5	+	-
N6	+	-
N7	-	-
N8	+	-
N9	+	-
N10	+	+
N11	+	-
N12	+	-
N13	+	-
N14	-	-
N15	-	-
N16	-	-

(A) Ripening Time: 48h

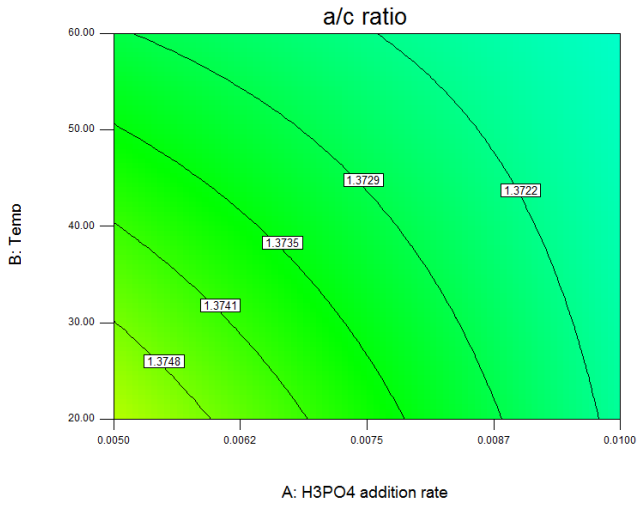

(B) Ripening Time: 24h

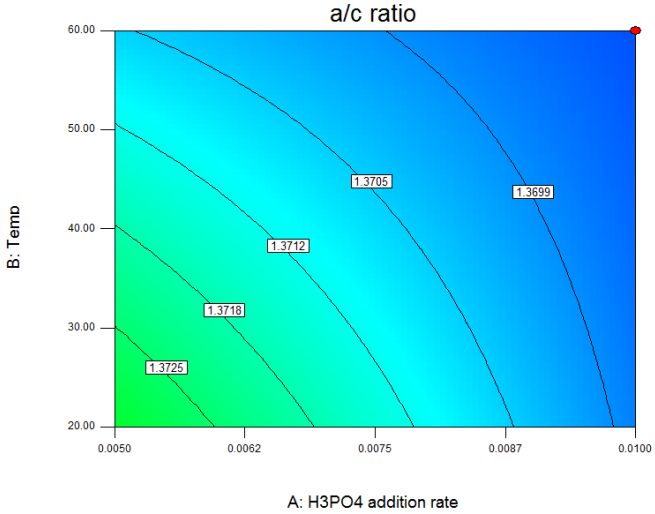

(C) Ripening Time: 0.5h

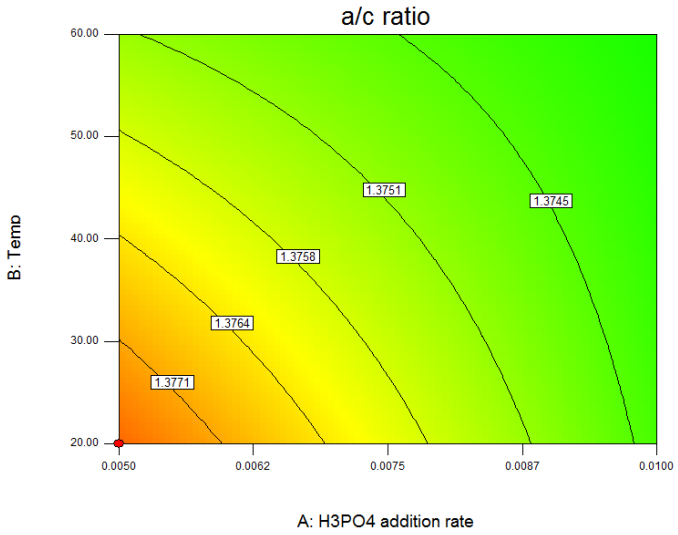

Figure 4-40: Effect of V_{ac} and T_o on the lattice parameter ration at (A) a ripening time of 48h; (B) a ripening time of 24h and (C) a ripening time of 0.5h, (under a controlled environment at V_{st} = 1500rpm and Ca^{2+} = 2.0M)

Table 4-21: Heterionic exchanges and ionic substitutions and their effect on the crystal structure [64]

Ion	Exchange for	Ion radius (nm)	Inclusion type	Lattice parameter change	Effect on crystal structure
CO_3^{2-}	OH^-		A-Type Substitution	a+ c-	C at Ca hexagonal centre, tilted at 30°
Cl^-	OH^-		subst/surf	a+ c-	
Zn		0.74		a+ c-	-Decreases crystallinity -Promotes β-TCP
Co		0.70		a+ c-	-Decreases crystallinity -Promotes β-TCP
Ni		0.69		a+ c-	-Decreases crystallinity -Promotes β-TCP
Cr		0.63		a+ c-	-Decreases crystallinity
Mg^{2+}	Ca^{2+}	0.66	subst/surf	a- c-	-Increases solubility -Inhibits ACP ->HAp -Decreases crystallinity -Promotes β-TCP
Cd^{2-}	Ca^{2+}	0.97	subst	a- c-	-Decreases crystallinity
Mn^{2+}	Ca^{2+}	0.80	subst	a- c-	-Decreases crystallinity -Subst Ca I in fluoro. And Ca II in chloro.
Cu		0.97		a- c-	-Decreases crystallinity -Reduces bone resorption

4.4.9 Development Of Particle Size Model

As with all the preceding models, the test for significance of the regression models and the test for significance on individual model coefficients were performed using the Design Expert statistical software. Selecting the backward regression method allowed for the elimination of the insignificant model terms, automatically. The ANOVA table for the reduced linear model relating to the particle size response is abstracted and presented in Table 4-21. For this model, the 'Prob. > F' value does not exceed 0.05, which indicates that the model developed is statistically significant. Also, the terms in this model have a significant effect on the response under investigation. The same tables show also the other adequacy measures such as the R^2, adjusted R^2 and predicted R^2 values. The entire adequacy measures are close to 1.00, and indicates adequacy of the model found for the particle size response. In this case the value of adequate precision is 18.284. An adequate precision ratio above 4 indicates adequate model discrimination.

The analysis of variance, indicates, that for the particle size model, all of the chemical precipitation parameters have a significant effect on the resulting model, either as a main or interaction effect with another parameter. The main effects of the reaction temperature (T_o), stirring speed (V_{st}), calcium concentration (Ca^{2+}), atmospheric control (atm.) and the two way interaction effects of acid addition rate and reaction temperature (V_{ac}* T_o), acid addition rate and calcium concentration (V_{ac}* Ca^{2+}), acid addition rate and atmospheric environment (V_{ac} * atm.) and the reaction temperature and ripening time (T_o * t_r) are the most significant model terms associated with affecting the particle size. The final mathematical model for the particle size response in terms of coded factors, as determined by the Design Expert software is shown in Equation 4-17. While, the final mathematical models in terms of actual factors are presented in Equations 4-18 and 4-19 for the response on the particle size, under an uncontrolled and inert atmospheric environment, respectively.

Table 4-22: ANOVA table for particle size reduced linear polynomial model

Source	Sum of squares	d.f.	Mean Square	*F* value	Prob >*F*
Model	3831.58	8	478.95	40.82	<0.0001
T_o	1485.52	1	1485.52	126.60	<0.0001
V_{st}	100.45	1	100.45	8.56	0.0222
Ca^{2+}	1389.24	1	1389.24	118.39	<0.0001
atm.	65.81	1	65.81	5.61	0.0497
V_{ac} * T_o	298.17	1	298.17	25.41	0.0015
V_{ac} * Ca^{2+}	215.28	1	215.28	18.35	0.0036
V_{ac} * atm.	200.15	1	200.15	17.06	0.0044
T_o * t_r	76.96	1	76.96	6.56	0.0375
Residual	82.14	7	11.73		
Corrected total	3913.73	15			

R^2 = 0.9790; predicted R^2 = 0.8903 ; adjusted R^2 = 0.9550; adequate precision = 18.284

Particle Size, = 39.34

P_s (μm) – 9.64 * T_o
– 2.51 * V_{st}
– 9.32 * Ca^{2+}
+ 2.03 * atm.
+ 4.32 * V_{ac}* T_o
– 3.67 * V_{ac}* Ca^{2+}
– 3.54 * V_{ac}* atm.
+ 2.19 * T_o * t_r *Equation (4-17)*

For an uncontrolled atmospheric environment:

Particle Size = +62.12231

P_s (μm) -0.92449 * Reaction Temp
-5.56806E-003 * Stirring Speed
+4.14248 * Ca^{2+} Conc.
+59.20540 * H_3PO_4 addition rate * Reaction Temp
-1860.13802 * H_3PO_4 addition rate * Ca^{2+} Conc.
+5.50000E-005 * Reaction Temp * Ripening Time *Equation (4-18)*

For a controlled (inert) atmospheric environment:

Particle Size, = +87.39981

Ps (µm) -0.92449 * Reaction Temp

-5.56806E-003 * Stirring Speed

+4.14248 * Ca^{2+} Conc.

+59.20540 * H_3PO_4 addition rate * Reaction Temp

-1860.13802 * H_3PO_4 addition rate * Ca^{2+} Conc.

+5.50000E-005 * Reaction Temp * Ripening Time *Equation (4-19)*

Figure 4-41 shows the relationship between the actual and predicted values of the particle size. This figure indicates that the developed model is adequate, since the residuals in the prediction of each response are small, with the residuals tending to be close to the diagonal line.

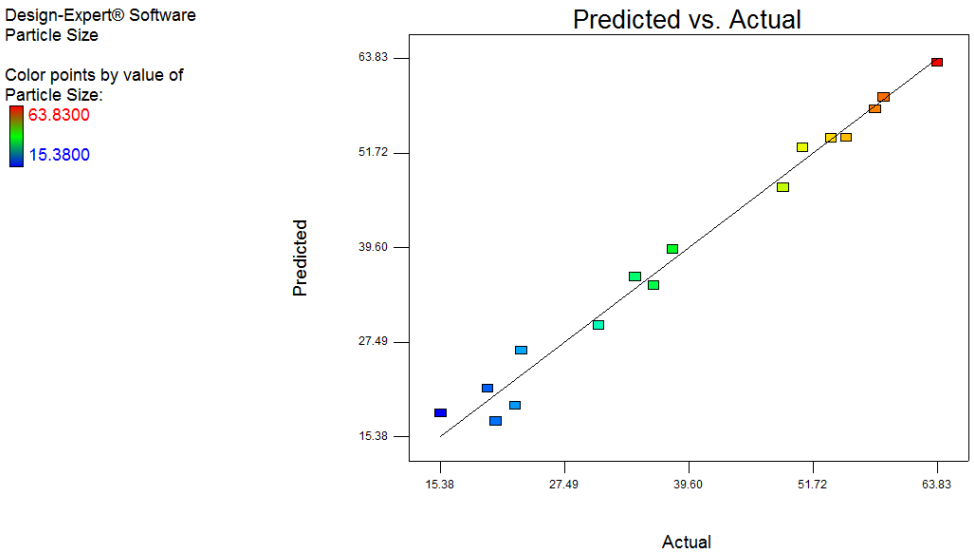

Figure 4-41: Scatter diagram for particle size

4.4.10 Effect Of The Process Parameters On The Particle Size

Particle size has a great effect on the final quality of the plasma sprayed HAp coating. The particle size will affect their melting characteristics within the plasma flame. Fine particles experience good heat transfer from the plasma flame causing them to melt, producing a dense coating with low porosity. Extremely fine particles, however, may evaporate before reaching the substrate. Very large particles (>100μm) are to be avoided, as they often remain unmelted. Unmelted particles may damage the coating surface by rebounding off it or may remain weakly connected to the rest of the coating, thus, reducing coating tougnhess [24, 103, 130]. Furthermore, osteoconductivity, solubility, sinterability and mechanical reliability of the HAp can be promoted by controlling its particle size [59]. The particle size distribution also influences the coating quality. During plasma spraying, HAp, of a narrow particle size range has better flow behaviour, in comparison to mixed sizes, comprising of both large and fine particles [24]. These studies clearly demonstrate the necessity in tailoring the HAp particle size and particle size distribution

The pareto chart for the particle size model, as illustrated in Figure 4-42, highlights the most significant parameters affecting the model. The order of the level of significance of the positive effects of the chemical precipitation process parameters on the actual particle size follows the order: $(V_{ac} * T_o) > (T_o * t_r) >$ (atm.) while the order of the level of significance of the negative effects on the lattice parameter ratio is as follows: $(T_o) > (Ca^{2+}) > (V_{ac} * Ca^{2+}) > (V_{ac} *$ atm.$) > (V_{st})$.

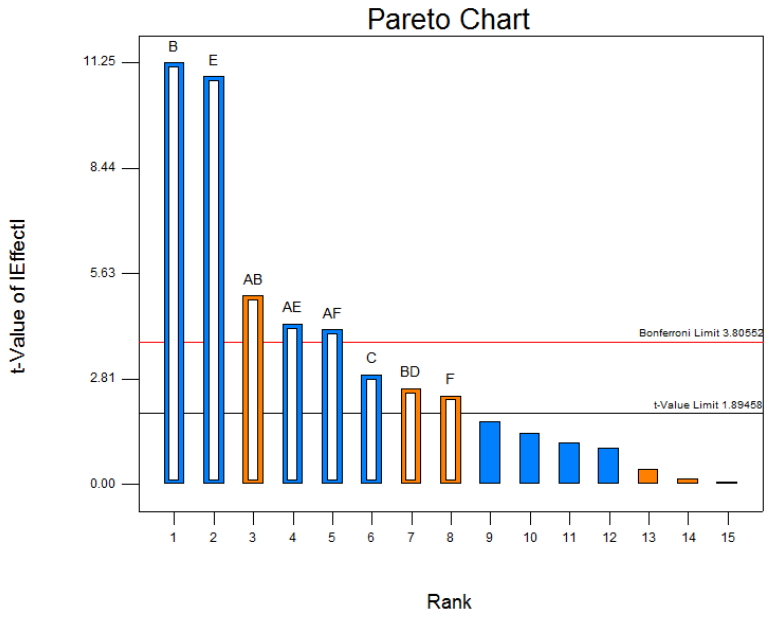

Figure 4-42: Pareto chart, examining the level of main and interaction effects (orange: positive effect and blue: negative effect) of the process parameter on the particle size; where A is V_{ac}, B is T_o, C is V_{st}, D is t_r, E is Ca^{2+} conc. and F is atm.

Hence, if low particle sizes are to be obtained, the top four most influencing effects for controlling this response are as follows:

1. Reaction temperature↑ (Main effect)
2. Calcium Concentration↑ (Main effect)
3. Acid addition rate * Reaction temperature↓ (Two-way interaction effect)
4. Acid addition rate * Calcium concentration↑ (Two-way interaction effect)

The top two most influencing factors affecting the particle size is the reaction temperature and calcium concentration, indicating an increase in both factors can result in a decrease for this response. However, the third most influencing effect suggests that the reaction temperature is also involved in an interaction effect with the acid addition rate and a reduction in both can yield higher powder particle sizes, as expected from literature [23]. The fourth most significant effect involves another two-way interaction between the acid addition rate and the calcium concentration, requiring an increase for a reduction in particle size.

Figure 4-43 shows a perturbation plot highlighting the effect of all parameters on the particle size under (a) an uncontrolled atmosphere and (b) a controlled inert environment. Contour plots examining the most significant effects are shown in Figure 4-44. These plots indicate that a larger particle size results when the addition rate of the acid is lowered and this phenomenon agrees well with that hypothesised by Afshar et al. [83]. The model also demonstrates that the lower acid addition rate coupled with a lower synthesis temperature is favoured in producing larger size HAp particles. However, the calcium concentration is shown to also play a major role in determining the final particle size.

(A) **(B)**

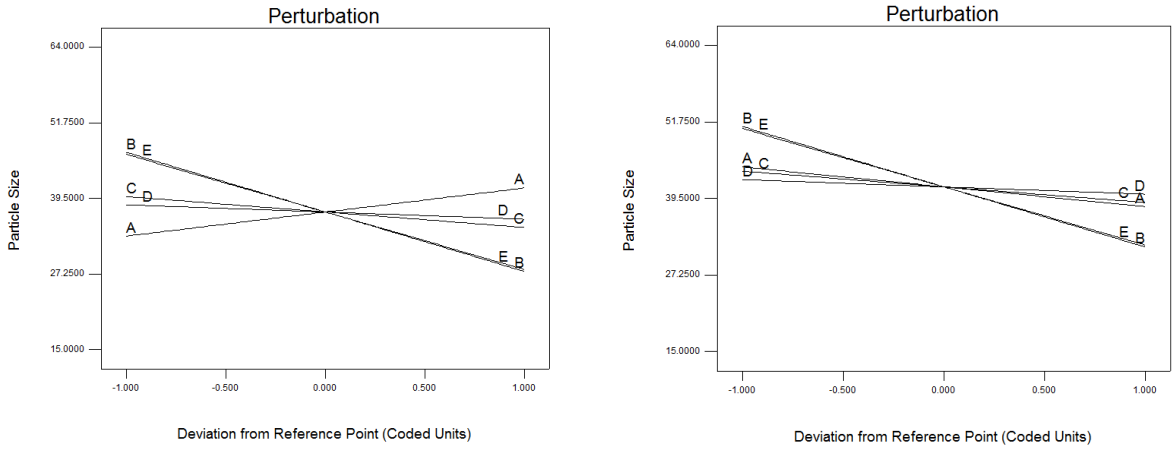

Figure 4-43: Perturbation plot showing the effect of all the parameters on the particle size under (A) an uncontrolled environment and (B) a controlled (inert) environment

(A) Ca^{2+} Conc.: 2.0M

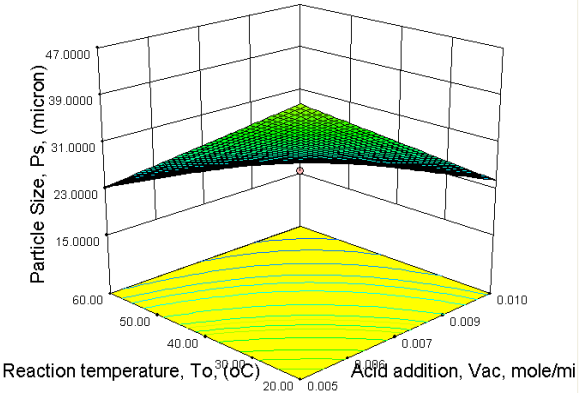

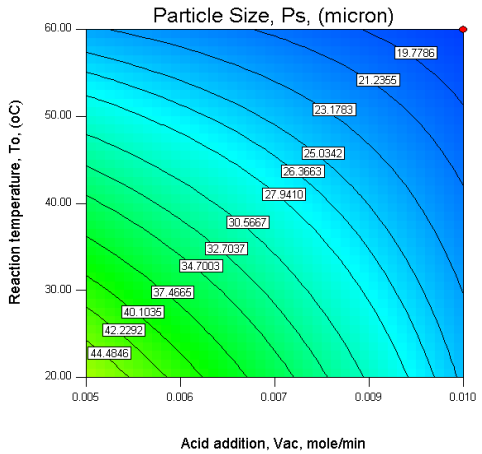

(B) Ca^{2+} Conc.: 1.0M

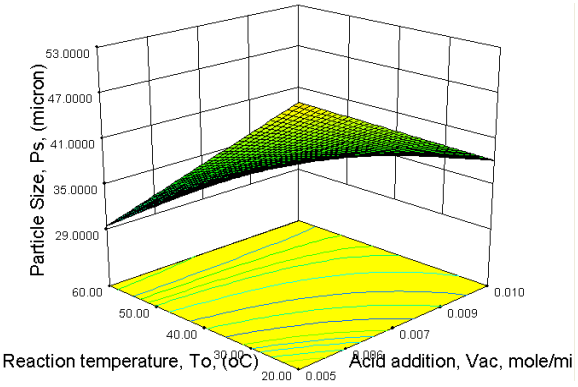

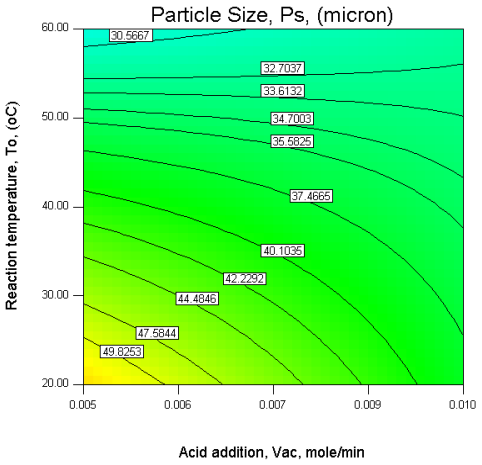

(C) Ca^{2+} Conc.: 0.1M

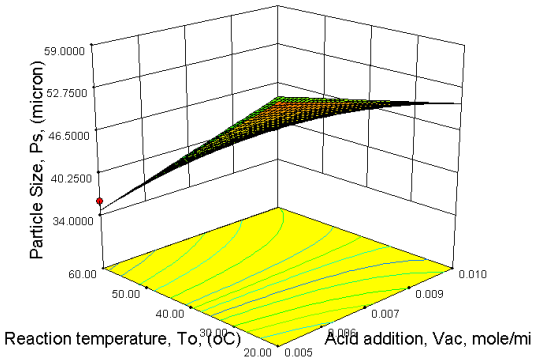

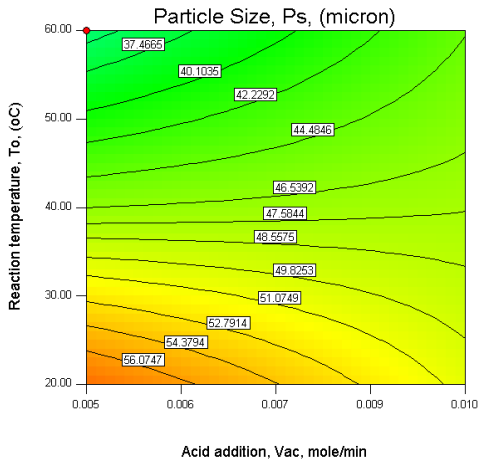

Figure 4-44: 3D surface and 2D contour plots of particle size at (A) a Ca^{2+} conc. of 2.0M; (B) a Ca^{2+} conc. of 1.0M and (C) a Ca^{2+} conc. of 0.1M (under a controlled environment at V_{st} = 1500rpm and t_r = 48h)

Table 4-23 outlines the average of three results recorded for mode, mean particle sizes and the percentage (10, 50 and 90%) of powder particles within a specific range. Figure 4-45 graphically compares the mean particle sizes obtained for the micron sized HAp powders analysed with and without a controlled (inert) environment. The order of mean particle size from the largest is as follows:

N9 → N1 → N6 → N5 → N14 → N12 →N4 → N2 → N15 → N13 → N10 → N3 → N8 → N11 → N7 → N16

The largest particle sizes (such as, N1, N5, N6, N9 and N14) were all synthesised at a reaction synthesis temperature of 20ºC, while the lowest particle sizes (such as, N3, N7, N8, N11 and N16) were synthesised at a higher reaction synthesis temperature of 60ºC. Adversely, previous literature highlights that during the course of precipitation, the particle size increases with an increase in temperature. An increase in the temperature, coupled with an increase in the calcium concentration (N6 to N8) and (N14 to N16) also demonstrates an increase in particle size, while lowering the acid addition rate is shown to also result in an increase of particle size (N4 to N1) and (N16 to N14).

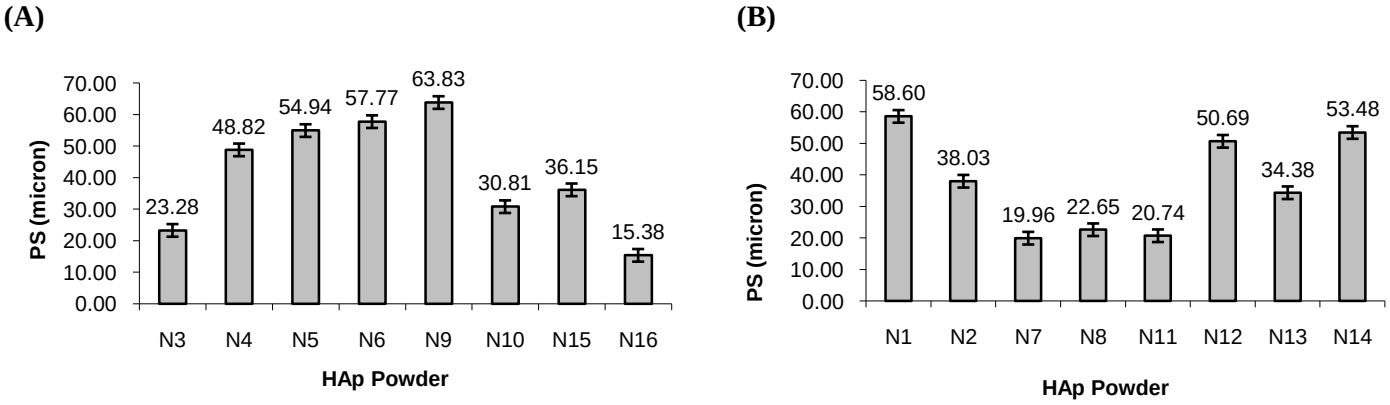

Figure 4-45: Comparison of the mean particle size results for HAp samples synthesised in (A) an uncontrolled atmosphere and (B) a controlled (inert) atmospheric environment

Consequently, there is a strong indication that a high reactant concentration, low acid addition rate and high synthesis temperature are the controlling factors in increasing the HAp powder particle size. The majority of the powders synthesised in this study, possess a narrow particle size distribution, as indicated in Figures 4-46 to 4-48. The

powders demonstrating a large particle size distribution (N11>N10>N2>N13>N8) are believed to have decreased flow behaviour during plasma spraying as opposed to a narrow particle size distribution. The order suggests that the powders synthesised under the lower level of stirring speed (600rpm) may have affected this distribution.

Table 4-23: Particle size analysis results: percentage diameter under 10, 50 and 90% micrometer, mean particle size, mode particle size and specific surface area data of the different HA samples for sixteen conditions of Fractional-Factorial (Res IV) experimental design

HAp Powder	Median	Diameter (µm) on:			Mean	Mode
	(µm)	10%	50%	90%	(µm)	(µm)
N1	20.00	14.33	52.98	111.21	58.60	76.32
N2	6.44	3.41	26.83	90.06	38.03	65.51
N3	9.24	4.71	19.44	47.76	23.28	30.53
N4	7.29	5.36	36.57	104.67	48.82	56.23
N5	11.13	6.53	48.61	110.01	54.94	76.32
N6	15.97	9.88	50.42	116.82	57.77	76.32
N7	10.07	5.64	16.06	39.43	19.96	19.31
N8	4.88	2.11	15.12	54.74	22.65	35.56
N9	8.10	7.96	56.15	130.35	63.83	88.91
N10	4.81	2.35	19.56	76.76	30.81	56.23
N11	4.11	1.71	11.71	54.36	20.74	12.21
N12	11.69	6.83	42.44	107.39	50.69	65.51
N13	6.01	2.99	23.51	82.23	34.38	56.23
N14	9.01	8.96	47.55	106.80	53.48	76.32
N15	8.24	8.43	30.79	70.92	36.15	41.43
N16	3.78	2.97	10.76	32.96	15.38	12.21

(A)

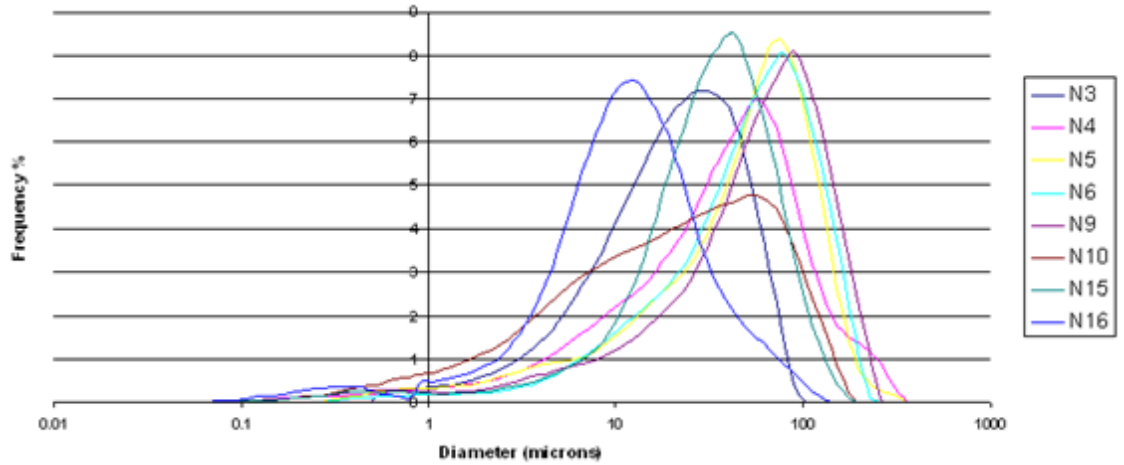

(B)

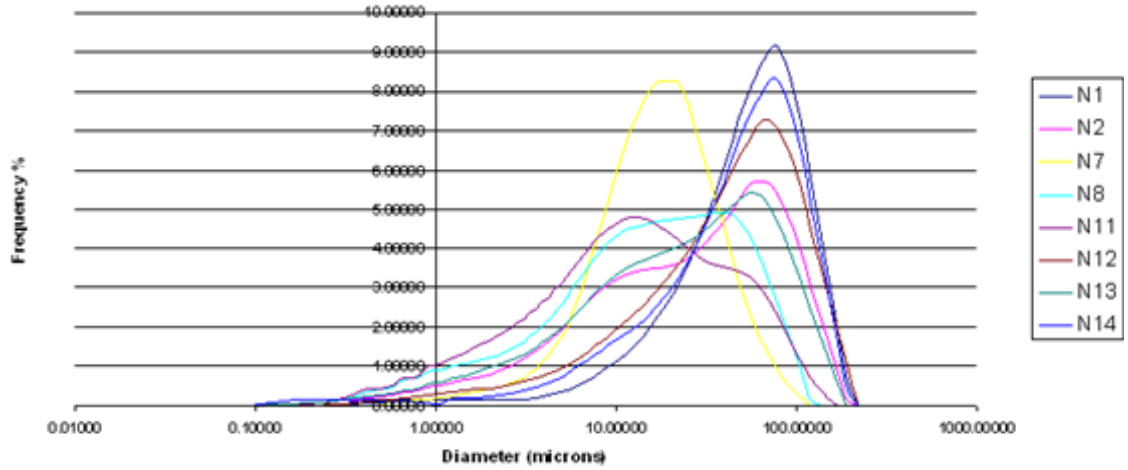

Figure 4-46: Comparison of particle size distributions obtained for screening experimental HAp powders synthesised under (A) an uncontrolled atmospheric environment and (B) a controlled (inert) environment

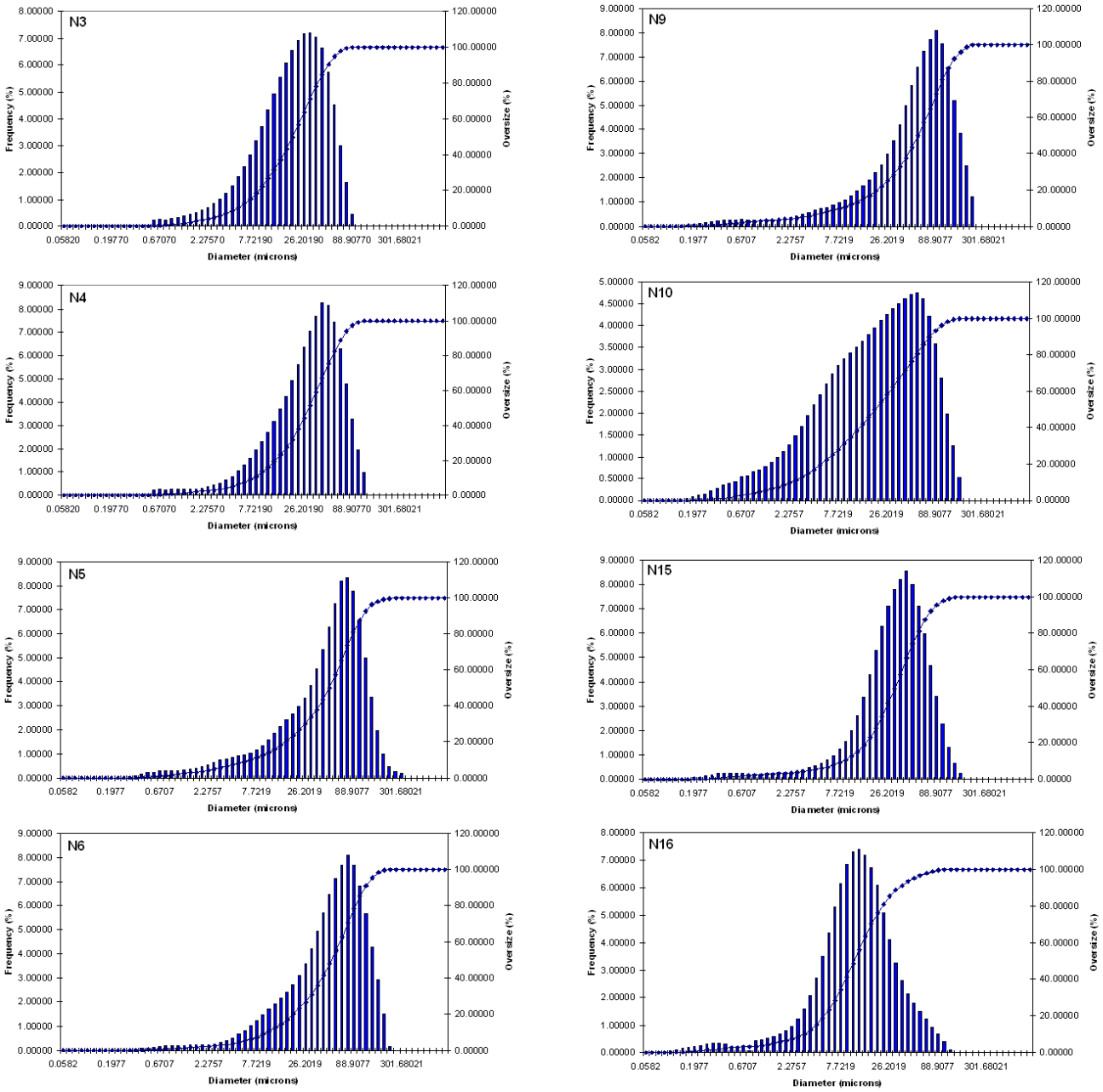

Figure 4-47: Comparison of particle size distributions obtained for screening experimental HAp powders synthesised under an uncontrolled atmospheric environment

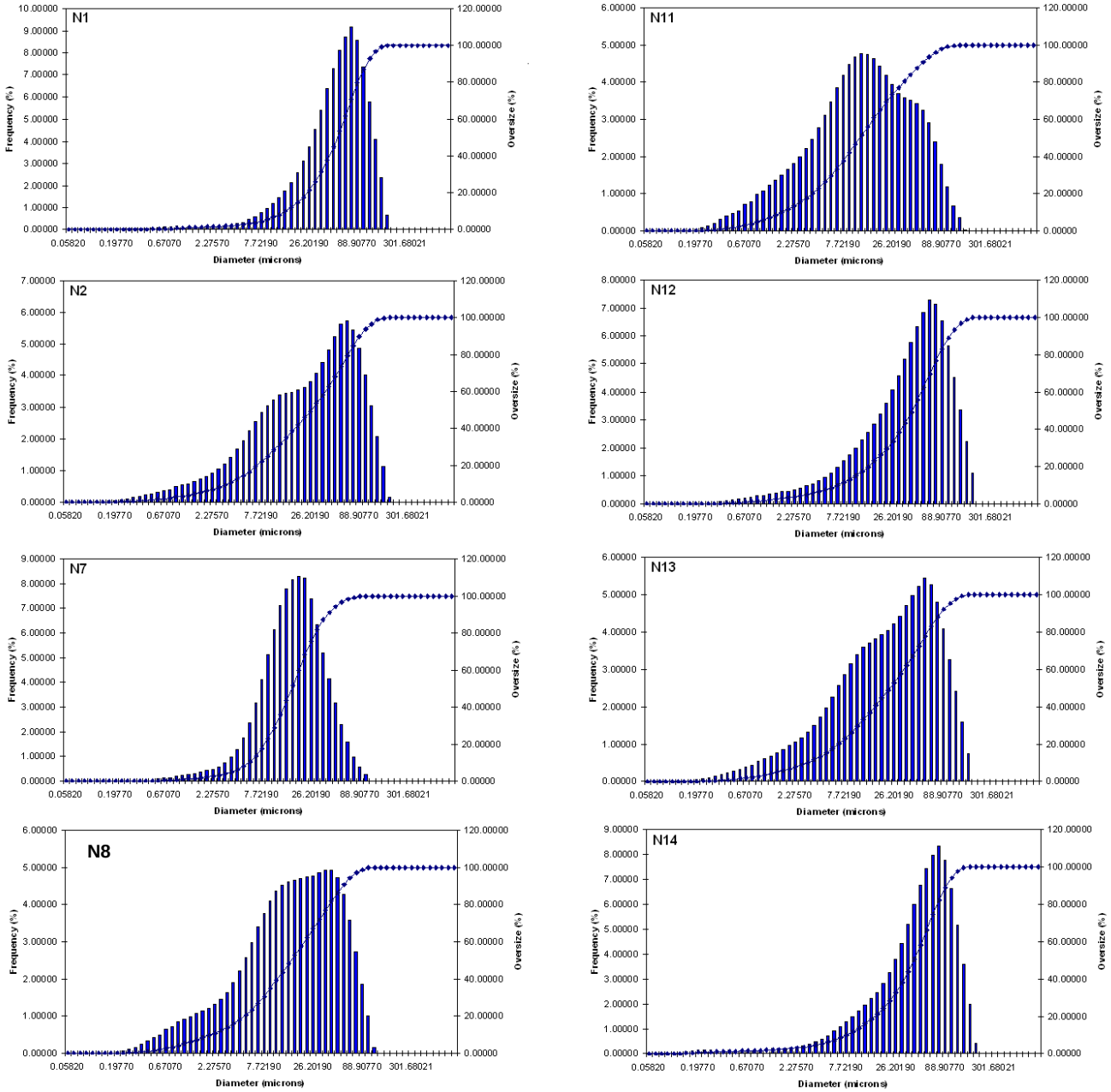

Figure 4-48: Comparison of particle size distributions obtained for screening experimental HAp powders synthesised under a controlled (inert) environment

4.4.11 Morphological Evaluation Of the HAp Powders

According to Kweh et al. [2], HAp powders of a spherical morphology produce excellent heat transfer characteristics and consistent melting behaviour, which increase the deposition efficiency of the HAp powder through plasma spray onto orthopaedic implants and decrease coating porosity. There is also evidence suggesting that angular Ca-dHAp powders produce relatively poor coating characteristics with large pores and cavities [21]. A poor structural integrity is attributed to the limited inter-particle cohesion. Some microstructural improvements are observed in using spherical powders with Joseph et al. [190] demonstrating that the surface morphology of HAp exerts a considerable influence on controlling the rheology of a HAp-HDPE composite.

The SEM micrographs of the HAp powders in Figure 4-49 and 4-50 reveal how the HAp powders can vary according to the process parameters implemented. An increase of the synthesis temperature (N1 to N4 and N14 to N16) is found to lead to more regular spherical HAp particles (see Figure 4-51). It has been reported elsewhere, that a low synthesis temperature results in HAp crystals possessing a needle-shape like morphology [94]. Pang and Bao [90] found that the particles synthesised at low reaction temperature were a bit thinner and longer, with more irregular and less clear contours. Also the particles showed a higher tendancy towards agglomeration. Moreover, they noticed that the change from irregular to regular particle morphology with the increase in synthesis temperature corresponds to the increase in the crystallinity of the HAp crystals, that is, more regular shape of the particles was observed when the powders had higher crystallinity. Hence, it is clear that the influence of the chemical precipitation process parameters on the morphology of the HAp powders must be inviestigated.

A qualitative examination of the effect of increasing the reaction synthesis temperature, coupled with an increase in the acid addition rate (N1 to N4 and N9 to N12) demonstrates how the powder particle size increases, as a result. Therefore, while a higher reaction synthesis temperature, is thought to increase the particle size, the effect of increasing the acid addition rate is more significant in controlling the particle size. Instead, the lower acid addition rate appears to be the more controlling

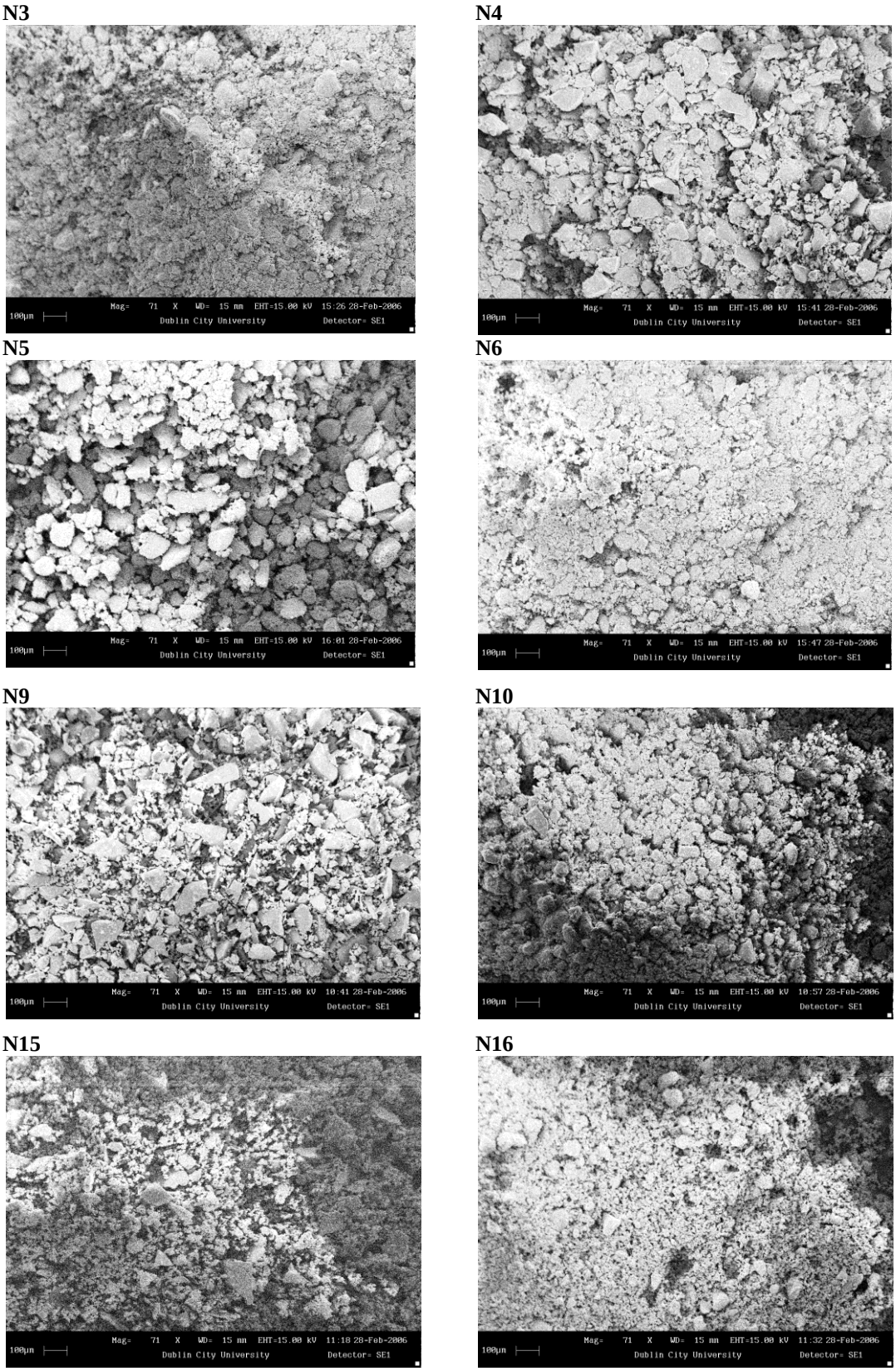

Figure 4-49: Comparison of the powder morphology for HAp samples synthesised under uncontrolled environment

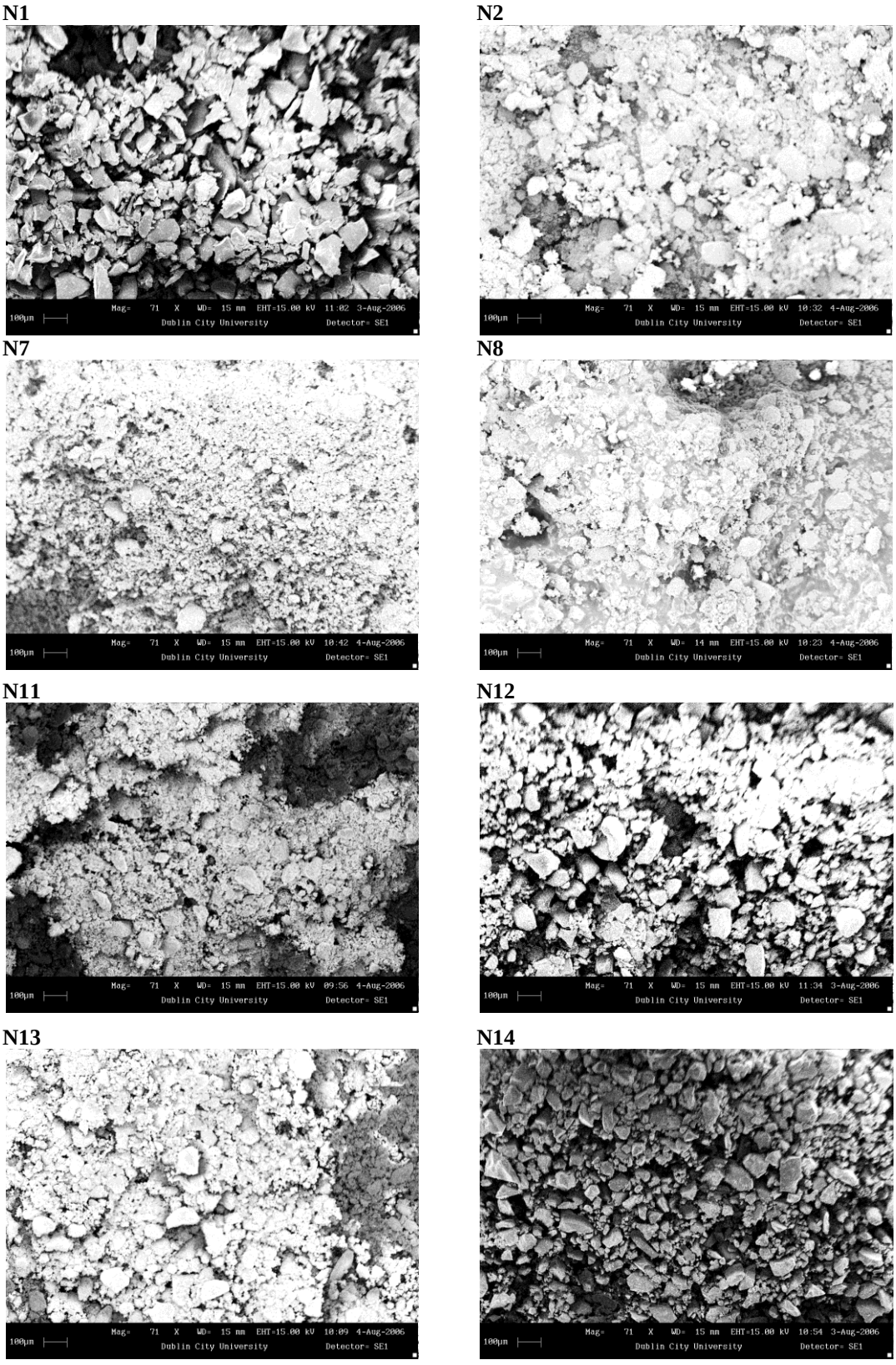

Figure 4-50: Comparison of the powder morphology for HAp samples synthesised under a controlled (inert) environment

factor in increasing the particle size, as previosuly demonstrated by Afshar et al. [83]. The results for particle size and powder morphology also indicate how a lower calcium concentration favour an increase in particle size (N6 to N8 and N14 to N16).

(A) Reaction Temperature (20ºC)

N1

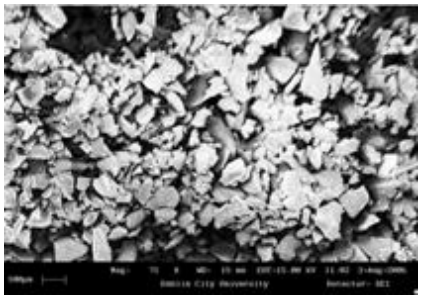

N14

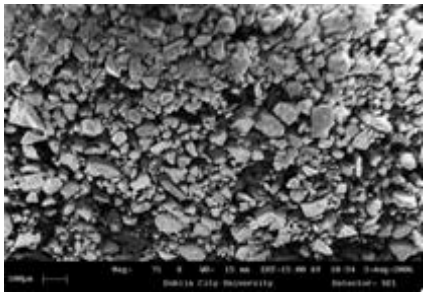

(B) Reaction Temperature (60ºC)

N4

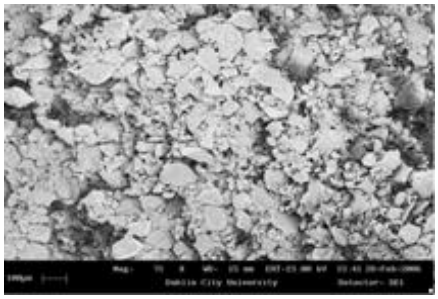

N16

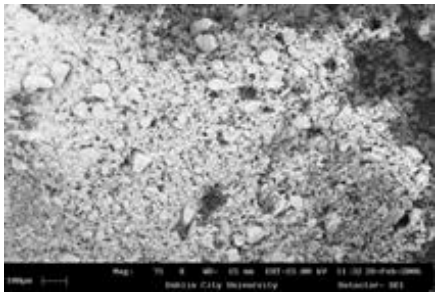

Figure 4-51: Effect of reaction synthesis temperature at (A) 20ºC and (B) 60ºC on powder morphology

Both N4 and N16 where also synthesised under a controlled inert environment, which may also suggest that it may be an influencing factor in controlling the morphological properties of the powder particle. Visible colour changes from white to light blue were evident after the sintering stages of the HAp powder (N12 and N13). According to Gross et al. [70], these colour changes are due to the presence of transitional elements located in the crystal lattice structure. Although they may not have any significant effect on the biocompatibility of HAp, the FDA criterion requires powders of a pure white colour [137].

4.4.12 Powder Flowability Evaluation

The flowability of the powders, as determined according to ASTMB213-03 [183] can be seen in Figure 4-52. As discussed previously, there exists a direct correlation between the particle size and the resulting powder flowability. For large powder particles (N1, N5, N6, N9, N14) the flow rate of the powders ranges between 0.24 to 0.28 g/s, whereas the finer powder particles (N3, N7, N8, N10, N11, N13, N16) demonstrate a flow rate ranging between 0.186 to 0.19 g/s. All powder flows were observed to flow discontinuously (that is, in a pulsating manner), the degree of which was dependent upon its morphology. The flowability of the powder studied in this investigation follow the same order as that of the mean particle size:

N9 → N1 → N6 → N5 → N14 → N12 →N4 → N2 → N15 → N13 → N10 → N3 → N8 → N11 → N7 → N16

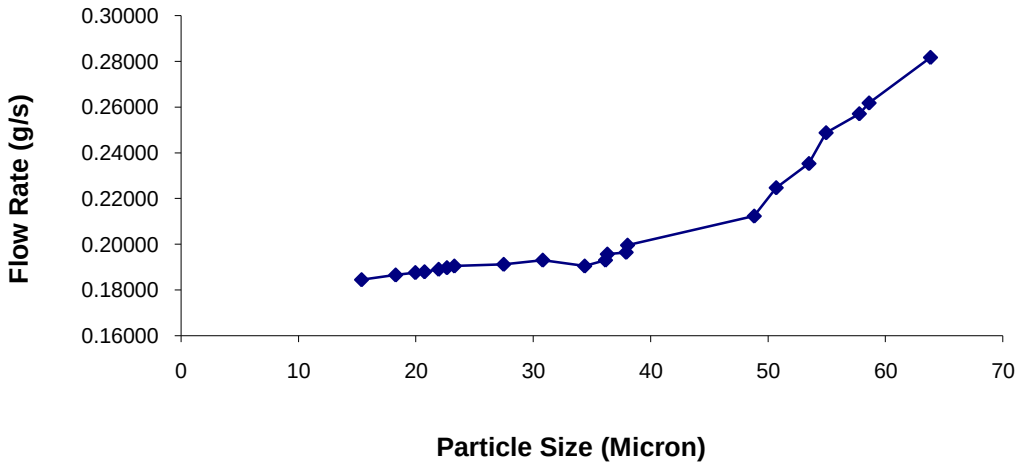

Figure 4-52: The powder flow rate as a function of the powder particle size

4.4.13 Main Findings Of Screening (Stage I) In Experimental Design

The critical responses for design control in this study are primarily the HAp phase purity and crystallinity (both >95% to aid in satisfying regulatory requirements) and particle size (<100μm) for plasma spraying application) obtained as a result of varying the factors between the two levels investigated. As previously indicated (refer to Table 4-21), a reduced lattice parameter ratio would indicate a decrease in the *a* direction and an increase in the *c* direction, which appears more favourable than an increased level of a/c ratio, which is shown to effectively decrease the crystallinity response [64]. Table 4-24(a) outlines the effect (main and interaction) of the top four most significant factors influencing the final desired responses, based on the models developed in the preceding sections. Hence, the increase or decrease of the top four most influencing main and interaction effects to obtain ↑phase purity, ↑crystallinity, ↑crystallite size, ↓a/c ratio and ↓particle size are depicted in Table 4-24(a). To achieve these desired responses, it appears that an increase in the majority of the main factors is required. Use of a controlled atmospheric environment is compromised between requirement for ↑phase purity and a ↑crystallinity. However, experiment N16 demonstrates that its synthesis with a controlled environment results in values >95% for both responses. Calcium concentration and acid addition rate, however appear to have little effect on the final powder characteristics, with the acid addition rate controlling only the crystallographic properties in comparison to the remaining three factors (that is, reaction temperature, stirring speed and ripening time).

Table 4-24(b) outlines the requirement of the three most critical process parameters affecting three or more responses to obtain the desired final powder characteristics. In summary, all of the factors studied have an impact (of minor and major significance) on one or more of the responses investigated, either as a main or interaction effect. Both the ripening time and stirring speed significantly affect the majority of the responses (effecting five responses), with the reaction temperature also having a significant effect on the purity, a/c ratio and particle size. However, from Table 4-24(a), the interaction effect of the acid addition rate and calcium concentration is also shown to effect three of the responses, but the inclusion of these factors (to attain this interaction) would produce an optimisation design (Box-Behnken) taking account of all the factors (with the exclusion of atmospheric control), analogous to the screening

design (Fractional-Factorial) and this would require a minimum of 45 experiments instead of the 17 experiments used (using 5 centre points in both instances).

Therefore, the optimisation design of experiments in Section 4.6 will not include the latter two effects. At this stage, it must be noted that the models produced as a result of eliminating these two effects may not be as statistically relevant as those produced at for the screening design. However, this will allow researchers to predict the ideal settings for the reaction temperature, stirring speed and ripening time effects and whether any interactions occur between the three parameters.

Table 4-24: Summary of findings after the screening stage of experimental design

(A)

Effects	Responses					
	↑Purity X_p	↑Crystallinity X_c	↑Crystallite Size L_{002}	↑Crystallite Size L_{300}	↓a/c ratio	↓Particle Size P_s
Main						
(A) V_{ac}				↓		
(B) T_o	↑				↑	↑
(C) V_{st}				↑	↑	
(D) t_r	↑	↑		↓	↑	
(E) Ca^{2+}			↑			↑
(F) atm.		↓	↑			
Interaction						
A * C	↑					
A * B						
A * C						
A * D			↑			
A * E		↑			↑	↑
A * F						
B * D			↑			
B * F		↑				
A * B * F	↑					

(B)

Effects	Responses					
	↑Purity X_p	↑Crystallinity X_c	↑Crystallite Size L_{002}	↑Crystallite Size L_{300}	↓a/c ratio	↓Particle Size P_s
Main						
(B) T_o	↑				↑	↑
(C) V_{st}		↑	↑	↑	↑	↑
(D) t_r	↑	↑	↓	↓	↑	

4.5 INFLUENCE OF HAp PARTICLE SIZE, CRYSTALLINITY AND MORPHOLOGY ON OSTEOBLAST BEHAVIOUR

The aim of the following investigation is to study the possible mechanism of various HAp with different crystallinity, morphology and particle size on a well studied osteoblast-like cell line (MG-63) commonly used to test in vitro bone-biomaterials biocompatibility. The HAp properties were controlled via modulating the experimental parameters (reaction synthesis temperature, reactant concentration, acid addition rate, stirring speed and ripening time) of the synthesis process. Powders were synthesised without the presence of a controlled environment, since it was found to have a negative effect on the final crystallinity. Eight kinds of HAp were used in this study, obtained at the screening (stage 1) investigation and produced through implementing the process parameters outlined in Table 4-25. HAp1 (Irish industry Hap powder) and HAp5 (British commercial HAp powder) (see section 4.1) were used as the control powders in this study to compare the powders produced against industrial and commercial powders.

Table 4-25: Experimental conditions used to produce various types of HAp for biological evaluation

Exp Name	H_3PO_4 addition rate (mol/min)	Temperature (ºC)	Stirring speed (rpm)	Ripening time (h)	Calcium concentration (M)
N3	0.005	60	600	0.5	2
N4	0.1	60	600	0.5	0.1
N5	0.005	20	1500	0.5	2
N6	0.1	20	1500	0.5	0.1
N9	0.005	20	600	48	0.1
N10	0.1	20	600	48	2
N15	0.005	60	1500	48	0.1
N16	0.1	60	1500	48	2

4.5.1 Physico-Chemical Characterisation of HAp Powders

(A) Crystallinity

The crystallinity of the control powders and the eight various types of HAp are presented in Table 4-26. These may be classified from the lowest level of crystallinity, as follow:

N3 < N5 < N6 <N4 < N9 < N10 < N15 < HAp1 < HAp5 < N16.

Table 4-26: Overview of the crystallinity for the various HAp and control HAp powders

HAp	Crystallinity (%)	Control HAp Powders	Crystallinity (%)
N3	45.69 ±2	HAp1	93.94 ±2
N4	67.38±2	HAp5	97.31 ±2
N5	54.85 ±2		
N6	57.68 ±2		
N9	58.50 ±2		
N10	73.21 ±2		
N15	90.95 ±2		
N16	99.33 ±2		

(B) Particle size analysis

The mean particle size and specific average surface area results are shown in Table 4-27 and Figure 4-53 (as represented earlier in Table 4-23). The HAp mean particle size varies from 15.38 µm for N16 to 63.83 µm for N9. The HAp powders are classified from the finest particle size, as follow:

N16 < HAp1 < N3 < N10 < N15 < HAp5 < N4 < N5 < N6 < N9.

Table 4-27: Particle size evaluation for control powders and various HAp

HAp Powder	Diameter (µm) on:			Mean	Mode	SSA
	10%	50%	90%	(µm)	(µm)	(m^2/g)
N3	4.71	19.44	47.76	23.28	30.53	0.65
N4	5.36	36.57	104.67	48.82	56.23	0.82
N5	6.53	48.61	110.01	54.94	76.32	0.54
N6	9.88	50.42	116.82	57.77	76.32	0.38
N9	7.96	56.15	130.35	63.83	88.91	0.74
N10	2.35	19.56	76.76	30.81	56.23	1.25
N15	8.43	30.79	70.92	36.15	41.43	0.73
N16	2.97	10.76	32.96	15.38	12.21	1.59
HAp1	**5.70**	**18.86**	**41.83**	**21.94**	**21.26**	**0.63**
HAp5	**3.38**	**36.83**	**69.22**	**37.91**	**48.27**	**0.53**

(A) **(B)**

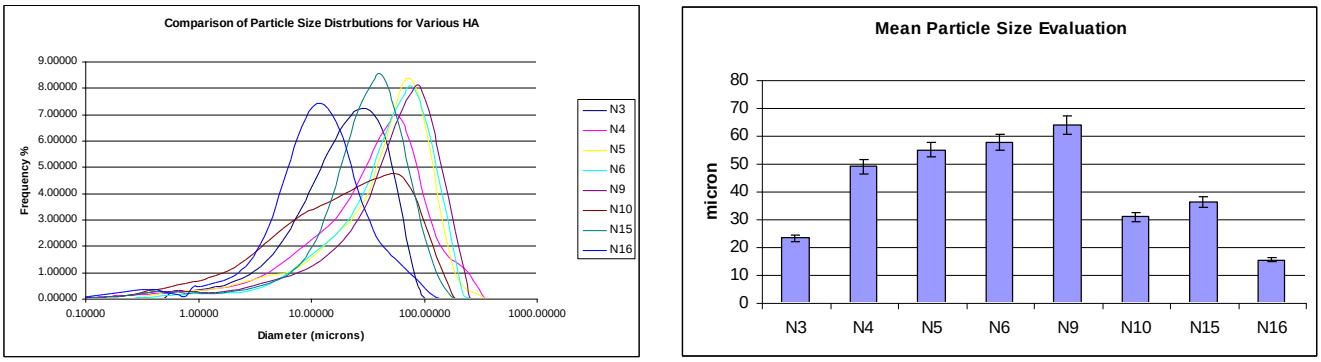

Figure 4-53: Comparison of (A) particle size distribution and (B) mean particle size for HAp

(C) Cell content and viability

Figure 4-54 shows the proliferation of MG-63 osteoblast-like cells in contact with the various HAp (N3, N4, N5, N6, N9, N10, N15 and N16) compared to proliferation on both industrial and internationally marketed powders, HAp1 and HAp5, respectively. Osteoblast-like cells proliferated without any contact with HAp was used as a control (T_e). Initially, the cell population was 20,000 cells per well. Thus, it is evident, that the additions of the various HAp particles to the osteoblast culture significantly affected cell counts, particularly after 14 days. Changes in cell populations of various preparations at 1 day, 7 days and 14 days were all statistically significant ($p < 0.00001$) by ANOVA test. These results suggest that both the HAp powders and the controls are favourable for MG-63 differentiation.

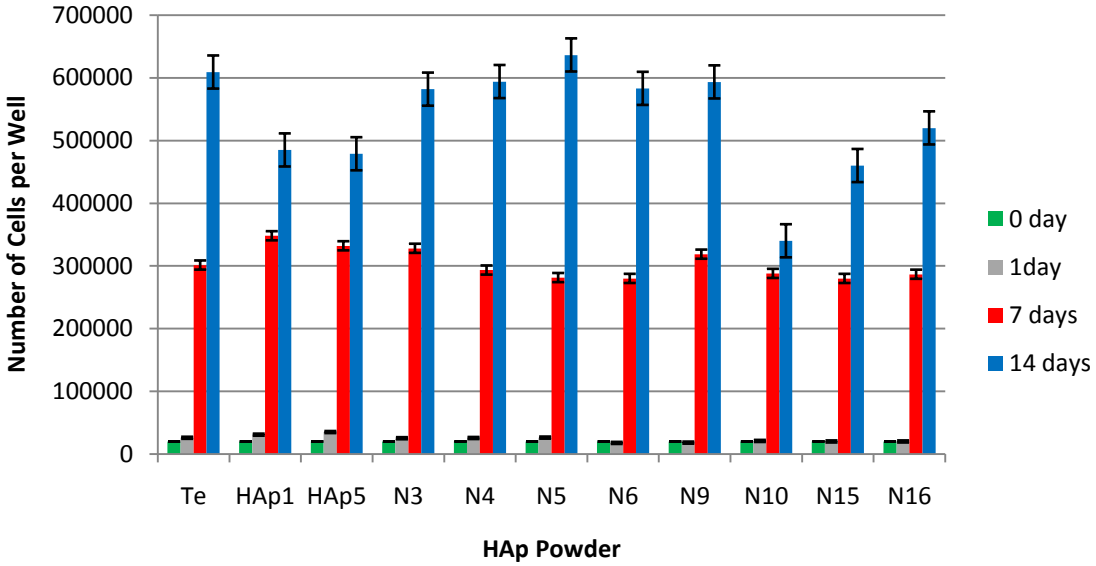

Figure 4-54: Proliferation of MG-63 osteoblast-like cells cultured on marketed HAp1 and HAp5 (control) and on various HAp at 0, 1, 7 and 14 days

Concerning the cell-viability, Figure 4-55 indicates that there is no significant difference, when the MG-63 osteoblast like cells are cultured on either the controls or the various HAp after an incubation period of 1 day. Instead, the effect becomes more significant between incubation periods of 4 and 7 days. N16 after 7 days appears to suggest that powders possessing a higher crystallinity have the capacity to yield higher counts of cell viability.

(A) Incubation Time: 1 day

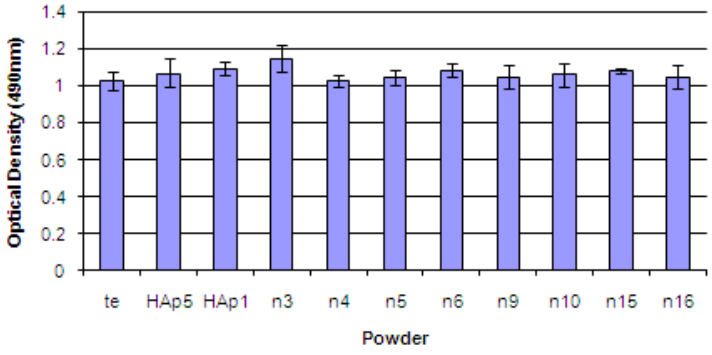

(B) Incubation Time: 4 days

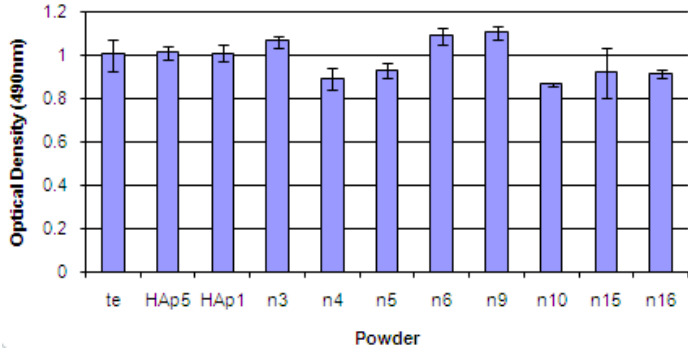

(C) Incubation Time: 7 days

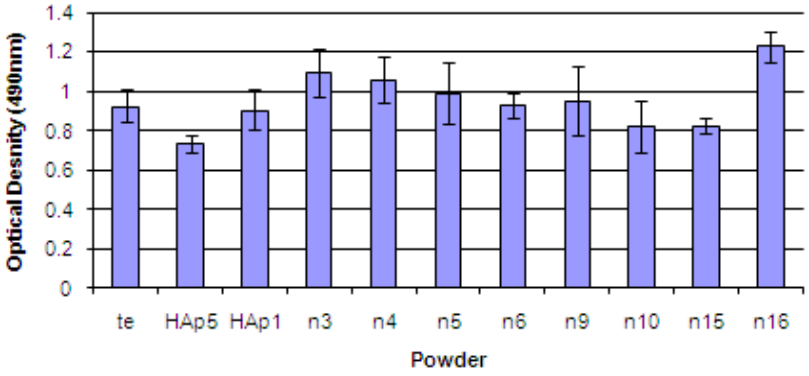

Figure 4-55: Cell viability of MG-63 cells cultured on marketed HAp (controls) and on various types of HAp from 1 to 7 days. The optical density was measured at 490 nm by ELISA reader. No significant difference in optical density between HAp powders and control at each culture period were observed using Student t test ($p > 0.05$) after 1 days incubation only.

The most significant change, however, occurred in cell populations in contact with N9, N10, N15, N16. However, a non significant change was evident among the powders with particle sizes larger than about 50 microns. The reduction in growth rate of the cells seen in these experiments could be due to an increase in the death rate of the cells to a decrease in their mitotic rate [191]. Decrease in cell number after exposure to the test material can be used as a marker for toxicity [192].

4.5.2 Influence Of HAp Particle Size

The cells behaviour in contact with HAp1, HAp5, N3, N4, N5 and N6 can be explained by the finer particle size of these powders in direct comparison to the four others. These results reflect the classical data: fine particles are generally related to a higher inflammatory cytokine rate in culture [193], or to an increase of bone resorption factors such as prostaglandin E2 and a lower proliferation cell rate [191, 194, 195].

It has been previously suggested that toxicity due to direct contact of particles with cells occurs with particles smaller than about 5 μm in diameter [196]. Later, Sun et al. [191] demonstrated that for HAp particles smaller than 53 μm, Osteoblast counts significantly decreased compared to those with larger-sized HAp particles (>177 μm). Fine particles of HAp are normally a very non toxic material; yet are shown to cause cell damage in vitro [196]. This toxicity depends on direct contact between cells and particles and it was associated with membrane damage. For an equal volume, lower granulometries offer a larger contact surface with the biological environment, inducing greater interactions between marrow cells, extracellular substances, and ceramic. In deed, smaller (~10 - 20 microns) particles may be directly phagocytosed by inflammatory cells, thereby leading to a faster reduction of cells growth ceramic in contact with HAp with lower granulometries. Evans [196] showed that the phagocytosis of 3.7μm HAp particles by cultured fibroblasts is consistent with lower cell development and a higher nuclear picnotic level. Moreover, Higashi et al. [197] performed pulpar fibroblast cultures showing a higher proliferation rate with 300μm than 40μm particles. Invocation of mechanism involving direct contact does not exclude other mechanisms such as leaching of toxic ions. The tested HAp may have a low level of toxicity which is not sufficient to kill cells but may inhibit normal cell function [198].

4.5.3 Influence Of HAp Crystallinity

In addition to the difference of mean particles size, XRD analyses showed that the crystallinity of fine HAp particle size was significantly lower than that of larger ones in our prepared powders (see Table 4-27). Figure 4-56 shows that the cells counts increase with the increase of powder crystallinity. Indeed, osteoblast grows well on N16, N15, N10 and N9 powders having crystallinity in the range of ~70 to ~95% than on the others.

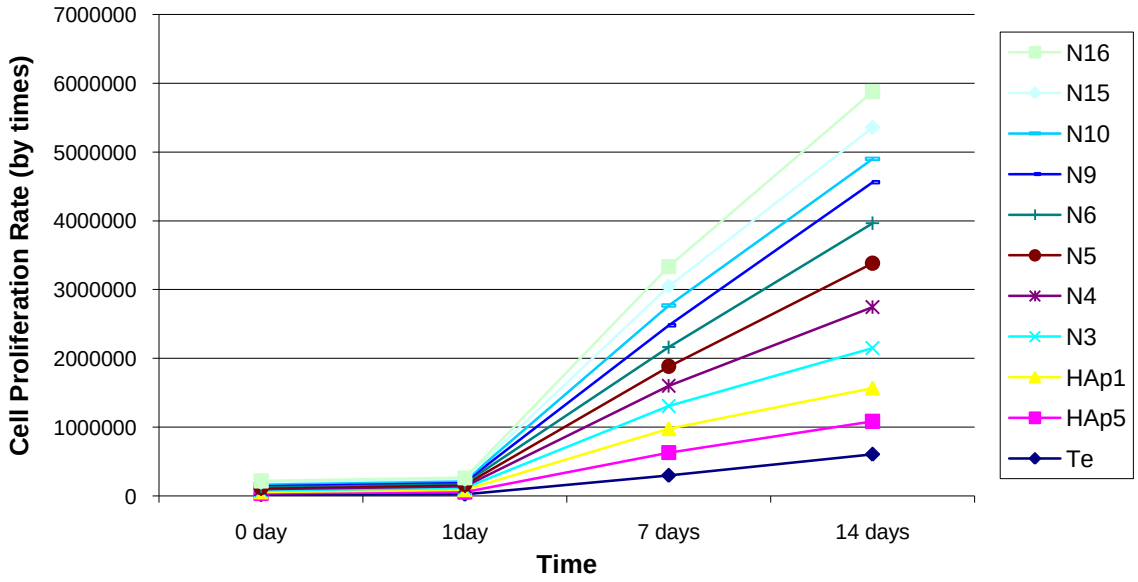

Figure 4-56: Rate of cell proliferation (by times) for MG-63 osteoblast-like cells in contact with controls and various HAp powders

The same osteoblast behaviour has been already reported by Qu et al. [199] but only after 3 days incubation. They demonstrated that the cells cultured on higher crystallinity ceramics showed higher proliferation at initial time and reached the highest proliferation after 3 days. Then the proliferation decreased with cultured time. This discordance can be explained by the fact that the influence of particle size dominates that of crystallinity. Indeed, Evans et al. [200] showed that the mechanism of cell damage *in vitro* depends on a direct interaction between cells and particles and is largely independent of the chemical nature of the particles. Moreover, the osteoblasts tested in this work had different origin. Lang et al. already reported that the human osteoblast-like cells reacted slightly more sensitive to toxic substances of

the materials tested than rat osteoblast-like cells [201]. This comportment can be attributed to the alkaline pH of the surrounding environment. Indeed, it has been already indicated the rate of calcium phosphate ceramic dissolution correlated with the increase of Ca and P ion concentrations and pH value of surrounding environment. This dissolution in body fluids or in vitro is more important for lower crystallinity. This alkaline pH would lead to a cytotoxic effect inhibiting DNA and protein synthesis and cell proliferation in cell culture. This result agreed well with other literature.

4.5.4 Influence Of HAp Particle Morphology

SEM micrographs of the source powders (in their particulate form), studied in this investigation are shown in Figures 4-13 and 4-49 - 4-50. The micrographs shown in Figures 4-57 to 4-59 represent the typical cell morphology at each culture period, since all osteoblast-like cells do not spread at the same rate. At 1 days, on the Thermanox surface, the MG-63 osteoblast-like cells without any contact with the HAp powders, spread extensively, and are totally flattened on the surface (Figure 457(-)). After 7 days however, the cells appear to progress to a monolayer of cells with the classical fibroblast spindle shape (Figure 4-59(-)). These SEM micrographs shows that cells are densely colonised in N9, N10, N15, N16 wells after 1, 4 and 7 days. However, they are still sparsely colonised in the wells with HAp1, HAp2, N3, N4, N5 and N6, even after 7 days of incubation. SEM analysis of the cultured cells show a good compatibility of the osteoblasts to all the powders tested. In particular, in contact with N3, N10, N15 and N16 powders, the cells showed a diffuse spread-like morphology with several cytoplasmatic extensions contacting the powder (see Figure 4-59), while in the case of N4, N5, N6 and N9, the cells were elongated with fewer extensions interacting with apatite granules. Control cultures (HAp1 and HAp5) showed a uniform layer of confluent cells with a frequent elongated shape and also overlapping growth (see Figures 4-57 to 4-59).

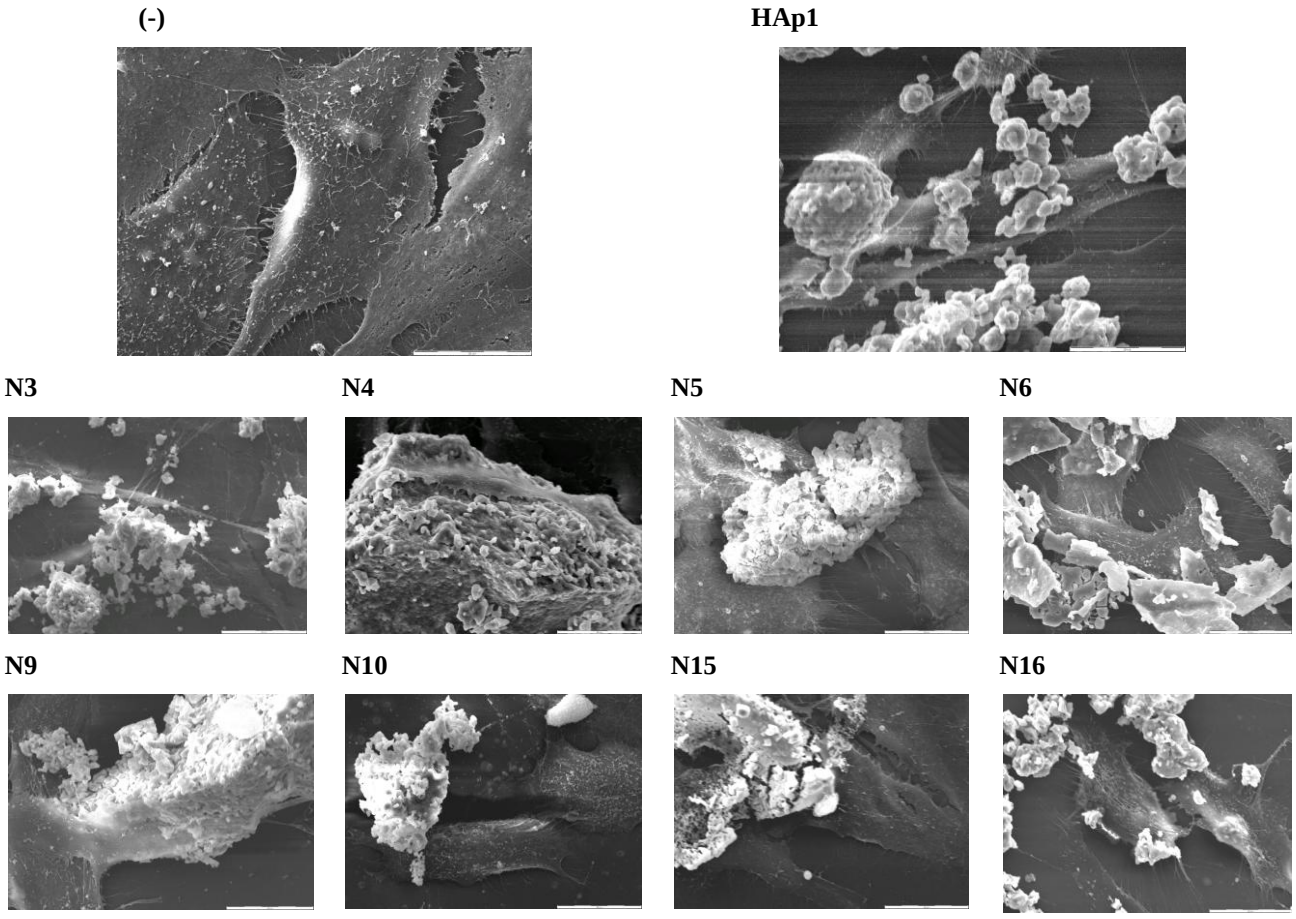

Figure 4-57: SEM micrograph showing the morphology of MG-63 osteoblast- like cells cultured on a thermanox surface (-) and in contact with control powder (HAp1) and various HAp (N3, N4, N6, N9, N10, N15, N16) at 1 day (micro scale bar length = 50µm at magnification x1500)

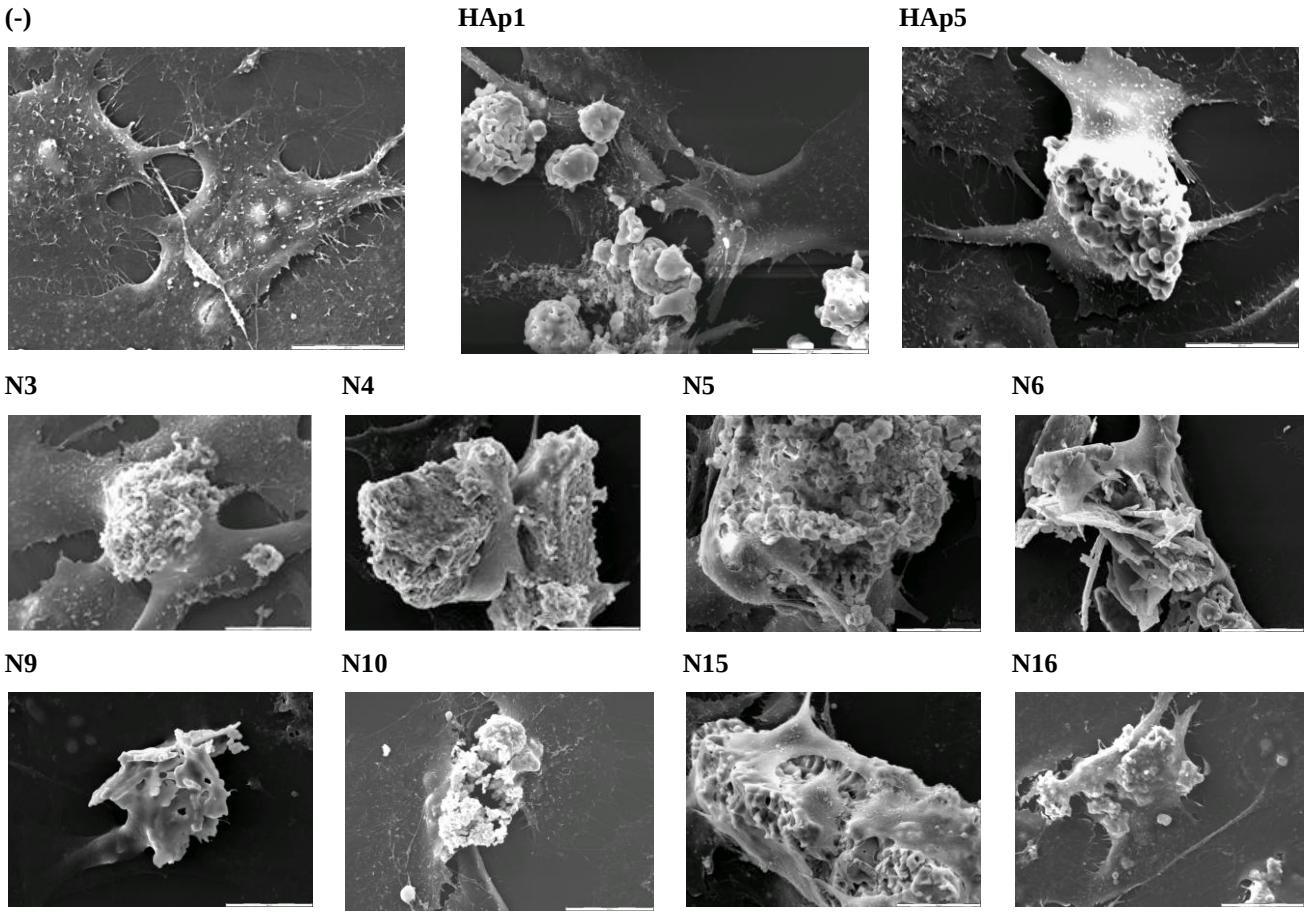

Figure 4-58: SEM micrograph showing the morphology of MG-63 osteoblast- like cells cultured on a thermanox surface (-) and in contact with control powders (HAp1 and HAp5) and various HAp (N3, N4, N6, N9, N10, N15, N16) at 4 days (micro scale bar length = 50µm at magnification x1500)

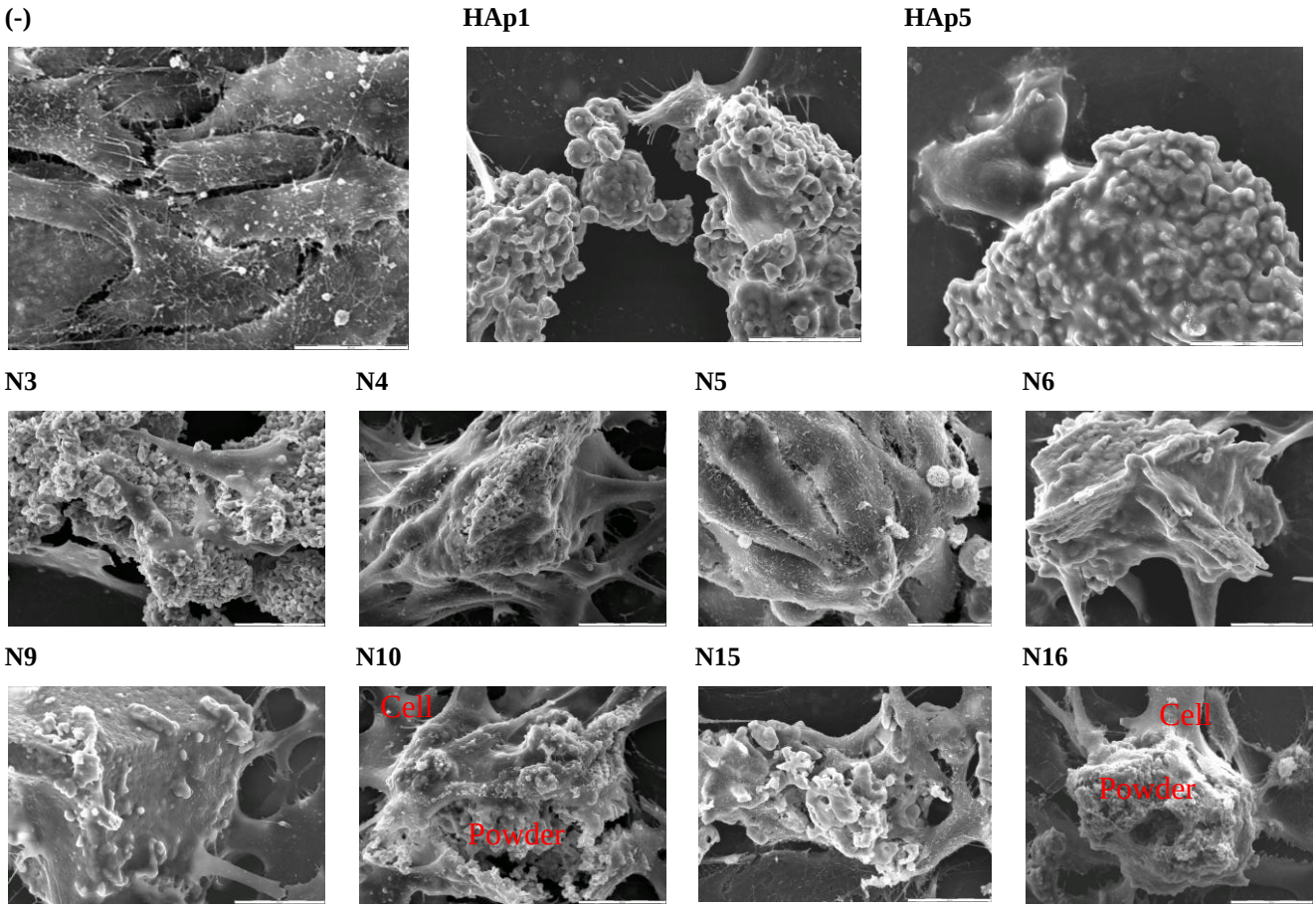

Figure 4-59: SEM micrograph showing the morphology of MG-63 osteoblast- like cells cultured on a thermanox surface (-) and in contact with control powders (HAp1 and HAp5) and various HAp (N3, N4, N6, N9, N10, N15, N16) at 7 days (micro scale bar length = 50µm at magnification x1500)

4.5.5 Summary

The formation of new bone is a multi-step cascade, initiated with chemotaxis and adhesion of osteogenic cells to the implant. The adhesive cells undergo a sequence of cell functions (such as, proliferation and synthesis of extracellular matrix proteins formation of mineral deposits). In order to enhance osteoblast proliferation, which promotes new bone formation, it is necessary to employ suitable Ca-P ceramics, which simulate the natural normal, healthy bone. This present study, therefore, provides evidence that the development of a new generation of bioactive ceramics, through the control of the crystallinity, particle size and morphology, to promote osseointegration, which is vital for the clinical success of orthopaedic implant.

4.6 OPTIMISATION OF CHEMICAL PRECIPITATION PROCESS PARAMETERS

In this section, the experimental design used, the range of each chemical precipitation process parameter and experimental layout are presented. This section demonstrates the results for the optimisation of the chemical precipitation process parameters, in terms of the ANOVA analysis for each response investigated, and the validation of the models produced. The effects of the process parameters on each response are described and discussed. Furthermore, the results of the phase purity, crystallinity, crystallite size, lattice parameters and particle size are illustrated and discussed to distinguish the effects of the process parameters on the final HAp powder properties obtained, with a view to optimising the investigated parameters. The processing window for each factor was limited to the region over which existing literature indicated as optimum values and was also selected based on the results as obtained at the screening stages of the design of experiments. The lower levels selected in the screening investigation were shown to have little influence in obtaining the desired powder characteristics. Therefore the lower levels have been increased for the optimisation studies. Based on these observations, the key controllable process factors investigated in the optimisation model include the three most critical parameters (see Table 4-24(a) and (b)) as observed during the screening design: *Factor A:* Temperature (40 - 60°C), *Factor B:* Stirring Speed (900 – 1500rpm) and *Factor C:* Ripening Time (24 – 48h).

A Box-Behnken experimental design, with three levels on the three most influential factors was used to allow the estimation of a full quadratic model, including interaction effects. Box-Behnken designs have two parts: (i) centerpoints, and (ii) points lying on one sphere, equally distant from the centerpoint. The latter points consist of small two-level full factorials where some factors are fixed at their center values. The number of centerpoints is chosen to establish rotatability. The levels selected for the optimisation experiments are shown in Table 4-28 (denoted as -1, 0 and +1). The other parameters (Ca^{2+} conc. (2.0M), acid addition rate (0.01 mol/min) with atmospheric control) were kept constant in all cases. As only the main effects were considered in the building of the optimisation design, the optimisation models developed for each response will vary from those developed during the screening

stage, since the interaction between other factors (such as, acid addition rate and calcium concentration) is set (see Section 3.6.2).

Table 4-28: Experimental factors and level of factors

	Variable	*Level -1*	*Level 0*	*Level +1*
A	Reaction Temperature, T_o	40°C	50°C	60°C
B	Stirring Speed, V_{st}	900rpm	1200rpm	1500rpm
C	Ripening Time, t_r	24h	36h	48h

The experiments were carried out according to the design matrix shown in Table 4-29 in a fully randomised order to avoid any systematic error. Conditions for N13 – 17 are replicated to assess the reproducibility at a given set of process conditions. For the optimisation, several mathematical models were developed successfully to predict the following responses: phase purity (X_p), crystallinity (X_c), crystallite size (X_s, L_{002} and L_{300}), lattice parameters (*a* and *c*) and the powder particle size (P_s). The responses obtained were calculated according to the experimental design matrix, characterized as per experimental methods outlined in Chapter 3 and are discussed in the following sections. The averages for three measurements are presented in Table 4-30.

Table 4-29: Box-Behnken experimental design, real values

Exp. Number	T_o(°C)	V_{st} (rpm)	t_r (h)
N1	40	900	36
N2	60	900	36
N3	40	1500	36
N4	60	1500	36
N5	40	1200	24
N6	60	1200	24
N7	40	1200	48
N8	60	1200	48
N9	50	900	24
N10	50	1500	24
N11	50	900	48
N12	50	1500	48
N13	50	1200	36
N14	50	1200	36
N15	50	1200	36
N16	50	1200	36
N17	50	1200	36

Table 4-30: Phase purity (X_p), crystallinity (X_c), crystallite size (X_s, L_{002} and L_{300}), lattice parameter ratio (a/c) and mean particle size (P_s) of the different HAp samples for various conditions of temperature (T_o), stirring speed (V_{st}), and ripening time (t_r)

Sample	Purity, X_p, (%)	Crystallinity, X_c, (%)	Crystallite Size, X_s, L_{002} (nm)	Crystallite Size, X_s, L_{300} (nm)	Lattice Parameter, *a* (nm)	Lattice Parameter, *c* (nm)	Mean Particle Size, P_s (µm)
N1	72.24	75.12	57.42	58.29	9.4195	6.8934	28.04
N2	49.62	76.47	51.34	47.29	9.4484	6.8858	24.63
N3	84.56	76.4	56.53	81.38	9.4058	6.8650	28.20
N4	57.79	82.36	53.52	61.78	9.4246	6.8867	26.71
N5	61.04	77.95	48.99	62.37	9.4279	6.8650	26.45
N6	23.53	82.52	80.01	72.55	9.4720	6.8498	40.95
N7	60.26	78.94	53.68	72.55	9.4282	6.8780	26.62
N8	18.71	80.98	69.41	65.10	9.4312	6.8565	34.22
N9	50.50	72.81	66.00	56.00	9.4322	6.8558	37.07
N10	71.16	79.18	59.19	69.65	9.4775	6.8525	27.99
N11	55.27	73.87	51.44	48.84	9.4245	6.8859	25.55
N12	84.73	77.36	57.78	48.84	9.4456	6.8887	32.28
N13	48.62	72.10	51.16	72.59	9.4186	6.8681	24.36
N14	49.79	73.00	51.66	72.59	9.4186	6.8681	26.39
N15	47.98	71.78	51.26	73.00	9.4186	6.8681	27.37
N16	47.65	72.05	51.68	72.56	9.4186	6.8681	28.17
N17	48.55	72.55	51.17	72.67	9.4186	6.8681	27.99

4.6.1 Development Of Phase Purity Model

As a result of analysing the measured responses using the Design Expert software, the fit summary selected the highest order polynomial where the additional terms are significant and the model is not aliased. Choosing the step-wise regression method led to the elimination of the insignificant model terms automatically. Table 4-31 presents the ANOVA results for the phase purity and shows the significant model terms. The same tables show also the other adequacy measures R^2, Adjusted R^2 and Predicted R^2. These were shown to be high, thus the model is statistically significant and leaving out the calcium concentration did not significantly affect the results here as it did not have a major influence on the purity results in the screening study. A significant lack of fit can also be attributed to the elimination of the acid addition rate as a controlling factor. An Adequate Precision ratio of 21.046 indicates adequate model discrimination [160].

The result of the Analysis of Variance for the phase purity model shows that the main effect of two of the chemical precipitation parameters and the quadratic effect of the stirring speed are significant model terms. However, the reaction synthesis temperature is the factor which possesses the most significant main effect on the phase purity, with the stirring speed containing a lesser effect. However, the quadratic effect of the stirring speed is found to have a more significant effect, in comparison to being considered solely as a main effect. This result correlates well with literature, which suggests that both the temperature and stirring speed is critical in controlling the final phase purity [89]. The order of significance for these effects follows the order: $T_o > V_{st}^2 > V_{st}$. The final model in terms of coded factors is shown in Equation 4-20, while the final model in terms of coded factors is presented in Equation 4-21.

Table 4-31: ANOVA table for phase purity, X_p, reduced quadratic model

Source	Sum of squares	d.f.	Mean Square	F value	Prob >F	
Model	4484.04	3	1494.68	41.13	< 0.0001	significant
T_o	2062.61	1	2062.61	56.75	< 0.0001	
V_{st}	623.25	1	623.25	17.15	0.0012	
V_{st}^2	1798.18	1	1798.18	49.48	< 0.0001	
Residual	472.47	13	36.34			
Lack of Fit	469.81	9	52.20	78.44	0.0004	significant
Pure Error	2.66	4	0.67			
Corrected Total	4956.51	16				

R^2 = 0.9047; predicted R^2 = 0.8205; adjusted R^2 = 0.8827; adequate precision = 21.046

Phase Purity = +45.13

Xp (%) -16.06 * T_o

+8.83 * V_{st}

+20.61 * V_{st}^2 *Equation (4-20)*

Phase Purity, = +419.78901

Xp (%) -1.60570 * Reaction Temp

-0.52005 * Stirring Speed

+2.28946E-004 * (Stirring Speed)^2 *Equation (4-21)*

The above equation (4-20) indicates that the order of the level of significance of the positive effects of the chemical precipitation process parameters on the phase purity follows the order: (V_{st}^2) > (V_{st}) while the order of the level of significance of the negative effects on the lattice parameter ratio is as follows: (T_o). Fig 4-60 shows the relationship between the actual and predicted values of the phase purity. This figure indicates that the developed model is adequate, since the residuals in the prediction of each response are small, with the residuals tending to be close to the diagonal line.

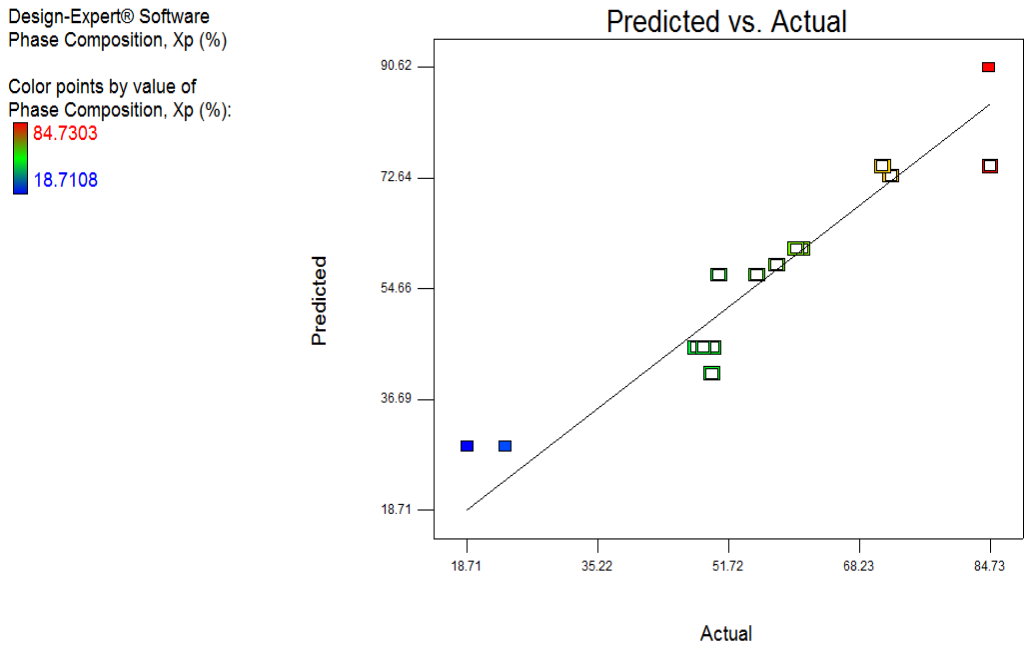

Figure 4-60: Scatter diagram for phase purity

4.6.2 Effect Of The Process Parameters On Phase Purity

The 3-D surface and 2-D contour plots illustrated in Figure 4-61 examine the effects of the two significant factors (reaction temperature and stirring speed) on the phase purity response. The results indicate that both the reaction synthesis temperature and the stirring speed exert a significant effect on the response for phase purity. The positive response of the stirring speed indicates that higher levels of stirring speed are required, while the negative effect for the reaction synthesis temperature indicates that a lower temperature, in the range of about 40°C is optimum for increased responses of phase purity. This optimum temperature is in good agreement with Afshar [83] and Saeri [84].

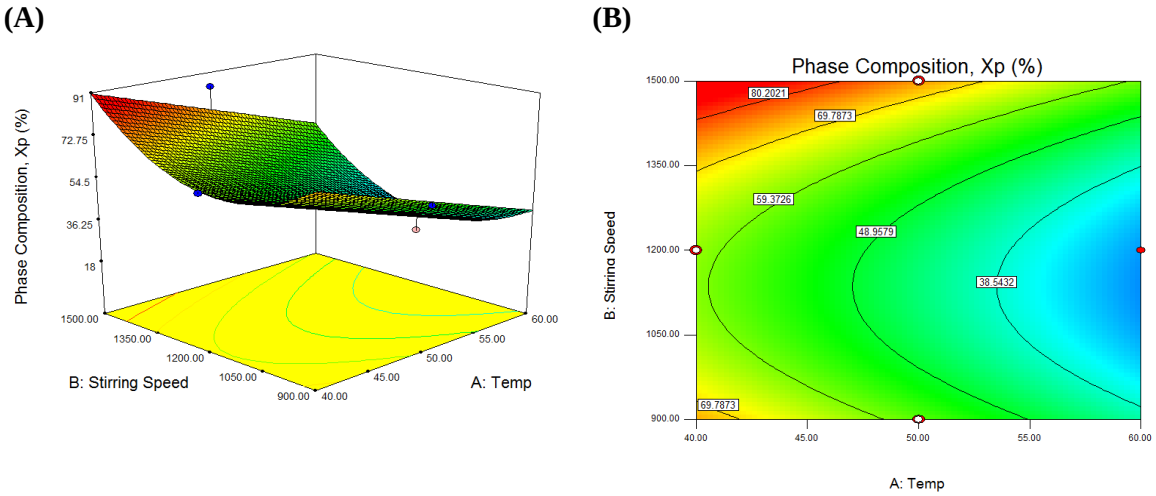

Figure 4-61: 3D surface (A) and 2D contour plot (B) of phase purity at a ripening time of 48h

The perturbation plot shown in Figure 4-62 helps to compare the effect of both the significant factors at a particular point in the design space. This plot shows a comparison between the effects of the reaction synthesis temperature and stirring speed on the maximum phase purity, X_p. It is evident from this illustration that in the case of the steep curvilinear effect representing the stirring speed, the response is highly sensitive to this factor, with a sharp increase in phase purity. While the steep slope in the case of the reaction synthesis temperature indicates that the response is relatively sensitive to this factor, with an increase of parameter resulting in a decrease of the phase purity obtainable.

Table 4-32 shows the effects of increasing the reaction temperature, stirring speed or ripening time on experimental results obtained during the optimisation (BBD) and on the original screening (FFD) study.

Table 4-33 shows the top four most influencing main and interaction effects (if any), in chronological order, for both the screening (FFD) and optimisation (BBD) with respect to attaining high levels of phase purity. Firstly, interactions involving the acid addition rate and calcium concentration did not appear in the BBD, as it was excluded from this design. One main influencing factor that appeared in the screening but not in the optimisation is the ripening time. Clearly, this has no significant effect on the ranges studied for the optimisation (24 - 48h) as opposed to the broader range (0.5 – 48) investigated during the screening stage.

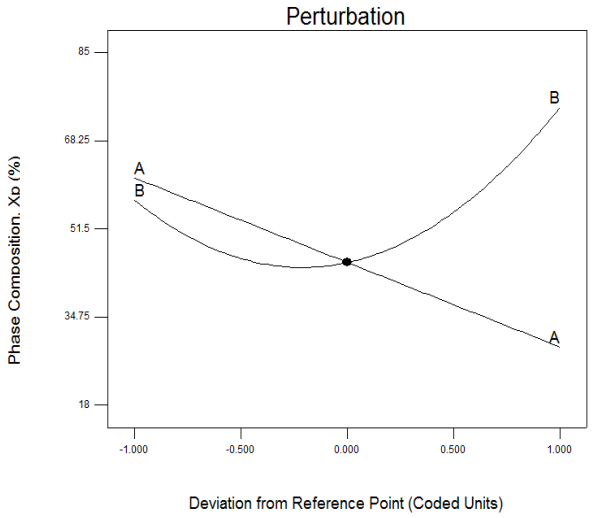

Figure 4-62: Perturbation plot demonstrating the effect of the three parameters on phase purity

The stirring speed has both a linear and quadratic effect on the Box-Behnken design and therefore is the most important factor along with the reaction temperature. The increase of the effect of the stirring speed on the ranges investigated for optimisation can also be attributed to the loss of significance on the ripening time for achieving high purity.

Table 4-32: Effect of increasing process factors on phase purity

Experimental Design	Sample	Factors			Response
		T_o (°C)	V_{st} (rpm)	t_r (h)	X_p (%)
Increasing Temperature					
BBD	**N5**	40	1200	24	61.0433
BBD	**N6**	60	1200	24	23.5338
BBD	**N7**	40	1200	48	60.2630
BBD	**N8**	60	1200	48	18.7108
Increasing Stirring Speed					
BBD	**N9**	50	900	24	50.4973
BBD	**N10**	50	1500	24	71.1554
Increasing Ripening Time					
BBD	**N4**	60	1500	36	57.79250
FFD	**N16**	60	1500	48	98.88860

BBD = Box Behnken Design (Optimisation), FFD – Fractional Factorial Design (Screening)

Table 4-33: Comparison of significant effects for screening (stage I) and optimisation (stage II) for phase purity, X_p

Order of Significance	Fractional Factorial Design (FFD)	Box – Behnken Design (BBD)
	↑Purity, Xp (%)	
1	$\uparrow V_{ac} * V_{st}$	$\uparrow V_{st}^2$
2	$\uparrow V_{ac} * T_o$ * atm.	$\downarrow T_o$
3	$\uparrow t_r$	$\uparrow V_{st}$
4	$\uparrow T_o$	

Both the reaction temperature and the stirring speed were discussed in terms of their influence on the phase purity during the screening stage. Therefore, it is assumed their effects also stand here.

4.6.3 Development Of Crystallinity Model

As a result of analysing the measured responses using the same statistical software used at the screening stage of this study, the fit summary output indicated that for the response concerning crystallinity, the quadratic model is statistically recommended for further analysis as this has the maximum predicted and adjusted R^2. The test for significance of the regression model, the test for significance on individual model coefficients and the lack of fit test were performed for this response. By selecting the step-wise regression method, the insignificant model terms were automatically eliminated. The resulting ANOVA tables (Table 4-34) for the reduced quadratic models outline the analysis of variance of each response and show the significant model terms. The same tables show also the other adequacy measures R^2, Adjusted R^2 and Predicted R^2, with an Adequate Precision Ratio of 28.021, to indicate adequate model discrimination was achieved and shows that elimination of the acid addition rate and the calcium concentration did not have an influence on attaining a significant model . The order of significance for these effects follows the order: $T_o^2 > t_r^2 > V_{st} > T_o > T_o * V_{st} > V_{st} * t_r > T_o * t_r > V_{st}^2$

Table 4-34: ANOVA table for crystallinity, X_c, reduced quadratic model

Source	Sum of squares	d.f.	Mean Square	F value	Prob >F	
Model	214.86	8	26.86	104.98	< 0.0001	significant
T_o	23.99	1	23.99	93.76	< 0.0001	
V_{st}	36.52	1	36.52	142.73	< 0.0001	
$T_o * V_{st}$	5.13	1	5.13	20.05	0.0021	
$T_o * t_r$	1.62	1	1.62	6.32	0.0362	
$V_{st} * t_r$	2.08	1	2.08	8.12	0.0215	
T_o^2	97.11	1	97.11	379.55	< 0.0001	
V_{st}^2	1.09	1	1.09	4.28	0.0725	
t_r^2	37.88	1	37.88	148.08	< 0.0001	
Residual	2.05	7	0.26			
Lack of Fit	1.12	4	0.28	1.21	0.4283	not significant
Pure Error	0.93	4	0.23			
Corrected Total	216.91	16				

R^2 = 0.9906; predicted R^2 = 0.9381; adjusted R^2 = 0.9811; adequate precision = 28.021

The final model in terms of coded factors is shown below in Equation 4-22, while the final model in terms of coded factors is presented in Equation 4-23.

Crystallinity, = 72.29

X_c, (%)	+ 1.73	$*T_o$	
	+ 2.14	$*V_{st}$	
	+ 1.13	$*T_o * V_{st}$	
	- 0.64	$*T_o * t_r$	
	- 0.72	$*V_{st} * t_r$	
	+ 4.80	$*T_o^2$	
	+0.51	$*V_{st}^2$	
	+3.00	$*t_r^2$	*Equation (4-22)*

Crystallinity =+189.50859

X_c, (%)	-4.69975	* Reaction Temp	
	-0.013023	* Stirring Speed	
	+3.77508E-004	* Reaction Temp * Stirring Speed	
	-0.011957	* Reaction Temp * Ripening Time	
	-3.77806E-004	* Stirring Speed * Ripening Time	
	+0.048503	* Reaction Temp^2	
	+6.19594-006	* Stirring Speed^2	
	+0.014503	* Ripening Time^2	*Equation (4-23)*

The above equation (4-22) indicates that the order of the level of significance of the positive effects of the chemical precipitation process parameters on the crystallinity follows the order: $(T_o^2) > (t_r^2) > (V_{st}) > (T_o) > (T_o * V_{st}) > (V_{st}^2)$ while the order of the level of significance of the negative effects on the lattice parameter ratio is as follows: $(V_{st} * t_r) > (T_o * t_r)$.

Figure 4-63 shows the relationship between the actual and predicted values of the crystallinity. This figure indicates that the developed model is adequate, since the residuals in the prediction of each response are small, with the residuals tending to be close to the diagonal line.

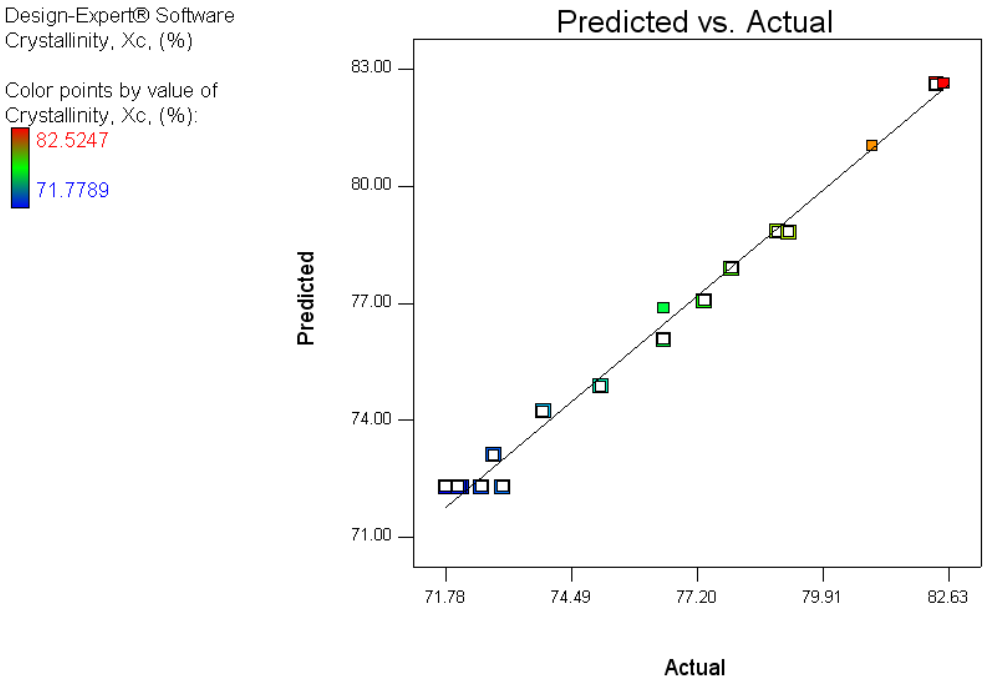

Figure 4-63: Scatter diagram for crystallinity

4.6.4 Effect Of The Process Parameters On The Crystallinity

One of the response surface methodology advantages over the one factor at a time experimental procedure is its ability to specify the interaction effect between any two factors. Figure 4-64(a) to (c) shows the 3-D surface and 2-D contour graphs, highlighting the significant interaction effect between the reaction temperatures and stirring speed at ripening times of between 24 to 48h. It is clear from this figure that an increase in both factors results in a marked increase in crystallinity, while the ripening time has little effect between 24 to 48h, demonstrating a difference in crystallinity of 2.7126%. The maximum crystallinity of 86.9629% occurs at a reaction synthesis temperature of 60ºC and a stirring speed of 1500rpm at a ripening time of 24h.

The cube plot shown in Figure 4-65 displays the relationship between three significant factors and is especially useful in interpreting the interaction effects (such as, T_o* $V_{st,}$ T_o* t_r and V_{st} * t_r). This type of figure presents the predicted values of the responses from the model for the combinations of the -1 and +1 levels of the three factors. This figure presents the effect of the three factors on the crystallinity by using a cube plot to represent this effect. It is noted that the process input parameters can be selected where the crystallinity would be minimum or maximum.

The perturbation plot aids in comparing the effect of all the factors at a particular point in the design space. Figure 4-66 shows a comparison between the effects of reaction temperature, stirring speed and ripening time on the maximum crystallinity. It is evident from this figure that the stirring speed has a slightly positive effect on the crystallinity. In the case of the reaction temperature, the curvilinear effect demonstrates that increasing the temperature until it reaches its maximum value would result in enhanced crystallinity, with decreased levels obtained at approximately mid range (50ºC). The non significance of the ripening time is also demonstrated whereby there is little or no effect in varying the ripening time between 24 to 48h, with the minimum crystallinity being obtained at 36h. Increasing the stirring speed will result in a direct increase of crystallinity.

(A) Ripening Time: 24h

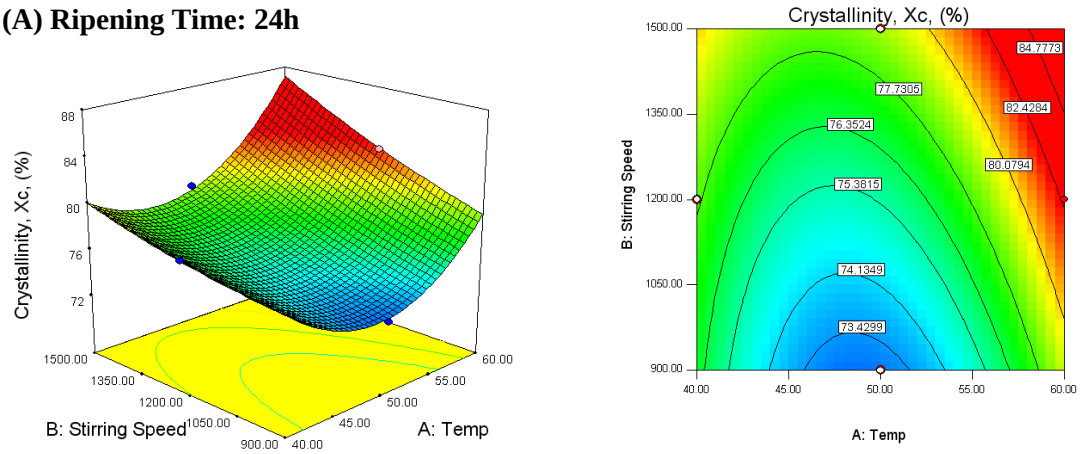

(B) Ripening Time: 36h

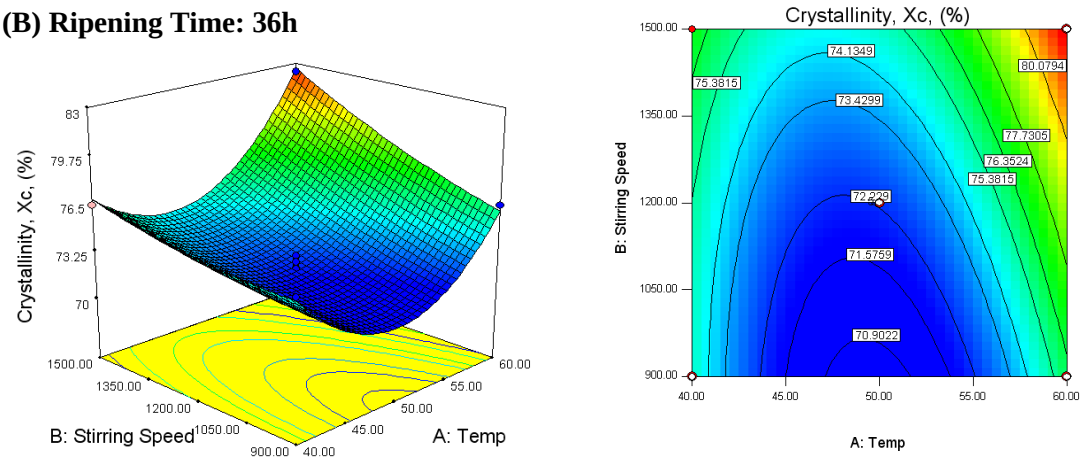

(C) Ripening Time: 48h

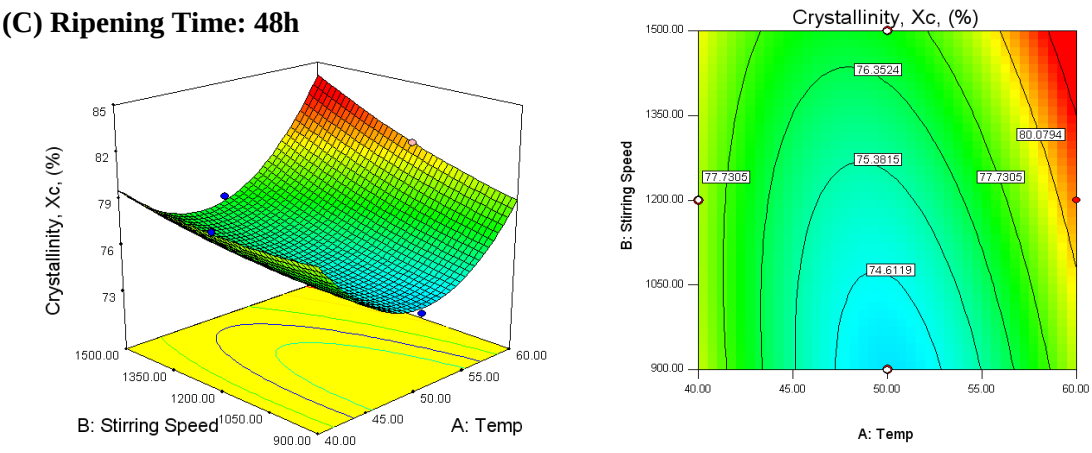

Figure 4-64: 3D surface and 2D contour plots of crystallinity at (A) a ripening time of 24h; (B) a ripening time of 36h and (C) a ripening time of 48h

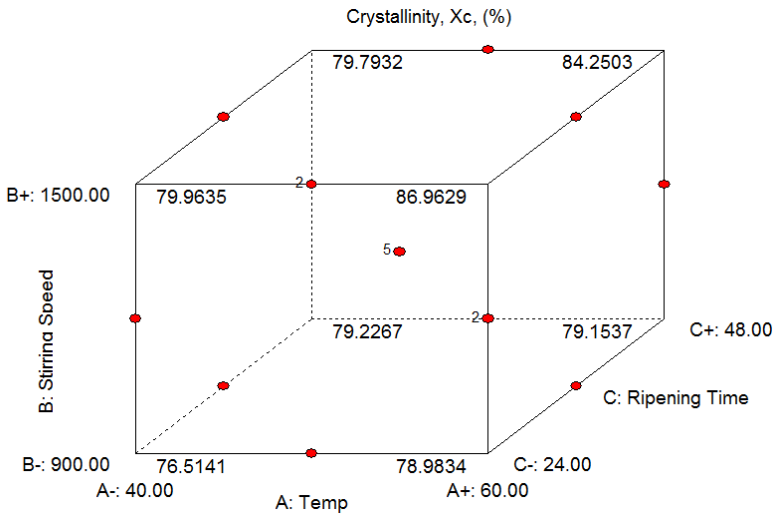

Figure 4-65: Cube graph demonstrating the effect of the three parameters on crystallinity

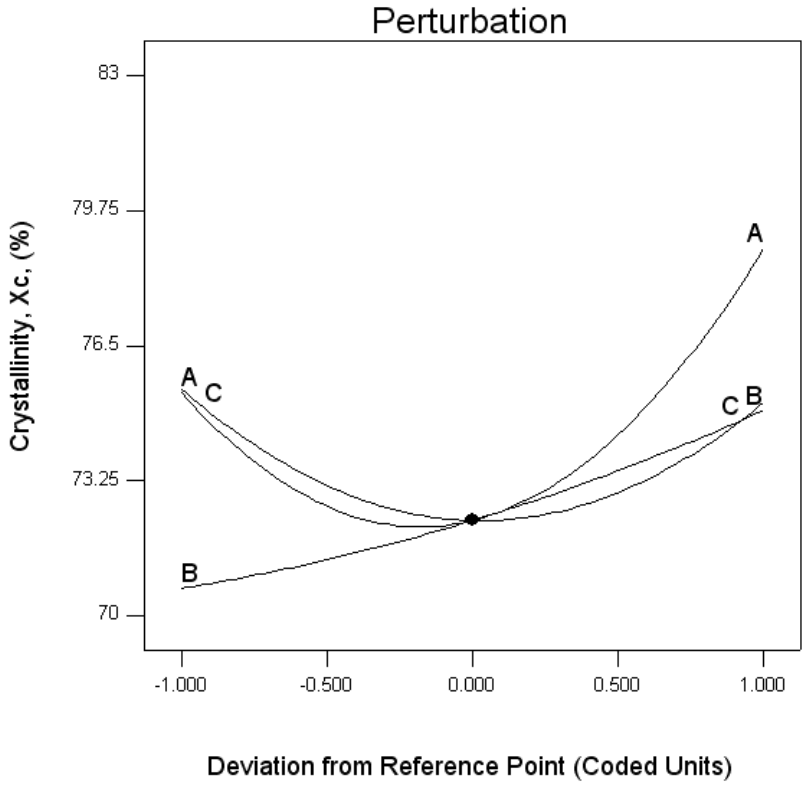

Figure 4-66: Perturbation plot demonstrating the effect of the three parameters on crystallinity

Table 4-35 shows the top four most influencing main and interaction effects (if any), in chronological order, for both the screening (FFD) and optimisation (BBD) with respect to attaining high levels of crystallinity.

Table 4-35: Comparison of significant effects for screening (stage I) and optimisation (stage II) for crystallinity, X_c

Order of Significance	Fractional Factorial Design (FFD)	Box – Behnken Design (BBD)
	↑Crystallinity, Xc (%)	
1	↑t_r	↑ T_o^2
2	↑T_o * atm.	↑ t_r^2
3	↓atm.	↑ V_{st}
4	↑V_{ac} * Ca^{2+}	↑T_o

Since the acid addition rate, calcium concentration and atmospheric control (as factors) were eliminated from the optimisation study; their effects do not appear as being significant in the BBD model developed for crystallinity. The reaction temperature and the ripening time effects appear in both models. However, their quadratic effects included on the BBD model, shows that their level of significance has increased dramatically within the ranges investigated. These factors were discussed, at the screening stage, in relation to their effects on crystallinity. Hence, these observations will also apply here. However, the stirring speed is now introduced as a significant main effect in the top four most influencing factors effecting crystallinity during optimisation. Instead, the screening results show the stirring speed to have a less significant effect on the crystallinity (marked 6^{th}, Figure 4-27). Therefore, it has increased in level of significance due to the elimination of other factors (such as, acid addition rate, calcium concentration and atmospheric control). It would be expected that the stirring speed would affect the crystallinity as high mixing intensity is required to attain high levels of crystallinity [86].

4.6.5 Development Of Crystallite Size Models (L_{002} and L_{300})

As a result of analysing the measured responses using the Design Expert software, the fit summary selected the highest order polynomial where the additional terms are significant and the model is not aliased. Choosing the step-wise regression method led to the elimination of insignificant model terms automatically. Tables 4-36 and 4-37 present the ANOVA results for crystallite size in the 002 and 300 plane, respectively. The same tables show also the other adequacy measures R^2, Adjusted R^2 and Predicted R^2, with an Adequate Precision ratio of 6.1602 and 8.227, respectively, showing that adequate model discrimination has been achieved for both models [160]. The lack of fit in both cases is significant, with a transformation required in the case of the crystallite size in the 300 plane to improve model adequacy. Again, this may be attributed to eliminating the factors (acid addition rate, calcium concentration and atmospheric control) included in the screening study, as it had either an interaction effect (V_{ac} * t_r, ranked 4^{th}) or a main effect (ranked 3^{rd}) and interaction effect (V_{ac} * atm., ranked 4^{th}) for the crystallite size, L_{002} and L_{300}, respectively. Therefore, eliminating the acid addition rate and atmospheric control appears to affect the models produced here and produce a significant lack of fit.

The result of the ANOVA for the crystallite size model, L_{002}, shows that while the main effect of the reaction temperature has a significant effect on the crystallite size in this plane, the quadratic effect of ripening time has a greater level of significance. The order of significance for these effects follows the order: $t_r^2 > T_{o.}$ The ANOVA for the crystallite size model, L_{300}, shows instead, that the stirring speed (main and quadratic) is the most significant factor, while the quadratic effect of ripening time has a lesser significance on the final crystallite size for the 300 plane. The order of significance for these effects follows the order: $V_{st} > V_{st}^2 > t_r^2$.

The final mathematical models for the crystallite size response, L_{002} in terms of coded and actual factors as determined by the Design Expert software are shown in Equations 4-24 to 4-25. While, the final mathematical models in terms of coded and actual factors for L_{300} are presented in Equations 4-26 to 4-27.

Table 4-36: ANOVA table for crystallite size, L_{002} reduced quadratic polynomial model

Source	Sum of squares	d.f.	Mean Square	F value	Prob >F	
Model	445.49	2	222.74	4.94	0.0237	significant
T_o	177.45	1	177.45	3.94	0.0671	
t_r^2	268.04	1	268.04	5.95	0.0286	
Residual	630.65	14	45.04			
Lack of Fit	630.37	10	63.04	900.14	< 0.0001	significant
Pure Error	0.28	4	0.070			
Corrected Total	1076.14	16				

R^2 = 0.4140; predicted R^2 = 0.0315; adjusted R^2 = 0.3302; adequate precision = 6.162

Table 4-37: ANOVA table for crystallite size, L_{300} reduced quadratic polynomial model

Source	Sum of squares	d.f.	Mean Square	F value	Prob >F	
Model	976.19	3	325.40	11.11	0.0007	significant
V_{st}	548.61	1	548.61	18.73	0.0008	
V_{st}^2	314.46	1	314.46	10.73	0.0060	
t_r^2	92.82	1	92.82	3.17	0.0984	
Residual	380.81	13	29.29			
Lack of Fit	380.69	9	42.30	1372.37	< 0.0001	significant
Pure Error	0.12	4	0.031			
Corrected Total	1357.00	16				

R^2 = 0.7194; predicted R^2 = 0.4415; adjusted R^2 = 0.6546; adequate precision = 8.227

Crystallite Size, = +52.86

L_{002} (nm) +4.71 * T_o

+7.96 * t_r^2 *Equation (4-24)*

Crystallite Size, = +36.21562

L_{002} (nm) +0.47097 * Reaction Temp

-2.31882E-003 * Ripening Time^2 *Equation (4-25)*

The above equation (4-24) indicates that the two effects are positively affecting the crystallite size (L_{002}) in the same order as shown previously: $t_r^2 > T_{o.}$

Crystallite Size, = +71.86

L_{300} (nm)	+8.28	* T_o	
	-8.63	* T_o^2	
	-4.69	* t_r^2	*Equation (4-26)*

Crystallite Size, = -101.01519

L_{300} (nm)	+0.26403	* Stirring Speed	
	-9.85094E-005	* Stirring Speed^2	
	-3.07859E-003	* Ripening Time^2	*Equation (4-27)*

The above equation (4-26) indicates that the only positive effects of the chemical precipitation process parameters on the crystallite size (L_{300}) is (T_o) while the order of the level of significance of the negative effects on the lattice parameter ratio is as follows: (T_o^2) > (t_r^2).

Fig 4-67(a) and (b) shows the relationship between the actual and predicted values of the L_{002} and L_{300} crystallite sizes, respectively. The figures indicate that the developed models are relatively adequate, since the residuals in the prediction of each response are small, with the residuals tending to be close to the diagonal line.

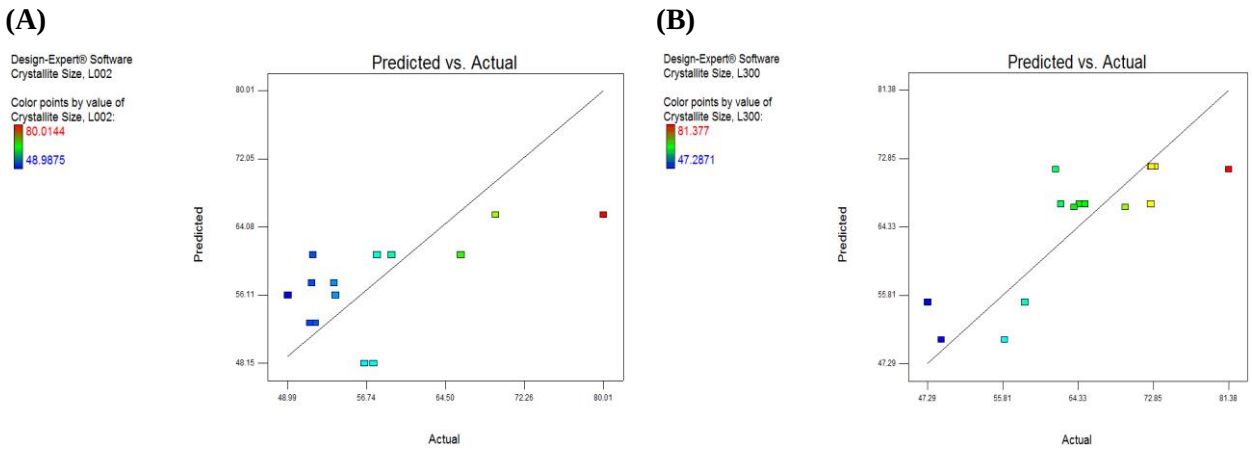

Figure 4-67: Scatter diagram for (A) crystallite size, L_{002} and (B) crystallite size L_{300}

4.6.6 Effect Of The Process Parameters On The Crystallite Size

The perturbation plot aids in comparing the effect of the significant factors at a particular point in the design space. Figure 4-68(a) shows a comparison between the significant effects of reaction temperature and ripening time on the crystallite size, L_{002}, while Figure 4-68(b) shows a comparison between the significant effects of stirring speed and ripening time on the crystallite size. In Figure 4-68(a), it is evident that the positive linear relationship of the reaction temperature indicates that an increase in this parameter will directly increase the crystallite size, while the curvilinear relationship of the ripening time shows that the L_{002} crystallite size is at its minimum mid-range (at 36h). Figure 4-68(b) shows the comparison between the significant effects of both the stirring speed and ripening time, both of which exhibit curvilinear relationships with the crystallite size in the 300 plane. For this plane, an increase of stirring speed will result in an increase of the crystallite size, while the crystallite size is at its minimum at a ripening time of 36h and highest values at 24 and 48h ripening.

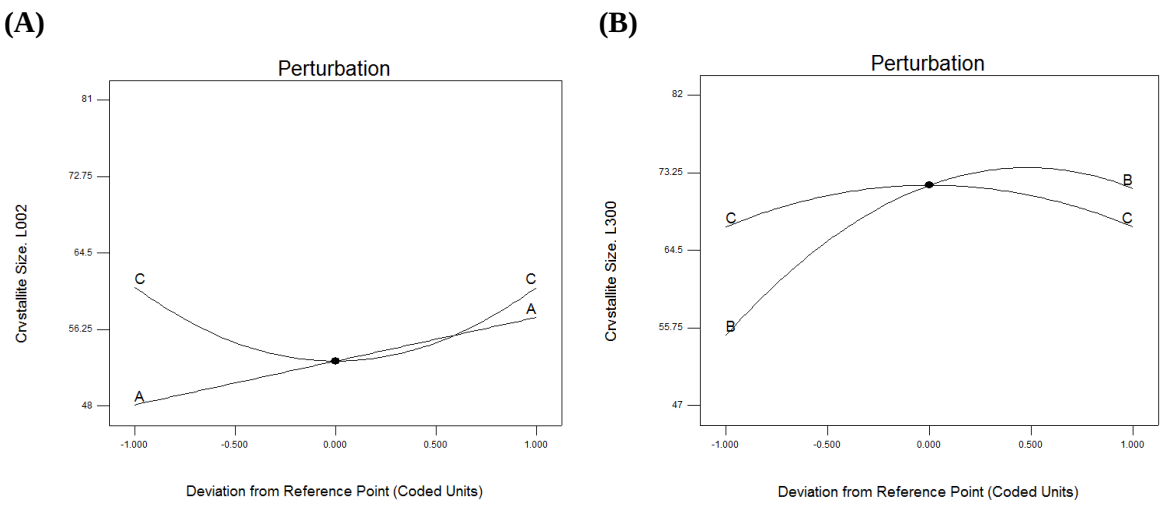

Figure 4-68: Perturbation plot showing the effect of all the parameters on the crystallite size, L_{002} (A) and L_{300} (B)

Tables 4-38 and 4-39 shows the top four most influencing main and interaction effects (if any), in chronological order, for both the screening (FFD) and optimisation (BBD) with respect to attaining high levels of crystallite size in the 002 and 300 plane, respectively.

Table 4-38: Comparison of significant effects for screening (stage I) and optimisation (stage II) for crystallite size, L_{002}

Order of Significance	Fractional Factorial Design (FFD)	Box – Behnken Design (BBD)
	↑Crystallite Size, L_{002} (nm)	
1	↑atm.	↑ T_o
2	↑T_o * t_r	↑ t_r^2
3	↓ Ca^{2+}	
4	↑V_{ac} * t_r	

For L_{002}, atmospheric control, calcium concentration and acid addition rate were eliminated in the Box-Behnken design. Therefore, the remaining factors (T_o and t_r) that were originally found to affect this response have increased in their level of significance in attaining a high crystallite size. While for L_{300}, the same approach applies. However, the significance of the stirring speed is now included during optimisation. This factor was previously ranked the 5^{th} most influencing factor for this response. Therefore, it may be assumed that the removal of the other factors has resulted in this increase of significance. Clearly, it is noted that it has an influence similar to that for crystallinity. However, the stirring speed and reaction temperature do not appear to significantly affect the crystallite size for the 002 and 300 plane, respectively. The difference for these models (screening and optimisation) may be attributed to the variance in the range of factors selected.

Table 4-39: Comparison of significant effects for screening (stage I) and optimisation (stage II) for crystallite size, L_{300}

Order of Significance	Fractional Factorial Design (FFD)	Box – Behnken Design (BBD)
	↓Crystallite Size, L_{300} (nm)	
1	↑t_r	↑ V_{st}
2	↑T_o * atm.	↑ V_{st}^2
3	↓atm.	↑t_r^2
4	↑V_{ac} * Ca^{2+}	

4.6.7 Development Of Lattice Parameter Ratio Model

As a result of analysing the measured responses using the Design Expert software, the fit summary selected the highest order polynomial where the additional terms are significant and the model is not aliased. Choosing the step-wise regression method led to the automatic elimination of the insignificant model terms. Table 4-39 presents the ANOVA results for the lattice parameter ratio and shows the significant model terms. The same tables show also the other adequacy measures R^2, Adjusted R^2 and Predicted R^2. An Adequate Precision ratio of 17.249 indicates adequate model discrimination [160]. The predicted R^2 in this mode is not as high as that obtained for the screening model, so therefore the elimination of the factors (acid addition rate, calcium concentration and atmospheric) has resulted in this decrease, since the interaction of the acid addition rate and calcium concentration was ranked as the fourth most significant effect in the screening model and moreover, either of the two factors were involved in interactions with other factors at ranks below this.

The result of the ANOVA for the lattice parameter ratio model shows that the main effect of all three of the chemical precipitation parameters investigated have a significant effect on the lattice parameter ratio. An interaction effect between the reaction synthesis temperature and the stirring speed quadratic effect of the stirring speed are significant model terms, while the quadratic effects of both the stirring speed and ripening time are also shown to be influencing factors. The order of significance for these effects follows the order: $t_r > t_r^2 > T_o > V_{st}^2 > T_o * V_{st} > V_{st}$

The final model in terms of coded factors is shown in Equation 4-28, while the final model in terms of coded factors is presented in Equation 4-29.

Table 4-40: ANOVA table for a/c ratio reduced quadratic polynomial model

Source	Sum of squares	d.f.	Mean Square	F value	Prob >F	
Model	0.0003147	6	0.0003147	19.80	< 0.0001	significant
T_o	0.0000265	1	0.0000265	10.02	0.0101	
V_{st}	0.0000120	1	0.0000120	4.51	0.0596	
t_r	0.0001335	1	0.0001335	50.40	< 0.0001	
$T_o * V_{st}$	0.0000133	1	0.0000133	5.02	0.0490	
V_{st}^2	0.0000163	1	0.0000163	6.17	0.0323	
t_r^2	0.0001175	1	0.0001175	44.35	< 0.0001	
Residual	0.0000265	10	0.0000265			
Lack of Fit	0.0000265	6	0.0000044			
Pure Error	0.000	4	0.000			
Corrected Total	0.0003412	16				

R^2 = 0.9223; predicted R^2 = 0.5867; adjusted R^2 = 0.8757; adequate precision = 17.249

a/c ratio = +1.37

+1.821E-003 * T_o

+1.223E-003 * V_{st}

-4.086E-003 * t_r

-1.823E-003 * T_o * V_{st}

-1.968E-003 * V_{st}^2

+5.276E-003 * t_r^2 *Equation (4-28)*

a/c ratio = +1.34913

+9.11212E-004 * Reaction Temp

+8.69209E-005 * Stirring Speed

-2.97829E-003 * Ripening Time

-6.07562E-007 * Reaction Temp * Stirring Speed

-2.18615E-008 * Stirring Speed^2

+3.66365E-005 * Ripening Time^2 *Equation (4-29)*

Equation 4-28 indicates that the order of the level of significance of the positive effects of the chemical precipitation process parameters on the lattice parameter ratio follows the order: $(t_r^2) > (T_o) > (V_{st})$ while the order of the level of significance of the negative effects on the lattice parameter ratio is as follows: $(t_r) > (V_{st}^2) > (T_o * V_{st})$.

Figure 4-69 shows the relationship between the actual and predicted values of the lattice parameter ratio. This figure indicates that the developed model is adequate, since the residuals in the prediction of each response are small, with the residuals tending to be close to the diagonal line.

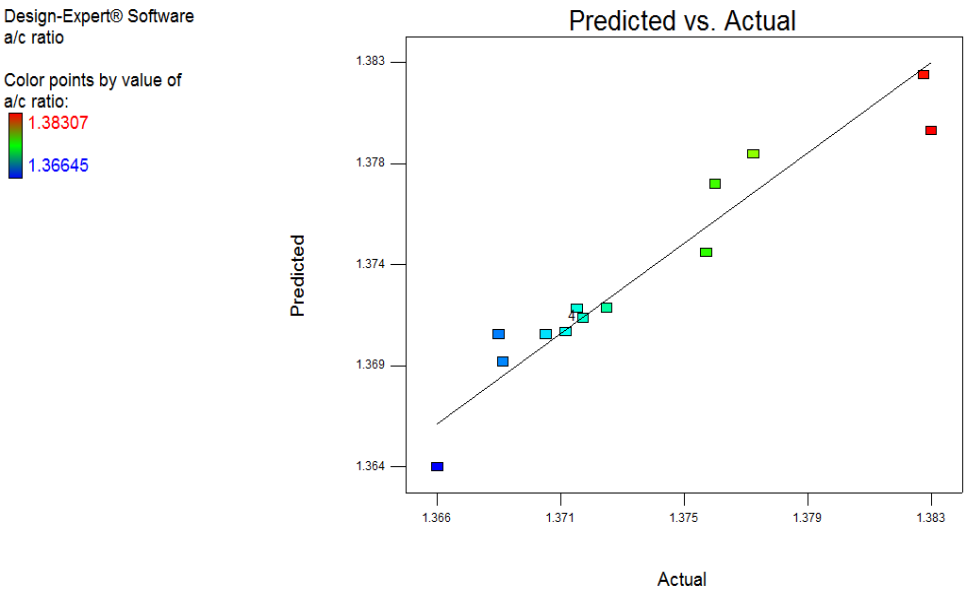

Figure 4-69: Scatter diagram for lattice parameter ratio

4.6.8 Effect Of The Process Parameters On The Lattice Parameter Ratio

Figure 4-70(a) to (c) shows the 3-D surface and 2-D contour graphs, highlighting the significant interaction effect between the reaction temperatures and stirring speed at ripening times of between 24 to 48h. It is clear from this figure that an increase in the reaction temperature produces a marked increase in ratio, while a reduction in the ripening time appears to favour this response. A median value (1200rpm) of stirring speed also appears to favour an increase in lattice parameter ratio.

The cube plot shown in Figure 4-71 displays the relationship between three significant factors and is especially useful in interpreting the interaction effects (such as, T_o* $V_{st,}$). This type of figure presents the predicted values of the responses from the model for the combinations of the -1 and +1 levels of the three factors. This figure presents the effect of the three factors on the a/c ratio by using a cube plot to represent this effect. It is noted that the process input parameters can be selected where the a/c ratio would be minimum or maximum. The perturbation plot shown in Figure 4-72 shows a comparison between the effects of reaction temperature, stirring speed and ripening time on the maximum a/c ratio. This confirms how a direct increase of the reaction temperature can increase the resulting a/c ratio, while a curvilinear

(A) Ripening Time: 24h

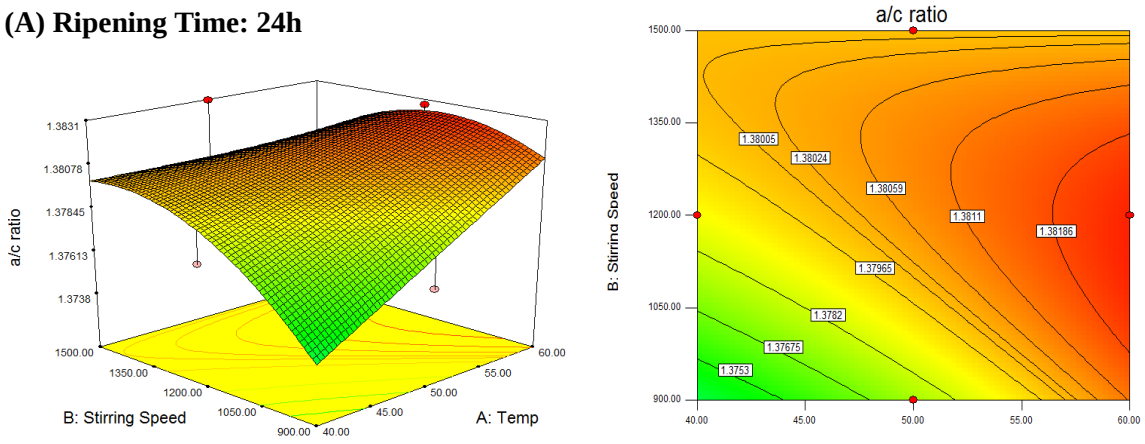

(B) Ripening Time: 36h

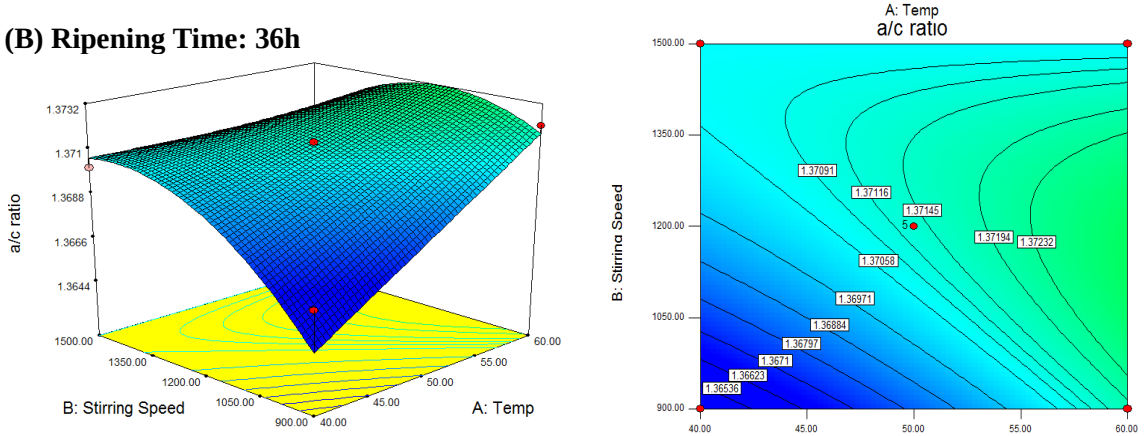

(C) Ripening Time: 48h

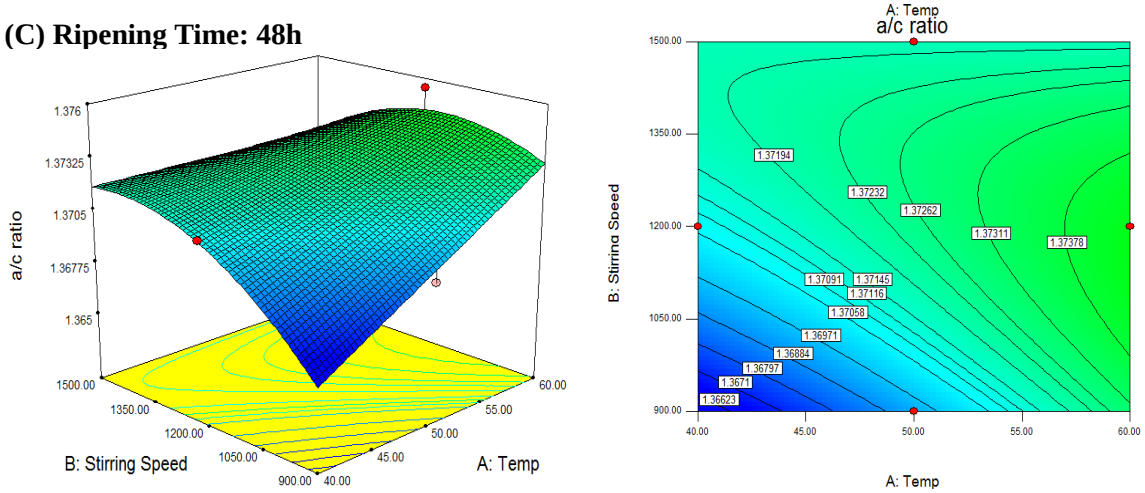

Figure 4-70: 3D surface and 2D contour plots of lattice parameter ratio at (A) a ripening time of 24h; (B) a ripening time of 36h and (C) a ripening time of 48h (under an inert environment)

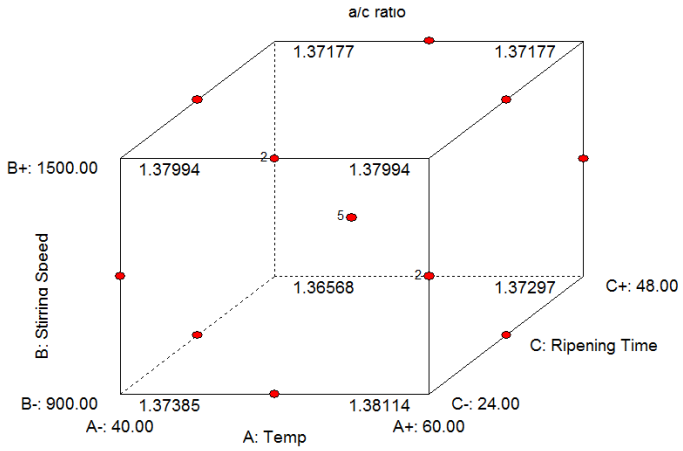

Figure 4-71: Cube graph demonstrating the effect of the three parameters on the lattice parameter ratio

relationship for the ripening time represents a high sensitivity of this factor to the a/c ratio, with decreased ripening times dramatically increasing this response. A less pronounced curvilinear effect for the stirring speed demonstrates how the maximum lattice ratio between 1200 – 1500rpm.

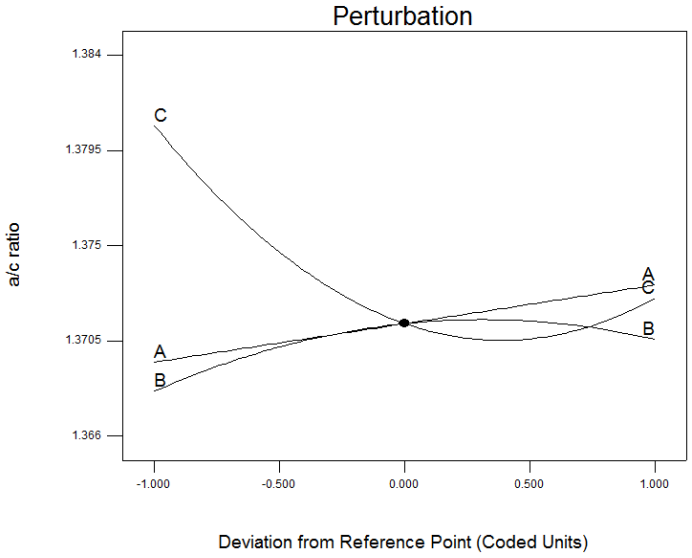

Figure 4-72: Perturbation plot showing the effect of all the parameters on the lattice parameter ratio

Table 4-41 shows the top four most influencing main and interaction effects (if any), in chronological order, for both the screening (FFD) and optimisation (BBD) with respect to attaining lattice parameters within a desired range.

Table 4-41: Comparison of significant effects for screening (stage I) and optimisation (stage II) for the lattice parameter ratio, a/c

Order of Significance	Fractional Factorial Design (FFD)	Box – Behnken Design (BBD)
	↓Lattice parameter ratio, *a/c*	
1	$\uparrow t_r$	$\downarrow t_r^2$
2	↑Vst	$\uparrow t_r$
3	$\uparrow T_o$	$\uparrow V_{st}^2$
4	$\uparrow V_{ac} * Ca^{2+}$	$\uparrow T_o * V_{st}$

With the exception of the calcium concentration, all the other factors (t_r, V_{st} and T_o) were the same for both models, with the quadratic effects of certain factors included in the optimisation model. The reasons for their influencing the lattice parameter ratio are valid for both models, as discussed previously, in the screening results.

4.6.9 Development Of Particle Size Model

As a result of analysing the measured responses using the Design Expert software, the fit summary selected the highest order polynomial where the additional terms are significant and the model is not aliased. Choosing the step-wise regression method led to the automatic elimination of the insignificant model terms. Table 4-42 presents the ANOVA results for the particle size shows the significant model terms. The same tables show also the other adequacy measures R^2, Adjusted R^2 and Predicted R^2. An Adequate Precision ratio of 7.330 indicates adequate model discrimination [160]. However, factors (such as acid addition rate and calcium concentration) were found to be included as one of the top four most influencing factors having an effect on the particle size in the screening model are not accounted for in this model.

The result of the ANOVA for the particle size model shows that the main effect of one (reaction synthesis temperature) of the chemical precipitation parameters investigated have a significant effect on the lattice parameter ratio. An interaction effect between the stirring speed and the ripening time and a quadratic effect of the ripening time are the significant model terms influencing final response for particle size. The order of significance for these effects follows the order: $t_r^2 > V_{st} * t_r > T_{o.}$

Table 4-42: ANOVA table for particle size reduced quadratic polynomial model

Source	Sum of squares	d.f.	Mean Square	F value	Prob >F	
Model	247.13	3	82.38	7.22	0.0042	significant
T_o	36.98	1	36.98	3.24	0.0950	
$V_{st} * t_r$	62.49	1	62.49	5.48	0.0358	
t_r^2	147.66	1	147.66	12.95	0.0032	
Residual	148.27	13	11.41			
Lack of Fit	148.27	9	16.47			
Pure Error	0.000	4	0.000			
Corrected Total	395.40	16				

R^2 = 0.6250; predicted R^2 = 0.3185; adjusted R^2 = 0.5385; adequate precision = 7.330

The final model in terms of coded factors is shown in Equation 4-30, while the final model in terms of coded factors is presented in Equation 4-31.

Particle Size, = +25.49

P_s (μm) +2.15 * A

+3.95 * B * C

+5.90 * C^2 *Equation (4-30)*

Particle Size, = +19.51609

P_s (μm) +0.21500 * Reaction Temp

-6.24224E-006 * Stirring Speed * Ripening Time

-1.26938E-003 * Ripening $Time^2$ *Equation (4-31)*

The above equation (4-30) indicates that all of the significant effects are positively affecting the lattice parameter ratio in the same order as shown previously: $(t_r^2) > (V_{st} * t_{r)} > (T_o)$.

Figure 4-73 shows the relationship between the actual and predicted values of the particle size. This figure indicates that the developed model is adequate, since the residuals in the prediction of each response are small, with the residuals tending to be close to the diagonal line.

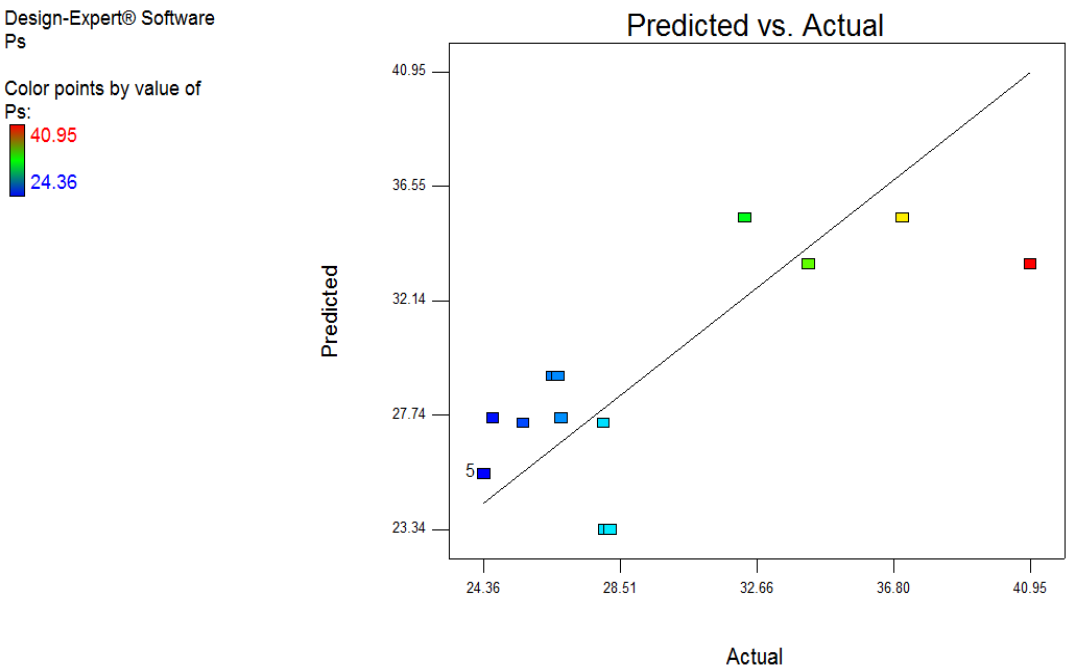

Figure 4-73: Scatter diagram for particle size

4.6.10 Effect Of The Process Parameters On The Particle Size

Figure 4-74(a) to (c) shows the 3-D surface and 2-D contour graphs, highlighting the significant interaction effect between the reaction temperatures and stirring speed at ripening times of between 24 to 48h. It is clear from this figure that for an increase in ripening time, an increase in both the stirring speed and the ripening time is required for an increased particle size.

The cube plot shown in Figure 4-75 displays the relationship between three significant factors and is especially useful in interpreting the interaction effects (such as, V_{st} * t_r). This type of figure presents the predicted values of the responses from the model for the combinations of the -1 and +1 levels of the three factors. This figure presents the effect of the three factors on the particle size by using a cube plot to represent this effect. It is noted that the process input parameters can be selected where the particle size would be minimum or maximum. However, it must also be noted that all the experimental results for particle size showed that the experimental conditions used for each experiment yielded a particle size of less than the required 100µm. Therefore, it is not our aim in this study to maximise or minimise this response.

The perturbation plot shown in Figure 4-76 shows a comparison between the effects of reaction temperature, stirring speed and ripening time on the maximum particle size. This confirms how an increase in both the reaction temperature and the ripening time can significantly increase the resulting particle size, while a linear response for the stirring speed is shown to have little effect on tailoring the desired particle size. The curvilinear relationship of the ripening time demonstrates a high sensitivity of this factor to the final response with the minimum response for particle size found at 36h and its maximum found at the lower (24h) and upper (48h) limits. The linear response for the reaction temperature indicates a less significant response. However, the plot also demonstrates how a direct increase in the reaction temperature can also maximise the final particle size.

(A) Ripening Time: 24h

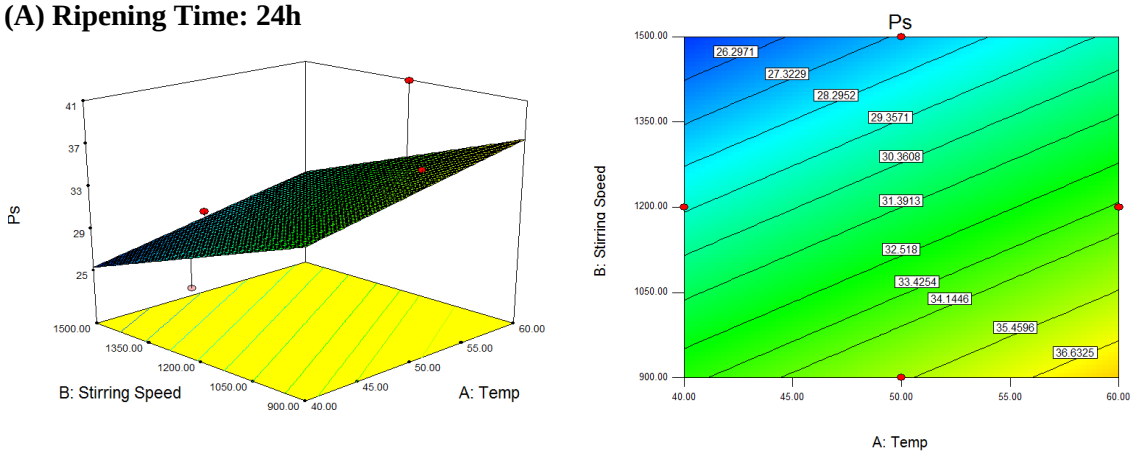

(B) Ripening Time: 36h

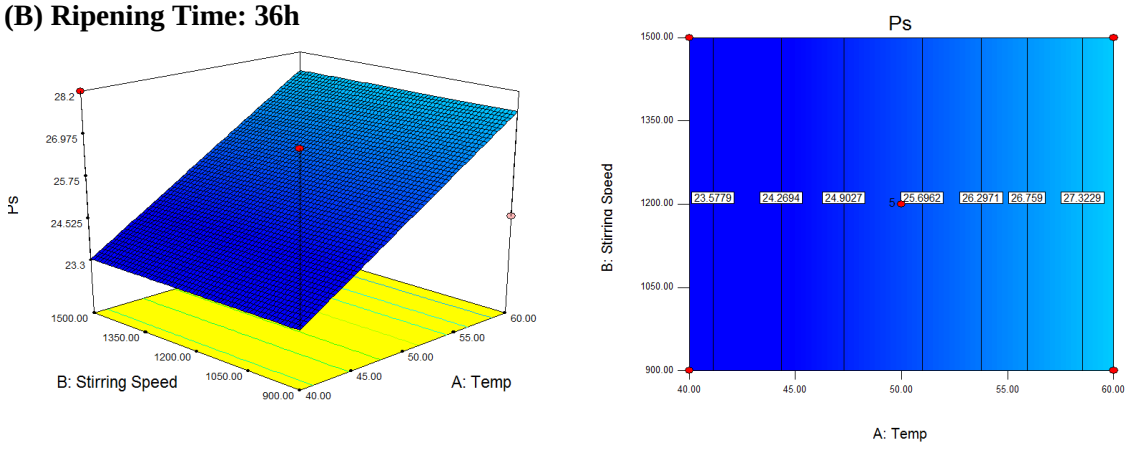

(C) Ripening Time: 48h

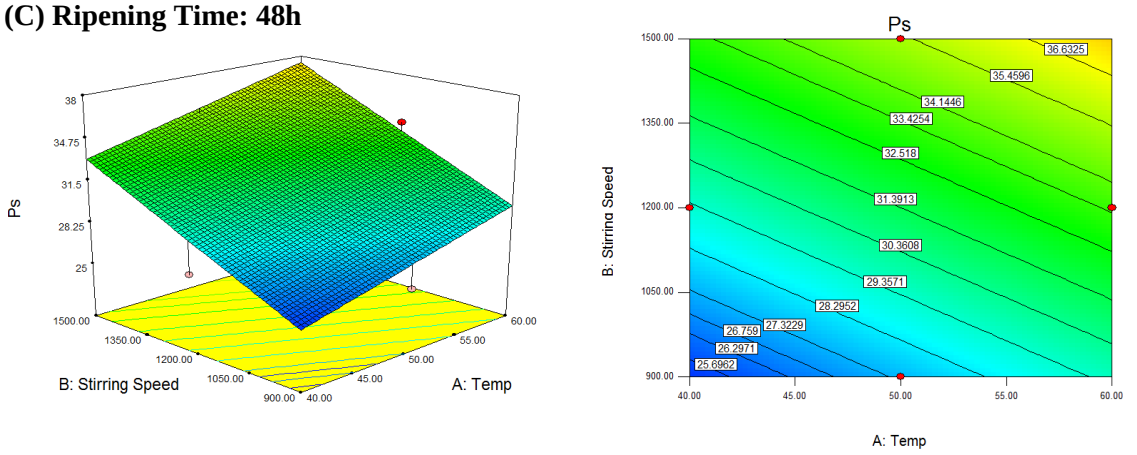

Figure 4-74: 3D surface and 2D contour plots of particle size at (A) a ripening time of 24h; (B) a ripening time of 36h and (C) a ripening time of 48h (under an inert environment)

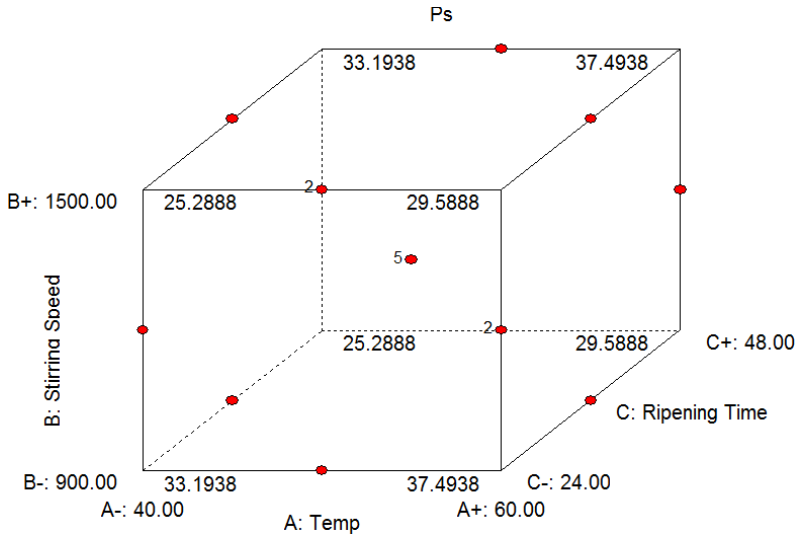

Figure 4-75: Cube graph demonstrating the effect of the three parameters on the lattice parameter ratio

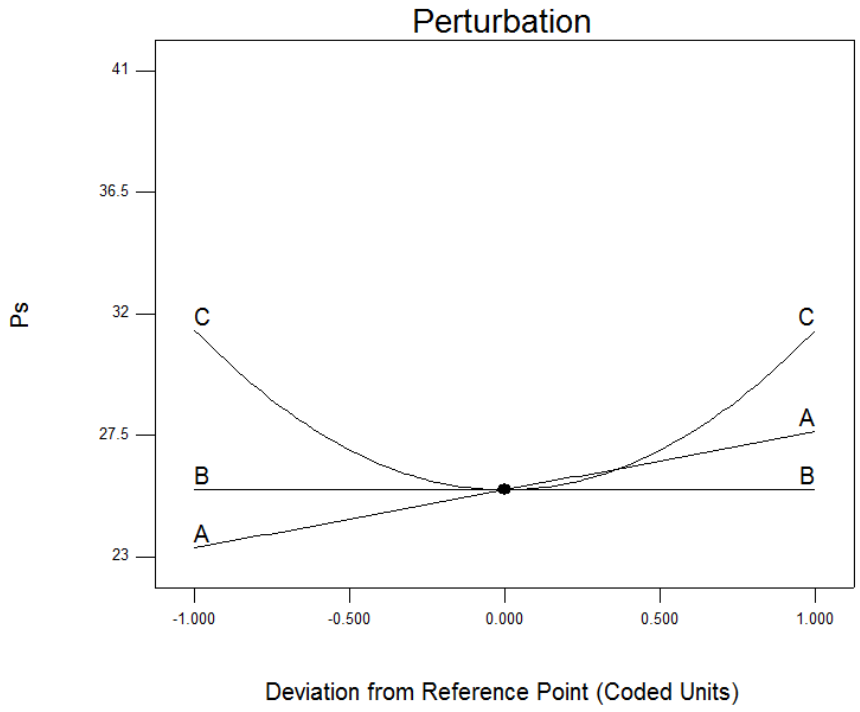

Figure 4-76: Perturbation plot showing the effect of all the parameters on the particle

Table 4-43 shows the top four most influencing main and interaction effects (if any), in chronological order, for both the screening (FFD) and optimisation (BBD) with respect to attaining particle sizes with the desired range.

Table 4-43: Comparison of significant effects for screening (stage I) and optimisation (stage II) for the particle size, P_s

Order of Significance	Fractional Factorial Design (FFD)	Box – Behnken Design (BBD)
	↓Particle size, P_s	
1	↑To	$\downarrow t_r^2$
2	$\uparrow Ca^{2+}$	$\downarrow V_{st} * t_r$
3	$\downarrow V_{ac} * T_o$	$\downarrow T_o$
4	$\uparrow V_{ac} * Ca^{2+}$	

Comparing the top four most influencing effects in both models, it is obvious that the reaction temperature, as expected, has a major influence over the resulting particle size. However, the influence of this factor appears to have the opposite effect: requiring an increase in the screening model and a decrease in the optimisation model to effectively increase the particle size. This may be explained by the fact that the temperature range varies between the models developed (that is, 20 - 60ºC for screening and 40 - 60ºC for optimisation). As a result it may be interpreted that, while an increase in the reaction temperature is known to result in an increase in particle size, the optimum temperature for acquiring the largest particle size may in fact lie around 40 - 50ºC. The desirability approach (used at a later stage), however, also indicates that use of a high reaction temperature is required to increase the particle size.

As discussed previously, it is also noted that all the experimental results for particle size demonstrated how the experimental conditions used for each experiment yielded a particle size of less than the required 100µm. Therefore, it is not our aim in this study to either maximise or minimise this response, as it is already found to be within acceptable limits. Instead, understanding the effects of the parameters and their influence on the resulting response obtained for particle size is of interest.

With the acid addition rate and calcium concentration factors eliminated in the optimisation, the stirring speed, as an interaction effect with ripening time is now included as one of the top four most influencing factors. This factor, however, was previously ranked the 6^{th} most influencing factor in the screening model and therefore, it may be assumed that the removal of the other factors has resulted in this increase of its level of significance.

Table 4-40 outlines the average of three results recorded for mode, mean particle sizes and the percentage (10, 50 and 90%) of powder particles within a specific range. Figure 4-77 graphically compares the mean particle sizes obtained for the micron sized HAp powders analysed in this study. The order of mean particle size from the largest is as follows:

N6 → N9 → N8 → N12 → N3 →N16 → N1 → N17 = N10 → N15 →N4 →N7 → N5 → N14 → N11 → N2 → N13

Table 4-44: Particle size analysis results: percentage diameter under 10, 50 and 90% micrometer, mean particle size, mode particle size and specific surface area data of the different HAp samples for various conditions of Box-Behnken experimental design

HAp Powder	Median	Diameter (µm) on:			Mean	Mode
	(µm)	10%	50%	90%	(µm)	(µm)
N1	5.210	2.520	21.750	63.410	28.040	41.430
N2	4.650	2.330	17.530	57.950	24.630	41.430
N3	4.500	2.720	22.130	63.240	28.200	48.266
N4	5.610	3.040	19.440	61.530	26.710	41.430
N5	5.180	2.300	19.840	60.970	26.450	48.265
N6	9.280	9.220	37.630	77.620	40.950	56.229
N7	4.890	2.120	20.310	61.160	26.620	48.265
N8	6.800	4.850	28.910	72.190	34.220	48.265
N9	7.760	6.020	32.130	76.080	37.070	56.229
N10	4.920	2.270	19.860	66.000	27.990	48.265
N11	5.460	2.800	19.540	57.620	25.550	41.430
N12	6.060	2.980	23.650	71.410	32.280	41.430
N13	5.050	2.780	19.340	53.730	24.360	35.562
N14	5.870	2.900	20.400	59.270	26.390	41.430
N15	5.990	3.020	21.140	61.300	27.370	41.430
N16	6.250	3.210	21.750	63.040	28.170	41.430
N17	6.150	3.050	21.230	63.300	27.990	41.430

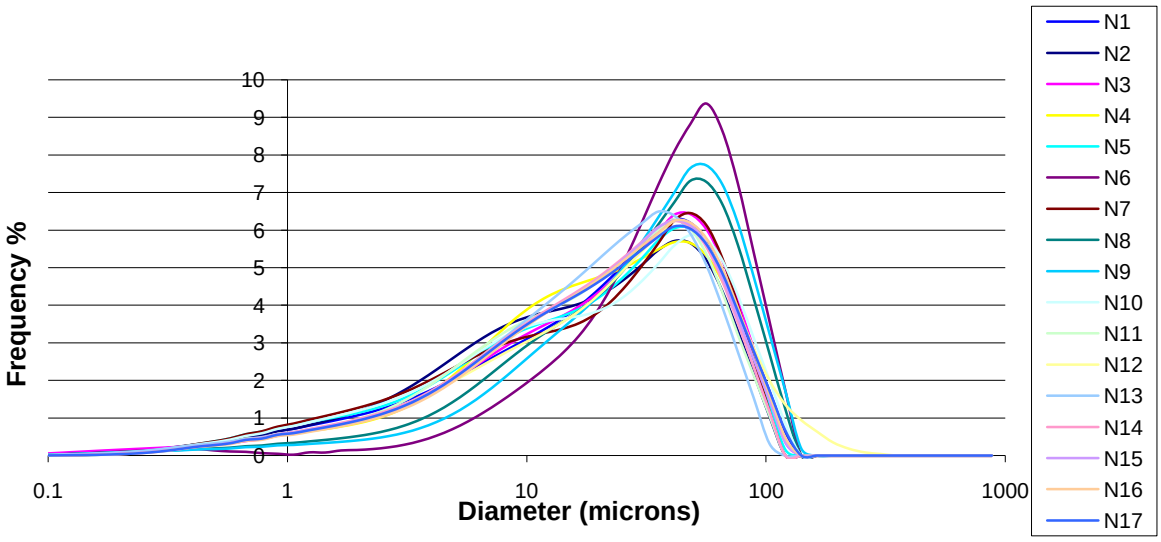

Figure 4-77: Comparison of particle size distributions obtained for various HAp powders synthesised according to the Box-Behnken design

The majority of the powders synthesised in this study, possess a narrow particle size distribution, as indicated in Figures 4-78 to 4-79.

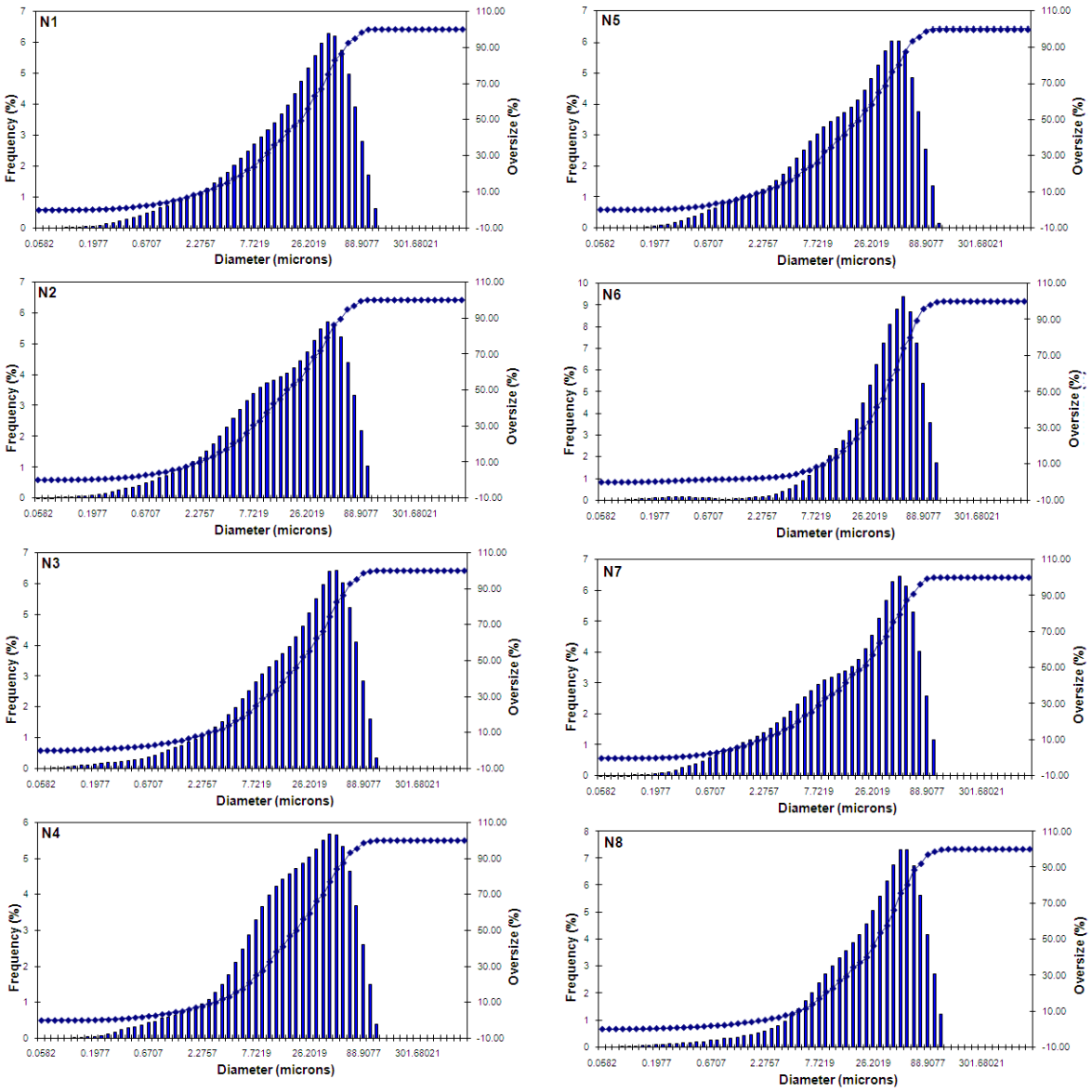

Figure 4-78: Comparison of particle size distributions obtained for optimisation experimental conditions (N1 – N8)

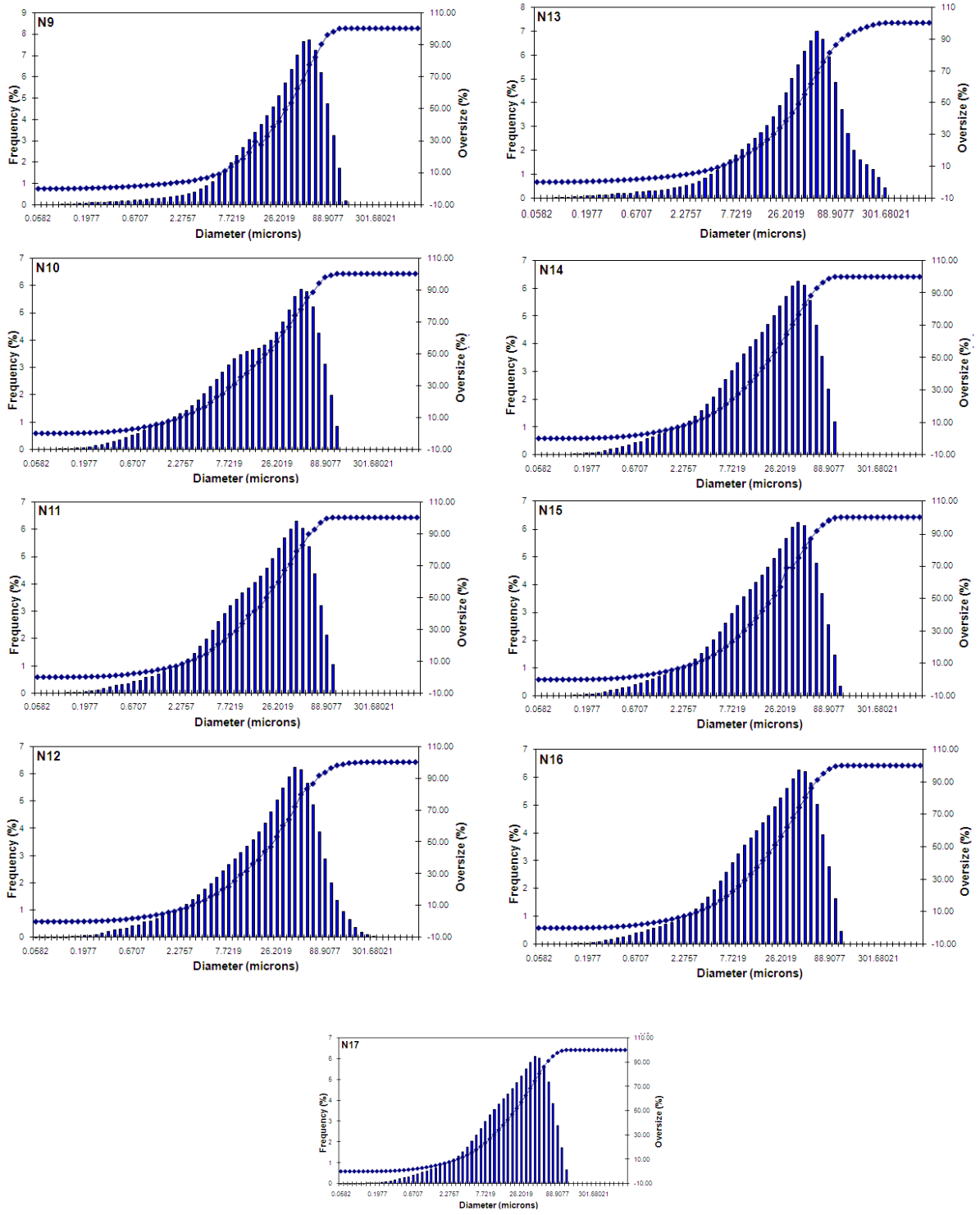

Figure 4-79: Comparison of particle size distributions obtained for optimisation experimental conditions (N9 – N17)

4.6.11 Morphological Evaluation Of the HAp Powders

The SEM micrographs of the HAp powders in Figures 4-80 to 4-82 reveal how the HAp powders can vary according to the process parameters implemented in the optimisation study. An increase of the synthesis temperature (N1 to N2) is found to lead to more regular spherical HAp particles. These findings agree well with those reported by Bouyer [94], showing that a low synthesis temperature can lead to HAp crystals possessing needle-shape like morphology [94]. Pang and Bao [90] also confirmed that the particles synthesised at a low reaction temperature were a bit thinner and longer, with more irregularity and less clear contours. Also the particles in these comparisons also show a higher tendancy towards agglomeration. Moreover, it is also noticed that the change from irregular to regular particle morphology with the increase in synthesis temperature corresponds to the increase in the crystallinity of the HAp crystals, that is, more regular shape of the particles was observed when the powders possessing a higher crystallinity. Hence, it is clear that the influence of the chemical precipitation process parameters on the morphology of the HAp powders must be inviestigated. A qualitative examination of the positive effect of the interaction between the reaction temperature and the srirring speed (N9 to N5 and N6 to N10) demonstrates how the powder particle size increases in correspondence to a more idealised spherical morphology. Examining the effect of increasing the stirring speed (N9 to N10), in isolation of the other factors, however also demonstrates a favaourable effect on the resultant morphology. Another positive interaction effect between the stirring speed and the ripening time (N5 to N3), while a reduction in the stirring speed coupled with an increase in ripening time also demonstrates an enhanced spherical powder morphology. This would suggest that the stirring speed is the least significant factor affecting this resposne.

No visible colour changes from white to light blue were evident post sintering for all powders synthesised in this study, which meets with requirements outlined by the FDA. According to Gross et al. [70], these undesired colour changes are due to the presence of transitional elements located in the crystal lattice structure. Although they may not have any significant effect on the biocompatibility of HAp, the FDA criterion requires powders of a white colour [137].

N1

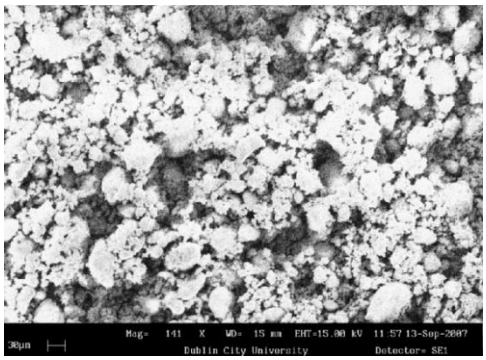

N2

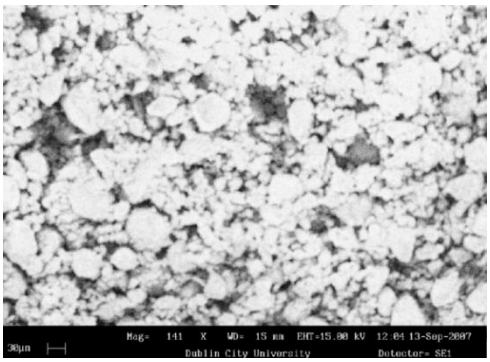

N3

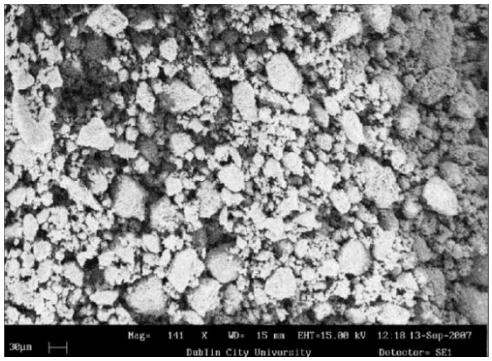

N4

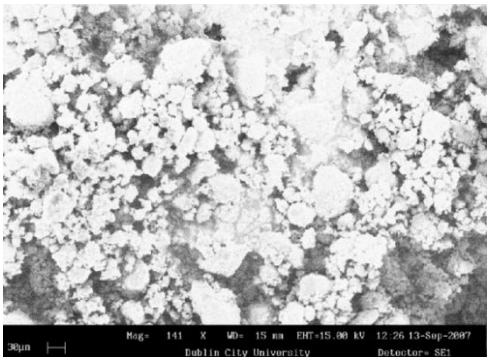

N5

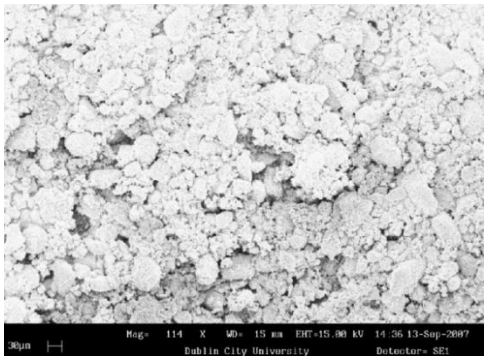

N6

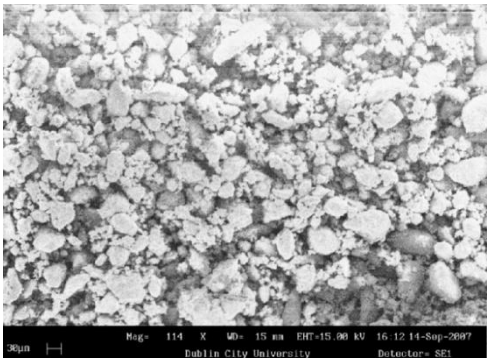

N7

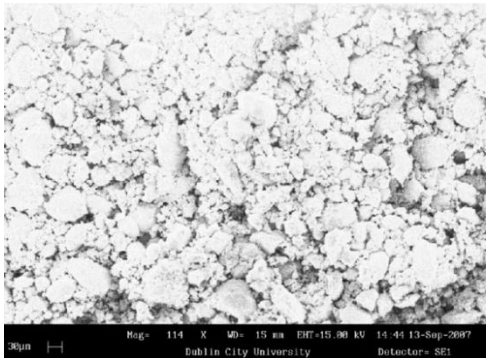

N8

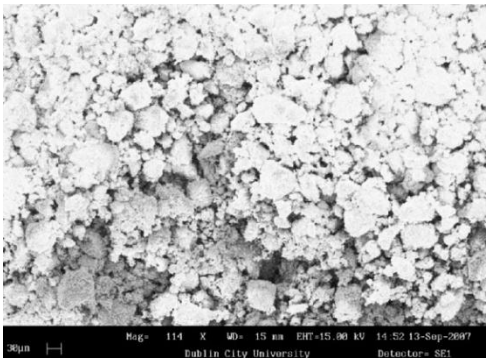

Figure 4-80: Comparison of the powder morphology for HAp samples synthesised using experimental conditions in the Box-Behnken Design (N1 to N8)

N9

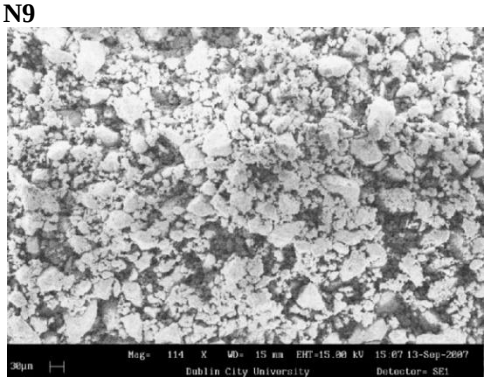

N10

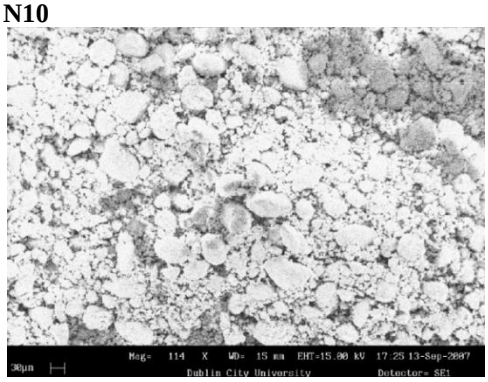

N11

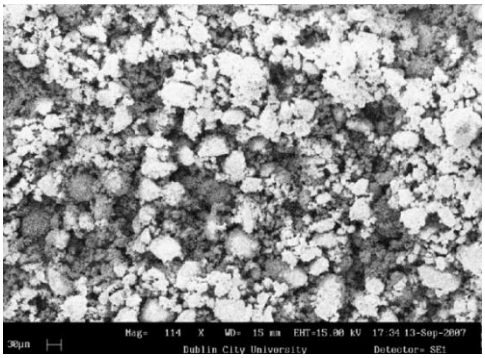

N12

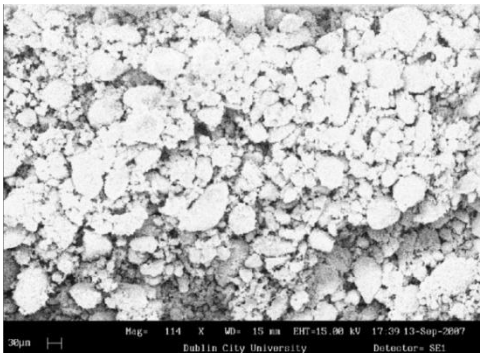

N13

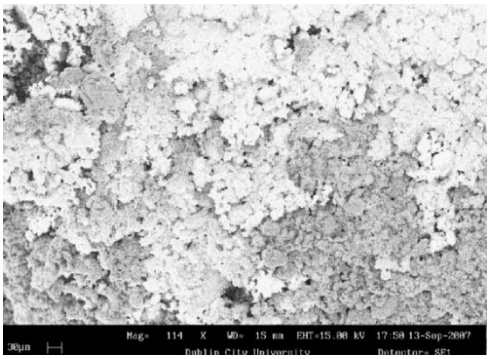

N14

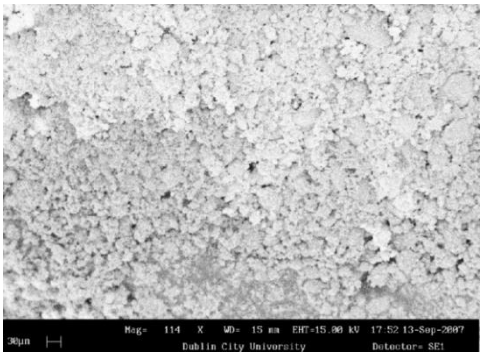

N15

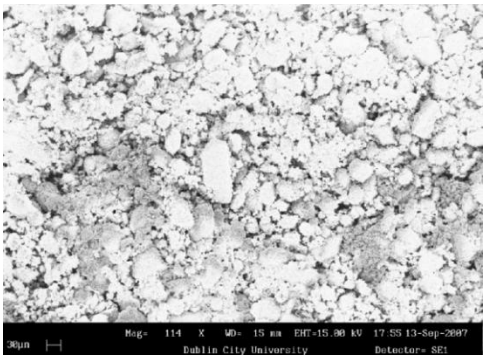

N16

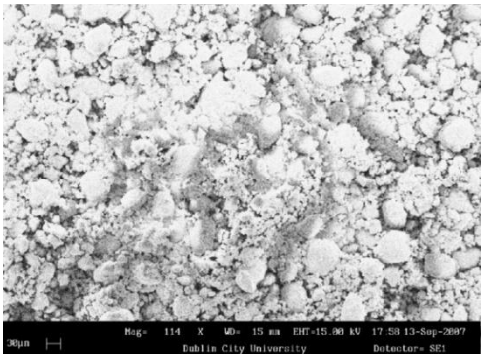

Figure 4-81: Comparison of the powder morphology for HAp samples synthesised using experimental conditions in the Box-Behnken design (N9 to N16)

N17

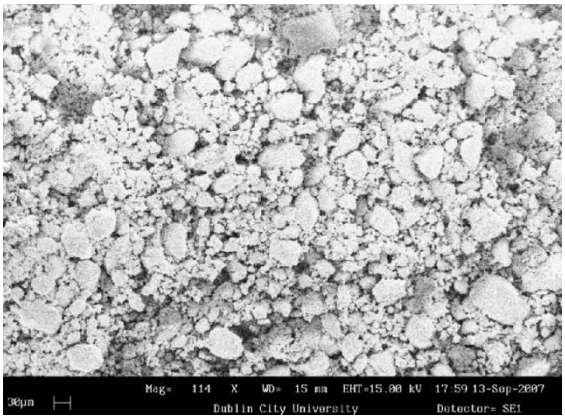

Figure 4-82: Comparison of the powder morphology for HAp samples synthesised using experimental conditions (N17)

4.6.12 Optimisation Of Chemical Precipitation Factors

The RSM study has aided in the development of six response models, relating the phase purity, crystallinity, crystallite sizes (L_{002} and L_{300}), lattice parameter ratio and particle size to the three factors investigated. However, the design of experiments in this investigation excluded any experiment being conducted, which examined the effect of setting all three factors at the upper level, and for this reason the models developed in the fractional factorial design study (screening) are instead used to identify the most appropriate combination of factors in order to achieve the optimum response, with respect to the HAp powder characteristics studied. These models also incorporated the full list of chemical precipitation parameters (acid addition rate, reaction temperature, stirring speed, ripening time, initial calcium concentration, atmospheric control) of which have been shown in literature to determine the final powder characteristics.

(A) HAp Powder Characteristics Optimisation

The HAp powder characteristics were optimised again using the Design Expert software. The models developed for each response were used for the process optimisation. Design Expert enables both Numerical Optimisation and Graphical Optimisation. The Numerical Optimisation step was carried out first, since it is most efficient in the determination of optimal zones. This approach can be applied in Industry to save costs associated to the control of each factor (such as, an increase of reaction temperature, ripening time, stirring speed) to yield the desired response. Each response for optimisation was given a goal and a level of importance attached to it.

The desired optimisation aims to produce a highly phase pure and crystalline (both >95%) HAp powder with a particle size not exceeding 100µm. This HAp powder will fully satisfy regulatory requirements for successful coating application onto orthopaedic implants via the thermal spraying technique. In order to achieve the desired powder characteristics, the phase purity, crystallinity and crystallite sizes (L_{002}) were maximised in the optimisation. This is to ensure that levels of impurities are kept to a minimum to ensure that the final coatings do not dissolve at a quicker rate *in vivo* and that increased

levels of crystallinity can also provide stability in the final coating as opposed to amorphous ones which are found to dissolve quickly and lead to undesirable coatings. The crystallite size in the 300 plane however was minimised: since this crystallite size has previously been suggested to be smaller than that of the 002 plane in previous work carried out by Smiciklas et al. [85]. The lattice parameter ratio was also minimised, as this is related to the introduction of impurities incorporated into the final lattice. An increased ratio (+*a* and -*c*) has also been reported to decrease crystallinity and promote β-TCP [64]. Since particles, exceeding 100µm are undesired, the response for particle size was kept within the range based on those obtained for each model.

The importance level for each response within this desired optimisation analysis was selected. The phase purity and crystallinity were set to an importance level of 5. The lattice parameter ratio was set to an importance level of 3, while the particle size and crystallite sizes in the 002 and 300 plane were set to an importance level of 2. The goal and importance for each optimisation parameter used is shown in Table 4-45.

Table 4-45 Design optimisation parameters

	Goal	**Importance**
Phase purity (%)	Maximise	+++++
Crystallinity (%)	Maximise	+++++
Crystallite Size, L_{002} (nm)	Maximise	++
Crystallite Size, L_{300} (nm)	Minimise	++
Lattice parameter ratio, a/c	Minimise	+++
Particle size (µm)	In Range	++

Design Expert has the capability in generating numerous possible solutions based on the optimisation criteria selected. The desirability (0 to 1) of each solution is indicated. The preferred settings can then be selected manually. The optimum solutions for the Fractional Factorial and Box-Behnken models are shown in Table 4-46 and compared against actual experimental results obtained at the same experimental conditions (that is, N16 from the fractional factorial (screening) model. The fractional factorial solution

shows that the model is predicting each response to be smaller in comparison to those obtained experimentally at the same conditions (N16). This can be attributed to the fact that the model is predicting the responses through incorporating the full set of models obtained, while the experimental conditions represent a true indication of the real values which can be obtained at the same conditions (factors). However, the model and the experimental conditions succeeded in verifying that the same set of factors were required in order to tailor the desired powder characteristics to meet with minimum regulatory requirements. The Box-Behnken design, however, provides a set of factors which do not match that of the N16 experimental set-up. Although it shows a high desirability of 0.695 (in comparison to 0.447 for the Fractional Factorial design), the main regulatory requirements for minimum phase purity and crystallinity is not attained. Therefore, the effect of leaving out the acid addition rate, calcium concentration and atmospheric control is found to exert a major effect on producing a HAp powder satisfying the minimum regulatory requirements. Thus, researchers [71] cannot accurately optimise the desired HAp powder characteristics, while eliminating any of the influences for all of the precipitation process parameters as proved by Table 4-46. The other factors (acid addition rate, calcium concentration and atmospheric control) must also be included.

A desirability bar graph for each response in both the Fractional Factorial and Box-Behnken design is shown in Figure 4-83. The bar charts show that less important responses, (requiring control for regulatory purposes) received a high desirability rating than the more critical responses (such as, phase purity and crystallinity). However, in terms of actual, predicted and experimental results (N16), the overall realistic outcome benefits what is desired.

Table 4-46: HAp powder characteristics optimisation results

	Optimised Solutions		Experimental Values	FDA Req.
	BBD	**FFD**	**N16**	
Factor				
Acid addition rate (mol/min)	0.01	0.01	0.01	
Reaction temperature (°C)	40	60	60	
Stirring speed (rpm)	900	1500	1500	
Ripening time (h)	48	48	48	
Calcium concentration (M)	2.0	2.0	2.0	
Atmospheric control (yes / no)	yes	no	no	
Response				
Phase purity (%)	72.9638	97.5919	98.8886	>95
Crystallinity (%)	79.2267	91.2467	95.1881	>95
Crystallite Size, L_{002} (nm)	56.1037	102.0189	107.9240	
Crystallite Size, L_{300} (nm)	50.2599	85.6456	90.5307	
Lattice parameter ratio, a/c	1.3658	1.3692	1.3692	
Particle size (µm)	25.2888	19.2181	15.3800	<100
Desirability	**0.695**	**0.447**		

Figure 4-83 further confirms that all of the process factors studied (3 or more) need to be set as high as possible in order to obtain the desired responses for a phase pure and highly crystalline HAp, of particle size not exceeding 100µm.

(A)

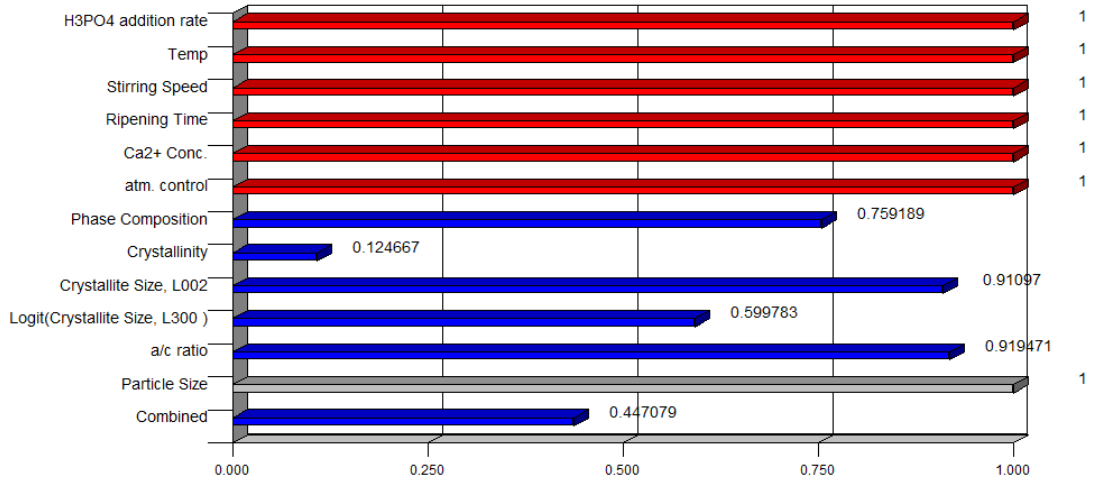

(B)

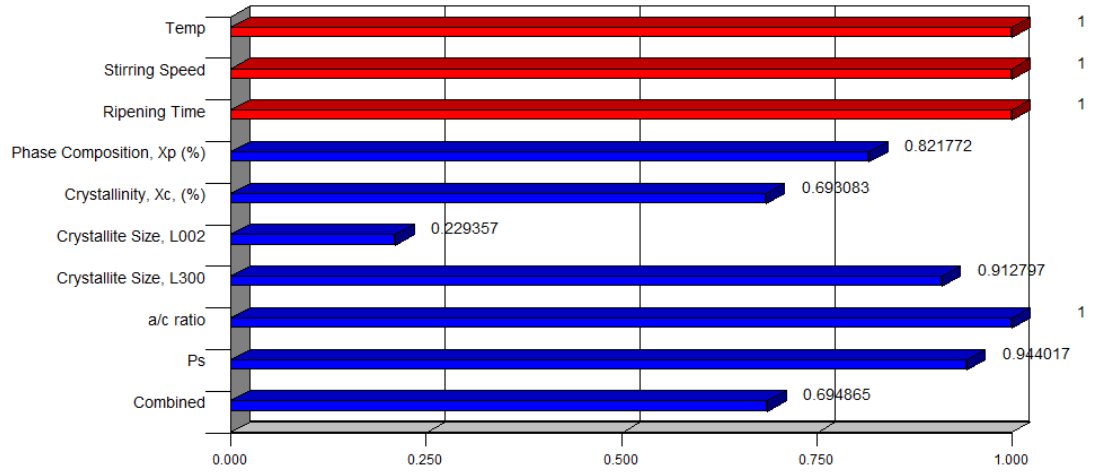

Figure 4-83: Desirability bar graph obtained for (A) the fractional factorial model and (B) the box-behnken model

HAp possessing optimum powder characteristics for orthopaedic application via a thermal spray technique can therefore be prepared using the following chemical precipitation process parameters: Reaction Temperature 60ºC, Ripening Time 48h and Stirring Speed 1500rpm using high reagent concentrations. The presence of an inert environment is less critical at this temperature, as opposed to a lower temperature range of 20ºC. In the case of HAp synthesis at lower temperatures, the atmospheric control is desired in order to achieve high phase purity and crystallinity.

5 CONCLUSIONS AND RECOMMENDATIONS

5.1 Conclusions

In this study, the effect of the chemical precipitation process parameters were quantified, using mathematical models developed using the Design Expert software, in order to assess their main and interaction effects on the final HAp powder characteristics obtained under the experimental conditions based on the experimental design. This aided in an optimisation of the precipitation parameters to produce HAp powders which fully satisfy minimum regulatory requirements. The synthesis of such HAp, however, having attained these desired characteristics is heavily dependent on numerous precipitation process parameters. The conclusions resulting from the investigation are summarised into sections as follows:

HAp Powder Characteristics

The preliminary investigation of this study involved analysing the HAp powder characteristics of commercial powders (HAp3 - HAp5) and comparing these against the HAp powder properties currently being produced by industry in Ireland and America (HAp1 and HAp2 respectively). HAp was synthesised in-house (HAp6), under the same conditions as that disclosed by the HAp manufacturing company in Ireland: characterised and compared against that of the HAp1 and also against the commercial powders to gain an understanding of the most important synthesis parameters influencing the HAp powder characteristics. The main findings at this stage include:

(A) Phase composition and purity

- Concerning the phase composition, XRD patterns shows that no foreign elements, such as sodium (Na^{2+}), ammonium (NH_4^+), potassium (K+), chloride (Cl-) and nitrate (NO_3^-) ions were involved in any of the reaction syntheses. The absence of these elements can be explained by the nature of the raw material ($Ca(OH)_2$ and H_3PO_4) used as precursors. Moreover, for all the HAp studied, no CaO was observed. This indicated that there was small or indeed no carbonation of the HAp having occurred during the synthesis. For HAp1 and HAp6 produced without the aid of atmospheric condition, the absence of CaO indicated that this parameter had no significant influence on the final HAp purity.

- Although no foreign elements were found for the six HAp: a significant amount of (β-TCP) phase was observed in the HAp6 powder. Minor traces of this phase were also observed for HAp3 and HAp5. Insignificant levels of α-TCP were also observed for HAp3 and HAp6. This concludes that the conditions imposed in the synthesis of these three powders resulted in the formation of Ca-dHAp. The obtained patterns showed that the amount of this TCP varies with the HAp origin. The HAp6 powder contains the highest content of β-TCP while the HAp2 and HAp4 are the purest powders. The apparition of the β-TCP can be attributed to the high calcination temperature (1210ºC) or to the Ca-deficient nature of all HAp powders. The synthesis of such Ca-dHAp is attributed to the low reaction synthesis temperature (~20ºC), insufficient stirring speed (1000rpm), high acid addition rate (1.5 ml/min) and maturation time (24h). The calculated purity allowed the HAp classification as follows:
  HAp2 = HAp4 > HAp5 > HAp3 > HAp1 > HAp6.

(B) Crystallinity, lattice parameters and crystallite size

- The crystallinity of the six HAp powders demonstrated that all powders, with the exception of HAp6, have crystallinity greater than the 95% minimum regulatory requirement. These results are attributed to the reaction conditions. The crystallinity depends on the temperature, ripening time and acid addition rate. The increase of the synthesis temperature and the ripening time and the decrease of the acid addition rate are found to improve the HAp crystallinity. The study of the influence of the heat treatment on crystallinity for HAp shows that sintering at 1210ºC increases the HAp crystallinity from 71.06% to 92.60%. According to the crystallinity and purity results, HAp1 and HAp6 fail to meet regulatory (FDA) requirement. Therefore, a higher temperature, ripening time, stirring speed and lower acid addition rate appears to improve these essential HAp powder characteristics. The calculated crystallinity allowed the HAp classification as follows:
  HAp3 > HAp4 > HAp5 > HAp6 > HAp2 > HAp1

- A relationship was found between the purity and the lattice parameters for the size HAp. With decreasing purity of HAp, the a/c ratio increased; that is, the lattice parameter of the a-axis slightly decreases, while that of the c-axis increased. This comportment can be due to a change in the Ca/P ratio and/or Ca/OH ratio in the HA. The highest lattice parameter in the a-axis of HAp6 compared to the pure HAp4 confirms the Ca-deficient nature of this powder. The calculated lattice parameter ratio allowed the HAp classification as follows:
  HAp1 > HAp6 > HAp5 ~ HAp3 > HAp4 > HAp2

- Similar crystallite sizes were obtained for HAp1, HAp2 and HAp6, since all three HAp were prepared at ambient reaction temperature of the same synthesis route as opposed to the HAp3 and HAp4. HAp5 possessed the lowest level of crystallinity, which can be attributed to unknown processing parameters. Irish spray dried HAp with crystallite size of ~41nm was found to increase to ~122nm post sintering.

(C) Particle size, specific surface area, particle size distribution and density

- For all six HAp studied, the particle size and specific surface area was determined. The order of mean particle size from the largest is as follows: HAp5 > HAp4 > HAp2 > HAp1 > HAp3 > HAp6. All the HAp analysed have 90% of their particles <100μm; which is a requirement for the powder for successful thermal plasma spraying application onto orthopaedic implants. The fine particles of HAp1-3 and HAp6, compared to HAp4 and HAp5, can be due to low synthesis temperature, low reactant concentration, high acid addition rate and short maturation time. The influence of the ripening time appears clearly in the case of HAp6 matured during 24h compared to HAp1 and HAp2, of which were matured for longer ripening times.

- The sintering temperature is also found to have an impact on the final HAp particle size obtained. Sintering carried out on the HAp6 at 1200ºC, increased the average particle size from 9.22μm to 13.39μm and HAp1 from 11 – 14μm up to 21.94μm.

- The particle size distributions for the six HAp were determined. The results show that HAp1, HAp2, HAp4 and HAp5 demonstrated a unimodal distribution, while HAp3 and HAp6 possessed a bimodal distribution. The bimodal distribution is due to the finer particle size of both these HAp. The study of the influence of the sintering on the particle size distribution demonstrated that HAp6 cyclone spray dried HAp (particle size= 9.76μm) presents a bimodal distribution pre and post sintering, while HAp6 chamber spray dried HAp (9.22μm) attains a bimodal distribution post sintering. The appearance of the bimodal distribution after sintering is probably due to the agglomeration of the finer particle size.

- The density results indicated that all HAp met with the minimum requirement of FDA regulation. This means that the particle size of all the HAp were fine enough to reach desired density values.

(D) Morphology

- HAp3 and HAp4 possessed the most spherical and regular shaped particles, indicative of enhanced rheological properties. This may also be attributed to the fact that the powders may have been synthesised at higher reaction temperatures, longer ripening times, lower concentration and idealised spray drying condition. Post heat-treatments (such as, flame spheroidisation) may also have been implemented to enhance its spherical nature. HAp5 appeared the most irregular in morphology. This may be explained by the hydrothermal route in which the powders were prepared.

- HAp1, HAp2 and HAp6 possessed a similar morphology, with regular shaped agglomerated particles, with a lower surface smoothness than that of HAp3 and HAp4. An increased ripening time may be required here to increase the surface smoothness.

(E) Rheology and density

- In addition to the reaction conditions, the HAp powder quality can also be influenced by the spray drying conditions. During HAp spray drying, in addition to the process parameters, the HAp slurry rheology has an effect on the final dried powder properties. In order to succeed this step the evolution of the suspension rheology properties during HAp synthesis was studied. Rheology measurements are also useful in following the course of a chemical reaction. The obtained results showed that the dynamic viscosity was found to increase from 15 – 17 mPa.s, during calcium hydroxide synthesis to 35 mPa.s after a 24h maturation phase. Time-dependent behaviour was exhibited for all HA slurry analyses during HAp production. During calcium hydroxide formation dilatent behaviour of the HAp slurry was most evident, while additions of orthophosphoric acid indicated thixotropic behaviour.

- The kinematic viscosities (ratio of dynamic viscosity to density) of the HAp1 and HAp6 are calculated and compared against the range of kinematic viscosities recommended by Luo et al. [108] to aid in producing non-porous controlled morphology (spherical) HAp powder particles in the desired micron range for plasma spray onto orthopaedic implants. The results indicate that both HAp1 and HAp6 slurries are within the range after the maturation phase of 24h. However, further mixing of the slurry prior to spray drying was found to significantly increase the kinematic viscosity of the HAp1 slurry.The HAp1 slurry density was also measured during the synthesis of HAp 1 and HAp6 (as shown in Section 4.3). The results indicate the increase of density during the HAp preparation. This behaviour is due to the increase of the powder particle size.

- Rheological properties of the powders were found to linearly increase with increasing the particle size.

Screening of Chemical Precipitation Process Parameters

The effects of the chemical precipitation process parameters (V_{ac}, T_o, V_{st}, t_r, Ca^{2+} and atm.) were investigated using a fractional factorial design on several responses (purity, crystallinity, crystallite size, lattice parameter ratio and particle size). The mathematical models developed to predict each response showed the order of factors to the level of significance relating to each response analysed, as follows:

(A) Study of Effects

- The order of the level of significance of the positive effects of the chemical precipitation process parameters on the phase purity follows the order: (V_{ac}* V_{st}) > (V_{ac}* T_o* atm.) > (t_r) > (T_o) > (V_{ac}* t_r) > (atm.) > (T_o* atm.) while the order of the level of significance of the negative effects on the phase purity is as follows: (T_o* t_r) > (V_{ac}* Ca^{2+}) > (Ca^{2+}).

- The order of the level of significance of the positive effects of the chemical precipitation process parameters on crystallinity follows the order: (t_r) > (T_o* atm.) > (V_{ac}* Ca^{2+}) > (V_{st}) > (T_o* t_r) > (V_{ac}) while the order of the level of significance of of the negative effects on the phase purity is as follows: (atm.) > (V_{ac}* V_{st}) .

- The order of the level of significance of the positive effects on the L_{002} model, from the most significant, follows the order: (atm.) > (T_o* t_r) > (Ca^{2+}) > (V_{ac}* t_r) > (V_{st}) > (T_o * atm.), while the only negative effect to significantly affect the L_{002} model is the ripening time (t_r). The order of the level of significance of the most significant positive effects on the L_{300} model follows the order: (V_{st}) > (V_{ac} * T_o * atm.) > (T_o * t_r) > (V_{ac} * T_o), while the order of the level of most significant negative effects follows the order: (V_{ac}* atm.) > (t_r) > (V_{ac}) > (V_{ac}* atm.) for the L_{002} model.

- The order of the level of significance of the positive effects of the chemical precipitation process parameters on the a/c ratio follows the order: $(Ca^{2+}) > (V_{ac}* T_o)$ while the order of the level of significance of the negative effects on the lattice parameter ratio is as follows: $(t_r) > (V_{st}) > (T_o) > (V_{ac}* Ca^{2+}) > (V_{ac}* V_{st})$.

- The order of the level of significance of the positive effects of the chemical precipitation process parameters on the actual particle size follows the order: $(V_{ac}* T_o) > (T_o * t_r) >$ (atm.) while the order of the level of significance of the negative effects on the lattice parameter ratio is as follows: $(T_o) > (Ca^{2+}) > (V_{ac}* Ca^{2+}) > (V_{ac}*$ atm.$) > (V_{st})$.

(B) Morphology

- An increase of the synthesis temperature (N1 to N4 and N14 to N16) is found to lead to more regular spherical HAp particles.

(C) Powder flowability

- The flowability of the powder studied in this investigation follow the same order as that of the mean particle size:

  N9 → N1 → N6 → N5 → N14 → N12 →N4 → N2 → N15 → N13 → N10 → N3 → N8 → N11 → N7 → N16

In summary, both the ripening time and stirring speed significantly affect the majority of the responses (effecting five responses), with the reaction temperature also having a significant effect on the purity, a/c ratio and particle size.

Osteoblast Behaviour in Contact with HAp

(A) Cell content and viability

- The most favourable result during the cell viability test were for N16, where after a 7 day incubation period, it appears to suggest that powders possessing a higher crystallinity have the capacity to yield higher counts of cell viability.

(B) Cell proliferation

- The cells counts increase with the increase of powder crystallinity. Indeed, osteoblast grows well on N16, N15, N10 and N9 powders having crystallinity in the range of ~70 to ~95% than on the others.

(C) Morphology

- In contact with N3, N10, N15 and N16 powders, the cells showed a diffuse spread-like morphology with several cytoplasmatic extensions contacting the powder, while in the case of N4, N5, N6 and N9, the cells were elongated with fewer extensions interacting with apatite granules. Control cultures (HAp1 and HAp5) showed a uniform layer of confluent cells with a frequent elongated shape and also overlapping growth

Optimisation of Chemical Precipitation Process Parameters

The effects of the chemical precipitation process parameters (T_o, V_{st}, t_r,) were investigated using a box-behnken design on several responses (purity, crystallinity, crystallite size, lattice parameter ratio and particle size). The mathematical models developed to predict each response showed the order of factors to the level of significance relating to each response analysed, as follows:

(A) Study of Effects

- The order of the level of significance of the positive effects of the chemical precipitation process parameters on the phase purity follows the order: (V_{st}^2) > (V_{st}) while the order of the level of significance of the negative effects on the lattice parameter ratio is as follows: (T_o).

- The order of the level of significance of the positive effects of the chemical precipitation process parameters on the crystallinity follows the order: (T_o^2) > (t_r^2) > (V_{st}) > (T_o) > (T_o * V_{st}) > (V_{st}^2) while the order of the level of significance of the negative effects on the lattice parameter ratio is as follows: (V_{st}* t_r) > (T_o * t_r).he order of significance for these effects follows the order: $T_o^2 > t_r^2 > V_{st} > T_o > T_o * V_{st} > V_{st} * t_r > T_o * t_r > V_{st}^2$

- The two effects are positively affecting the crystallite size (L_{002}) in the same order as shown previously: $t_r^2 > T_o$.

- The only positive effects of the chemical precipitation process parameters on the crystallite size (L_{300}) is (T_o) while the order of the level of significance of the negative effects on the lattice parameter ratio is as follows: (T_o^2) > (t_r^2).

- The order of the level of significance of the positive effects of the chemical precipitation process parameters on the lattice parameter ratio follows the order:

(t_r^2) > (T_o) > (V_{st}) while the order of the level of significance of the negative effects on the lattice parameter ratio is as follows: (t_r) > (V_{st}^2) > $(T_o * V_{st})$.

- All of the significant effects are positively affecting the lattice parameter ratio in the order as follows: (t_r^2) > $(V_{st} * t_{r)}$ > (T_o).

- The order of mean particle size from the largest is as follows:
  N6 → N9 → N8 → N12 → N3 →N16 → N1 → N17 = N10 → N15 →N4 →N7 → N5 → N14 → N11 → N2 → N13

(B) Morphology

- This experimental conditions of the box-behnken design confirm that an increase of the synthesis temperature (N1 to N2) is found to lead to more regular spherical HAp particles.
- A qualitative examination of the positive effect of the interaction between the reaction temperature and the srirring speed (N9 to N5 and N6 to N10) demonstrates how the powder particle size increases in correspondence to a more idealised spherical morphology.
- Examining the effect of increasing the stirring speed (N9 to N10), in isolation of the other factors, however also demonstrates a favaourable effect on the resultant morphology. Another positive interaction effect between the stirring speed and the ripening time (N5 to N3), while a reduction in the stirring speed coupled with an increase in ripening time also demonstrates an enhanced spherical powder morphology. This would suggest that the stirring speed is the least significant factor affecting this resposne.

HAp possessing optimum powder characteristics for orthopaedic application via a thermal spray technique can therefore be prepared using the following chemical precipitation process parameters: Reaction Temperature 60ºC, Ripening Time 48h and Stirring Speed 1500rpm using high reagent concentrations. The presence of an inert environment is less critical at this temperature, as opposed to a lower temperature range of 20ºC. In the case of HAp synthesis at lower temperatures, the atmospheric control is desired in order to achieve high phase purity and crystallinity.

5.2 Recommendations For Future Work

The results documented in this research are significant, however further recommendations are as follows:

Chemical Analyses

Chemical testing of the HAp during the course of precipitation could be conducted through either XRF (X-ray Flourescence) or simple chemical analyses, such as EDTA and photospectrophotometry in order to evaluate the calcium and phosphate content of the HAp, respectively. This could be used to determine the specific Ca/P ratio throughout the course of the precipitation reaction, and hence determine the minimum ripening time required to produce stoichiometric HAp for each set of conditions.

Kinetics study

To investigate the HAp precipitation mechanisms, the transformation process could be investigated under different conditions, including the optimal ones. The results obtained could be used for the determination of the kinetic equation of the transformation and in some cases for some applications to guide the choice of the appropriate ripening time in function of the desired crystallinty, phase composition, particle size, density, specific surface area and powder particle morphology.

Investigation of the precipitation mechanisms

In literature, only Liu et al. [91] have studied the kinetic equation of transformation under determined conditions. They demonstrated that the reaction of the transformation from ACP to HAP was a particle surface reaction controlled process whose magnitude of activation energy was 22.7 kcal/mol energy greater than the activation energy of other reactions in solution (5 kcal/mol). However, no precision was given about the mechanisms that limit such precipitation reaction. Therefore, an investigation could be carried out to make it clear that, it was controlled either by the dissolution of the grains or by the entrance of calcium and phosphate ions into the vacancy of crystal lattice. The results could then be used as the theoretical foundation for solving the scale-up problem for HAp synthesis.

Modelling

Modelling using computational fluid dynamics (such as, MixSim) could be used to better understand the complicated phenomena of the precipitation process. The moment transformations of the population balances, taking into account the chemical and crystallisation kinetics to describe the generation and transportation of the crystal phase. The influence of hydrodynamics in the stirred tank, as characterised by the stirrer speed, impeller location and feed location on the distribution of supersaturation and subsequent crystal size distribution could also be investigated to examine the effect of the stirrer set-up on the final homogeneity of the HAp powder.

Further Experimental Design Investigation

Further work could extend to building a Box-Behnken design, incorporating all six of the influencing factors (reaction temperature, acid addition rate, stirring speed, ripening time, initial calcium concentration and atmospheric control) and obtaining mathematical based models to accurately predict their effect on the HAp powder characteristics.

PUBLICATIONS ARISING FROM THIS RESEARCH

- Kehoe, S., Stokes, J., and Ardhaoui, M., (2007), "Experimental Design Optimisation of the Synthesis of Bioceramic Hydroxyapatite as Feedstock for Plasma Spraying Application", Book of Abstracts, Plasma Processeses for Biomedical Applications, (Dublin City University, 24th May, 2007)

- Kehoe, S., Stokes, J., Looney, L. and Ardhaoui, M., (2006), "Optimisation of the Synthesis of Hydroxyapatite (HA) for Orthopaedic Application via the Chemical Precipitation Method", Proceedings of the 6th Annual Conference for Biomaterials in Regenerative Medicine (Vienna, 22-25th October, 2006)

- Kehoe, S., Stokes, J., Looney, L. and Ardhaoui, M., (2006), "Optimisation of the Synthesis of Hydroxyapatite (HA) for Orthopaedic Application via the Chemical Precipitation Method", Conference Proceedings of the 20th European Conference on Biomaterials (Nantes, France, 27th September – 1st October, 2006)

- Kehoe, S., Ardhaoui, M. and Stokes, J., (2006), "Critical Analysis of the Production of Hydroxyapatite (HA) Powder Applied onto Orthopaedic Implants", Proceedings of the 12th Annual Conference of the Section of Bioengineering of the Royal Academy of Medicine in Ireland (Galway, 27-28th January, 2006)

- Kehoe, S., Ardhaoui, M. and Stokes, J., (2005), "Investigation into the Powder Production and Application of Hydroxyapatite (HA) onto Femoral Implants" Conference Proceedings of the European Congress on Advanced Materials and Processes (Prague, 5-8th September, 2005)

The following papers have been sent to the Journal of Biomedical Materials Research, Part B: Applied Biomaterials

- Ardhaoui, M., Kehoe, S. and Stokes, J., (2008),"Influence of Hydroxyapatite Particle Size, Crystallinity and Morphology on Human Osteoblast-Like Cells Behaviour", In Press, 2008

- Ardhaoui, M., Kehoe, S. and Stokes, J., (2008),"Hydroxyapatite (HAp) Synthesis Routes: Effect of the Chemical Precipitation Conditions on the HAp Properties" Hydroxyapatite Review Paper, In Press, 2008

The following papers are being considered to be sent to the Journal of Materials Engineering and Performance

- Kehoe, S. and Stokes, J., (2008),"Design of Experiments Study of Hydroxyapatite Synthesis for Orthopaedic Application using Fractional Factorial Design"

- Kehoe, S. and Stokes, J., (2008)," Design of Experiments Study of Hydroxyapatite Synthesis for Orthopaedic Application using Box-Behnken Design"

6 REFERENCES

[1] Vallet-Regi, M., (2000), "Ceramics for Medical Applications", The Royal Society of Chemistry, Dalton Transactions, pp. 97 – 108

[2] Kweh, S. W. K. et al., (1999), "The Production and Characterisation of Hydroxyapatite (HA) Powder", Journal of Materials Processing Technologies, Vol. 89-90, pp. 373 – 377

[3] Thummler, F. and Oberacker, R., (1993), "Introduction to Powder Metallurgy", The Institute of Materials Series on Powder Metallurgy, ISBN: 0 - 90176 - 26 – X

[4] Reilly, M. O., (2003), "A Critical Investigation into the Spray Drying of Powders for Thermal Spray Applications", Final Year Project Thesis, School of Mechanical & Manufacturing Engineering, Dublin City University

[5] Koutsopoulos, S. et al., (2002), "Synthesis and Characterisation of Hydroxyapatite Crystals: A Review Study on the Analytical Methods", Wiley Periodicals, Inc.

[6] Weiner, S. and Wagner, H. D., (1998), "The Material Bone: Structure-Mechanical Function Relations", Annual Review of Materials Science, Vol. 28, pp. 271 – 298

[7] Hellmich, C. and Ulm, F. J., (2002), "Micromechanical Model for Ultrastructural Stiffness of Mineralized Tissues", Journal of Engineering Mech., Vol. 128, Issue 8, pp. 898 – 908

[8] Rho, J. Y. et al., (1998), "Mechanical Properties and the Hierarchical Structure of Bone", Medical Engineering Physics, Vol. 20, pp. 92 – 102

[9] Liu, Y., et al., (2005), "BMP-2 Liberated from Biomimetic Implant Coatings Induces and Sustains Direct Ossification in an Ectopic Rat Model. Bone, Vol. 36, pp. 745 – 757

[10] Martin, R. B. et al., (1998), "Skeletal Tissue Mechanics", Springer-Verlag, New York, ISBN: 0-387-98474-7

[11] Burger, E. H., (2001), "Experiments on Cell Mechanosensitivity: Bone Cells as Mechanical Engineers", In: Bone Mechanics Handbook. Cowin SC (ed). CRC Press, New York.

[12] Orlovskii, V. P. et al., (2002), "Hydroxyapatite and Hydroxyapatite-Based Ceramics", Inorganics Materials, Vol. 38, pp. 973 – 984

[13] Puajindanetr, S., (1993), "Characterisation and Sintering of Precipitated Hydroxyapatite", Ph.D. Thesis, Queen Mary and Westfield College London, Great Britain

[14] Brown, P. A, (1994), "Hydroxyapatite and Related Materials", CRC Press, Inc., ISBN: 0 - 8493 - 4750 – 5

[15] Slosarczyk, A. et al., (2005), "FTIR and XRD Evaluation of Carbonated Hydroxyapatite Powders Synthesised by Wet Methods", Journal of Molecular Structure, Volumes 744-747, pp. 657 – 661

[16] Zhu, X., (2005), "Nano Hydroxyapatite/Collagen, Nano Hydroxyapatite and Anodic Oxides on Titanium – Preparation, Characterization and Biological Response",, Inaugural Dissertation, Medical Faculty, Eberhard-Karls-University

[17] Kapanen, A., (2002), “Biocompatibility of Orthopaedic Implants on Bone Forming Cells”, Academic Dissertation, Faculty of Medicine, University of Oulu

[18] Tovar, A., (2004), “Bone Remodelling as a Hybrid Cellular Automaton Optimization Process”, Ph.D. Thesis, University of Notre Dame

[19] Jallot, E., (2005), “Nanoscale Physico-Chemical Reactions at Bioceramics-Bone Tissues Interfaces”, Handbook of Nanostructured Biomaterials and their Applications in Nanobiotechnolog, pp. 495 – 509

[20] Young, R. A. and Holcomb, D. W., (1982),"Variability of Hydroxyapatite Preparations", Calcified Tissue International, Vol. 34, pp. 17 – 32

[21] Cheang, P. and Khor, K. A., (1996),"Addressing Processing Problems Associated with Plasma Coating of Hydroxyapatite Coatings", Biomaterials, Vol. 17, pp. 537 – 544

[22] Raynaud, S. et al., (2002), "Calcium Phosphate Apatite’s with Variable Ca/P Atomic Ratio I., Synthesis, Characterization and Thermal Stability of Powders", Biomaterials, Vol. 23, pp. 1065 – 1072

[23] Liu, J. et al., (2003), "The Influence of pH and Temperature on the Morphology of Hydroxyapatite Synthesised by Hydrothermal Method", Ceramics International, Vol. 29, pp. 629 – 633

[24] Suchanek, W. and Yoshimura, M., (1998), "Processing and Properties of Hydroxyapatite-Based Biomaterials for use as Hard Tissue Replacement Implants", Journal of Materials Research, Vol. 13, pp. 94 – 114

[25] Bernard. L. et al., (1999), "Preparation of Hydroxyapatite by Neutralization at Low Temperature - Influence of Purity of the Raw Material", Powder Technology, Vol. 103, pp. 19 – 25

[26] Kehoe, S., (2008), "Calcium Phosphates for Medical Applications", Dublin City University, J. Stokes, Ed., Materials Processing Research Centre, Materials Processing Research, ISBN 1-87232-752-X

[27] Rhee, S. H., (2002), "Synthesis of Hydroxyapatite via Mechanochemical Treatment", Biomaterials, Vol. 23, pp. 1147 – 1152

[28] Zhang, H. et al., (2002), "Morphology and Formation Mechanism of Hydroxyapatite Whiskers from Moderately Acid Solution", Materials Research, Vol. 6, pp. 111 – 115

[29] Zhang, H. et al., (2005), "Mechanochemical–Hydrothermal Synthesis and Characterization of Fluoridated Hydroxyapatite", Materials Research Bulletin, Volume 40, pp. 1326 - 1334

[30] Hu, J. et al, (2001), "Production and Analysis of Hydroxyapatite from Australian corals via hydrothermal process", Journal of Materials Science Letters, vol. 20, pp. 85 – 87, 2001

[31] Bogdanoviciene, I. et al., (2006), "Calcium Hydroxyapatite, $Ca_{10}(PO_4)_6(OH)_2$ Ceramics Prepared by Aqueous Sol–Gel Processing", Materials Research Bulletin, Vol. 41, pp. 1754 – 1762

[32] Morgan, H. et al., (2000), "Preparation and Characterisation of Monoclinic Hydroxyapatite and its Precipitated Carbonate Apatite Intermediate", Biomaterials, Vol. 21, Issue 6, pp. 617 – 627

[33] Jha, L. J. et al., (1997), "Preparation and Characterisation of Fluoride-Substituted Apatite's", Journal of Materials Science: Materials in Medicine, Vol. 8, pp. 185 – 191

[34] Bohner, M., (2000), "Calcium Orthophosphate in Medicine: from Ceramics to Calcium Phosphate Cements", Injury, Vol. 31, pp. 37 – 47

[35] Chow, L. C. et al., (2004), "Properties of Nanostructured Hydroxyapatite Prepared by a Spray Drying Technique", Journal of Research of the National Institute of Standards and Technology, Vol. 109, pp. 543 - 551

[36] McGrath, P. J. and Laine, R. M., (1992), "Theoretical Process Development for Freeze-Drying Spray-Frozen Aerosols", Journal of American Ceramic Society, Vol. 75, pp. 1223

[37] Itatani, K. et al., (2000), "Preparation of Various Calcium-Phosphate Powders by Ultrasonic Spray Freeze-Drying Technique", Materials Research Bulletin, Vol. 30, pp. 575 – 585

[38] Lin, K. et al., (2007), "Hydrothermal Microemulsion Synthesis of Stoichiometric Single Crystal Hydroxyapatite Nanorods with Mono-Dispersion and Narrow-Size Distribution", Materials Letters, Vol. 61, pp. 1683 – 1687

[39] Kim, W. et al., (2001), "Sonochemical Synthesis of Hydroxyapatite from H_3PO_4 Solution with $Ca(OH)_2$", Ultrasonics Sonochemistry, Vol. 8, pp. 85 – 88

[40] Yang, Z. et al., (2004), "Preparation and Thermal Stability Analysis of Hydroxyapatite Derived from the Precipitation Process and Microwave Irradiation Method", Materials Letters, Vol. 58, pp. 3586 – 3590

[41] Kumar, T. S. S. et al., (2000), "Synthesis of Carbonated Calcium Phosphate Ceramics using Microwave Irradiation", Biomaterials, Vol. 21, pp. 1623 – 1629

[42] Yasuda, H. Y. et al., (2000), "Microstructure and Mechanical Property of Synthesised Hydroxyapatite Prepared by Colloidal Process", Biomaterials, Vol. 21, pp. 2045 – 2049

[43] Rivera, E. M. et al., (1999), "Synthesis of Hydroxyapatite from Eggshells", Materials Letters, Vol. 41, pp. 128 - 134

[44] Weng, W. et al., (1997), "A New Synthesis of Hydroxyapatite" Journal of the European Ceramic Society, Vol. 17, pp. 1151 – 1156

[45] Ylinen, P., (2006), "Applications of Coralline Hydroxyapatite with Bioabsorbable Containment and Reinforcement as Bone Graft Substitute", Ph.D Thesis, University of Helsinki, Faculty of Medicine, Institute of Clinical Medicine and Helsinki University Central Hospital and University of Helsinki

[46] Aoki, M., (1991), "Science and Medical Applications of Hydroxyapatite", Takayama Press System. Center Co., Inc., Tokyo

[47] Kalita, S. J. et al., (2004), "Effects of MgO-CaO-P_2O_5-Na_2O-Based Additives on Mechanical and Biological Properties of Hydroxyapatite", Journal of Biomedical Materials Research, Vol. 71A, Issue I, pp. 35 – 44

[48] Boeree, N. R., et al., (1993), "Development of a Degradable Composite for Orthopaedic Use: Mechanical Evaluation of an Hydroxyapatite - Polyhydroxybutyrate Composite Material", Biomaterials, Vol. 14, pp. 793 – 796

[49] Nadir, S. et al., (1996), "Synthèse par Neutralisation d'une Hydroxyapatite Pure à Partir de L'acide Orthophosphorique Technique et de la Calcite", Phosphorus Sulfur and Silicon, Vol. 112**,** pp. 33 – 40

[50] SRM2910, (2003), "Certificate of Analysis for Standard Reference Material (SRM2910: Calcium Hydroxyapatite)" National Institute of Standards Technology, SRM Program, Gaithersburg, MD 20899, U.S.A, pp. 1 – 9

[51] Calderin, L. et al., (2005), "A Shell Model of the Lattice Dynamics of Hydroxyapatite", Physics Review: B, Vol. 72, pp. 224304-16

[52] Haverty, D. et al., (2005), "Structure and Stability of Hydroxyapatite: Density Functional Calculation and Rietveld Analysis", Physics Review: B, Vol. 71, pp. 094103 – 9

[53] Corno. M., (2006), "Periodic *ab initio* Study of Structural and Vibrational Features of Hexagonal Hydroxyapatite, $Ca_{10}(PO_4)_6(OH)_2$", Phys. Chem. Chem. Phys., Vol. 8, pp. 2464 – 2472

[54] Kumar. R. et al., (2001), "RF Plasma Processing of Ultra-Fine Hydroxyapatite Powders", Journal of Materials Processing Technology, Volume 113, Issues 1-3, pp. 456 – 462

[55] Kuriakose, T. A. et al., (2004), "Synthesis of Stoichiometric Nano Crystalline Hydroxyapatite by Ethanol Based Sol - Gel Technique at Low Temperature", Journal of Crystal Growth, Vol. 263, pp. 517 – 523

[56] Santos, M. H. et al., (2004), "Synthesis Control and Characterization of Hydroxyapatite Prepared by Wet Precipitation Process", Synthesis Control Materials Research, Vol. 7, No. 4, pp. 625 – 630

[57] LeGeros, R. Z. et al., (1981), "Trace Elements: Incorporation of Monovalent Cations, Na^+, K^+, Li^+", Journal of Dental Research, Vol. 60B, pp. 452 – 458

[58] Suzuki, T. et al., (1981), "Synthetic Hydroxyapatites Employed as Inorganic Cation-Exchangers", Journal of Chemistry Society Faraday Transactions, Vol. 77, pp. 1059 – 1062

[59] LeGeros, R. Z. et al., (1982), "The Effect of Fluoride on the Stability of Synthetic and Biological (Bone) Mineral Apatites", In: Menczel J, Robin GC, Makin M, Steinbeg R, editors. Osteoporosis. New York: Wiley; pp. 327 – 341

[60] Kreidler, E. R. et al., (1970), "The Crystal Chemistry of Apatite: Structure Fields of Fluor and Chloroapatite", American Mineral, Vol. 55, pp 171 – 184

[61] Azimov, S. Y. et al., (1981), "Synthetic Silicophosphates, Silicovanadates, and Silicoarsenates with the Apatite Structure", Inorganic Materials, Vol. 17, pp. 1384 – 1387

[62] Lacout, J. L. et al., (1998), "Strontium – Cadmium Substitution in Hydroxyl and Fluorapatites", Ann. Chim. Science Materials, Vol. 23, pp. 57 – 60

[63] Rey, C., (1998), "Calcium Phosphates for Medical Applications", In: Zahid A, editor. Calcium Phosphates in Biological and Industrial Systems. Boston: Kluwer Academic Publishers, pp. 217 – 251

[64] Hench, L. L. and Wilson, J., (1998), "An Introduction to Bioceramics", Adv Ser Ceram 1 World Scientific Publishing Co.Pte.Ltd., London, Hong Kong, Singapure, 139-80

[65] Kannan, S. et al., (2007), "Aqueous Precipitation Method for the Formation of Mg-Stabilized β-Tricalcium Phosphate: An X-ray Diffraction Study", Ceramics International, vol. 33, pp. 637 – 641, 2007

[66] Ducheyne, P. et al., (1999), "Bioactive Ceramics: The effect of Surface Reactivity on Bone Formation and Bone Cell Function", Biomaterials, Vol. 20, pp. 2287 – 2303

[67] Kivrak, N. et al., (1998), "Synthesis of Calcium Hydroxyapatite Tricalcium Phosphate (HA-TCP) Composite Bioceramic Powders and their Sintering Behavior", Journal of American Ceramics Society, Vol. 81, pp. 2245 – 2252

[68] Driessens, F. et al., (1998), "Relation between Physico - Chemical Solubility and Biodegrability of Calcium Phosphates", In: de Putter C, de Lange GL, de Groot K, Lee AJC, eds. Implant materials in biofunction. Advances in Biomaterials. Amsterdam: Elsevier, pp. 48 – 52

[69] Elliott, J., (1994), "Structure and Chemistry of Apatites and Other Calcium Orthophosphates", Amsterdam, Elsevier

[70] Gross, K.A. et al., (1997), "Thermal Processing of Hydroxyapatite for Coating Production", Journal of Biomedical Materials Research, Vol. 39, Issue 4, pp. 580 – 587

[71] Lazic, S. et al., (2001), "The effect of Temperature on the Properties of Hydroxyapatite Precipitated from Calcium Hydroxide and Phosphoric Acid", Thermochimica Acta, Vol. 374, pp. 13 – 22

[72] Eanes, E. D., (1998), "Amorphous Calcium Phosphate: Thermodynamic and Kinetic Considerations, in Calcium Phosphates in Biological and Industrial Systems", Z. Amjad, ed., Kluwer Academic Publisher, Boston, pp. 21 – 40

[73] Okamoto, K. et al., (1998), "RGD Peptides Regulate the Specific Adhesion Scheme of Osteoblast to Hydroxyapatite but not to Titanium", Journal of Dental Research, Vol. 77, pp. 481 – 487

[74] Richard, D. et al., (2005), "Behavior of Human Osteoblast-Like Cells in Contact With Electrodeposited Calcium Phosphate Coatings", Journal of Biomedical Materials Research Part B: Applied Biomaterials, pp. 108 – 115

[75] Martin, J. Y. et al., (1995), "Effect of Titanium Surface Roughness on Proliferation, Differentiation, and Protein Synthesis of Human Osteoblast-like Cells (MG63)", Journal of Biomedical Materials Research, Vol. 29, pp. 389 – 401

[76] Thomas, K. A. et al., (1985), "An Evaluation of Variables Influencing Implant Fixation by Direct Bone Apposition", Journal of Biomedical Materials Research, Vol. 19, pp. 875 – 901

[77] Boskey, A. L. and Posner, A. S., (1976), "Formation of Hydroxyapatite at Low Supersaturation", Journal of Physical Chemistry, Vol. 80, pp. 41 – 45

[78] Seckler, M. M. et al., (1999), "Influence of Process Conditions on Hydroxyapatite Crystallinity Obtained by Direct Crystallization", Materials Research, Vol. 2, No. 2, pp. 59 – 62

[79] Lazic, S. et al., (1996), "Properties of Hydroxyapatite Crystallized from High Temperature Alkaline Solutions", Journal of Crystal Growth, Vol. 165, pp. 124 – 128

[80] Mostafa, N. Y., (2005), "Characterisation, Thermal Stability and Sintering of Hydroxyapatite Powders Prepared by Different Routes", Materials Chemistry and Physics, Vol. 94, Issues 2 – 3, pp. 333 – 341

[81] Conn, J. F. et al., (1982), “Process for Producing Hydroxyapatite”, Patent Number: US 4,324,772

[82] Luo, P. and Nieh, T. G., (1995), "Synthesis of Ultrafine Hydroxyapatite Particles by a Spray Dry Method", Materials Science & Engineering: C3, pp. 75 – 78

[83] Afshar, A. et al., (2003), "Some Important Factors in the Wet Precipitation of Hydroxyapatite", Materials and Design, Vol. 24, pp. 197 – 202

[84] Saeri, M. R. et al., (2003), "The Wet Precipitation Process of Hydroxyapatite", Materials Letters, Vol. 57, pp. 4064 – 4069

[85] Smiciklas, I. et al., (2005), "Experimental Design Approach in the Synthesis of Hydroxyapatite by Neutralization Method", Separation and Purification Technology, Volume 44, Issue 2, pp. 97 – 102

[86] Giulietti, M. et al., (2001), "Industrial Crystallisation and Precipitation from Solutions: State of the Technique", Brazilian Journal of Chemical Engineering, Vol. 15, Issue 4, pp. 423 – 440

[87] Tampieri, A. et al., (2000), "Characteristics of Synthetic Hydroxyapatites and Attempts to Improve their Thermal Stability", Materials Chemistry and Physics, Vol. 64, pp. 54 –61

[88] Kumar, R. et al., (2004), "Temperature Driven Morphological Changes of Chemically Precipitated Hydroxyapatite Nanoparticles", Langmuir, Vol. 20, pp. 5196 – 5200

[89] Kothapalli, C. et al., (2004), "Influence of Temperature and Concentration on the Sintering Behaviour and Mechanical Properties of Hydroxyapatite", Acta Materialia, Vol. 52, pp. 5655 – 5663

[90] Pang, Y. X. et al., (2003), "Influence of Temperature, Ripening Time and Calcination on the Morphology and Crystallinity of Hydroxyapatite Nanoparticles", Journal of the European Ceramic Society, Vol. 23, pp. 1697 – 1704

[91] Liu, C et al., (2001), "Kinetics of Hydroxyapatite Precipitation at pH 10 to 11", Biomaterials, Vol. 22, pp. 301 – 306

[92] Markovic, M., (2004), "Preparation and Comprehensive Characterization of a Calcium Hydroxyapatite Reference Material", Journal of Research of the National Institute of Standards and Technology, Vol. 109, pp. 553 – 568

[93] Bernard. L. et al., (2000), "Modelling of the Dissolution of Calcium Hydroxide in the Preparation of Hydroxyapatite by Neutralization", Chemical Engineering Sciences, Vol. 55, pp. 5683 – 5692

[94] Bouyer, E., (2000), "Morphological Study of Hydroxyapatite Nanocrystal Suspension", Journal of Materials Science: Materials in Medicine, Vol. 11, pp. 523 – 531

[95] Aizawa, M. et al., (2006), "Syntheses of Calcium - Deficient Apatite Fibres by a Homogeneous Precipitation Method and their Characterizations", Journal of the European Ceramic Society, Vol. 26, pp. 501 – 507

[96] Knowles, J. C., (2000), "Characterisation of the Rheological Properties and Zeta-Potential of a Range of Hydroxyapatite Powders", Biomaterials, Vol. 21, pp. 1387 – 1392

[97] Tian, J., (2002), "Preparation and Characterisation of Hydroxyapatite Suspensions for Solid Freeform Fabrication", Ceramics International, Vol. 28, pp. 299 – 302

[98] Choi, D. et al., (2007), "Mechano-Chemical Synthesis and Characterisation of Nano-Structured β – TCP Powder", Materials Science and Engineering: C, Vol. 27, pp. 377 – 381

[99] Sridhar, T. M. et al., (2003), "Sintering Atmosphere and Temperature Effects on Hydroxyapatite Coated Type 316L Stainless Steel", Corrossion Science, Vol. 45, issue 10, pp. 2337-2359

[100] Liao, C. et al., (1999), "Thermal Decomposition and Reconstitution of Hydroxyapatite in Air Atmosphere", Biomaterials, vol. 20, pp. 1807-1813

[101] Deram, V. et al., (2003), "Microstructural Characterizations of Plasma Sprayed Hydroxyapatite Coatings", Surface and Coatings Technology, Vol. 166, pp. 153-159

[102] Fazan, F., (2000), "In Vitro Behaviour of Plasma Sprayed Hydroxyapatite Coatings", Ph.D., University of Birmingham, Birmingham

[103] Levingstone, T., (2008), "Ceramics for Medical Applications", Dublin City University, L. Looney, Ed., Materials Processing Research Centre, ISBN 1-87232-752-4

[104] Reed, J. S., (1988), "Introduction to the Principles of Ceramic Processing", Wiley Interscience, ISBN 0 - 471 - 84554 – X

[105] Kim, W. et al., (2001), "Sonochemical Synthesis of Hydroxyapatite from H_3PO_4 Solution with $Ca(OH)_2$", Ultrasonics Sonochemistry, Vol. 8, pp. 85 – 88

[106] ASM International Handbook Committee, (1991), "Ceramics and Glasses", Engineered Materials Handbook, Vol. 4

[107] Hino, T. et al., (2000), "Development of a New Type Nozzle and Spray-drier for Industrial Production of Fine Powders", European Journal of Pharmaceutics and Biopharmaceutics, Vol. 49, pp. 79 – 85

[108] Luo, P. and Nieh, T. G., (1999), "Preparing Hydroxyapatite Powders with Controlled Morphology", Journal of Materials Processing Technology, Vol. 89 - 90, pp. 550 – 555

[109] Murtaza, Q., (2006), "A Critical Analysis into the Spray Drying of Hydroxyapatite Powder for Thermal Spray Application", Ph.D. Thesis, Dublin City University, Materials Processing Research Centre

[110] Liang, H. et al., (2001), "Analysis of Constant Rate Period of Spray Drying of Slurry", Chemical Engineering Sciences, Vol. 56, pp. 2205 – 2213

[111] Kieviet, F., (1997), "Modelling Quality in Spray Drying", Eindhoven University of Technology, ISBN 90 - 386 - 1008 – 4

[112] Ramachandra Rao, R. et al., (2002), "Sintering and Synthesis of Hydroxyapatite - Zirconia Composites", Materials Science and Engineering C., Vol. 20, pp. 187 – 193

[113] Lee, W. E. et al., (1994), "Ceramic Microstructures: Property Control by Processing", Chapman & Hall, ISBN: 0 - 412 - 43140 – 8

[114] Sung, Y. M. et al., (2004), "Crystallization and Sintering Characteristics of Chemically Precipitated Hydroxyapatite Nanopowder", Journal of Crystal Growth, Vol. 262, pp. 467 – 472

[115] Kim, S. et al., (2002), "Effect of Calcinations of Starting Powders on Mechanical Properties of HA-Alumina Bioceramic Composite", Journal of Materials Science: Materials in Medicine, Vol. 13, pp. 307 – 310

[116] Juang, H. Y. et al., (1996), "Effect of Calcination on Sintering of Hydroxyapatite", Biomaterials, Vol. 17, pp. 2059 – 2064

[117] Ramesh, S. et al., (2001), "Grain Size - Properties Correlation in Polycrystalline Hydroxyapatite Bioceramic", Malaysian Journal of Chemistry, Vol. 3, No. 1, pp. 35 – 40

[118] Chai, C. et al., (1994), "Hydroxyapatite – Thermal Stability of Synthetic Hydroxyapatites", International Ceramic Monographs, Vol. 1, no. 1, pp. 79 – 85

[119] Gomez-Morales, J. et al., (2001), "Precipitation of Stoichiometric Hydroxyapatite by a Continuous Method", Crystal Research Technology, Vol. 36, pp. 15 – 26

[120] ASTM B214, (2007), "Standard Test Method for Sieve Analysis of Metal Powders", ASTM International

[121] Papadopoulos, N. et al., (1999), "Viscosity Measurement: A Virtual Experiment", Journal of Chemical Education, Vol. 76, No. 11, pp. 1600

[122] Padilla, S. et al., (2004), "Concentrated Suspensions of Hydroxyapatite for Gelcasting Shaping", Key Engineering Materials, Vols. 254 - 256, pp. 35 – 38

[123] Prescott, J. K. and Barnum, R. A., (2000), "On Powder Flowability", Pharamceutical Technology, Vol. 63, pp. 60 – 84

[124] Freeman, R., (2003), “The Importance of Air Content on the Rheology of Powders - An Empirical Study using the FT4 Powder Rheometer", Particulate Systems Analysis Conference, Harrogate, UK - August 2003

[125] Freeman, R., (2001), "The Flowability of Wet and Dry Powders", 20th Pharamaceutical Technology Conference

[126] Freeman, R., (2000), "The Classification of Powders in Relation to Flowability", 19th Pharamaceutical Technology Conference

[127] Freeman, R., (2001), "New Insights into Powder Flowability", Innovations in Food Technology

[128] Freeman, R., (2000), "The Flowability of Powders - An Empirical Approach", International Conference on Powder and Bulk Solids Handling, IMechE HQ, London

[129] Oldshue, J. Y., (1983), "Fluid Mixing Technology", Professional and Reference Books, McGraw Hill Book Company, ISBN 0 - 07 - 047685 – 3

[130] Levingstone, T., (2008), “Optimisation of Plasma Sprayed HA Coatings”, Ph.D Thesis, Dublin City University, Materials Processing Research Centre

[131] Pawlowski, L., (1995), "The Science and Engineering of Thermal Sprayed Coatings", John Wiley & Sons Ltd., ISBN: 0 - 471 - 95253 – 2

[132] Stokes, J., (2003), "Production of Coated and Free-Standing Engineering Components Using the HVOF (High Velocity Oxy-Fuel) Process", Ph.D. Thesis, Materials Processing Research Centre, Dublin City University, Ireland

[133] Sun, L. et al., (2003), "Phase, Structural and Microstructural Investigations of Plasma Sprayed Hydroxyapatite Coatings", Materials Science & Engineering, A360, pp. 70 – 84

[134] Lynn, A. K. and DuQuesnay, D. L., (2002), "Hydroxyapatite-coated Ti-6Al-4V Part 1: The Effect of Coating Thickness on Mechanical Fatigue Behaviour", Biomaterials, Vol. 23, pp. 1937 – 1946

[135] Xue, C. et al., (2004),"In Vivo Evaluation of Plasma Sprayed Hydroxyapatite Coatings Having Different Crystallinity", Biomaterials, Vol. 25, pp. 415 – 421

[136] Heimann, R. B., (1996), "Plasma-Spray Coating", VCH Publishers, Inc., New York, NY (USA), ISBN 3 – 527 – 29430 – 9

[137] U.S. Food and Drug Administration, (1992), "Calcium Phosphate (Ca-P) Coating Draft Guidance for Preparation of FDA Submissions for Orthopaedic and Dental Endosseous Implants"

[138] ASTM F1609, (2003), "Standard Specification for Calcium Phosphate Coatings for Implantable Materials"

[139] ISO 13779, Part 1, (2000), "Implants for Surgery – Hydroxyapatite-Part 1: Ceramic Hydroxyapatite", International Standards Organisation

[140] ASTM F1185, (2003), "Standard Specification for Composition of Hydroxylapatite for Surgical Implants", American Society for Testing and Materials

[141] ASTM F1088, (2003), "Standard Specification for Beta-Tricalcium Phosphate for Surgical Implantation", American Society for Testing and Materials

[142] ISO 13779, Part 3, (2000), "Implants for Surgery – Hydroxyapatite - Part 3: Chemical Analysis and Characterisation of Crystallinity and Phase Purity", International Standards Organisation

[143] JCPDS 9-342, "Hydroxylapatite", Joint Committee for Powder Diffraction Standards, International Committee for Diffraction Data

[144] Cullity, B.D. (1978), "Elements of X-Ray Diffraction", 2nd Ed., Addison-Wiley Series in Metallurgy and Materials, ISBN 0 – 201 – 01174 – 3

[145] Xue, C. et al., (2004),"In Vivo Evaluation of Plasma Sprayed Hydroxyapatite Coatings Having Different Crystallinity", Biomaterials, Vol. 25, pp. 415 – 421

[146] ISO 13779, Part 2, (2000), "Implants for Surgery - Hydroxyapatite - Part 2: Coatings of Hydroxyapatite", International Standards Organisation

[147] ISO 13779, Part 4, (2002), "Implants for Surgery - Hydroxyapatite - Part 4: Determination of Coating Adhesion Strength", International Standards Organisation

[148] ASTM F2024, (2000), "Standard Practice for X-ray Diffraction Determination of Phase Content of Plasma-Sprayed Hydroxyapatite Coatings", American Society for Testing and Materials

[149] ISO 10993, Part 1, (2003), "Biological Evaluation of Medical Devices - Guidance on Selection of Tests", International Standards Organisation

[150] ISO 10993, Part 5, (1999), "Biological Evaluation of Medical Devices - Tests for Cytotoxicity—In Vitro Methods", International Standards Organisation

[151] ISO 10993, Part 6, (2007), "Biological Evaluation of Medical Devices - Tests for Local Effects after Implantation", International Standards Organisation

[152] ISO 10993, Part 9, (1999), "Biological Evaluation of Medical Devices - Degradation of Materials Related to Biological Testing", International Standards Organisation

[153] ISO 10993, Part 11, (2006), "Biological Evaluation of Medical Devices - Tests for Systemic Toxicity", International Standards Organisation

[154] ISO 10993, Part 12, (2002), "Biological Evaluation of Medical Devices - Sample Preparation and Reference Materials", International Standards Organisation

[155] Nickel Electro Ltd., (2004), "The Clifden Range – Stirred Baths: NE4 Series", User's Manual

[156] Hanna Instruments, (2002), "HI9813 Instructions Manual"

[157] Watson – Marlow, (2006), "Watson - Marlow Bredel Manuals: Watson-Marlow 323E, 323S, 323U and 323Du pumps"

[158] Kuzmanic, N. et al., (2001), "Suspension of Floating Solids with Up-Pumping Pitched Blade Impellers; Mixing Time and Power Characteristics", Chemical Engineering Journal, Vol. 84, pp. 325 – 333

[159] Naher, S. et al, (2003), "Simulation of The Stir Casting Process, Journal of Materials Processing Technology, Vol. 143 - 144, pp. 567 – 571

[160] Design-Expert Software, Version 7.1.4, (2005), "User's Guide, Technical Manual", Stat-Ease Inc., Minneapolis, MN

[161] Tang, B., (2001), "Theory of J-Characteristics for Fractional Factorial Designs and Projection justification of Minimum G_2-Aberration", Biometrika, Vol. 88, pp. 401 – 407

[162] Butler, N. A., (2003), "Minimum Aberration Construction Results for Nonregular Two - Level Fractional Factorial Designs", Vol. 90, pp. 891 – 898

[163] Box, G. E. P. et al., (2005), "Statistics for Experimenters: Design Innovation, and Discovery, 2nd Ed. Hoboken, NJ: John Wiley & Sons

[164] Box, G. and Behnken, D., (1960), "Some New Three. Level Designs for the Study of Quantitative. Variables", Technometrics, Vol. 2, pp. 455 – 475

[165] Chatterjee, S. et al., (1977), "Regression Analysis by Example", 2nd Ed., Wiley and Sons, Inc., pp. 200-202

[166] Pierlot, C., (2008), "Design of Experiments in Thermal Spraying: A Review", Surface and Coatings Technology, Vol. 202, pp. 4483 - 4490

[167] Montgomery, D, C., (1984), "Design and Analysis of Experiments", 2nd Edition, John Wiley & Sons, New York

[168] Louer, D., (1998), "Advances in Powder Diffraction Analysis", Acta Crystallographica, Vol. A54, pp. 922 – 933

[169] Rogers, K., (2004), "The use of diffraction for the analysis of biomaterials", 2nd Annual Biomaterials Workshop, Cranfield University, UK

[170] Santos, E. A. et al., (2008), "Surface Energy of Hydroxyapatite and β-Tricalcium Phosphate Ceramics Driving Serum Protein Adsorption and Osteoblast Adhesion", Journal of Materials Science: Materials in Medicine, Vol. 19, pp. 2307–2316

[171] CelRef 3.0, (1989), "Least squares Cell Refinement Program'', CNRS. Grenoble

[172] McLaughlin, M. et al., (2005), "Particle Size Analysis- When to use the Fraunhofer Approximation versus the Mie Theory", PDS-Analytical Development, Patheon Inc.

[173] ISO 13320, (1999), "Particle Size Analysis - Laser Diffraction Methods: Part 1: General Principles", International Standards Organisation

[174] ISO 14887, (2000), "Sample Preparation - Dispersing Procedures for Powders in Liquids", International Standards Organisation

[175] Kelleher, M., (2003), "Preparation of Metal Oxide Additive Particles via Mechanical Methods and their Influence on Subsequent Fabrication, Microstructural and Electrical Properties of Commercial ZnO Varsitors", Ph.D Thesis, Dublin City University

[176] Brunauer, S, et al., (1938), "Adsorption of Gases in Multimolecular Layers", Journal of the American Chemical Society, Vol. 60, pp. 309

[177] Micromeritics, (2001), "Porisometry", AutoPore III Porosimeter. Micromeritics Inc., Atlanta, GA.

[178] Micromeritics, (1992), "AccuPyc 1330 Pycnometer; Operator's Manual V2.01", Micromeritics Inc., Atlanta, GA.

[179] He, Y. B. et al., (2001), Particle Movement in Non-Newtonian Slurries: The Effect of Yield Stress on Dense Medium Separation", Chemical Engineering Science, Vol. 56, pp. 2991 - 2998

[180] He, J. H., (2004), "Variational principle for non-Newtonian lubrication: Rabinowitsch fluid model", Applied Mathematics and Computation, Vol. 157,pp. 281 – 286

[181] Rheology International Ltd., (2004), "Rheology International Series 2 Viscometer: RI:2:M Operational Manual"

[182] Maude, A. D. et al., (), "Approximate Theory for Oscillatory Experiments with a Cone-and-plate Viscometer", Nature, Vol. 201, pp. 913 – 914

[183] ASTM B213, (2003), "Standard Test Method for Flow Rate of Metal Powders", American Society of Testing and Materials

[184] Billiau, A. et al., (1977), "Human Interferon: Mass Production in a Newly Established Cell Line, MG-63. Antimicrobial Agents Chemotheraphy, Vol. 12, pp. 11 – 15

[185] CellTiter 96® AQ_{ueous} One Solution Cell Proliferation Assay (MTS), Promega

[186] JCPDS 9-169, "β-Tricalcium Phosphate", Joint Committee for Powder Diffraction Standards, International Committee for Diffraction Data

[187] Gibson, I. R. et al., (2001), "Effect of Powder Characteristics on the Sinterability of Hydroxyapatite Powders", Journal of Materials Science: Materials in Medicine, Vol. 12, pp. 163 – 171

[188] ISO 9276-1, (1998), "Representation of Results of Particle Size Analysis – Part 1: Graphical Representation", International Standards Organisation

[189] Suzuki, S. et al., (1998), "Preparation of Needle-Like Hydroxyapatite", Journal of Materials Science Letters, Vol.

[190] Joseph, R. et al., (2002), "Effect of Hydroxyapatite Morphology/Surface Area on the Rheology and Processibility of Hydroxyapatite Filled Polyethylene Composites", Biomaterials, Vol. 23, pp. 4295 – 4302

[191] Sun J. S. et al., (1997), "Effect of Hydroxyapatite Particle Size on Myoblasts and Fibroblasts", Biomaterials, Vol. 18, pp. 683 – 690

[192] Cheung H. A. et al., (1989), "Growth of Osteoblasts on Porous Calcium Phosphate Ceramic: An In Vitro Model for Biocompatibility Study", Biomaterials, Vol. 10, pp. 63 – 67

[193] Nakashima Y, et al., (1994), "Stimulatory Effects of Ceramic Particles on the Production of Bone Resorbing Mediators", Bioceramics, Vol. 7, pp. 305 – 309

[194] Saffar J. L. et al., (1993), "Regulation of Osteoclastic Resorption by Prostanoids *In Vivo*", C R Sci. Soc. Biol. Fil., Vol. 187, pp. 608 - 619

[195] Flanagan A. M. et al., (1995), "The Role of 1,25-dihydrocholecalciferol and prostaglandin E_2 in the Regulation of Human Osteoclastic Bone Resorption *In Vitro*", Int. J. Exp. Pathol., Vol. 76, pp. 37 – 42

[196] Evans E. J. et al., (1991), "Studies on the Mechanism of Cell Damage by Finely Ground Hydroxyapatite Particles *In Vitro*, Clinical Materials, Vol. 7, pp. 241 - 245

[197] Higashi T. et al, (1996), "Influence of Particle Size of Hydroxyapatite as a Capping Agent on Cell Proliferation of Cultured Fibroblasts", Journal of Endodontics, Vol. 22, pp. 236 – 239

[198] Andrade, J. D. et al., (1973), "Interfacial Phenomena and Biomaterials," Medical Instrumentation, Vol. 7, pp. 110 - 120

[199] Qu S. et al, (2001), "Effect of the Crystallinity of Calcium Phosphate Ceramics on Osteoblast Proliferation In Vitro", Journal of Materials Science Letters, Vol. 20, pp. 331 - 332

[200] Evans, E. J., (1994),"Cell Damage In Vitro Following Direct Contact with Fine Particles of Titanium, Titanium Alloy and Cobalt-Chromemolybdenum Alloy", *Biomaterials*, Vol. 15, pp. 713 - 717

[201] Lang, H. et al., (1989), "Comparative Test of the Soluble Toxicity of Hydroxyapatite Ceramics Using Human and Animal Osteoblasts", Deutsch Zahnarztl Z., Vol. 44, pp. 135 - 137

APPENDIX A

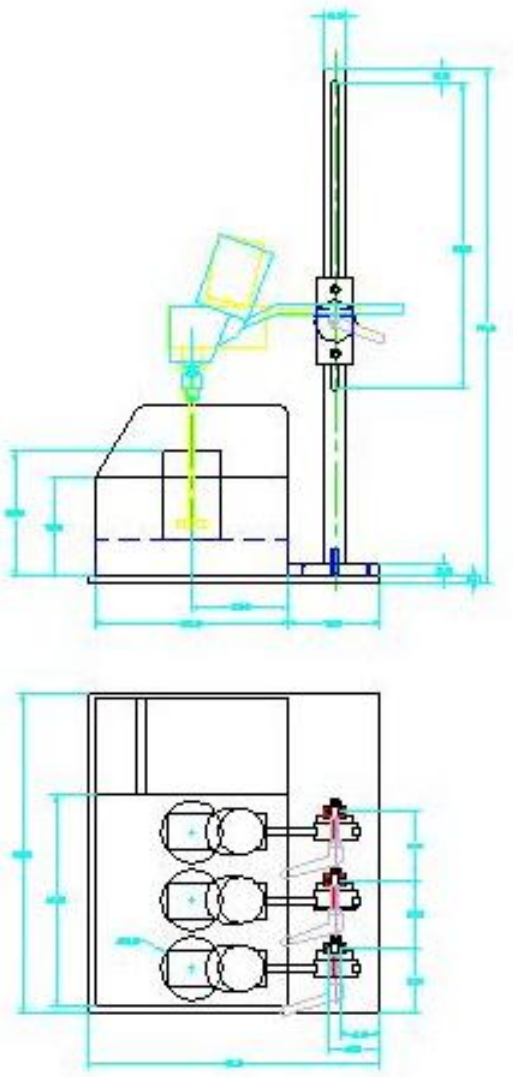

Figure A1: Computer aided drawing (2D) of the chemical precipitation set-up

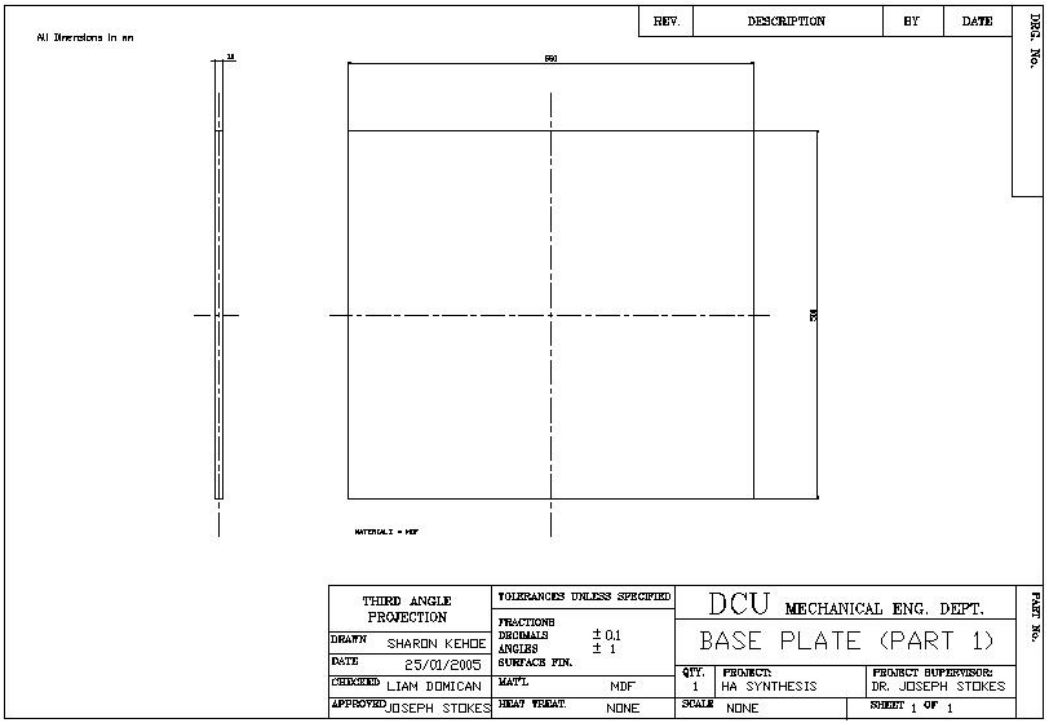

Figure A2: Computer aided drawing (2D) of the the base plate (part 1)

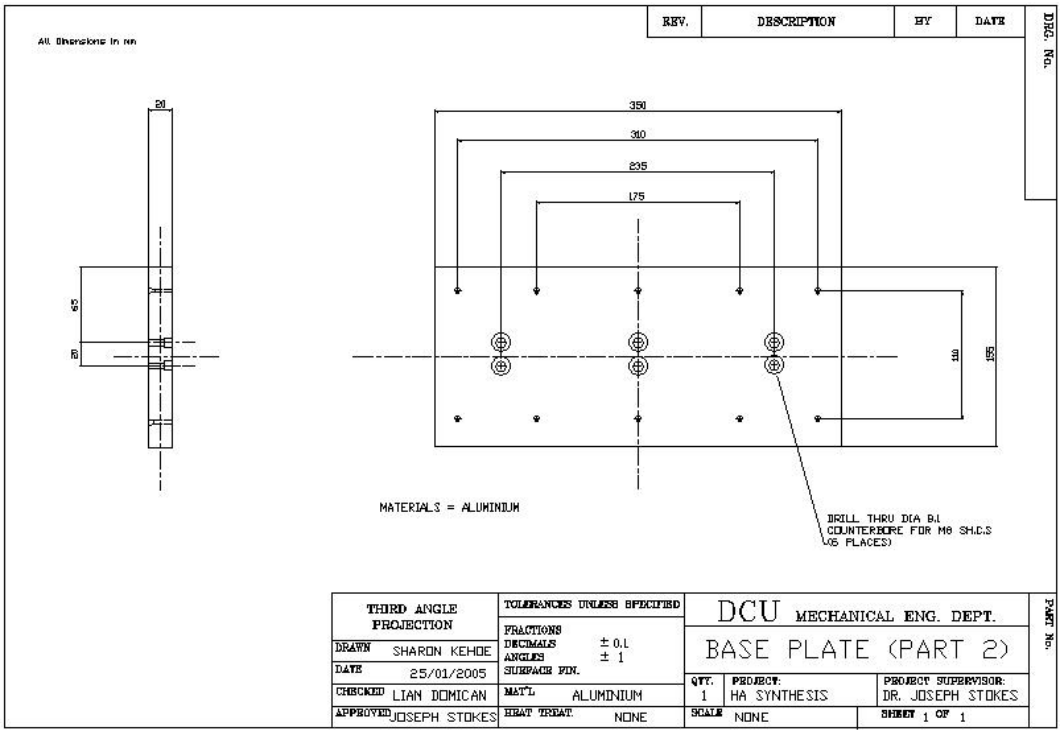

Figure A3: Computer aided drawing (2D) of the base plate (part 2)

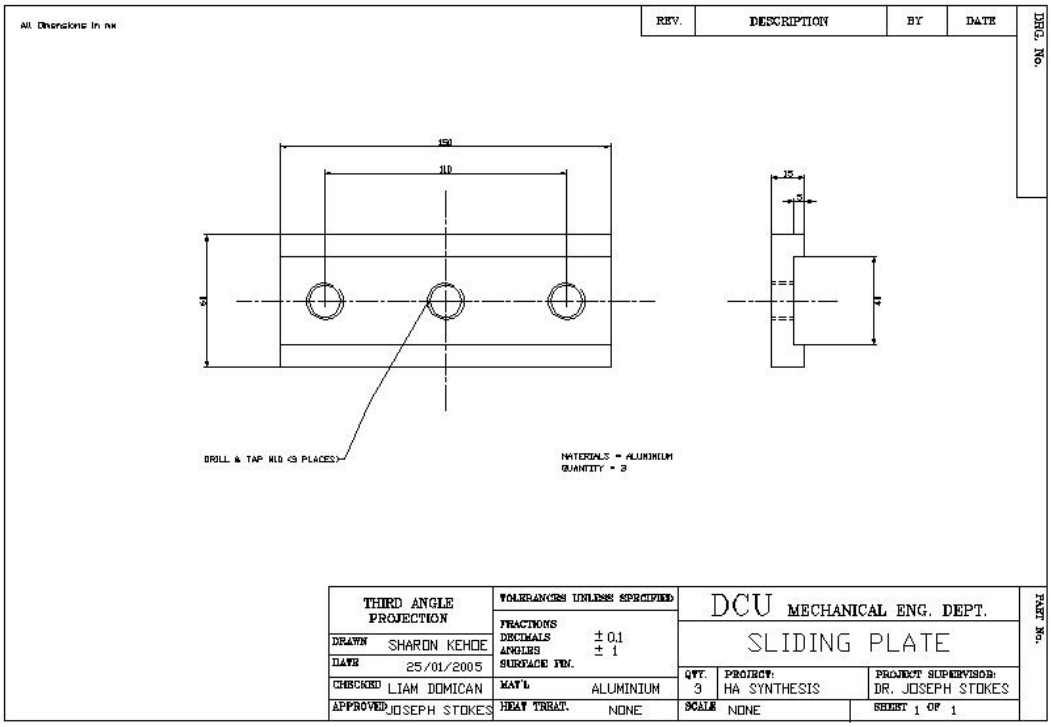

Figure A4: Computer aided drawing (2D) of the sliding plate

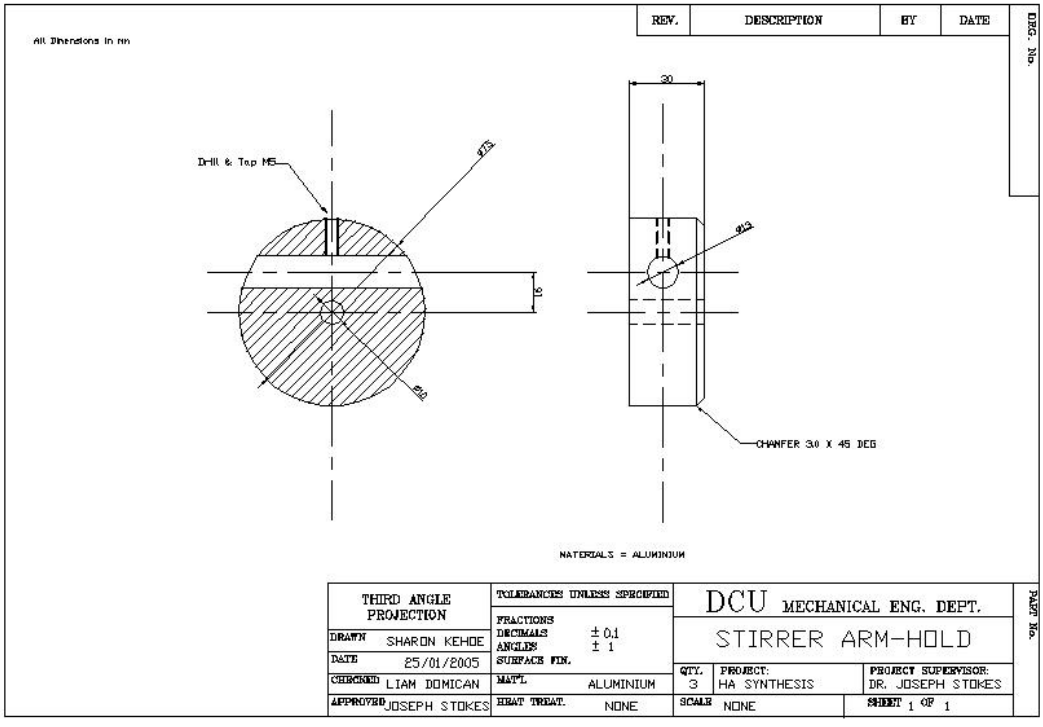

Figure A5: Computer aided drawing (2D) of the stirrer arm-hold

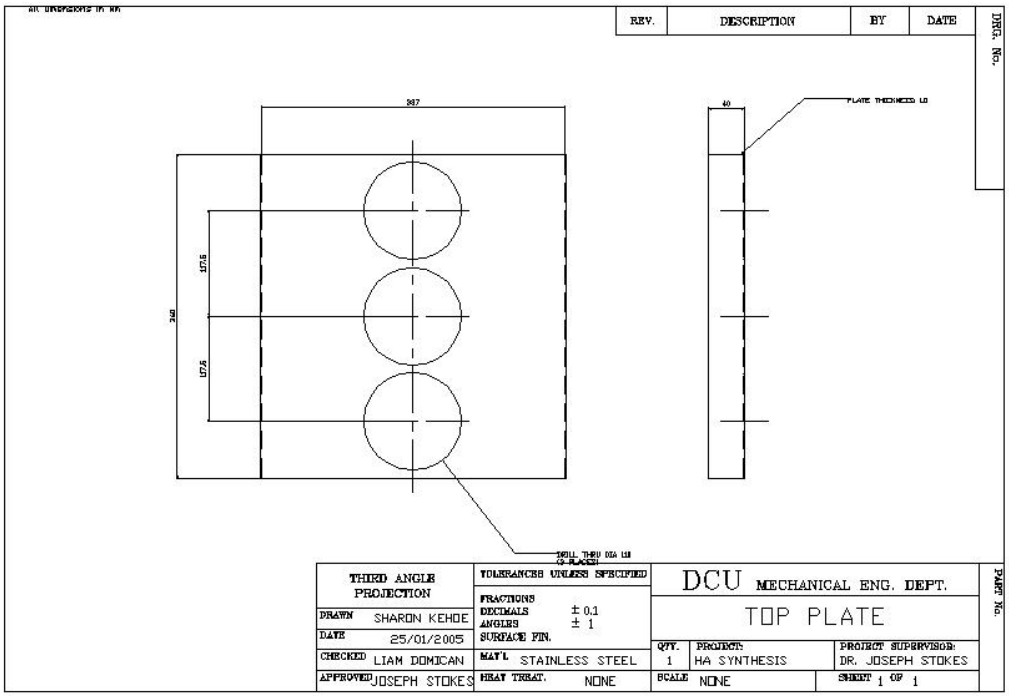

Figure A6: Computer aided drawing (2D) of the top plate

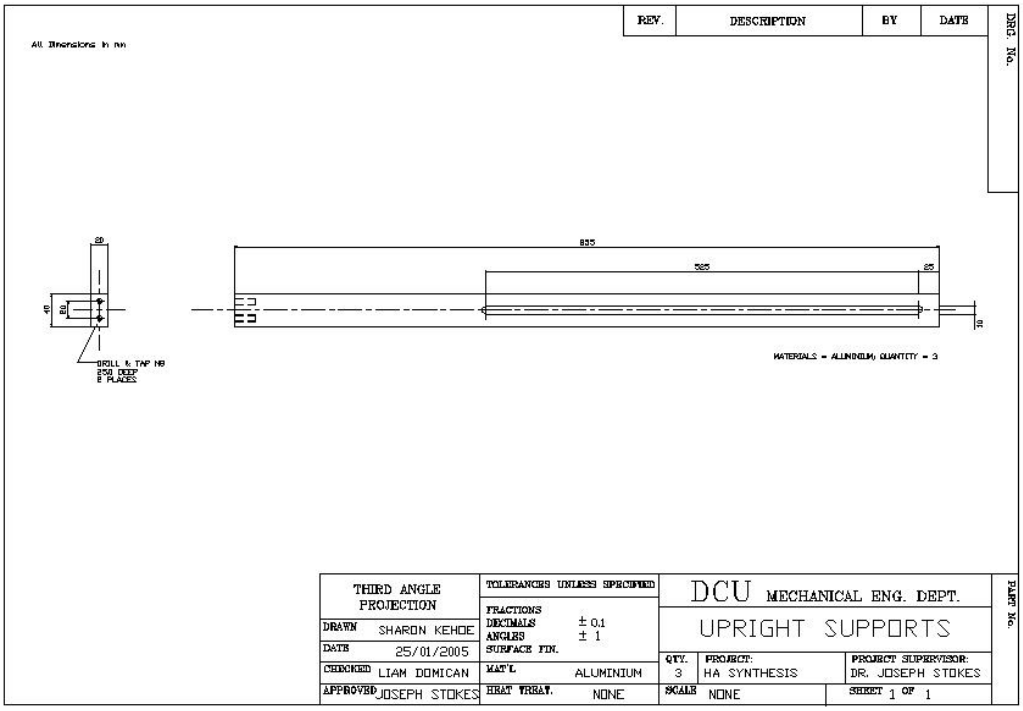

Figure A7: Computer aided drawing (2D) of the upright supports

APPENDIX B

Design Expert software was also used to correlate between the process factors and the responses using the Multiple Linear Regression (MLR) method for both the screening (fractional factorial) experimental design and the optimisation (box-behnken) design. With MLR, the coefficients of the model are computed to minimise the sum of squares of the residuals, (that is, the sum of squared deviations between the observed and fitted values of each response). The least squares regression method yields small variances for the coefficients and small prediction errors. It is also important to note that MLR separately fits one response at a time and hence assumes them to be independent

For both the screening and optimisation approach, an iterative model fitting process was used in this research. First, a full linear/quadratic model is assumed, and significance tests (t-tests) are performed on each model coefficient. Insignificant terms are removed and the fitting process is repeated again, using a linear/quadratic model. The significance tests are repeated and insignificant terms, if any, are removed. The process is repeated until there are no insignificant terms. At this point, if the model contains two-factor interaction or quadratic terms, it is checked for hierarchy. Hierarchical terms are linear terms that may be insignificant by themselves but are part of significant higher order terms. For example, x_1 and x_3 are hierarchical terms of x_1x_3, a two-factor interaction term. If x_1x_3 is a significant term in the model, x_1 and x_3 are usually included in the model to maintain hierarchy. A hierarchical model allows for conversion of models between different sets of units. The elimination of insignificant terms can be performed, either manually or automatically. The three automatic procedures of evaluating all possible regression equations (or selection of variables) are explained in the following sections [160].

A. Forward Selection Procedure

This procedure begins with only the constant term, and the first variable added is the one with the highest simple correlation with y. If the regression coefficient of this variable is significant it remains in the equation and a new search for the second variable with highest correlation with y is begin, after y has been adjusted for the effect of the first variable and the significance of the regression coefficient of the second variable is then tested. If the regression coefficient is significant, a search for a third variable is made in the same way. The procedure is completed when the last variable entered to the equation has insignificant regression coefficient or all variables are included. The test statistic for this selection procedure is the standard t or F-statistic (which equal to t^2).

B. Backward Elimination Procedure

In this procedure, the full equation is fitted and sequentially eliminates one variable each time. The variable with the smallest contribution to the reduction of error is eliminated first, or the variable with the smallest t ratio (that is, the ratio of the regression coefficient to its standard error) and so on. In the case of more than one variable that have insignificant t ratio, the procedure operates by dropping the variable with the smallest insignificant t ratio and the equation with the remaining variable is then fitted and the ratios for the new regression coefficient are tested. The procedure stopped when all the t ratios are significant or all but one variable has been deleted.

C. Stepwise Regression Method

This method is basically a Forward selection. However, the possibility of eliminating a variable that might be added in earlier stage, as in backward procedure, is considered. The calculation made for inclusion and deletion of variables are the same as Forward and Backward procedures. This procedure has the advantage of assuming different or similar levels of significance for inclusion or deletion of variables from the regression equation.

At this stage the final reduced model can be build up as determined by applying the above steps. This model contains only the significant terms and the terms, that necessary to maintain hierarchically. Also, a reduced quadratic ANOVA table can be produced.

Methods For Determining The Significance Of The Regression Coefficients (Experimental Factors)

Once the model fitting is performed, the next step is residual analysis to validate the assumptions used in the ANOVA and assess the graphical representations (such as, Pareto charts and normalized plots). A description of each is discussed in this section.

A. ANOVA

The ANalysis Of VAriance (ANOVA) was used to test the adequacy of the models developed. The statistical significance of the models developed and each term in regression equation were examined using the sequential F-test, lack-of-fit test and other adequacy measures (such as, R^2, Adj- R^2, Pred. R^2 and Adq. Precision ratio) using the same software to obtain the best fit. The Prob.>F (sometimes, it is called the p-value) of the model and of each term in the model can be computed by means of ANOVA. If the Prob.> F of the model and of each term in the model does not exceed the level of significance (α= 0.05) then the model may be considered adequate within the confidence interval of (1- α). For the lack-of-fit test, the lack of fit could be considered insignificant if the Prob.>F of the lack of fit exceeds the level of significance. Table 3-11 below shows a summary of the ANOVA table (from this research). The equations by which the adequacy measures can be calculated are shown below using Equations. 3.4 to 3.8 [160, 167].

Table C1: ANOVA table of full model in the box-behken design

Source	SS	df	MS	$F_{cal.}$- Value	p-value or Prob > F
Model	SS_M	p			
A-Synthesis Temperature	SS_1	1			
B-Stirring speed	SS_2	1			
C-Ripening Time	SS_3	1			From table or software library
AB	SS_{12}	1	Each SS divided by its df	Each MS divided by MS_E	
AC	SS_{13}	1			
BC	SS_{23}	1			
A^2	SS_{11}	1			
B^2	SS_{22}	1			
C^2	SS_{33}	1			
Residual	SS_R	N-p-1			-
Lack of Fit	SS_{lof}	$N - p - n_0$			From table
Pure Error	SS_E	n_{0-1}			-
Cor Total	SS_T	N - 1	-	-	-

Where; P is the number of coefficients in the model, N is the total number of runs, n_0 is the number of centre points, df is the degree of freedom, MS is the mean square and SS is the sum of squares

R^2 is a measure of the variation around the mean explained by the model, such that:

$$R^2 = 1 - \left[\frac{SS_R}{SS_R + SS_M} \right] \qquad \textit{Equation (1)}$$

Where, SS_R is the residual sum of squares and SS_M is the mean sum of squares. Adj R^2 is a measure of the variation around the mean explained by the model, adjusted for the number of terms in the model, such that:

$$AdjR^2 = 1 - \left[\left(\frac{SS_R}{df_R} \right) \times \left(\frac{SS_R + SS_M}{df_R + df_M} \right)^{-1} \right] \qquad \textit{Equation (2)}$$

Where SS_R is the residual sum of squares and SS_M is the mean sum of squares, df_M is the model degrees of freedom and df_R is the residual degrees of freedom. Predicted R^2 is a measure of the amount of variation in new data explained by the model, whereby:

$$\Pr edR^2 = 1 - \left[\frac{PRESS}{SS_R + SS_M} \right] \qquad \textit{Equation (3)}$$

Where PRESS is the predicted residual error sum of squares; a measure of how the model fits each point in the design. The PRESS is computed by first predicting where each point should be from a model that contains all other points except the one in question. The square residuals (difference between actual and predicted values) are then summed as follows:

$$PRESS = \sum_{i=1}^{n} (y_i - \hat{y}_{i,-i})^2 \qquad \textit{Equation (4)}$$

The Adequate precision is a signal to noise ratio and compares the range of the predicted values at the design points to the average prediction error. Ratios greater than 4 indicate adequate model discrimination.

$$Adeq.precision = \left[\frac{Max(\hat{Y}) - Min(\hat{Y})}{\sqrt{\frac{p \times MS_R}{n}}} \right] = \frac{\rho\delta 2}{n} \qquad \textit{Equation (5)}$$

Where; MS_R is the root mean square, p is the number of model parameters (including intercept b_0), n is the number of experiments, and δ^2 is the residual mean square from the ANOVA table.

B. Pareto Charts

A graphical display of data, Pareto charts and main effect plots, which were obtained after performing MLR and ANOVA, were used to identify the relationship between the input variables (for example, reaction synthesis temperature) and the system responses (for example, crystallinity). The change in response, produced by the change in the level of a variable, is the effect of that variable. The Pareto chart analyses the magnitude and the importance of each process variable effect. The length of bars in the bar chart is proportional to the standardized effect (estimated effect divided by its standard error). From this chart, absolute values of effects can be compared. The mean for a given level of variable is the average of all responses obtained for that level. So, the response means for each process variable level are plotted connecting the points for each process variable. The main effect plot is useful to determine which process variables influence the response and also to compare the relative strengths of effects. The relative magnitudes of the process variable effects can be compared by comparing the slopes of the lines (the greater the degree of departure from horizontal, the stronger the effect). In contrast to the Pareto chart, which compares absolute values of effects, the main effect plot provides additional information on whether the change between two variable levels decreases or increases the response. Plots such as main/interaction effects, 3D graphs and contours were also examined to present the factor effects on the responses found.

OPTIMISATION

Desirability Approach

The desirability method is recommended due to its simplicity, availability in the software and provides flexibility in weighting and giving importance for individual response. Solving such multiple response optimisation problems using this technique consists of using a technique for combining multiple responses into a dimension less measure performance called overall desirability function. The desirability approach consists of transforming of each estimated response, Y_i, into a dimensionless utilities bounded by $0 < d_i < 1$, where a higher d_i value indicates that the response value Y_i is more desirable, if $d_i = 0$ this means a completely undesired response or vice versa when $d_i = 1$ [160]. In the current research the individual desirability for each response d_i was calculated using Equations 3-9 to 3-12. The shape of the desirability function can be changed for each goal by the weight field 'wt_i'. Weights are used to give added emphasis to the upper/lower bounds or to emphasize the target value. Weights could be ranged between 0.1 and 10 where weight greater than one gives more emphasis to the goal, while weight less than one gives less emphasis to the goal. With weight value of one, this will make the d_i's vary from zero to one in a linear mode. In the desirability objective function (D), each response can be assigned an importance (r), relative to the other responses. Importance varies from the least important a value of 1(+), to the most important a value of 5(+++++). If the varying degrees of importance are assigned to the different responses, the overall objective function is shown below in Equation 3-13. Where n is the number of responses in the measure and T_i is the target value of i^{th} response [160].

For a goal of maximum response, the desirability would be defined by:

$$d_i = \begin{cases} 0 & , \quad Y_i \le Low_i \\ \left(\dfrac{Y_i - Low_i}{High_i - Low_i} \right)^{wt_i} & , \quad Low_i \langle Y_i \langle High_i \\ 1 & , \quad Y_i \ge High_i \end{cases} \qquad \textit{Equation (6)}$$

For a goal of minimum, the desirability defined by:

$$d_i = \begin{cases} 1 & , \quad Y_i \le Low_i \\ \left(\dfrac{High_i - Y_i}{High_i - Low_i} \right)^{wt_i} & , \quad Low_i \langle Y_i \langle High_i \\ 0 & , \quad Y_i \ge High_i \end{cases} \qquad \textit{Equation (7)}$$

For a goal as a target, the desirability defined by:

$$d_i = \begin{cases} \left(\dfrac{Y_i - Low_i}{T_i - Low_i} \right)^{wt_{1i}} & , \quad Low_i \langle Y_i \langle T_i \\ \left(\dfrac{Y_i - High_i}{T_i - High_i} \right)^{wt_{2i}} & , \quad T_i \langle Y_i \langle High_i \\ 0 & , \quad Otherwise \end{cases} \qquad \textit{Equation (8)}$$

For a goal within range:

$$d_i = \begin{cases} 1 & , \quad Low_i \langle Y_i \langle High_i \\ 0 & , \quad Otherwise \end{cases} \qquad \textit{Equation (9)}$$

the desirability will be defined by:

$$D = \left(\prod_{i=1}^{n} d_i^{r_i} \right)^{\frac{1}{\sum r_i}} \qquad \textit{Equation (10)}$$

Optimisation Approach In Design - Expert Software

The optimisation part in Design-Expert software searches for a combination of factor levels that simultaneously satisfy the requirements placed (that is, optimisation criteria) on each one of the responses and process factors (multiple response optimisation). Numerical and graphical optimisation methods were used in this work by choosing the desired goals for each factor and response. As mentioned previously, the numerical optimisation process involves combining the goals into an overall desirability function (D). The numerical optimisation feature in the design expert software package finds a point or more in the factors domain that would maximise this objective function. In a graphical optimisation with multiple responses, the software defines regions where requirements simultaneously meet the proposed criteria. Superimposing or overlaying critical response contours on a contour plot. Then, a visual search for the best compromise becomes possible. In the case of dealing with many responses, it is recommended to do numerical optimisation first, otherwise it could be impossible to uncover a feasible region. The graphical optimisation displays the area of feasible response values in the factor space. The regions that do not fit the optimisation criteria are therefore shaded [160].

Dynamic viscosity flow curves of the HAp slurry during HAp synthesis via the chemical precipitation technique, using calcium hydroxide and orthophosphoric acid as the reagents are presented in this Appendix.

APPENDIX C

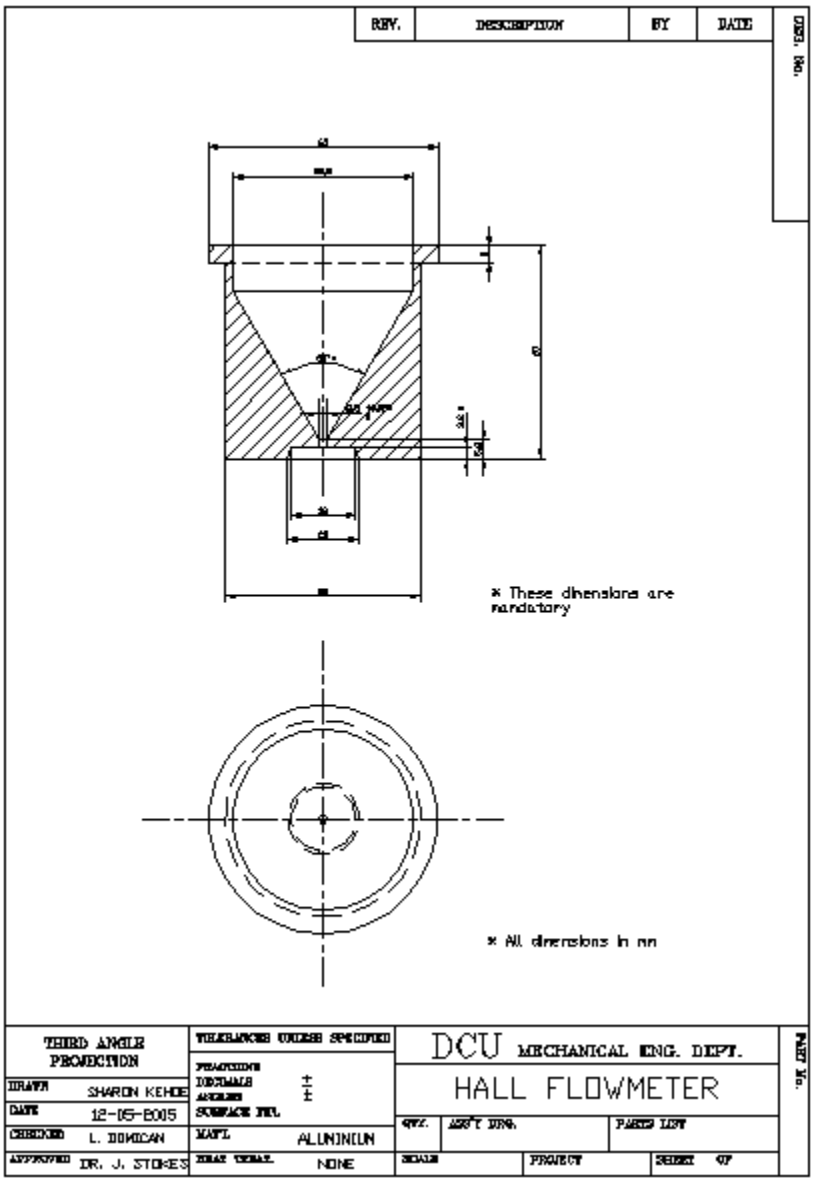

Figure B1: Computer aided drawing (2D) of the upright supports

APPENDIX D

Figure D1: Flow curves for HAp slurry during calcium hydroxide formation

(a)

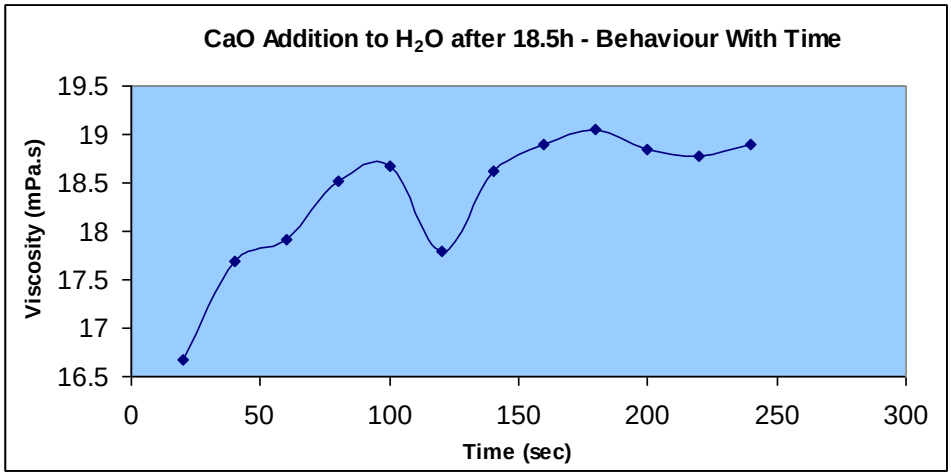

(b)

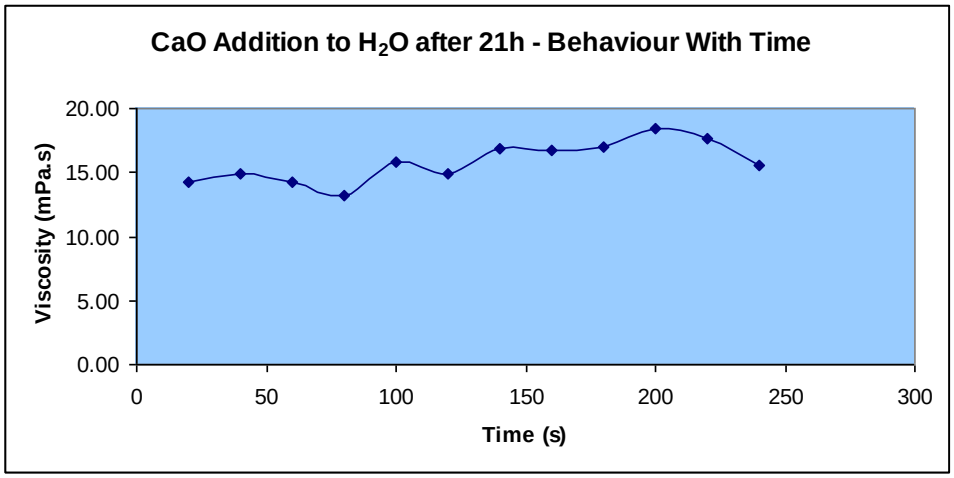

Figure D2: Flow curves for HAp slurry during addition of orthosphosphoric acid

(a)

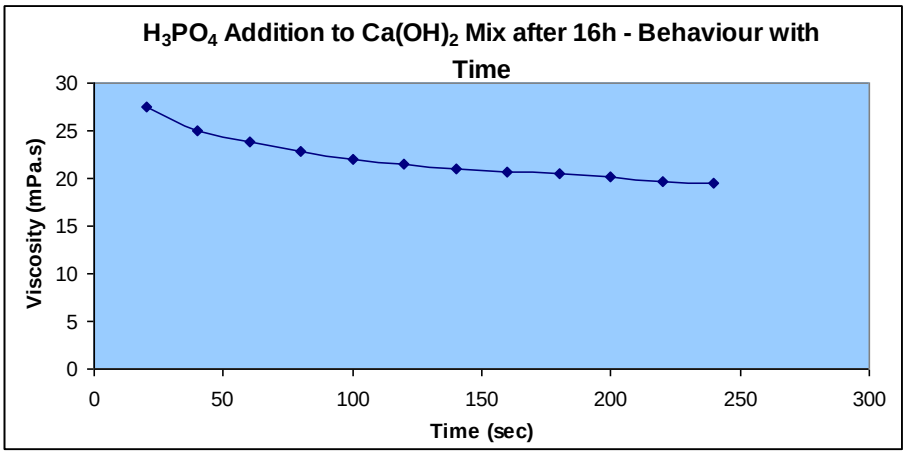

(b)

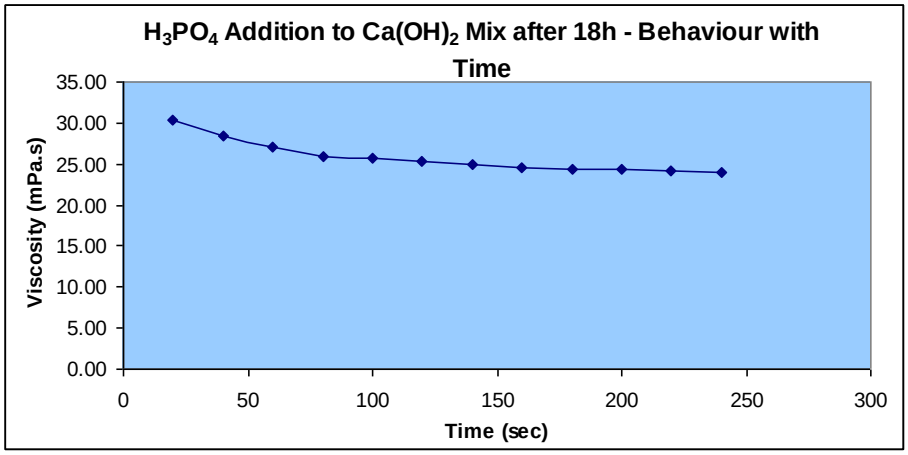

(c)

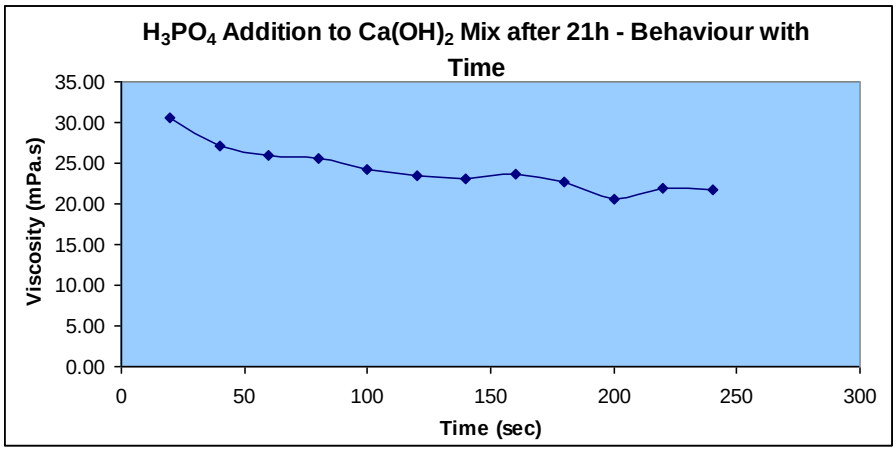

(d)

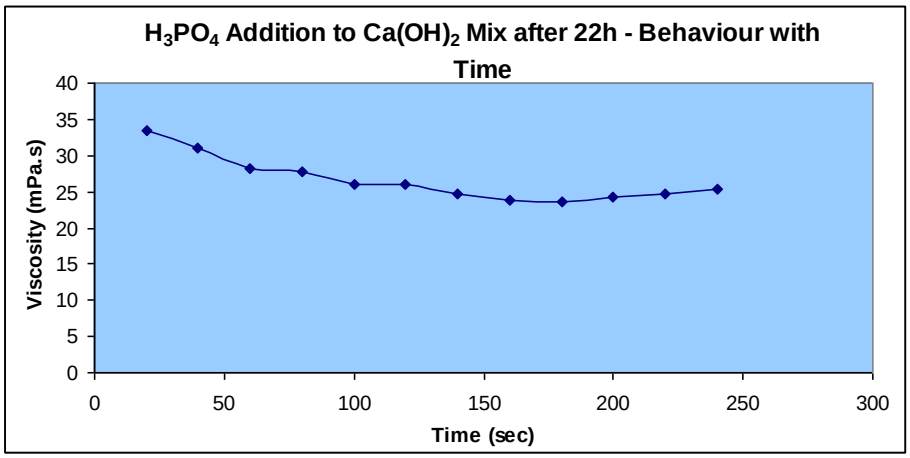
H3PO4 Addition to Ca(OH)2 Mix after 22h - Behaviour with Time
Viscosity (mPa.s)
0
5
10
15
20
25
30
35
40
0
50
100
150
200
250
300
Time (sec)

(e)

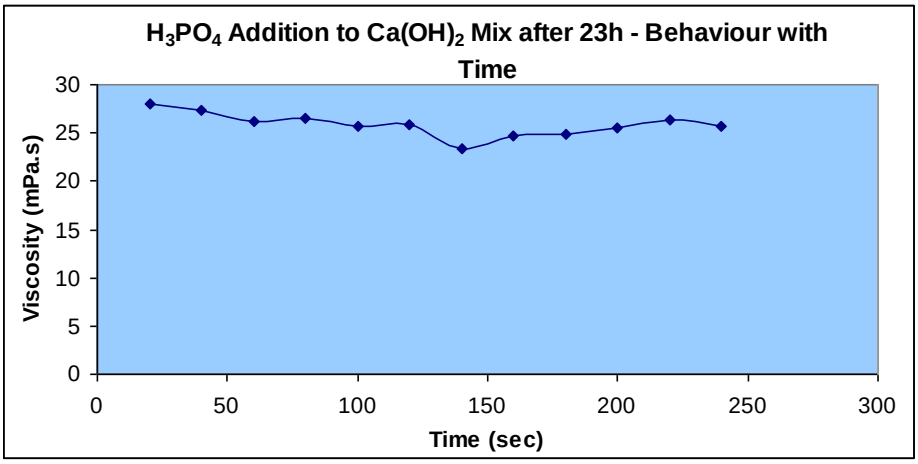
H3PO4 Addition to Ca(OH)2 Mix after 23h - Behaviour with Time
Viscosity (mPa.s)
0
5
10
15
20
25
30
0
50
100
150
200
250
300
Time (sec)

Figure D3: Flow curve for HAp slurry during HAp maturation

(a)

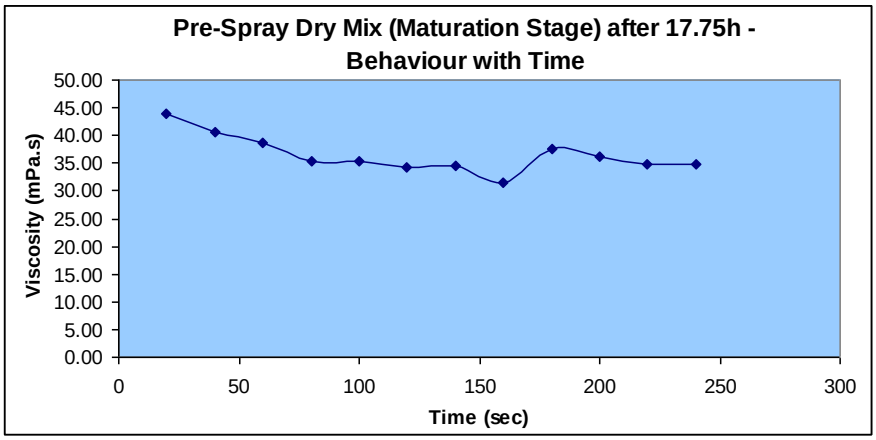

(b)

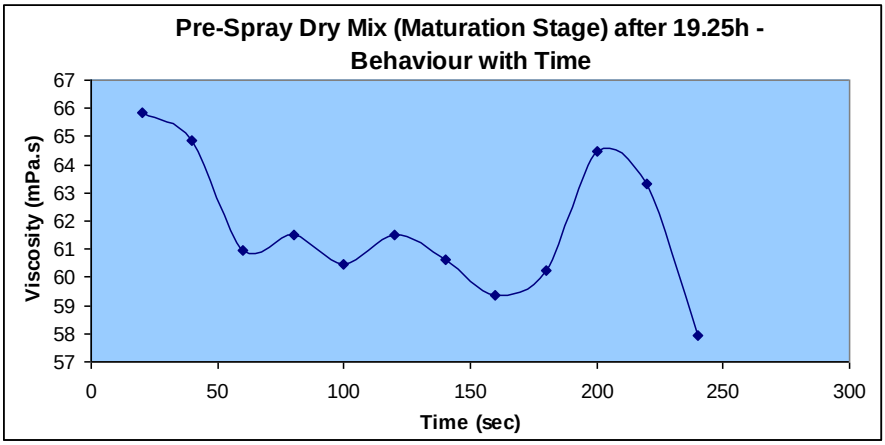

(c)

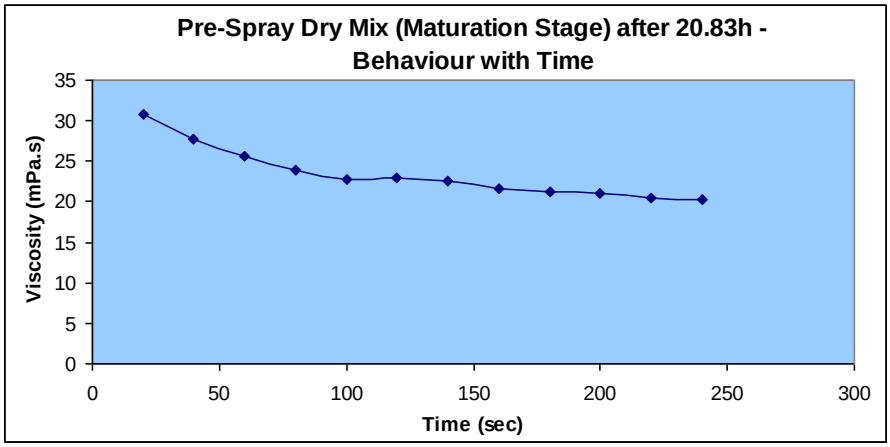

APPENDIX E

Figure E1: Repeatability results (for FFD) for phase purity (A), crystallinity (B), crystallite size in the 002 and 300 plane (C and D) and lattice parameters *a* and *c* (E and F)

(A)

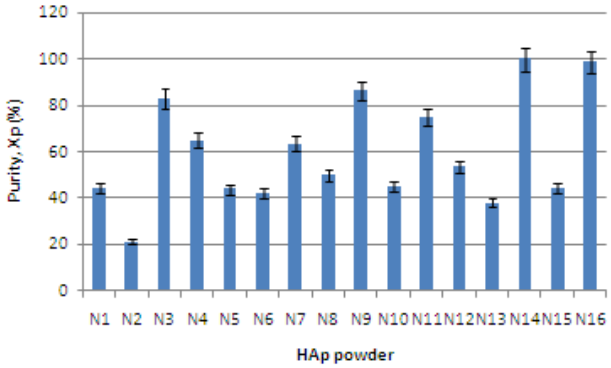

(B)

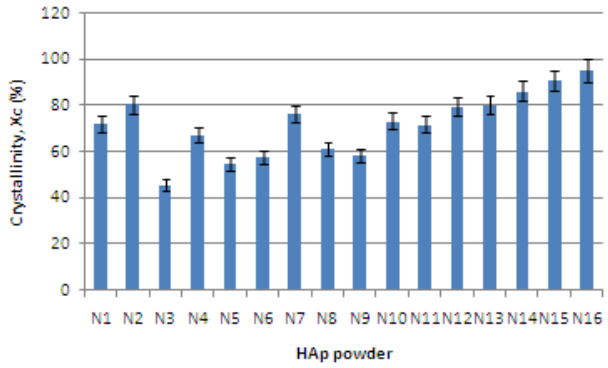

(C)

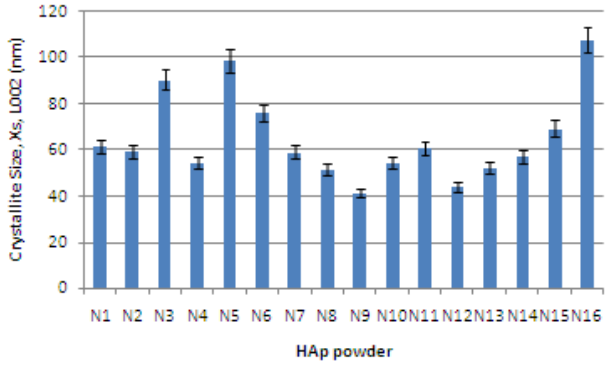

(D)

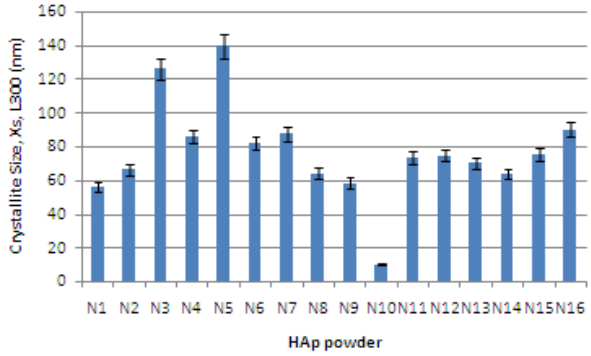

(E)

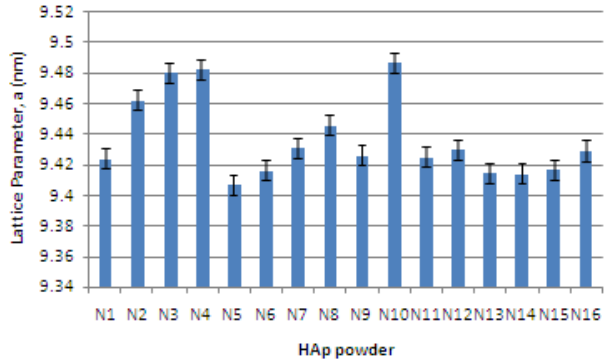

(F)

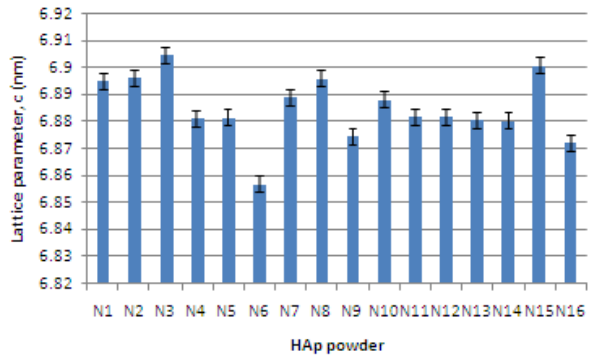

APPENDIX F

Figure F1: XRD patterns for N1, N2, N7 and N8

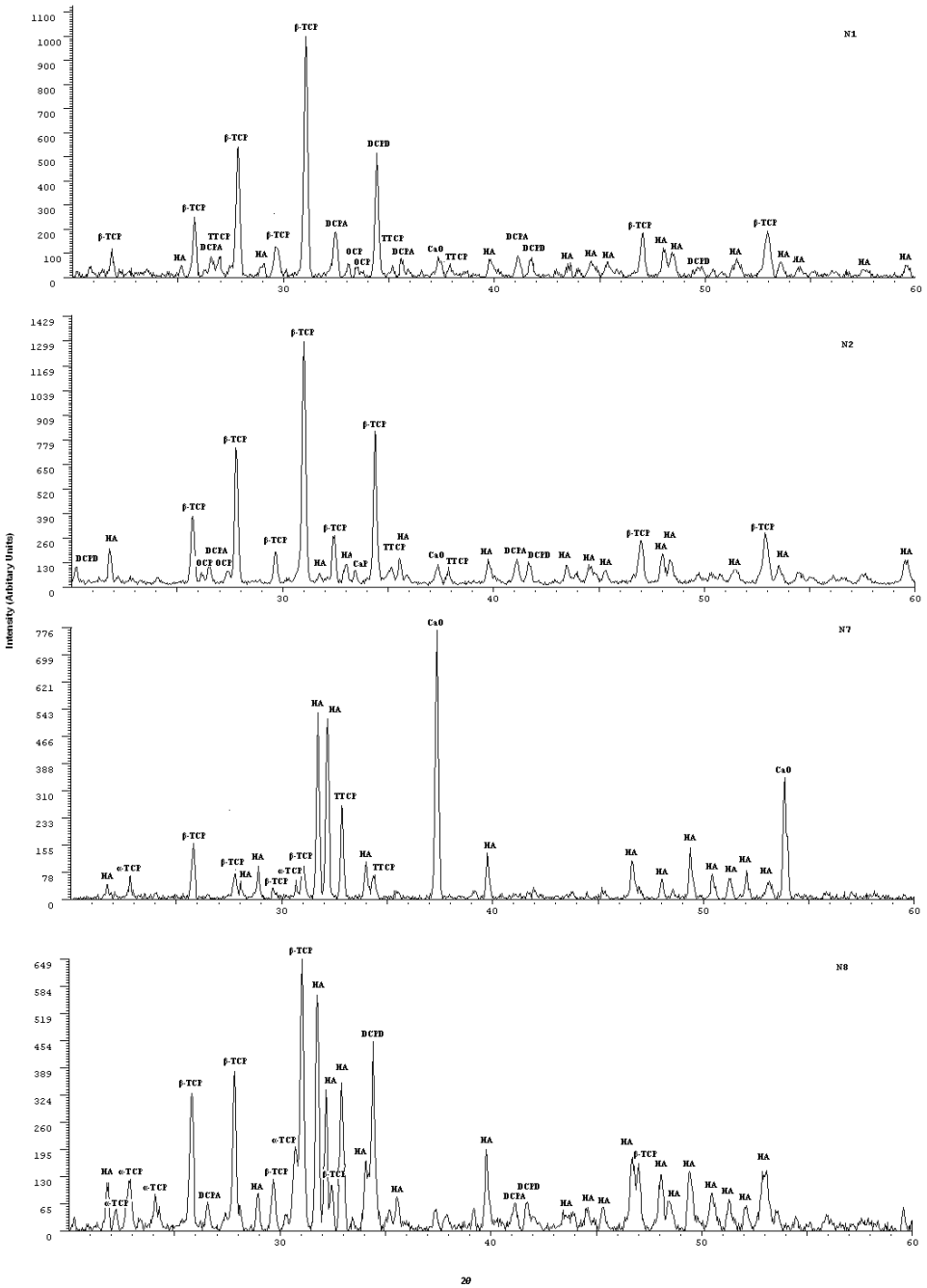

Figure F2: XRD patterns for N11 – N14

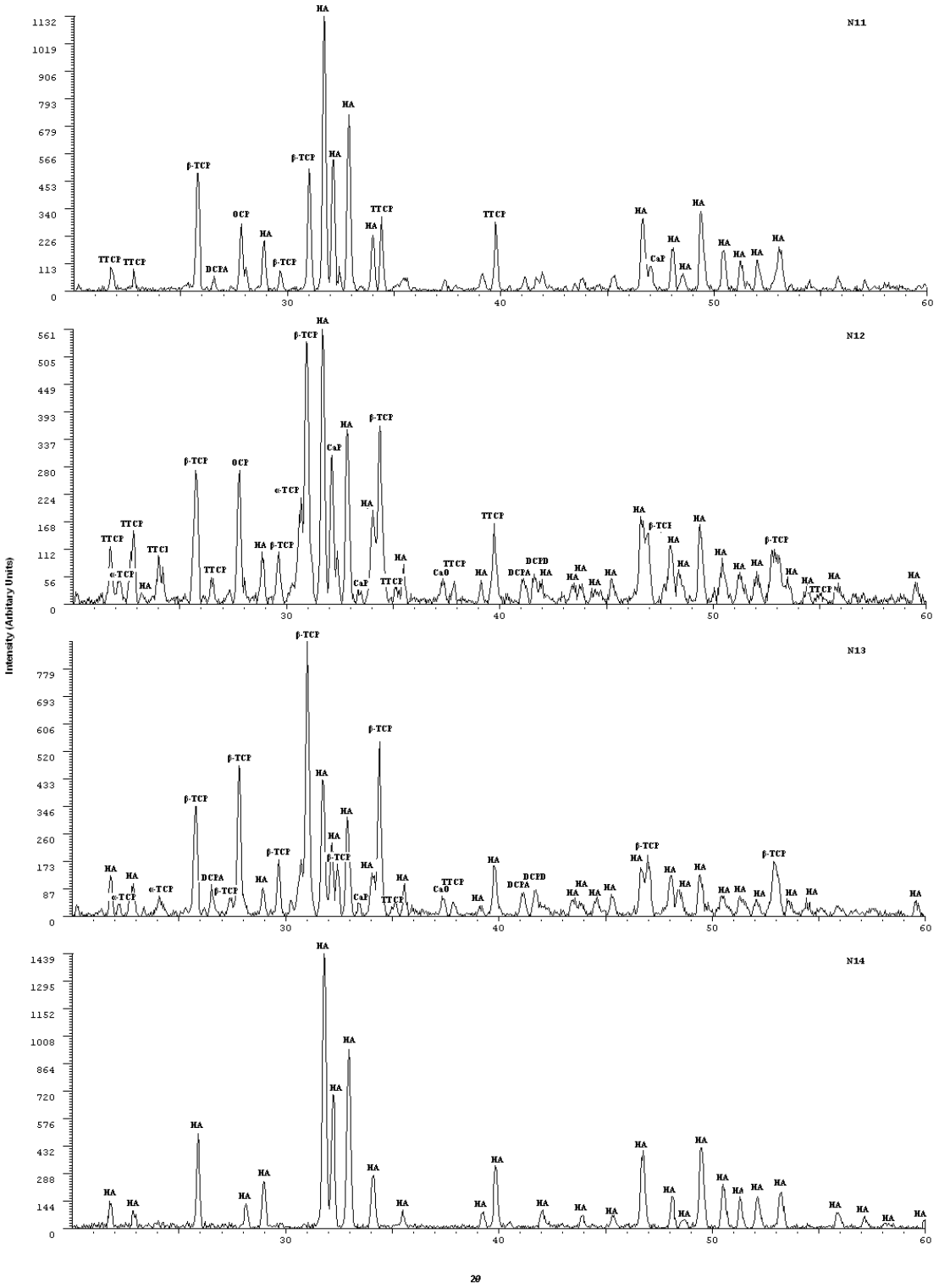

Figure F3: XRD patterns for N3 – N6

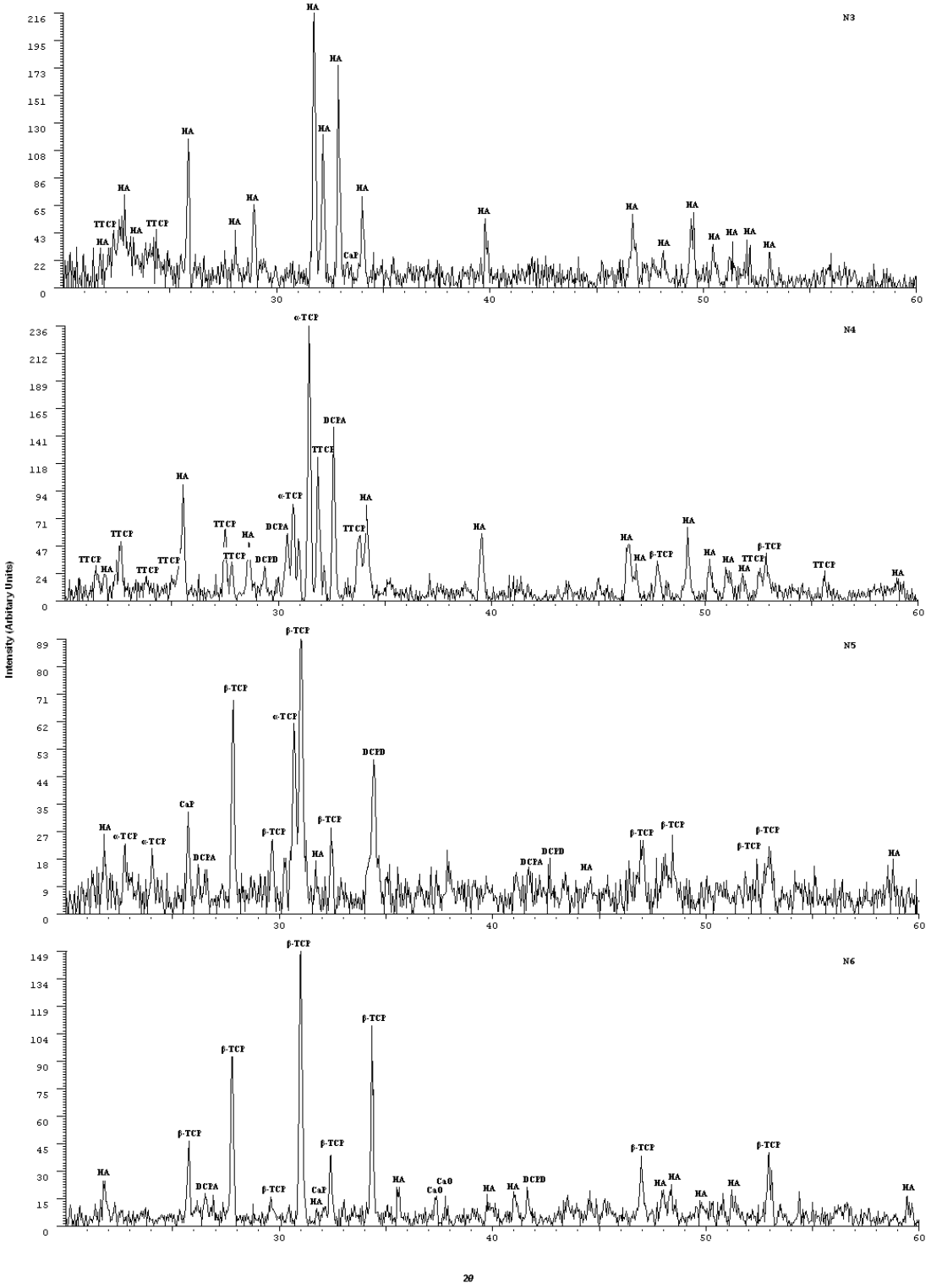

Figure F4: XRD patterns for N9, N10, N15 and N16